Final Scientific Report

Award Number: DE-EE0003850

Project Title: Optimization of Regenerators for AMRR Systems

Awardee: University of Wisconsin

Principal Investigator: Gregory Nellis

Co-Investigator: Sanford Klein

Contributing Team Members: William Brey
Alexandra Moine
Dr. Kaspar Nielsen

Reporting Period Ending: 12/31/2014

Acknowledgment: "This material is based upon work supported by the Department of Energy under Award Number DE-EE0003850."

Executive Summary
Active Magnetic Regenerative Refrigeration (AMRR) systems have no direct global warming potential or ozone depletion potential and hold the potential for providing refrigeration with efficiencies that are equal to or greater than the vapor compression systems used today. The work carried out in this project has developed and improved modeling tools that can be used to optimize and evaluate the magnetocaloric materials and geometric structure of the regenerator beds required for AMRR Systems.

There has been an explosion in the development of magnetocaloric materials for AMRR systems over the past few decades. The most attractive materials, based on the magnitude of the measured magnetocaloric effect, tend to also have large amounts of hysteresis. This project has provided for the first time a thermodynamically consistent method for evaluating these hysteretic materials in the context of an AMRR cycle. An additional, practical challenge that has been identified for AMRR systems is related to the participation of the regenerator wall in the cyclic process. The impact of housing heat capacity on both passive and active regenerative systems has been studied and clarified within this project. This report is divided into two parts corresponding to these two efforts. Part 1 describes the work related to modeling magnetic hysteresis while Part 2 discusses the modeling of the heat capacity of the housing.

A key outcome of this project is the development of a publically available modeling tool that allows researchers to identify a truly optimal magnetocaloric refrigerant. Typically, the refrigeration potential of a magnetocaloric material is judged entirely based on the magnitude of the magnetocaloric effect and other properties of the material that are deemed unimportant. This project has shown that a material with a large magnetocaloric effect (as evidenced, for example, by a large adiabatic temperature change) may not be optimal when it is accompanied by a large hysteresis. The trade-off between these various material properties and the proper design of an AMRR system can only be evaluated correctly using the comprehensive, physics-based model developed by this project.

The development of these modeling tools and optimization studies will provide the knowledge base that is required to achieve transformational discoveries. The widespread adoption of AMRR technology will change the character of energy demand in this country and provide manufacturing jobs as well as employment associated with retrofitting existing HVAC&R applications.

Comparison of Accomplishments with Goals & Objectives

This section revisits the objectives laid out in the original proposal (as individual tasks) and compares them with the accomplishments of the project.

Modeling Hysteresis in AMRR Systems

Objective: A history-dependent entropy term will be derived, verified and eventually integrated into the AMRR model. The term will include the magnetocaloric material properties that represent the impact of hysteresis; i.e., the result of sweeping out the entire hysteresis curve during each cycle which is analogous to the net generation of thermal energy in the bed. This thermal energy provides an additional refrigeration load and leads to a degradation in the cycle performance. The behavior of the modified model will be examined as hysteresis is added in order to understand this effect and verify that the model behavior is logical and consistent.

Accomplishment: The effect of magnetic hysteresis on AMRR systems was successfully modeled using first principles. Thermodynamically, hysteresis is treated as a source of entropy generation that is proportional to the area swept by the hysteresis loop experienced locally by the material during one refrigeration cycle. The 1-D numerical model originally presented by Engelbrecht (2008) was modified to include magnetic hysteresis. The strategy was published in the paper Brey et al. (2014) and presented at the 6th IIR/IIR International Conference on Magnetic Refrigeration, THERMAG VI.

Modeling Housing Heat Capacity in AMRR Systems

Objective: A passive and active regenerator model will be developed by coupling an additional equation set that represents the heat capacity of the housing at each axial location. The resulting model is substantially more complex than the 1-D models typically used to study regenerator behavior because the participation of the housing requires the radial transport of energy and therefore the equations will be two-dimensional and transient. The modified model will be verified against the original model in the limit of zero housing heat capacity.

Accomplishment: A 2-D transient numerical model was developed using the compiled language FORTRAN. The model was originally generated for a passive (i.e., non-magnetocaloric) material interacting with its housing. The model was verified and then extended to an active material interacting with its housing.

Assess the Limits of AMRR Systems with Advanced Materials

Objective: The model including hysteresis was integrated with measured material properties for several, first order giant Magnetocaloric materials. The model was used to carry out an optimization of the AMRR system.

Accomplishment: The AMRR model including hysteresis was utilized to examine the potential performance of a hysteretic material as compared to a non-hysteretic material. For a specified refrigeration capacity and load temperature, a bed layered with $La(Fe_{1-x}Si_x)_{13}H_y$ (a hysteretic material) showed a higher COP at relatively small volumes when compared to a bed layered with Gd-Er (a non-hysteretic material) (see Figure 1). Furthermore, for a specified refrigeration capacity and regenerator volume, a bed layered with $La(Fe_{1-x}Si_x)_{13}H_y$ was shown to outperform a

bed layered with Gd-Er at large temperature span (see Figure 2). As regenerator volume increases, hysteretic losses outweigh the capacity gains associated with adding more refrigerant.

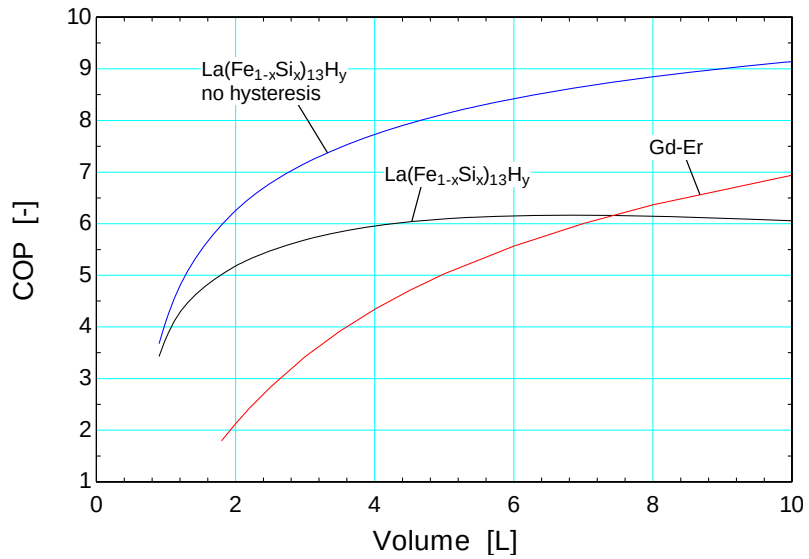

Figure 1: Coefficient of Performance (COP) as a function of regenerator volume for an AMRR spanning the temperature range 299 K to 310 K and providing 5 kW of refrigeration using a hysteretic vs non-hysteretic material. The impact of hysteresis is also shown by comparison with the no-hysteresis case.

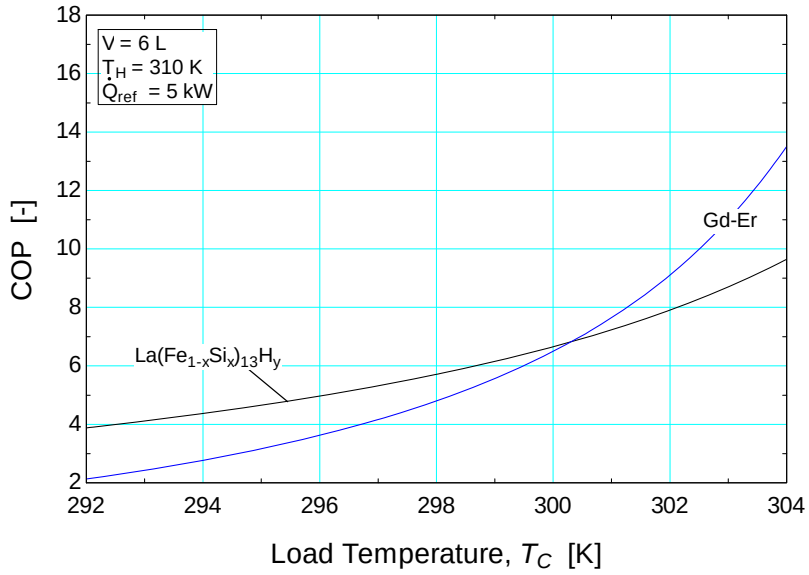

Figure 2: Coefficient of Performance (COP) as a function of load temperature with a fixed heat rejection temperature of 310 K for an AMRR using a hysteretic vs non-hysteretic material.

Examine the Trade-Off between Magnetocaloric Material Properties

Objective: The model will be used to assess the trade-off between various aspects of the magnetocaloric effect as characterized by material properties such as adiabatic temperature change and isothermal entropy change.

Accomplishment: The model was used to generate maps showing the performance of an optimally designed AMRR system in the parameter space of adiabatic temperature change and

isothermal entropy change by scaling the properties of both first- and second-order materials. The performance was quantified both in terms of COP (Figure 2) and volume-specific refrigeration. Magnetocaloric materials developers can use this map in order to assess the relative merit of their materials which might have both significant hysteresis and large magnetocaloric effect.

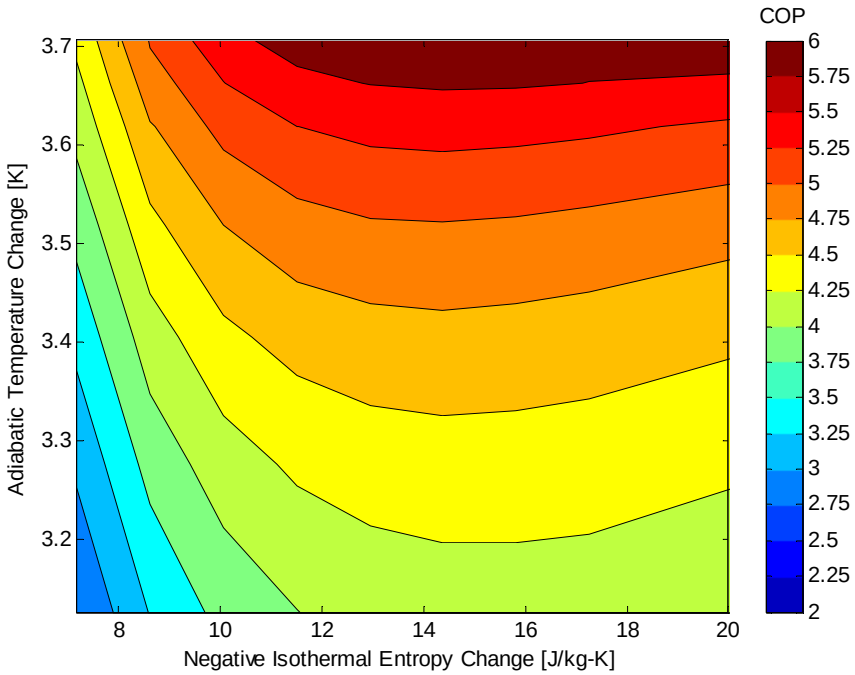

Figure 3. COP at the optimal aspect ratio as a function of negative isothermal entropy change and adiabatic entropy change for $La(Fe_{1-x}Si_x)_{13}H_y$ layered bed with a volume specific refrigeration capacity of 1.25 kW/L.

Examine the Impact of Housing Heat Capacity

Objective: Assess the importance of housing heat capacity on both a passive and active regenerator.

Accomplishment: The 2-D transient model was used to carry out a parametric study in terms of non-dimensional numbers that characterized the impact of the housing heat capacity on the performance of a passive regenerator under both oscillating and single-blow conditions as well as an AMRR system. Figure 4 illustrates the normalized COP (to the no-wall case) as a function of the two dimensionless parameters of interest: the thermal mass ratio (ψ) and the thermal wave propagation function (δ) for various values of Reynolds number.

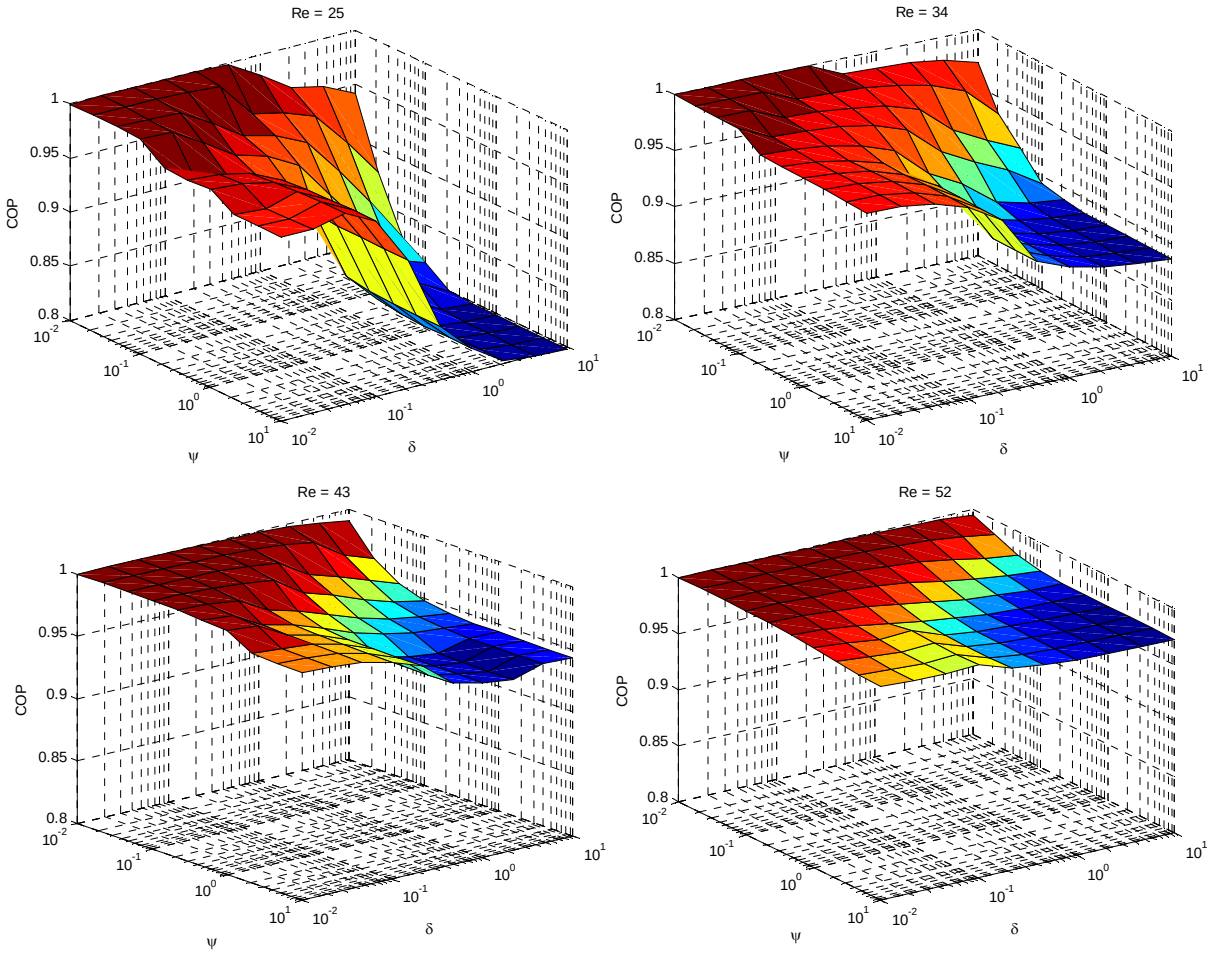

Figure 4: Surface plots showing normalized COP as a function of □ and □ for various values of Re.

Experimental Work

Objective: Use experimental data as available to improve/verify the model.

Accomplishment: The magnetocaloric measurements of an advanced material were obtained from Astronautics under conditions of increasing and decreasing field and temperature in order to quantify the magnetic and thermal hysteresis. For example, Figure 5 illustrates the magnetization of the sample under conditions of increasing temperature for both increasing and decreasing field. These data were then used within the model for the parametric study.

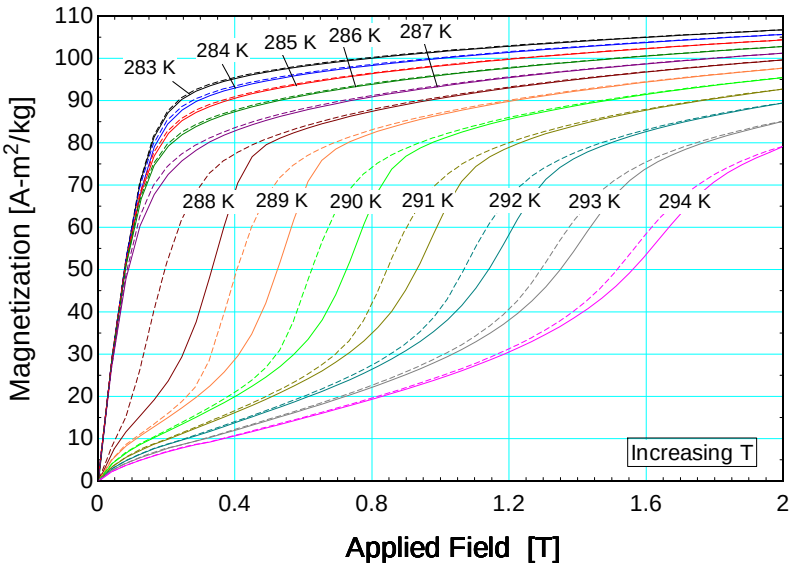

Figure 5: Magnetization as a function of applied field for increasing temperatures in JF1-142A. Solid lines indicate increasing field and dotted lines indicate decreasing field.

Model Dissemination

Objective: The model will be provided with a Graphical User Interface (GUI) and disseminated via download from the web.

Accomplishment: The model has been provided with a front-end interface (Figure 6) and can be downloaded from the UW-SEL web site and has been used by many research groups. The model is implemented in MATLAB. A baseline set of MATLAB files can be downloaded in order to simulate the most basic configuration, material, etc. These files are well-documented and so it is possible for the user to modify various aspects of the model in order to consider specific materials, regenerator geometries, applications, etc. The model is a complex, 1-D transient simulation and therefore it requires some user expertise to operate competently. This is true of any powerful engineering tool and cannot be avoided.

PART 1: MODELING AMRR CYCLES WITH HYSTERESIS

ABSTRACT

Active magnetic regenerative refrigeration (AMRR) has recently become an attractive alternative to vapor compression refrigeration due to its potential environmental benefits through the use of working materials with low ozone depletion potential (ODP). Several prototype machines have been constructed that achieve refrigeration at modest efficiencies with commercially available permanent magnets. Additionally, numerical modeling and experiment have shown that the efficiency of an AMRR device can be increased through layering with a tunable magnetic refrigerant. However, current numerical modeling is limited to second order magnetic transition (SOMT) materials that exhibit modest adiabatic temperature changes and no magnetic hysteresis. Since the discovery of the giant magnetocalotic effect (GMCE) in first order magnetic transition (FOMT) materials, there is increasing interest to investigate the performance of an AMRR cycle that uses these materials. Near the Curie temperature, FOMT materials yield large adiabatic temperature changes relative to SOMT materials, but also exhibit magnetic hysteresis in a changing magnetic field.

Currently there is no known numerical model that can accurately capture the effects of magnetic hysteresis on the performance of an AMRR cycle. This thesis quantifies the effects of magnetic hysteresis on the performance of AMRR cycles which use FOMT materials. Thermodynamically, magnetic hysteresis is treated as a source of entropy generation that is proportional to the area swept by a hysteresis loop for one refrigeration cycle. The one-dimensional numerical model presented by Engelbrecht (2008), is modified to include entropy generation from magnetic hysteresis in the regenerator energy equations

AMRR system performance losses due to magnetic hysteresis are shown to be directly proportional to regenerator volume. Thus at large refrigeration capacity to volume ratios, AMRR cycles operating

with layered FOMT materials significantly outperform the same cycle with layered SOMT type refrigerant under the same operating conditions.

TABLE OF CONTENTS

LIST OF FIGURES

LIST OF TABLES

NOMENCLATURE

A_c	cross-sectional area (m^2)
a_s	volume specific surface area (m^2/m^3)
AR	aspect ratio (-)
B_J	Brillouin function
C	Curie constant (K)
C_c	adiabatic temperature change scaling factor (-)
C_h	hysteresis scaling factor (-)
C_M	isothermal entropy change scaling factor (-)
C_W	Curie-Weiss constant
COP	coefficient of performance (-)
$c_{\mu_0 H}$	constant field specific heat capacity (J/kg-K)
d_h	hydraulic diameter (m)
d_p	particle diameter (m)
f	friction factor (-)
G	Gibbs free energy (J)
g_L	Landé g-factor (-)
H	applied magnetic field (A/m)
h	mass specific enthalpy (J/kg)
J	total molecular angular momentum number (-)
K	compressibility (m^2/N)
k	thermal conductivity (W/m-K)
k_B	Boltzmann constant (J/K)
L	regenerator length (m)
M	volume specific magnetic moment (A/m)
M_{an}	anhystretic magnetization (A/m)
M_{irr}	irreversible magnetization (A/m)
m	mass of magnetic refrigerant material (kg)
$\dot{m}$	mass flow rate (kg/s)
N	number of magnetic spins
N_L	number of layers in regenerator bed
Nt	number of time steps
Nx	number of spatial steps
Nu	Nusslet number (-)
P	pressure (Pa)
Pr	Prandtl number (-)
Q	heat transfer (J)
q	mass specific heat transfer (J/kg)
Re	Reynolds number (-)
S	entropy (J/K)
s	specific entropy (J/kg-K)
T	temperature (K)

t	time (s)
U	internal energy (J)
u	mass specific internal energy (J/kg)
V	volume (m^3)
v	mass specific volume (m^3/kg)
W	work (J)
w	mass specific work (J/kg)
x	regenerator axial position (m)

Greek

α	domain coupling constant (-)
ΔM	maximum irreversible magnetization (A/m)
Δs_M	mass specific isothermal entropy change (J/kg-K)
ΔT_{ad}	adiabatic temperature change (K)
$\Delta \mu_0 H$	change in magnetic field (T)
ε	bed porosity (-)
η	efficiency (-)
μ	viscosity (N-s/m^2) or magnetic permeability (T-m/A)
μ_0	permeability of a vacuum (T-m/A)
μ_B	Bohr magneton (J/T)
$\mu_0 H$	applied field (Tesla)
ρ	density (kg/m^3)
σ	dimensionless magnetization (-)
τ	cycle duration (s)
ω	dimensionless change in volume (-)

Subscripts

ad	adiabatic
amp	amplitude
an	anhysteretic
C	cold
Curie	Curie temperature
eff	effective
f	fluid or final
gen	generation
H	hot
i	spatial step index
irr	irreversible
j	temporal step index
mag	magnetic

max	maximum
mid	midpoint
min	minimum
motor	motor
r	regenerator material
ref	reference or refrigeration
s	saturation

Chapter 1 INTRODUCTION

1.1 The Magnetocaloric Effect

The magnetocaloric effect is a phenomenon by which a magnetic material experiences a decrease in internal entropy when it is exposed to an externally applied magnetic field. In ferromagnetic materials near the ordering temperature (the Curie temperature) or paramagnetic solids near absolute zero, the applied magnetic field causes the magnetic spin domains to align in a manner that decreases the internal disorder of the material, resulting in a decrease in the magnetic portion of the entropy in the system [1]. Under adiabatic conditions with no entropy generation, the total entropy of the material must remain constant. Therefore, the decrease in the magnetic entropy must result in an increase in the thermal entropy and an adiabatic temperature rise (ΔT_{ad}) is induced that is characteristic of a particular magnetocaloric material.

The thermodynamic relation for the internal energy (U) of a closed system can be expressed as:

$$dU = \delta Q - \delta W \tag{1-1}$$

where kinetic and potential energy effects have been neglected. The δQ term represents the differential heat flow *into* the system and the δW term represents the differential work done *by* the system. Because Eq. (1-1) holds true for all thermodynamic systems in (quasi-) equilibrium, an isothermal magnetization process can be compared to the isothermal compression of a gas. When a magnetocaloric material is magnetized isothermally, the magnetic portion of the entropy and therefore the overall entropy is decreased. Analogously, when a gas is compressed isothermally, the spatial component of the entropy is reduced, reducing the overall entropy of the system. This analogy is depicted in Figure 1-1.

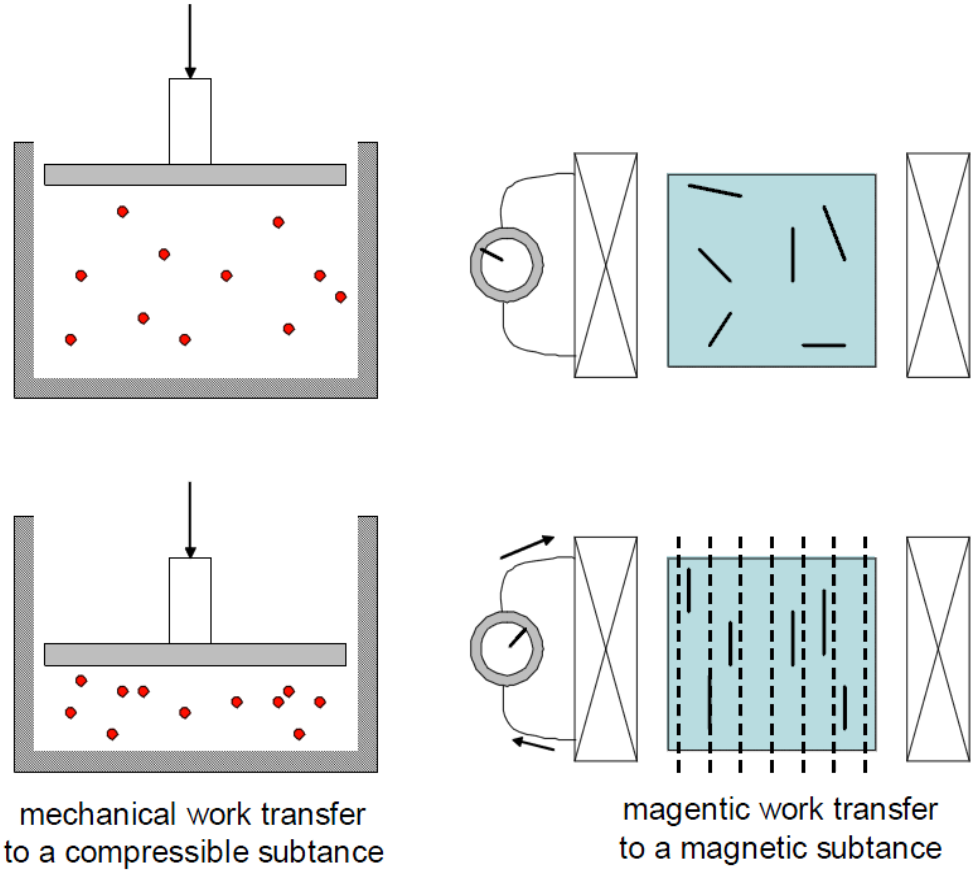

Figure 1-1. Analogy between mechanical work and magnetic work to reduce entropy

For expansion or compression of a gas, the differential work done *by* the system is represented by:

$$\delta W = P\,dV \tag{1-2}$$

where P is the pressure of the gas and dV is the differential volume of the gas. Similarly, the work term for magnetic work done *by* the system can be represented as:

$$\delta W = -\mu_0 H\, d\left(V\,M\right) \tag{1-3}$$

where $\mu_0 H$ is the applied magnetic field, V is the volume of the magnetic material, and M is the volume magnetization of the magnetic material. By comparing Eq. (1-2) and (1-3), it is clear that the applied field is analogous to the applied pressure and that the magnetization of the material is analogous to the

(inverse of) volume. Substituting Eq. (1-3) into Eq. (1-1) allows the internal energy of a magnetocaloric material to be expressed as:

$$dU = \delta Q + \mu_0 H \, d\left(V M\right) \tag{1-4}$$

The heat input term in Eq. (1-4), δQ , will be discussed in Chapter 3.

The magnetocaloric effect for a given material is typically reported in the literature in terms of either an isothermal entropy change or an adiabatic (isentropic, assuming no irreversible losses) temperature change. These two quantities describe the difference in entropy or temperature, respectively, between two lines of constant applied magnetic field on a temperature-specific entropy diagram. A temperature-specific entropy diagram for gadolinium is shown in Figure 1-2. Figure 1-3 (a) shows a temperature-specific entropy diagram for a typical ferromagnetic material and Figure 1-3 (b) shows the corresponding adiabatic temperature change and isothermal entropy change as a function of temperature near the Curie temperature of the material. Figure 1-2 shows that for all temperatures, the entropy of gadolinium decreases as the magnetic field is increased, and this effect is most dramatic near the Curie temperature of 293 K. Note that both figures report the volume specific entropy instead of the mass specific entropy. In the design of a magnetic refrigerator, volume is the important metric that must be minimized, not mass. However, the specific isothermal entropy change is most commonly reported in the literature on a mass basis, and will thus be written on a mass basis in the subsequent sections of this thesis as well. Most magnetocaloric materials can be assumed to be incompressible over the temperature range near the Curie temperature.

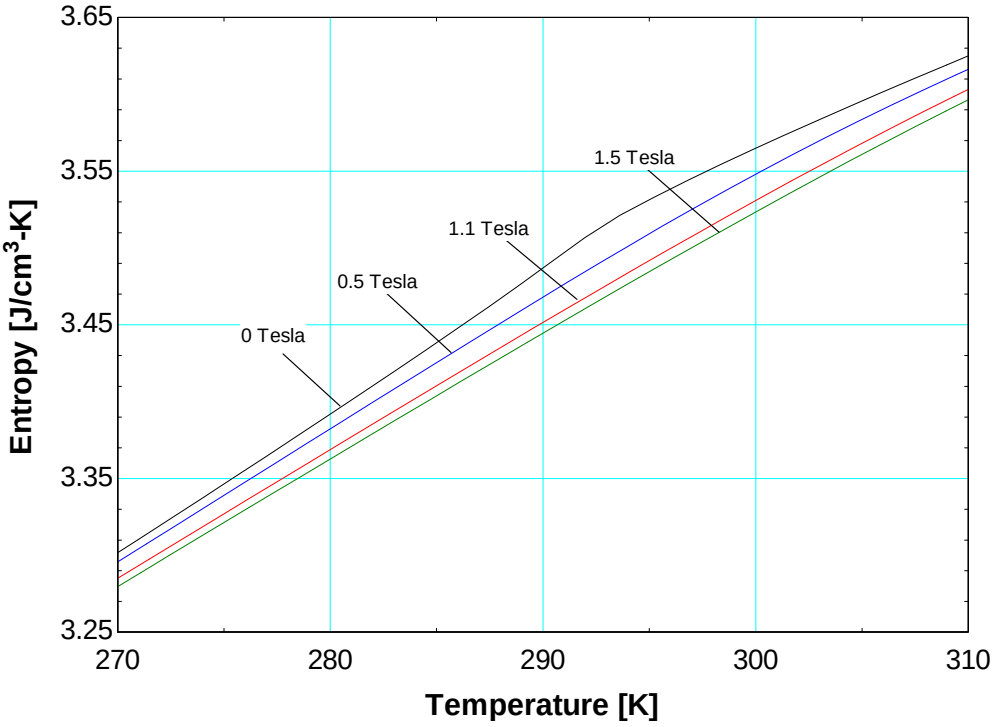

Figure 1-2. Temperature-volume specific entropy diagram for gadolinium for different applied magnetic fields near the Curie temperature (293 K)

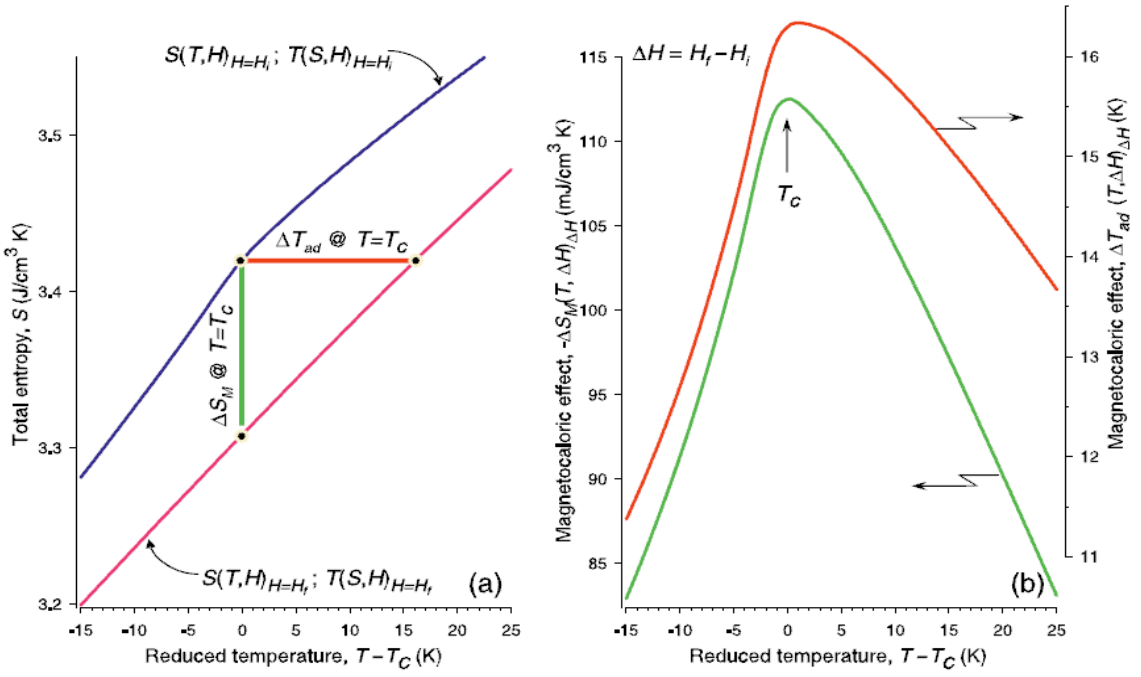

Figure 1-3. (a) Temperature-volume specific entropy diagram of a typical ferromagnetic material. (b) Negative magnetic isothermal entropy change and adiabatic temperature change as a function of temperature near the Curie temperature [1]

1.2 Magnetic Refrigeration

Since the discovery of the magnetocaloric effect by Emil Warburg in 1881, there has been an interest in exploiting the effect for the movement of heat in the form of a refrigeration cycle. More recently, the discovery of the giant magnetocaloric effect (GMCE) in $Gd_5(Si_xGe_{1-x})_4$ type materials in 1996 has stimulated research interest in room temperature magnetic refrigeration applications [2]. Several magnetic refrigeration cycles have been developed, most notably the adiabatic demagnetization refrigeration (ADR) cycle and the active magnetic regenerative refrigeration cycle (AMRR).

1.2.1 Adiabatic Demagnetization Refrigeration (ADR) Cycle

The adiabatic demagnetization refrigeration cycle (ADR) is the magnetic equivalent of a Carnot cycle for vapor compression systems. The cycle was first proposed by Debye (1926) and Giauque (1927) as a means of achieving temperatures below the boiling point of helium [3, 4]. The cycle was subsequently demonstrated by Giauque and MacDougall (1933) and successfully achieved sub-Kelvin temperatures [5]. Figure 1-4 depicts the ideal ADR cycle on a temperature-specific entropy diagram for pure gadolinium with lines of constant magnetic field shown.

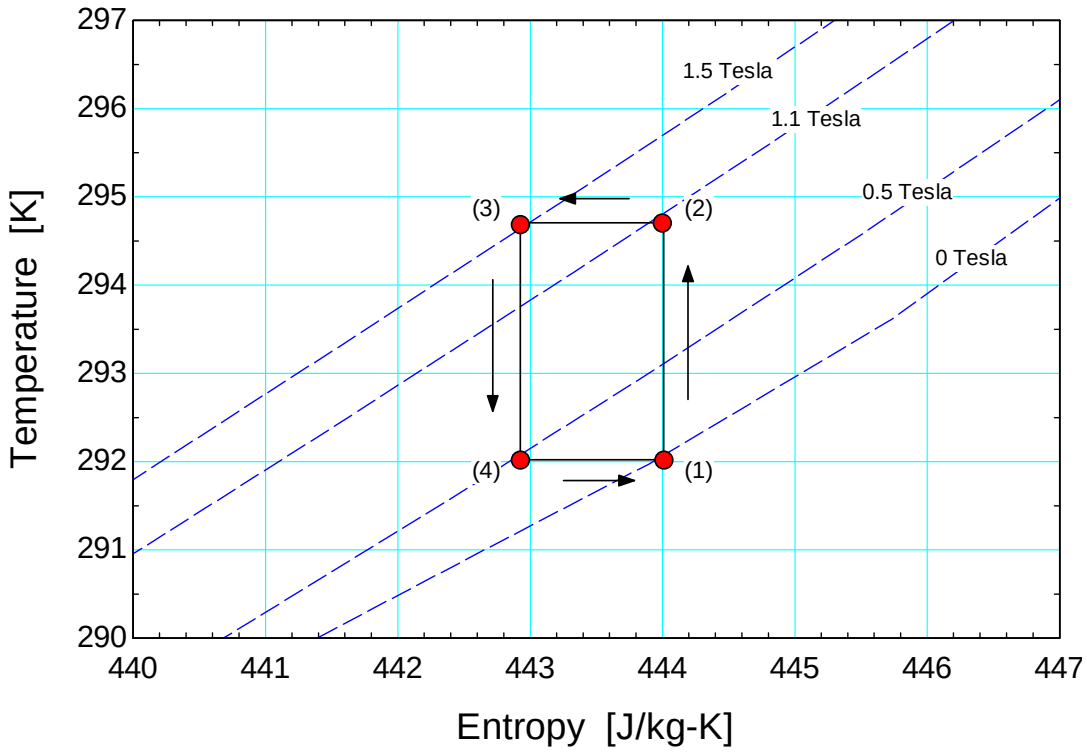

Figure 1-4. Adiabatic demagnetization refrigeration (ADR) or magnetic Carnot cycle for gadolinium.

The ideal ADR cycle shown in Figure 1-4 consists of four distinct processes that are summarized below:

1. Process 1 → 2: Adiabatic magnetization
2. Process 2 → 3: Isothermal heat rejection
3. Process 3 → 4: Adiabatic demagnetization
4. Process 4 → 1: Isothermal heat addition

In practice, it is difficult to reject heat isothermally, since the magnetic field must also be modulated properly in order to achieve this condition; this requires complex heat switches that limit heat flux rates. Also, the temperature lift of an ADR cycle is limited to the adiabatic temperature change of the material. The ADR cycle has therefore been limited to cryogenic sub-Kelvin refrigeration applications using paramagnetic salts as refrigerants.

1.2.2 Active Magnetic Regenerative Refrigeration (AMRR) Cycle

The active magnetic refrigeration (AMR) cycle is similar to the ADR cycle, but heat addition and rejection occurs at a constant magnetic field rather than at constant temperature. Isothermal heat rejection and addition is impractical to implement since the applied magnetic field must be modulated to match the temperature with the heat rejection rate. The AMR cycle is the magnetic equivalent of the Brayton cycle for a compressible fluid and is shown on a temperature-entropy diagram in Figure 1-5.

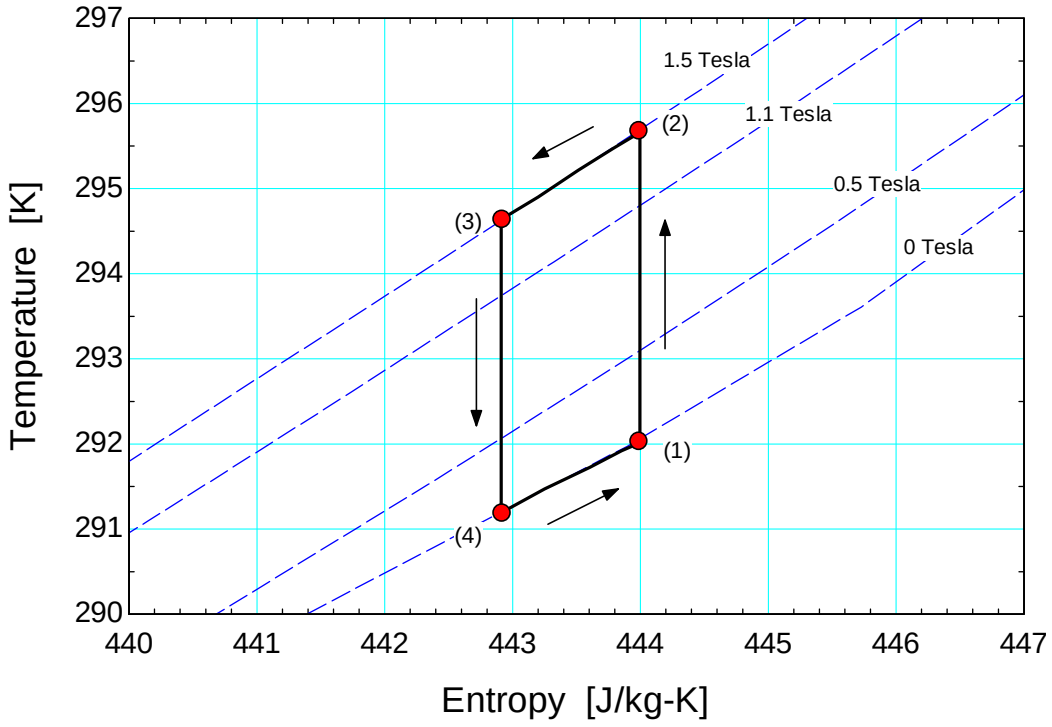

Figure 1-5. Temperature – Entropy diagram for an ideal Active Magnetic Refrigeration (AMR) cycle for gadolinium.

The ideal AMR cycle shown in Figure 1-5 consists of four distinct processes which are summarized as follows:

1. Process 1 → 2: Adiabatic magnetization
2. Process 2 → 3: Isofield heat rejection
3. Process 3 → 4: Adiabatic demagnetization

4. Process 4 → 1: Isofield heat addition

The achievable temperature span for a single AMR cycle near room temperature is limited to the adiabatic temperature change by the strength of the applied magnetic field change. Currently, the strongest permanent magnets (neodymium-based) can achieve fields near 1.5 Tesla, which does not take into account geometric limitations and demagnetization effects [6]. From Figure 1-5, the adiabatic temperature change for gadolinium near the Curie temperature for a field change from 0 to 1.5 Tesla is approximately $\Delta T_{ad} = 3.5$ K. This limited operating temperature range is not useful for most refrigeration applications. The solution to this problem is to arrange a porous matrix magnetocaloric material in a regenerator bed with a heat transfer fluid flowing through it. Each infinitesimal segment of the regenerator bed undergoes a unique thermodynamic refrigeration cycle and thermally interacts with an adjacent cycle through the flowing heat transfer fluid. In this arrangement, a much larger temperature span can be achieved. This cycle is called the active magnetic regenerative refrigeration (AMRR) cycle.

Practical AMRR cycles utilize either a porous matrix of packed magnetocaloric spheres housed in a regenerator bed or a parallel plate regenerator consisting of stacked parallel plates of magnetocaloric material. Brown (1976) first demonstrated a regenerative magnetic heat pump operating near room temperature with gadolinium as the refrigerant under a high magnetic field that varied between 0 to 7 Tesla. The regenerator was a vertical column with a stationary fluid and a moving regenerator of gadolinium plates, oscillating between the hot and cold reservoirs of the column [7]. More recently, Zimm et al. (2006) constructed a rotary regenerator that consists of six packed sphere regenerator beds of gadolinium operating with stationary permanent magnets. This system uses variable speed pumps with rotary valves to control the heat transfer fluid (water) flow [8]. Yu et al. (2010) provide a comprehensive review of AMRR prototype systems that have been built before the year 2010 [9].

The AMRR cycle consists of four processes that are similar to the AMR cycle. For an AMRR cycle operating at steady state, the first process is an adiabatic magnetization of the magnetocaloric matrix in thermal contact with the entrained fluid, resulting in a temperature rise across the bed. In this instance,

heat transfer occurs between the entrained fluid and the regenerator material, but the regenerator housing is assumed to be adiabatic. The second is an isofield heat rejection by the regenerator matrix and entrained fluid through a cold-to-hot flow of heat transfer fluid. In this process, the magnetic field is held constant while the heat transfer fluid flow is activated and flowing from the cold heat exchanger to the hot heat exchanger. As the third process begins, the fluid flow is halted, and the magnetic field begins to decrease. The third process is an adiabatic demagnetization of the regenerator material and entrained heat transfer fluid, resulting in a temperature decrease along the length of the bed. Once the bed is completely demagnetized (i.e., the field reaches zero Tesla) the fourth process begins in which a hot-to-cold fluid flow is activated and an isofield heat addition to the regenerator material and the entrained fluid occurs. A hot-to-cold fluid flow indicates that the heat transfer fluid is flowing from the hot heat exchanger to the cold heat exchanger (the opposite direction of process 2). At the end of the fourth process, the fluid flow is terminated and the cycle restarts.

Figure 1-6 shows the temperature-specific entropy diagram of the regenerator material in an AMRR cycle with a bed using a single material, a porous matrix of $Gd_{0.96}Er_{0.04}$, and water as the heat transfer fluid. The minimum and maximum applied field strengths are 0 and 3 Tesla, respectively. The temperature of the cold reservoir is 299 K and the temperature of the hot reservoir is 310 K. The Curie temperature is specified to be $T_{Curie} = 304.5$ K. Shown on the diagram are refrigeration cycles occurring at dimensionless regenerator positions of x/L = 0, 0.25, 0.5, 0.75 and 1. State points are only shown for the steady state AMRR cycle occurring at x/L = 0.5 for clarity, but occur simultaneously on each independent cycle curve. In this sense, they are not state "points" but spatially-dependent state "lines" that are projected on a two-dimensional temperature-entropy diagram. A three-dimensional projection of the temperature-specific entropy-length diagram is shown in Figure 1-7. This diagram shows a visualization of a three-dimensional 'tube' of temperature as a function of specific entropy through the spatial dimension of the AMRR cycle. The state points (or projections of state lines) shown in Figure 1-6 correspond to the AMRR processes as follows:

1. Process 1 → 2: Adiabatic magnetization transformation with entrained fluid
2. Process 2 → 3: Isofield heat rejection to heat transfer fluid
3. Process 3 → 4: Adiabatic demagnetization transformation with entrained fluid
4. Process 4 → 1: Isofield heat addition to heat transfer fluid

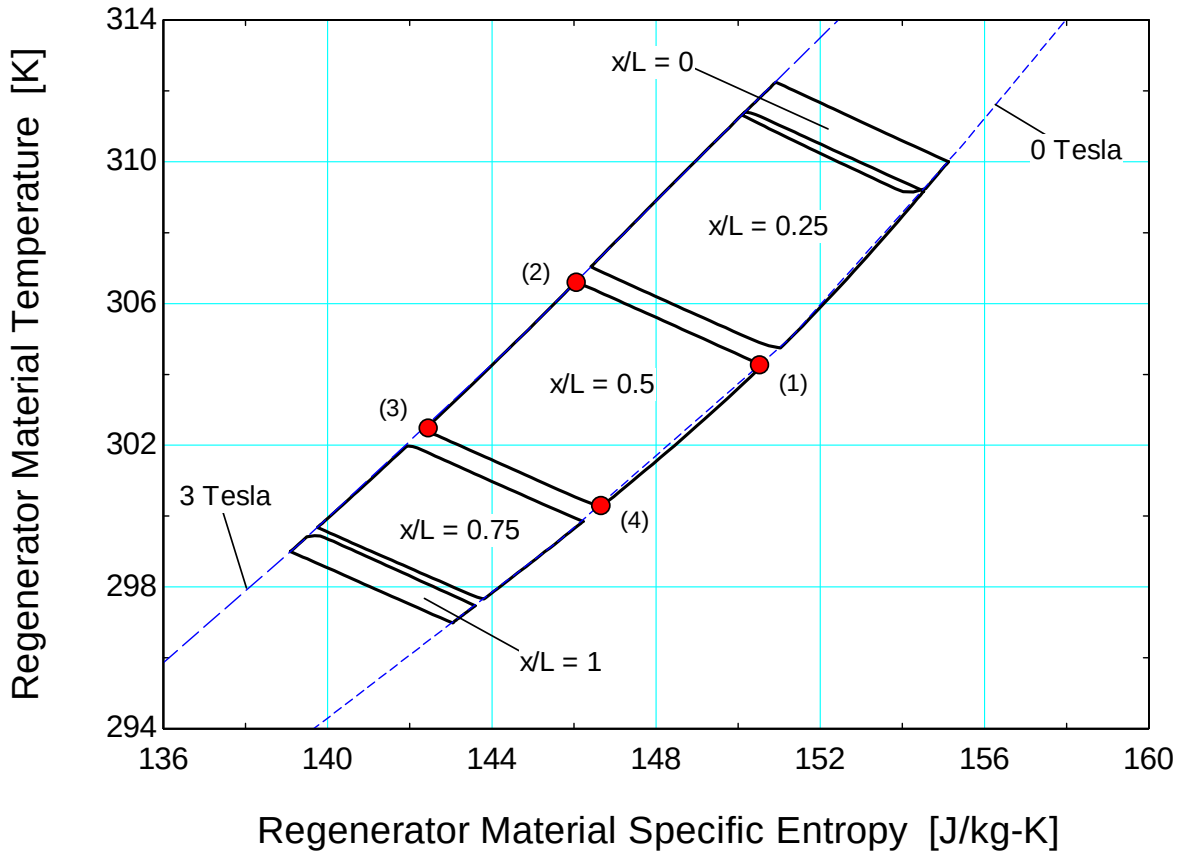

Figure 1-6. Temperature-Entropy diagram of the Active Magnetic Regenerative Refrigeration (AMRR) Cycle for a bed composed of $Gd_{0.94}Er_{0.6}$. State points are shown for the cycle occurring at x/L = 0.5.

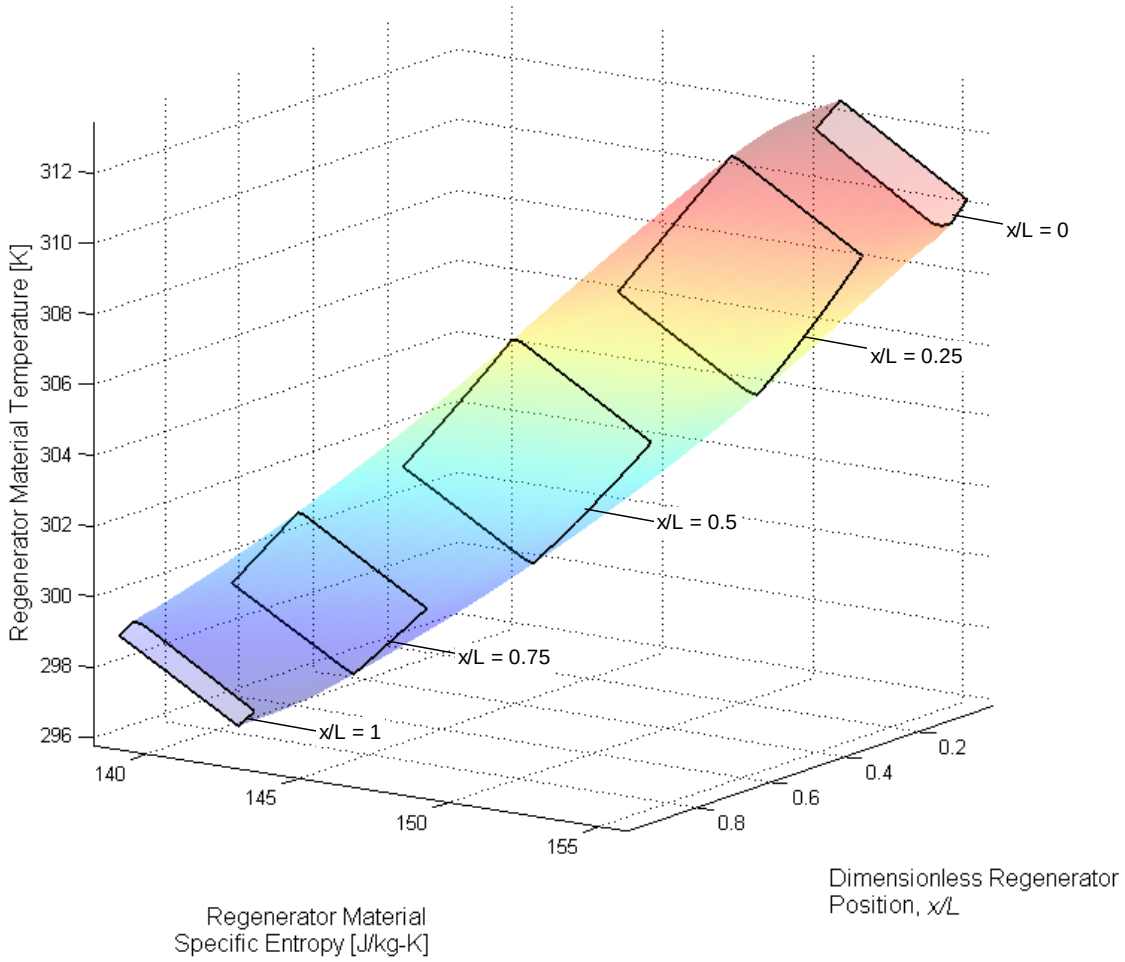

Figure 1-7. Three-dimensional projection of the Temperature-Entropy-Length diagram for AMRR cycle shown in Figure 1-6.

For an AMRR cycle operating with a single refrigerant material, the operating temperature can deviate significantly from the Curie temperature, where the magnetocaloric effect is largest. Thus, a regenerator bed that contains several materials with Curie temperatures near the spatially local operating temperature range would improve cycle performance. This type of arrangement is termed a 'layered' regenerator bed. Figure 1-8 shows the temperature-entropy diagram of the regenerator material in an AMRR cycle with an infinitely layered bed using a porous matrix of gadolinium-erbium alloy and water as the heat transfer fluid. The Curie temperature of the gadolinium-erbium alloy is controlled by altering the composition. For this study, the properties of $Gd_{0.96}Er_{0.04}$ are modulated by adjusting the Curie temperature in order to simulate an infinitely layered bed. The Curie temperature is modulated so that it

varies linearly between the hot and cold reservoir temperatures. The minimum and maximum applied field strengths are 0 and 3 Tesla, respectively. The temperatures of the cold and hot reservoirs are 299 K and 310 K, respectively. Isomagnetic field lines are shown only for the AMRR cycle occurring at x/L = 0.5 for clarity, however each spatial cycle operates with its own refrigerant material composition with separate magnetic properties. By direct comparison of Figure 1-8 and Figure 1-6, there is an increased total area of cycle operation below the cold reservoir temperature (299 K) for the layered bed than the single layered bed; this corresponds to an increased refrigeration capacity for the same operating conditions. Figure 1-9 is a three dimensional surface plot of the temperature-entropy-length diagram for the AMRR cycle with a layered regenerator material shown in Figure 1-8. The total enclosed volume of the temperature-entropy-length 'tube' below the cold reservoir temperature isotherm is the refrigeration capacity.

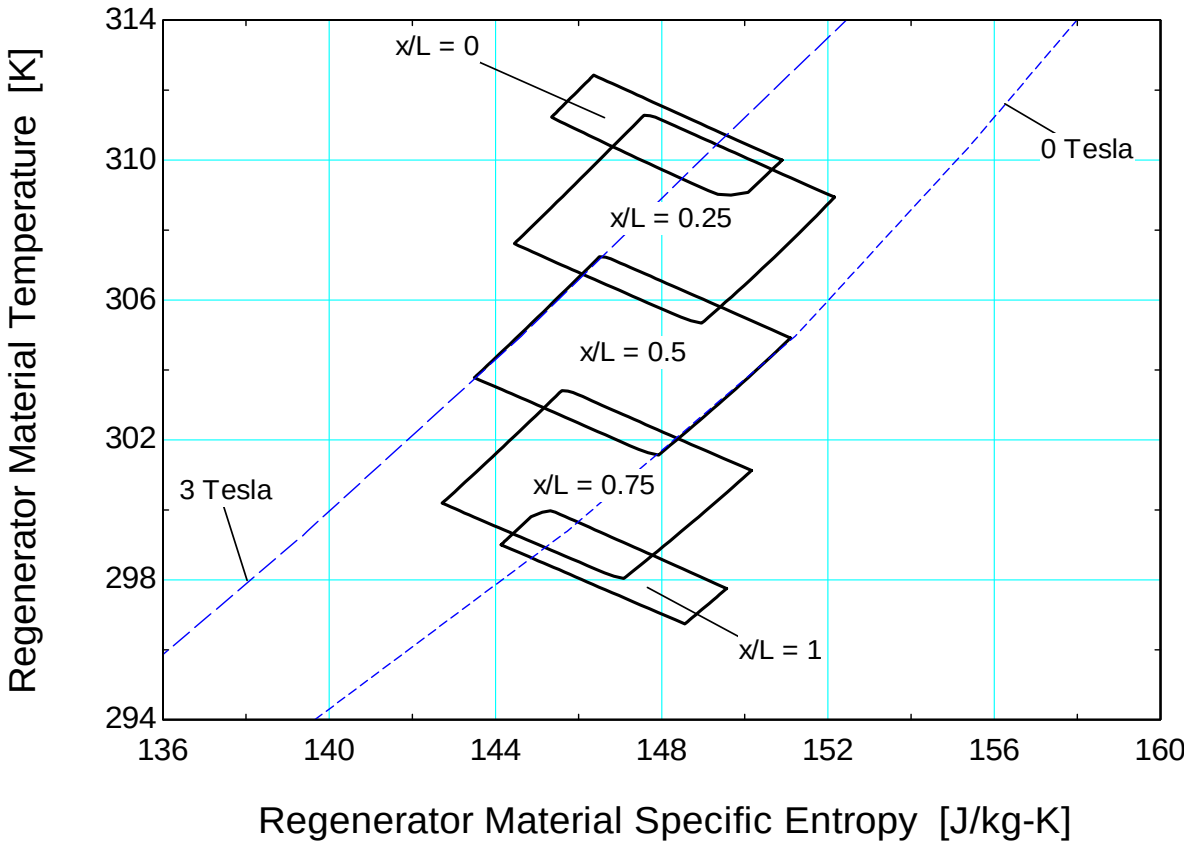

Figure 1-8. Temperature-Entropy diagram of the Active Magnetic Regenerative Refrigeration (AMRR) Cycle for gadolinium-erbium with an infinitely layered bed. Isofield lines for cycle occurring at x/L = 0.5 are shown.

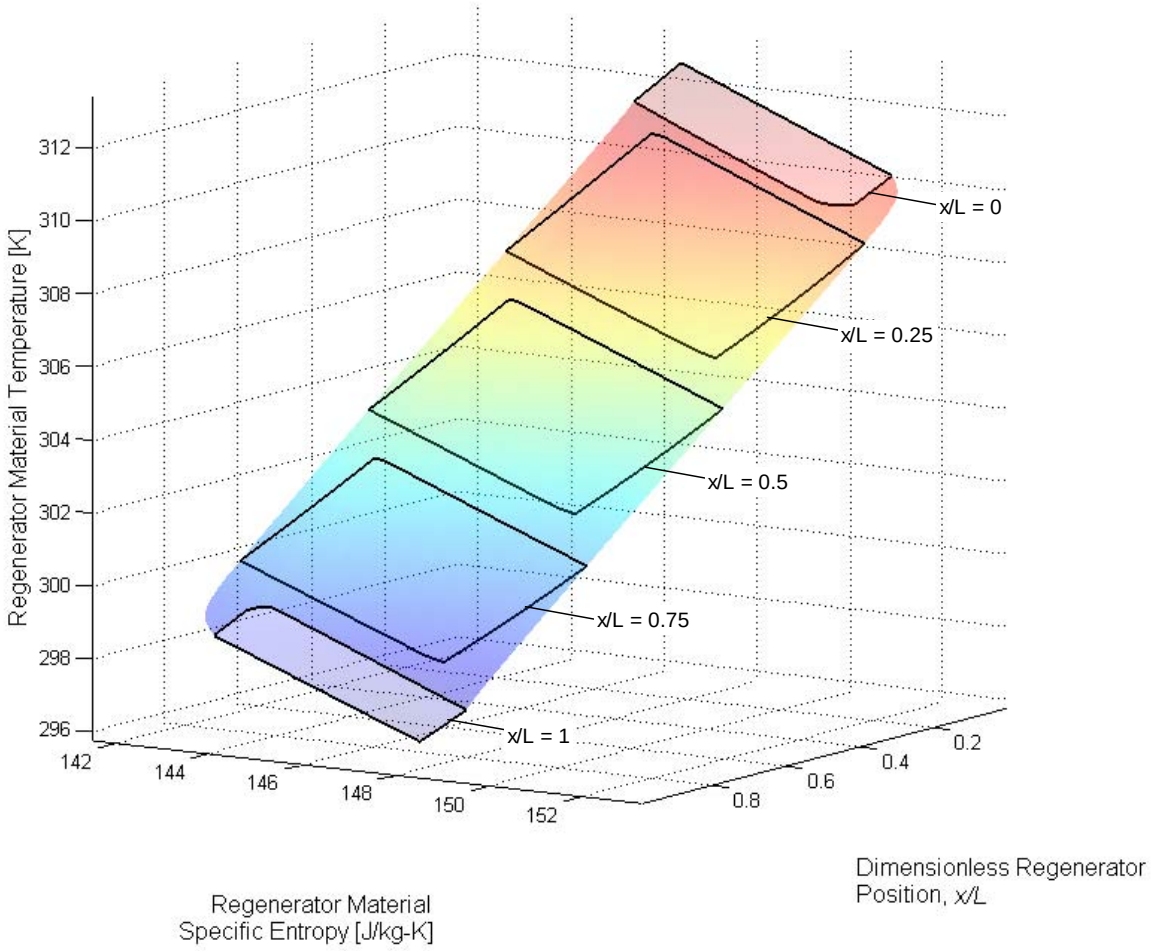

Figure 1-9. Three-dimensional projection of the Temperature-Entropy-Length diagram for AMRR cycle shown in Figure 1-8.

1.3 Magnetic Hysteresis

Magnetic hysteresis is a phenomenon exhibited in ferromagnetic materials when they are exposed to variable magnetic fields. These materials tend to retain a magnetization, even after an applied magnetic field is removed. This effect can be explained by the ability of microscopic magnetic domains to become 'caught' in a magnetized state caused by impedance from neighboring domains, resulting a remnant magnetization even at zero applied magnetic field [10]. Ferromagnetic materials are subdivided into 'hard' and 'soft' magnets. The term 'soft' magnet used to describe a material where a low applied coercive field is required for magnetization but the material does not tend to remain magnetized when the

field is removed. A 'hard' magnetic material is a material that requires a high applied coercive field for magnetization and retains its magnetization long after the applied field is removed. Thus, permanent magnets are 'hard' magnetic materials, and only exhibit significant hysteresis under very high magnetic fields [10].

Hysteresis is a causal process, where the present output is dependent on the present state as well as past input history. An example of a single cycle hysteresis loop, with arrows showing loop direction, is shown in Figure 1-10.

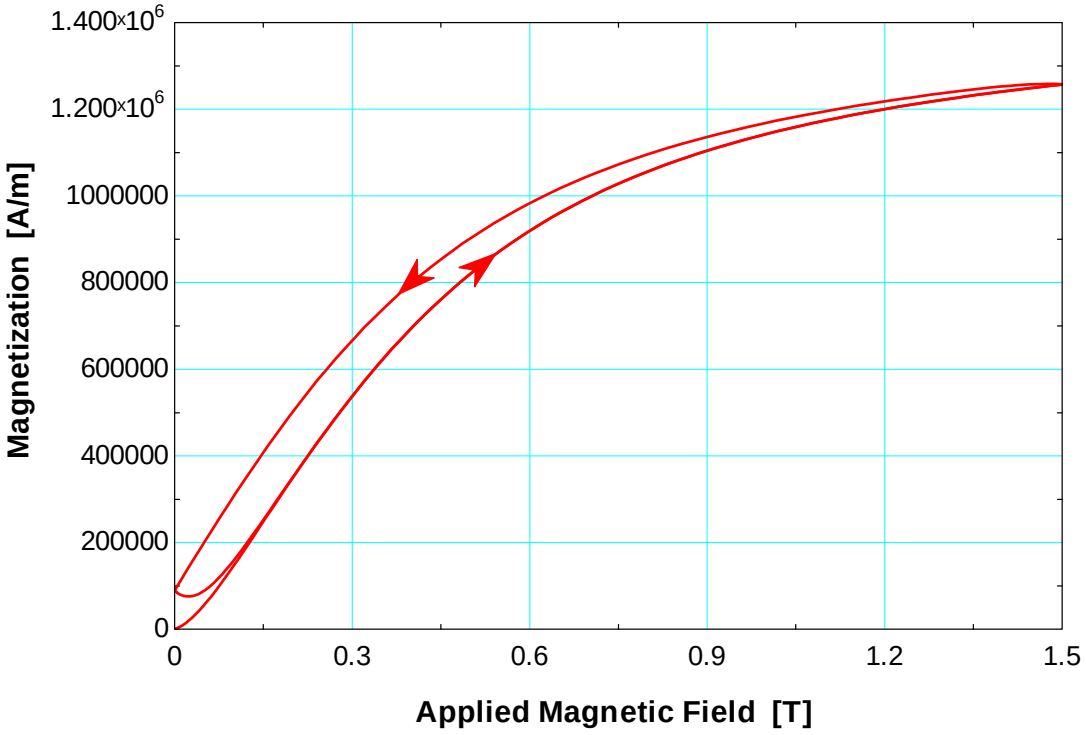

Figure 1-10. Example of a hysteresis loop with an applied magnetic field which cycles between 0 and 1.5 Tesla.

When the ferromagnetic material is first exposed to the applied magnetic field, it has zero magnetization and follows a path known as the anhysteric magnetization curve to the maximum applied field. When the applied field is ramped down again, remnant magnetization within the material causes it to follow a downward magnetization path and ultimately reach a nonzero magnetization when the applied

field reaches zero. When the magnetic field is ramped up again, it follows a path that begins from the non-zero remnant magnetization at zero applied field and eventually smoothly coincides with the anhysteric curve as shown in Figure 1-10. When plotted against time, the magnetization has higher field strength than the applied field due to the effective field within the material that takes contributions from both the applied field and magnetization of the internal domains. This relation is shown in Figure 1-11. There are several variables that influence the shape of the hysteresis curve: the applied field, saturation (or spontaneous) magnetization, material coercivity, susceptibility, and remanence.

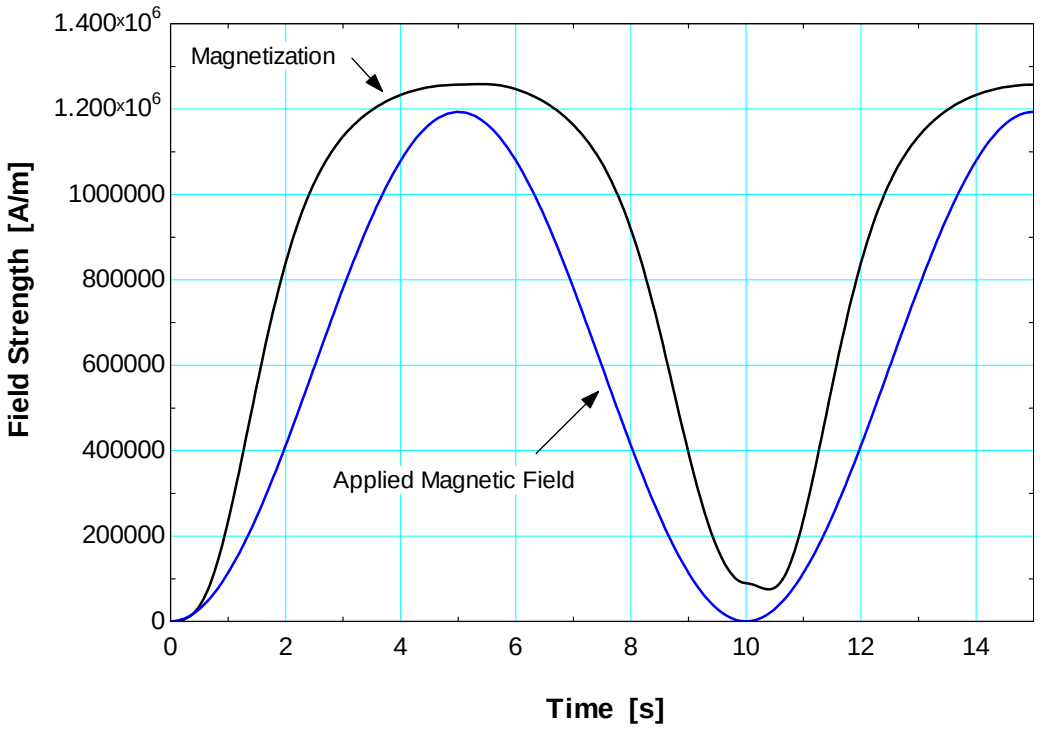

Figure 1-11. Magnetization and Applied Field as a function of time for hysteresis loop in Figure 1-10

The influence of the applied field on a hysteresis curve determines how large the loop spans on an *M-H* curve. The saturation magnetization is the upper limit of the magnetization that the hysteresis loop will approach asymptotically as the applied field approaches infinity. Remanence is defined as the magnetization that remains in a material after it has been exposed to a magnetic field and then removed from it. The coercivity is the applied field that is required to bring a material's magnetization to zero.

The magnetic susceptibility of a material determines the slope of the magnetization versus applied field curve.

The Jiles-Atherton and Preisach models are two common mathematical models for magnetic hysteresis. The Jiles-Atherton model is a deterministic model that empirically defines a hysteresis loop based on five macroscopic characteristic parameters that are based on the properties that characterize a hysteresis loop: saturation magnetization, remanence, coercivity, and anhysteretic magnetic susceptibility [11, 12]. The Preisach model of magnetic hysteresis is a probabilistic mathematical model of hysteresis that attempts to quantify hysteresis in terms of the microscopic magnetic domains rather than the macroscopic volume average magnetization [13].

LoBue et al. (2005) use the Preisach model to show the irreversibilities of magnetic hysteresis and its qualitative negative effects on the performance of AMRR systems. Ultimately, hysteresis results in a generation of entropy internal to the magnetocaloric material. Therefore, one approach for including hysteresis in an AMRR model is to treat it as a source of entropy generation that is physically linked to the hysteretic characteristics of the material as well as the operating conditions of the cycle; this is the approach used for the work in this thesis.

1.4 Magnetocaloric Materials

One of the most significant limitations on the performance of magnetic refrigeration systems is the magnetocaloric material (refrigerant) properties. These materials are generally characterized by an adiabatic temperature change due to magnetization (ΔT_{ad}), an isothermal specific entropy change due to magnetization (Δs_M), or both. The effect of varying these parameters on the performance of magnetic coolers is not well understood, but is generally accepted that increasing each independently improves system performance.

There exist two main groups of magnetocaloric materials: first order magnetic transition (FOMT) and second order magnetic transition (SOMT) type materials. In SOMT materials, the partial derivative

of the Gibbs free energy with respect to any intensive state variable (T or $\mu_o H$ for example) is continuous during the phase transition from a ferromagnetic to paramagnetic state. In these materials, the magnetocaloric effect is a consequence of a reduction in the heat capacity when exposed to a magnetic field [1]. Additionally, SOMT materials exhibit negligible magnetic hysteresis.

In FOMT materials, the partial derivative of the Gibbs free energy with respect to either temperature or applied field is discontinuous at the Curie temperature. The magnetocaloric effect in FOMT materials is a result of a shift in the Curie temperature in an applied magnetic field [1]. Furthermore, FOMT materials exhibit significant magnetic hysteresis. As a consequence of the nature of the first order phase transition, the magnetocaloric effect can be much larger in magnitude in FOMT than in SOMT materials, but generally occurs over a smaller range of temperatures. Furthermore, FOMT materials can exhibit considerable lag time between the application or removal of a magnetic field and the magnetization induced within the material (a phenomenon related to the physical mechanisms behind rate-dependent magnetic hysteresis) [10]. Slow magnetic phase transitions may cause inefficiencies in AMRR systems with small cycle times running with FOMT type materials.

Gschneidner and Pecharsky (2000) provide a detailed explanation of the complex relationship between the adiabatic temperature change and isothermal entropy change [14]. The adiabatic temperature change is dependent on variation of specific entropy with temperature as well as magnetic field in a variable applied field. In contrast, the isothermal entropy change is only dependent on the magnetic portion of the entropy contribution in a variable applied field. The authors also discuss in depth the physical mechanisms by which the two quantitative characteristics of the magnetocaloric effect arise in both FOMT and SOMT type ferromagnetic materials (as well as paramagnetic and antiferromagnetic materials).

The magnitude of magnetic hysteresis for a material is typically reported either as the measured temperature difference in the material after a single magnetization-demagnetization cycle or as a calculated exergy loss per cycle for a specified applied field change. This thesis will discuss another way

to quantitatively characterize magnetic hysteresis in terms of a magnetization loss or gain, which is based on the Jiles-Altherton model of magnetic hysteresis [12]. This method of characterizing magnetic hysteresis is the focus of Chapter 2.

1.4.1 Gadolinium and Gadolinium Alloys

Gadolinium is a rare earth element that exhibits a significant magnetocaloric effect near its Curie temperature (293 K). Pure gadolinium exhibits a second order magnetic transition from the ferromagnetic to paramagnetic phase when it is heated above its Curie temperature. Due to the nature of the SOMT, pure gadolinium shows negligible hysteresis when it is subjected to a variable applied magnetic field near its Curie temperature. Dan'kov et al. (1998) report the adiabatic temperature change of pure gadolinium to be near $\Delta T_{ad} = 5.5$ K and the isothermal entropy change to be approximately $\Delta s_M = -5.5 \frac{\text{J}}{\text{kg-K}}$ for an applied field change from 0 to 2 Tesla [15]. These measurements can vary slightly based on the measurement technique, applied magnetic field alignment with the crystalline structure, and gadolinium purity. The thermal conductivity of gadolinium is approximately $k = 10 \frac{\text{W}}{\text{m-K}}$ near 293 K, but increases nearly linearly to $12 \frac{\text{W}}{\text{m-K}}$ at 350 K [16].

The Curie temperature of gadolinium can be tuned through alloying with other rare earth lanthanides, while preserving the second order nature of the phase transition. $Gd_{1-x}R_x$ compounds (where R = Tb, Ho, Dy, or Er) have been shown to shift the Curie temperature of gadolinium to lower temperatures with a slight decrease in the magnitude of the magnetocaloric effect [17, 18]. Since the magnetocaloric properties of these materials are tunable, these materials are attractive for use in a layered regenerator bed.

1.4.2 $La(Fe_{1-x}Si_x)_{13}H_y$ Compounds

The lanthanum-iron-silicon hydrides are a promising material for use in active magnetic refrigerators since they exhibit a large magnetocaloric effect (MCE) near room temperature. These materials exhibit a first-order itinerant-electron metamagnetic phase transition between the ferromagnetic and paramagnetic phases, during which the material exhibits magnetic hysteresis [19]. The Curie temperature can be tuned

between approximately 200 K to 336 K by adjusting the concentration of hydrogen in the compound (y), depending on the concentration of iron and silicon (x) [20].

Figure 1-12 is the Curie temperature (T_{Curie}) and critical temperature (T_0) as a function of hydrogen concentration in $La(Fe_{1-x}Si_x)_{13}H_y$ with x = 0.12 [19]. The Curie temperature (T_{Curie}) is the temperature at which the phase transition from a ferromagnetic to paramagnetic phase begins when heated, and the material enters the metamagnetic phase transition region. The critical temperature (T_0) is the temperature at which the metamagnetic transition phase ends and the material becomes fully paramagnetic during heating, meaning magnetic hysteresis effects have also disappeared. As the figure shows, T_{Curie} is almost exactly a linear function of hydrogen concentration, and T_0 also correlates nearly linearly with hydrogen concentration. This linear dependence indicates that the material's Curie point can be tuned to a wide range of temperatures, which makes for ideal usage in a layered active magnetic refrigerator.

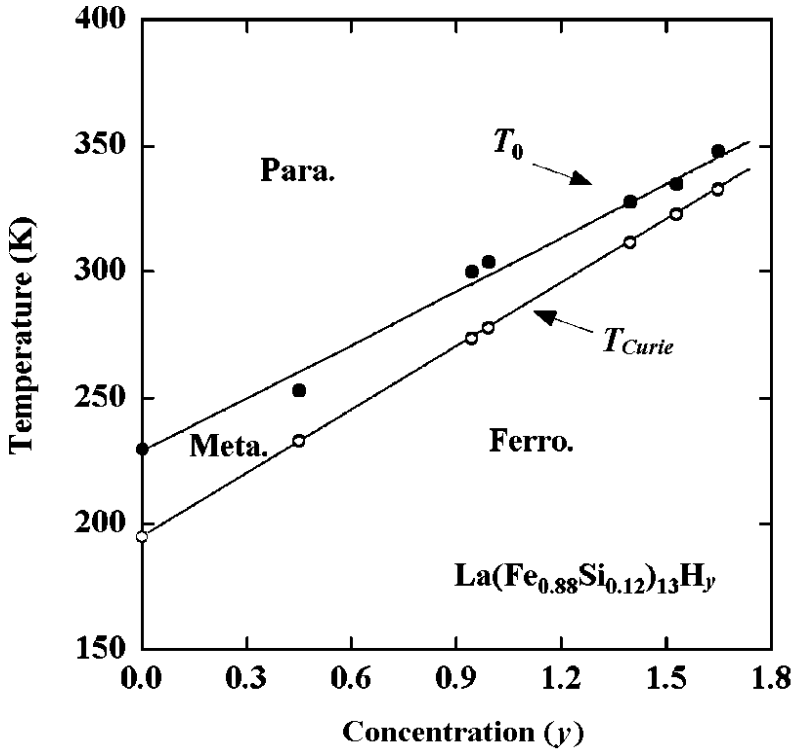

Figure 1-12. Curie temperature (T_{Curie}) and critical temperature (T_0) as a function of hydrogen concentration in $La(Fe_{1-x}Si_x)_{13}H_y$ with x = 0.12 [19].

Fujieda et al. (2002) report an isothermal entropy change of $\Delta s_M = -24 \frac{\text{J}}{\text{kg-K}}$ and an adiabatic temperature change of $\Delta T_{ad} = 6.9$ K for $La(Fe_{0.89}Si_{0.11})_{13}H_{1.3}$ for an applied field change from 0 to 2 Tesla. The particular composition with x = 0.11 and y = 1.3 has a Curie temperature of approximately 291 K, which can be approximately inferred from Figure 1-12. These materials tend to be less expensive to manufacture than pure gadolinium, but require precise and tedious processing to modulate the silicon and hydrogen compositions. Zhao et al. (2009) demonstrated that hysteresis losses may be reduced with the partial substitution of praseodymium for lanthanum with only a slight decrease in the magnetocaloric effect. $La_{0.5}Pr_{0.5}(Fe_{0.88}Si_{0.12})_{13}H_{1.6}$ exhibited a magnetocaloric effect of $\Delta s_M = -17.7 \frac{\text{J}}{\text{kg-K}}$ at a Curie temperature of approximately $T_{Curie} = 320$ K with a hysteresis loss per cycle of $2.3 \frac{\text{J}}{\text{kg}}$ [21].

1.4.3 $Gd_5(Si_{1-x}Ge_x)_4$ Compounds

1n 1997, Pecharsky and Gschneidner announced the discovery of the giant magnetocaloric effect (GMCE) in $Gd_5(Si_{1-x}Ge_x)_4$ type compounds [22]. The gadolinium-germanium-silicon family of magnetocaloric materials is of the FOMT type, and exhibit large isothermal entropy and adiabatic temperature changes for relatively modest applied field changes. For the composition type where x = 0.5, the adiabatic temperature and isothermal entropy change have been reported to be as large as $\Delta T_{ad} = 7$ K and $\Delta s_M = -27 \frac{\text{J}}{\text{kg-K}}$, respectively, for an optimally prepared material under an applied field change from 0 to 2 Tesla [23]. The Curie temperatures of these materials are tunable by varying the germanium content (x) of the alloy, and scale approximately linearly for $0.2 < x < 0.5$ [24]. These materials also exhibit significant magnetic hysteresis by nature of the FOMT, which is dependent on the specific composition of the material.

1.5 Research Objectives

The primary goal of this research is to develop a thermodynamic model of magnetic hysteresis for applications in magnetic cooling systems and evaluate the effect of hysteresis on their performance. Currently there is no known numerical model that can accurately capture the effects of magnetic

hysteresis on the performance of an AMRR cycle, but the effect has been simulated through the use of scaling factors applied to the efficiency of the system calculated without hysteresis [25]. This thesis will quantify the effects of magnetic hysteresis on the performance of AMRR cycles which use FOMT materials. Thermodynamically, magnetic hysteresis is treated as a source of entropy generation that is proportional to the area swept by a hysteresis loop for one refrigeration cycle.

The one-dimensional, numerical model presented by Engelbrecht (2008) [26], is modified to include entropy generation from magnetic hysteresis in the regenerator energy equations. This model accepts inputs such as the regenerator geometry, magnetic refrigerant material, and heat transfer fluid and calculates the steady-state temperature distribution for the complete AMRR cycle as a function of time and space through an iterative successive substitution technique that subject to a specified convergence tolerance. The final fluid and regenerator material temperature distributions are used to quantify the performance of the cycle.

The modified model is used to optimize the performance an AMRR cycle that uses FOMT materials and compare it to the performance of an AMRR cycle that uses SOMT materials. The effect of model input parameters such as regenerator volume, mass flow rate profile, regenerator aspect ratio, and bed layering geometry on the performance of the cycle is studied.

REFERENCES

1. Gschneidner, K.A., V.K. Pecharsky, and A.O. Tsokol, *Recent developments in magnetocaloric materials.* Reports on Progress in Physics, 2005. **68**(6): p. 1479.

2. Gschneidner Jr, K.A. and V.K. Pecharsky, *Thirty years of near room temperature magnetic cooling: Where we are today and future prospects.* International Journal of Refrigeration, 2008. **31**(6): p. 945-961.

3. Blumenfeld, P.E., et al., *High temperature superconducting magnetic refrigeration.* AIP Conference Proceedings, 2002. **613**(1): p. 1019-1026.

4. Debye, P., *The fundamental laws of electric and magnetic excitation from standpoint of the quantum theory (Die Grundgesetze der elektrischen und magnetischen Erregung vom Standpunkte der Quantentherie)*. Physikalische Zeitschrift, 1926. **27**(3): p. 67-74.

5. Giauque, W.F. and D.P. MacDougall, *Attainment of temperatures below 1^{o} absolute by demagnetization of $Gd_2(SO_4)_3 8H_2O$.* Phys. Rev., 1933. **43**: p. 768.

6. Dai, W., et al., *Application of high-energy Nd-Fe-B magnets in the magnetic refrigeration.* Journal of Magnetism and Magnetic Materials, 2000. **218**(1): p. 25-30.

7. Brown, G.V., *Magnetic heat pumping near room temperature.* Journal of Applied Physics, 1976. **47**(8): p. 3673-3680.

8. Zimm, C., et al., *Design and performance of a permanent-magnet rotary refrigerator.* International Journal of Refrigeration, 2006. **29**(8): p. 1302-6.

9. Yu, B., et al., *A review of magnetic refrigerator and heat pump prototypes built before the year 2010.* International Journal of Refrigeration, 2010. **33**(6): p. 1029-1060.

10. Bertotti, G., *Hysteresis in magnetism : for physicists, materials scientists, and engineers*. 1998, San Diego, CA: Academic Press. 558.

11. Jiles, D.C., J.B. Thoelke, and M.K. Devine, *Numerical determination of hysteresis parameters for the modeling of magnetic properties using the theory of ferromagnetic hysteresis.* IEEE Transactions on Magnetics, 1992. **28**(1): p. 27-35.

12. Jiles, D.C. and D.L. Atherton, *Theory of ferromagnetic hysteresis.* Journal of Magnetism and Magnetic Materials, 1986. **61**(1-2): p. 48-60.

13. LoBue, M., et al. *Entropy and entropy production in magnetic systems with hysteresis*. in *49th Annual Conference on Magnetism and Magnetic Materials*. 2005. Jacksonville, Florida (USA): AIP.

14. Gschneidner, K.A. and V.K. Pecharsky, *Magnetocaloric Materials.* Annual Review of Materials Science, 2000. **30**(1): p. 387-429.

15. Dan'kov, S.Y., et al., *Magnetic phase transitions and the magnetothermal properties of gadolinium.* Physical Review B, 1998. **57**(6): p. 3478.

16. Fujieda, S., et al., *Thermal transport properties of magnetic refrigerants $La(Fe_xSi_{1-x})_{13}$ and their hydrides, and $Gd_5Si_2Ge_2$ and MnAs.* Journal of Applied Physics, 2004. **95**(5): p. 2429-2431.

17. Pecharsky, V.K. and K.A. Gschneidner Jr, *Magnetocaloric effect and magnetic refrigeration.* Journal of Magnetism and Magnetic Materials, 1999. **200**(1-3): p. 44-56.

18. Nikitin, S.A., et al., *Magnetocaloric effect in rare-earth alloys Gd-Ho and Gd-Er.* Physics of Metals and Metallography, 1985. **59**(2): p. 104-108.

19. Fujita, A., et al., *Itinerant-electron metamagnetic transition and large magnetocaloric effects in $La(Fe_xSi_{1-x})_{13}$ compounds and their hydrides.* Physical Review B, 2003. **67**(10): p. 104416.

20. Fujieda, S., A. Fujita, and K. Fukamichi, *Large magnetocaloric effect in $La(Fe_xSi_{1-x})_{13}$ itinerant-electron metamagnetic compounds.* Applied Physics Letters, 2002. **81**(7): p. 1276-1278.

21. Jin-liang, Z., et al., *Reduction of magnetic hysteresis loss in $La_{0.5}Pr_{0.5}Fe_{11.4}Si_{1.6}H_x$ hydrides with large magnetocaloric effects.* Journal of Applied Physics. **107**(11): p. 113911 (5 pp.).

22. Pecharsky, V.K. and J.K.A. Gschneidner, *Giant Magnetocaloric Effect in $Gd_5(Si_2Ge_2)$.* Physical Review Letters, 1997. **78**(23): p. 4494.

23. Pecharsky, A.O., K.A. Gschneidner Jr, and V.K. Pecharsky, *The giant magnetocaloric effect of optimally prepared Gd5Si2Ge2.* Journal of Applied Physics, 2003. **93**(8): p. 4722-4728.

24. Pecharsky, V.K. and K.A. Gschneidner, Jr., *Tunable magnetic regenerator alloys with a giant magnetocaloric effect for magnetic refrigeration from approx.20 to approx.290 K.* Applied Physics Letters, 1997. **70**(24): p. 3299-3299.

25. Nielsen, K.K., et al., *Review on numerical modeling of active magnetic regenerators for room temperature applications.* International Journal of Refrigeration. **34**(3): p. 603-16.

26. Engelbrecht, K., *A Numerical Model of an Active Magnetic Regenerator Refrigerator with Experimental Validation* in *Mechanical Engineering*. 2008, The University of Wisconsin at Madison: Madison, WI. p. 267.

Chapter 2 HYSTERESIS MODELING

2.1 Entropy Generation due to Magnetic Hysteresis

This chapter presents a rigorous thermodynamic analysis of magnetic hysteresis in magnetocaloric materials. In this analysis, magnetic hysteresis is treated as a source of entropy generation in a system defined by a magnetocaloric material. The entropy generation associated with hysteresis is proportional to the area swept by the hysteresis curve on a applied field – magnetization (*H-M*) curve [1]. The *H-M* curve for a material is split into two components: anhysteretic or reversible magnetization and hysteretic or irreversible magnetization. This model of anhysteretic and hysteretic magnetization is based on the Jiles-Atherton model of magnetic hysteresis proposed in 1986 [2]. The irreversible magnetization (or hysteretic magnetization) is considered an applied field rate-independent property in this thesis, which may not be a valid treatment for systems with slow phase transitions relative to the time rate of change of the applied magnetic field [1]. Thermal hysteresis is also neglected in this analysis.

2.1.1 Entropy Balance without Magnetic Hysteresis

Consider an adiabatic process undergone by a magnetocaloric material without hysteresis. Such a process is assumed to be reversible and therefore an entropy balance on this system, carried out on a unit mass basis, requires that:

$$\frac{ds}{dt} = 0 \tag{2-1}$$

The time rate of change of the specific entropy in Eq. (2-1) is divided into its magnetic field ($\mu_o H$) and temperature (T) driven components:

$$\frac{ds}{dt} = \left(\frac{\partial s}{\partial T}\right)_{\mu_0 H}\left(\frac{dT}{dt}\right) + \left(\frac{\partial s}{\partial \mu_0 H}\right)_{T}\left(\frac{d\mu_0 H}{dt}\right) = 0 \tag{2-2}$$

where the temperature T and applied magnetic field $\mu_0 H$ are only functions of time. The partial derivative of specific entropy with respect to temperature at constant applied field can be written in terms of the constant field specific heat capacity, $c_{\mu_0 H}$:

$$\left(\frac{\partial s}{\partial T}\right)_{\mu_0 H} = \frac{c_{\mu_0 H}}{T} \tag{2-3}$$

A Maxwell relation is used to write the partial derivative of specific entropy with respect to applied field at constant temperature in terms of the mass specific anhysteretic magnetization ($v\,M_{an}$) [3]:

$$\left(\frac{\partial s}{\partial \mu_0 H}\right)_T = \left(\frac{\partial v M_{an}}{\partial T}\right)_{\mu_0 H} \tag{2-4}$$

Substituting Eqs. (2-3) and (2-4) into Eq. (2-2) leads to:

$$\frac{ds}{dt} = \frac{c_{\mu_0 H}}{T}\left(\frac{dT}{dt}\right) + \left(\frac{\partial v M_{an}}{\partial T}\right)_{\mu_0 H}\left(\frac{d\mu_0 H}{dt}\right) = 0 \tag{2-5}$$

For magnetic refrigeration systems, the term of interest in Eq. (2-5) is often the change in temperature with respect to time $\frac{dT}{dt}$ since we are typically interested in characterizing an adiabatic temperature rise for a given material. By inspection of this equation, it is evident that the temperature rise is a direct function of the change in the applied magnetic field, the magnitude of the constant field specific heat $c_{\mu_0 H}$ and the partial derivative of mass-specific anhysteretic magnetization vM_{an} with respect to temperature at constant field.

2.1.2 Entropy Balance with Magnetic Hysteresis

Since hysteresis is an irreversible process, it is necessary to model the phenomenon as an internal entropy generation. Consider an adiabatic process undergone by a magnetocaloric material with hysteresis. Such a process will be irreversible and therefore an entropy balance on this system, carried out on a unit mass basis, requires that:

$$\frac{ds}{dt} = \frac{\dot{S}_{gen}}{m} \tag{2-6}$$

where m is the mass of the material and $\dot{S}_{gen}$ is the rate of entropy generation, which must have a positive value. The rate of entropy generation per unit mass is defined using the irreversible magnetization (M_{irr}) and it is assumed to be related to the area within a hysteresis curve. The rate at which the hysteretic curve area is being swept out per time is given by:

$$T\frac{\dot{S}_{gen}}{m} = \nu M_{irr}\left|\frac{d\mu_0 H}{dt}\right| \tag{2-7}$$

or, solving for the entropy generation rate per unit mass:

$$\frac{\dot{S}_{gen}}{m} = \frac{\nu M_{irr}}{T}\left|\frac{d\mu_0 H}{dt}\right| \tag{2-8}$$

where ν is the specific volume of the magnetic material, M_{irr} is the irreversible magnetization per unit volume, T is the temperature of the magnetic material, and $\frac{d\mu_0 H}{dt}$ is the rate of change of the applied magnetic field. The irreversible magnetization is a function that must be unambiguously positive and represents the deviation of the magnetization from its anhysteretic value. The irreversible magnetization must be a function of temperature and applied field as well as the minimum and maximum values of the applied field experienced by the material during each cycle. Assuming that the degree of hysteresis does not depend on the rate of the process, the total magnetization induced in the material (M) is the sum of the anhysteretic (M_{an}) and hysteretic (M_{irr}) terms:

$$\begin{aligned} M\left(T, \mu_0 H, \mu_0 H_{min}, \mu_0 H_{max}, \frac{d\mu_o H}{dt}\right) &= M_{an}\left(T, \mu_0 H\right) \\ &\quad - M_{irr}\left(T, \mu_0 H, \mu_0 H_{min}, \mu_0 H_{max}\right)\mathrm{sign}\left(\frac{d\mu_o H}{dt}\right) \end{aligned} \tag{2-9}$$

Note that the sign function returns the sign of its argument and causes the irreversible magnetization to subtract from the anhysteretic magnetization during the time that the applied field is increasing and add to it when it is decreasing.

The value of M_{irr} must be equal to zero when the applied field reaches its minimum and maximum values:

$$\begin{aligned} M_{irr}\left(T,\mu_0 H=\mu_0 H_{min},\mu_0 H_{min},\mu_0 H_{max}\right)=0 \\ M_{irr}\left(T,\mu_0 H=\mu_0 H_{max},\mu_0 H_{min},\mu_0 H_{max}\right)=0 \end{aligned} \tag{2-10}$$

Note that the absolute value of the rate of change of the applied field is used in Eq. (2-8) in order to ensure that the entropy generation rate is unambiguously positive. Defining the entropy generation rate with an irreversible magnetization term permits the calculation of the entropy generation rate at any point along the *M-H* curve. Graphically, the irreversible magnetization can be thought of as a method of "fattening out" the *M-H* curve by adding or subtracting (depending on the direction of the rate of applied field change) it from the anhysteretic magnetization function. An example of a hysteresis curve that is defined using the irreversible magnetization function is shown in Figure 2-2.

The rate of change of specific entropy is again separated into its magnetic and temperature driven components, which yields:

$$\frac{ds}{dt}=\frac{c_{\mu_0 H}}{T}\left(\frac{dT}{dt}\right)+\left(\frac{\partial v M_{an}}{\partial T}\right)_{\mu_0 H}\left(\frac{d\mu_0 H}{dt}\right)=\frac{\dot{S}_{gen}}{m} \tag{2-11}$$

Note that the anhysteretic magnetization term, M_{an}, remains in Eq. (2-11) because the irreversibility associated with hysteresis is accounted for within the entropy generation term. By substituting Eq. (2-8) into Eq. (2-11):

$$\frac{c_{\mu_0 H}}{T}\left(\frac{dT}{dt}\right)+\left(\frac{\partial v M_{an}}{\partial T}\right)_{\mu_0 H}\left(\frac{d\mu_0 H}{dt}\right)=\frac{v M_{irr}}{T}\left|\frac{d\mu_0 H}{dt}\right| \tag{2-12}$$

which represents the final relation between temperature, applied field, irreversible magnetization, anhysteretic magnetization, and time for an adiabatic process.

2.2 Adiabatic Magnetization and Demagnetization with Hysteresis

The model of irreversible magnetization suggested in Section 1.1 is tested by using it to simulate a single piece of magnetic material that is exposed to an alternating magnetic field under adiabatic conditions. First the process is simulated with no hysteresis effects. Then the simulation is repeated with the addition of an irreversible magnetization term in order to simulate hysteresis.

In order to illustrate this approach, the simple Curie law equation of state for a paramagnetic material is used as the basis for the anhysteretic portion of the volume magnetization:

$$M_{an}\left(T,\mu_0 H\right)=\frac{C}{\mu_0}\frac{\mu_0 H}{T} \tag{2-13}$$

where C is the Curie constant. Substituting Eq. (2-13) into Eq. (2-9) leads to:

$$\begin{aligned} M\left(T,\mu_0 H,\mu_0 H_{min},\mu_0 H_{max},\frac{d\mu_0 H}{dt}\right)=&\frac{C}{\mu_0}\frac{\mu_0 H}{T}\\ &-M_{irr}\left(T,\mu_0 H,\mu_0 H_{min},\mu_0 H_{max}\right)\operatorname{sign}\left(\frac{d\mu_0 H}{dt}\right)\end{aligned} \tag{2-14}$$

One requirement for the irreversible magnetization function is that it must be equal to zero at the minimum and maximum applied fields experienced by the material, as shown in Eq. (2-10). One possibility for M_{irr} is therefore:

$$M_{irr}\left(T,\mu_0 H,\mu_0 H_{min},\mu_0 H_{max}\right)=\Delta M\sin\left(\frac{\pi\left(\mu_0 H-\mu_0 H_{\min}\right)}{\mu_0 H_{\max}-\mu_0 H_{\min}}\right) \tag{2-15}$$

where ΔM is a constant that represents the maximum irreversible magnetization. Substituting Eq. (2-15) into Eq. (2-14) provides:

$$M\left(T,\mu_0 H,\mu_0 H_{min},\mu_0 H_{max},\frac{d\mu_0 H}{dt}\right)=\frac{C}{\mu_0}\frac{\mu_0 H}{T} -\Delta M\sin\left(\frac{\pi\left(\mu_0 H-\mu_0 H_{\min}\right)}{\mu_0 H_{\max}-\mu_0 H_{\min}}\right)\operatorname{sign}\left(\frac{d\mu_0 H}{dt}\right) \tag{2-16}$$

For the cases considered in this report, $\mu_o H_{\min} = 0$ and therefore the magnetization is described by:

$$M\left(T,\mu_0 H,\mu_0 H_{min},\mu_0 H_{max},\frac{d\mu_0 H}{dt}\right)=\frac{C}{\mu_0}\frac{\mu_0 H}{T}-\Delta M\sin\left(\frac{\pi\mu_0 H}{\mu_0 H_{\max}}\right)\operatorname{sign}\left(\frac{d\mu_0 H}{dt}\right) \tag{2-17}$$

Figure 2-1 shows the irreversible magnetization function given by Eq. (2-15) as a function of the applied magnetic field for various values of $v\Delta M$ with $\mu_0 H_{\max} = 2$ T. Note that it satisfies the constraints of Eq. (2-10) as it is zero at the minimum and maximum applied field.

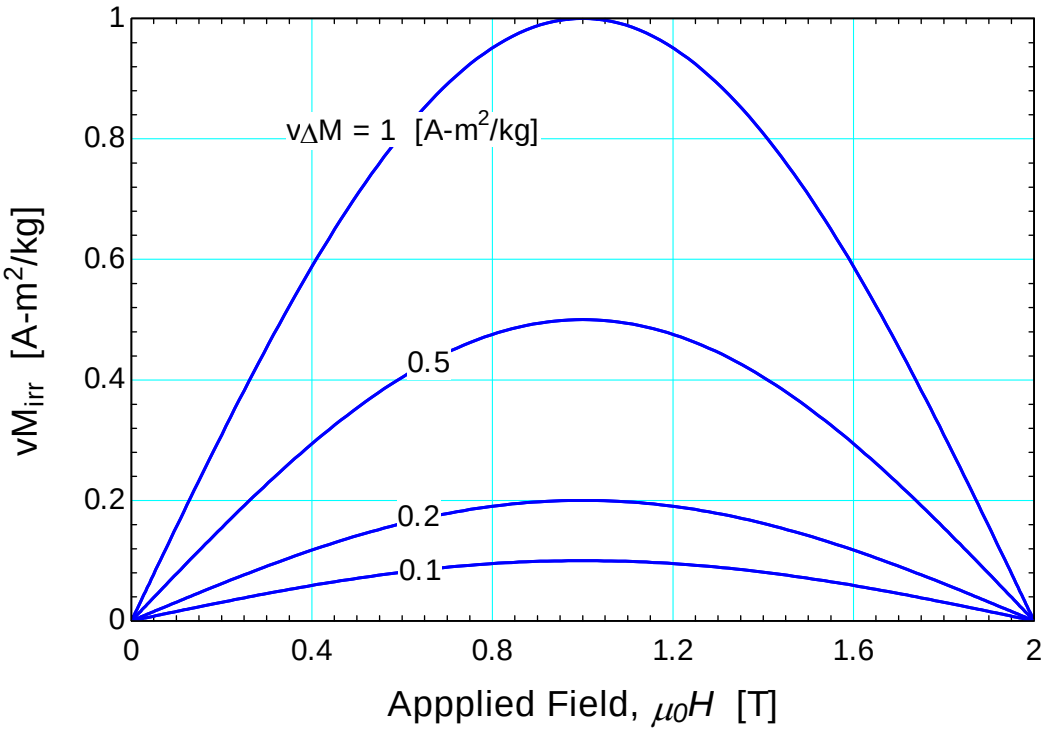

Figure 2-1. Irreversible magnetization function as a function of applied magnetic field for various values of $v\Delta M$ for the model considered.

For the magnetization-demagnetization adiabatic process, the material is exposed to an oscillating magnetic field that varies between zero and a maximum applied field, $\mu_0 H_{\max}$, in an assumed sinusoidal manner:

$$\mu_0 H(t) = \frac{\mu_0 H_{\max}}{2}\left(1 - \cos\left(\frac{2\pi t}{\tau}\right)\right) \tag{2-18}$$

where τ is the period of each cycle. The derivative of the applied field with respect to time is:

$$\frac{d\mu_0 H}{dt} = \frac{\mu_0 H_{\max}\,\pi}{\tau}\sin\left(\frac{2\pi t}{\tau}\right) \tag{2-19}$$

Equation (2-12) is solved for the temperature rate of change:

$$\frac{dT}{dt} = \frac{\left[\frac{vM_{irr}}{T}\left|\frac{d\mu_0 H}{dt}\right| - \left(\frac{\partial vM_{an}}{\partial T}\right)_{\mu_0 H}\left(\frac{d\mu_0 H}{dt}\right)\right]}{\frac{c_{\mu_0 H}}{T}} \tag{2-20}$$

Equation (2-15) is used to evaluate the first term in Eq. (2-20) and the Curie law, Eq. (2-13), is used to evaluate the second term:

$$\frac{dT}{dt} = \frac{\left[\frac{v\Delta M}{T}\sin\left(\frac{\pi\mu_0 H}{\mu_0 H_{\max}}\right)\operatorname{sign}\left(\frac{d\mu_0 H}{dt}\right)\left|\frac{d\mu_0 H}{dt}\right| + \frac{C}{\mu_0}\frac{v\mu_0 H}{T^2}\left(\frac{d\mu_0 H}{dt}\right)\right]}{\frac{c_{\mu_0 H}(\mu_0 H, T)}{T}} \tag{2-21}$$

or

$$\frac{dT}{dt} = \frac{v\Delta M}{c_{\mu_0 H}}\sin\left(\frac{\pi\mu_0 H}{\mu_0 H_{\max}}\right)\operatorname{sign}\left(\frac{d\mu_0 H}{dt}\right)\left|\frac{d\mu_0 H}{dt}\right| + \frac{C}{\mu_0}\frac{v\mu_0 H}{T c_{\mu_0 H}}\left(\frac{d\mu_0 H}{dt}\right) \tag{2-22}$$

Note that the ordinary differential equation has no simple closed form solution that would allow the temperature to be expressed explicitly in terms of time; therefore, numerical methods must be employed

to solve Eq. (2-22). The first-order Euler method can be employed, which approximates the temperature at the end of each time step according to:

$$T_{i+1} \approx T_i + \left(\frac{dT}{dt}\right)_i \Delta t \qquad i = 1 \ldots N \tag{2-23}$$

where N is the total number of time steps and Δt is a finite valued time step. This is an approximation using the first two terms of the Taylor expansion for T. For this approximation, the initial temperature must be known as an initial condition used to approximate the temperature at the first step forward in time. The single shot model was evaluated using the inputs listed in Table 2-1.

Table 2-1. Properties specified for magnetization-demagnetization model simulation

Variable	**Value**	**Variable**	**Value**
$\mu_0 H_{\max}$	2 *Tesla*	C/μ_0	273 $A-K/T-m$
$\mu_0 H_{\min}$	0 *Tesla*	τ	4 *s*
$c_{\mu_0 H=0}$	0.5 $J/kg-K$	ΔM	0.1 A/m
ρ	1 kg/m^3	$T(t=0)$	293 *K*

The values of the parameters used in Table 1 are arbitrary and were chosen in order to illustrate the impact of hysteresis in the model. The purpose of the simulation is to verify that the method described to add an irreversible magnetization term to the entropy balance equation is valid. Figure 2-2 illustrates the magnetization of the material as a function of applied field with the anhysteretic and hysteretic lines predicted by Eqs. (2-13) and (2-15), respectively, indicated. Note that the M_{irr} term essentially widens the curve by reducing the magnetization from the anhysteretic value as the field increases and increasing the magnetization from its anhysteretic value as the field is removed.

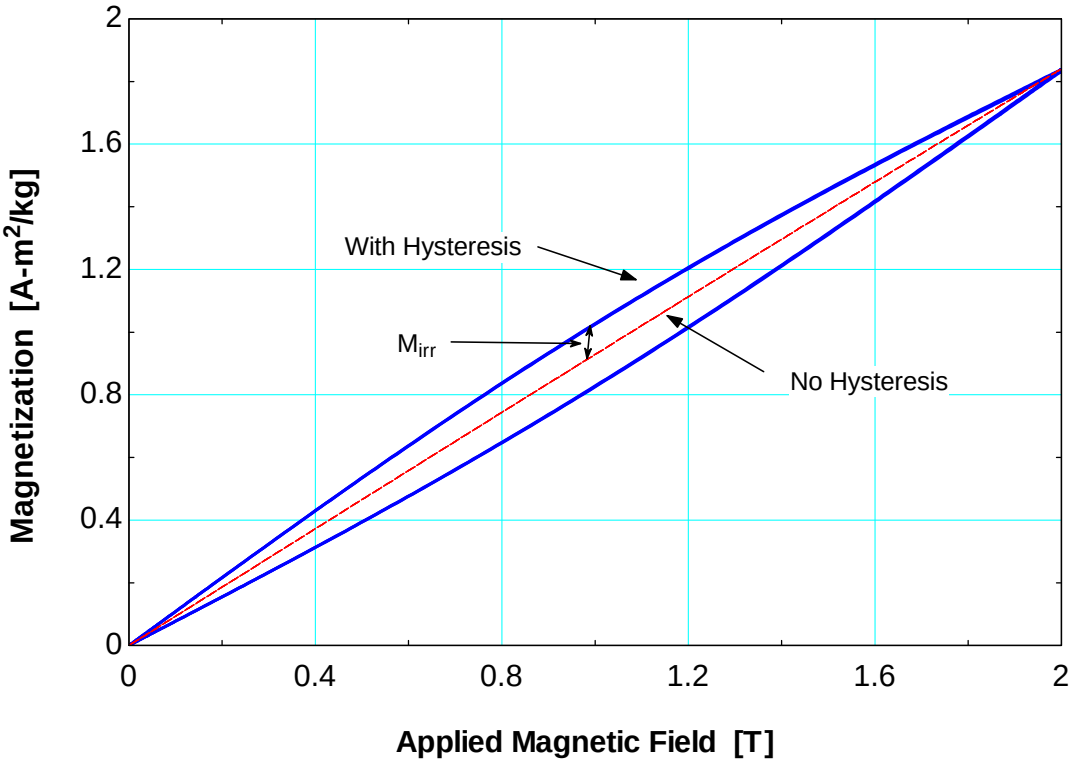

Figure 2-2. Magnetization as a function of applied magnetic field for a magnetic material predicted using Eqs. (2-13) and (2-15).

Figure 2-3 shows the temperature of the magnetic material as a function of time as it is exposed to the alternating applied magnetic field. For the case where it is modeled with no hysteresis ($\Delta M = 0$), the material experiences an isentropic temperature rise and then returns to its initial temperature as the field is removed. When hysteretic effects are included, the material experiences an adiabatic temperature change that is accompanied by an entropy increase due to the entropy generation. Therefore, when the field is removed the material does not return to its initial temperature because its entropy increases. Instead the temperature gradually rises as entropy increases during each successive cycle.

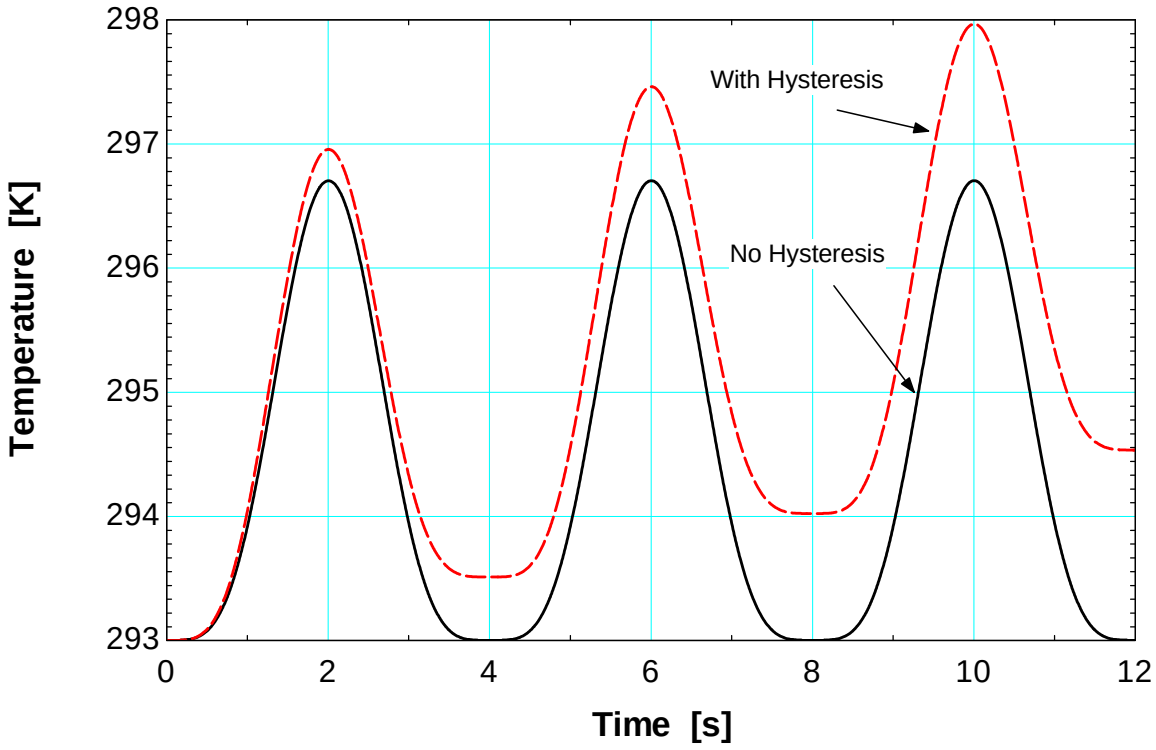

Figure 2-3. Temperature as a function of time for an adiabatic material exposed a sinusoidal applied field with and without hysteresis.

A temperature-specific entropy diagram for the adiabatic magnetization-demagnetization model is shown in Figure 2-4, with the isofield entropy lines shown. The results of the simulation with and without hysteresis are indicated.

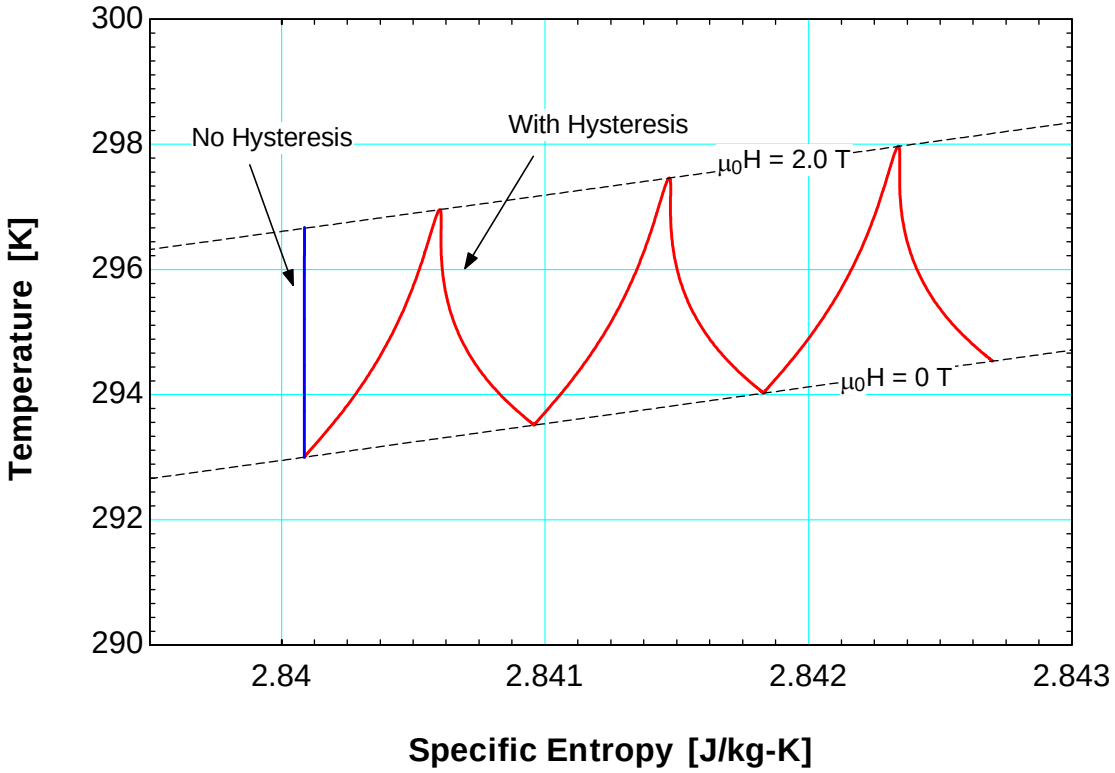

Figure 2-4. T-s diagram for single-shot model with and without hysteresis showing isofield entropy lines

The specific entropy values used to generate Figure 2-4 are calculated by eliminating the time derivatives and integrating Eq. (2-5) from a reference entropy (s_{ref}) at a reference applied field and temperature ($\mu_o H_{ref}$ and T_{ref}) to a final entropy (s) at an arbitrary applied field and temperature ($\mu_o H_f$ and T_f). The integration path proceeds first along a line of constant applied field ($\mu_o H_{ref}$) from T_{ref} to T_f:

$$s\left(T=T_f,\mu_0 H=\mu_0 H_{ref}\right)-s_{ref}=\int_{T_{ref}}^{T_f}\frac{c_{\mu_0 H=\mu_0 H_{ref}}}{T}dT=c_{\mu_0 H=\mu_0 H_{ref}}\ln\left(\frac{T_f}{T_{ref}}\right) \tag{2-24}$$

and then along a line of constant temperature (T_f) from the reference field $\mu_0 H_{ref}$ to $\mu_0 H_f$:

$$s\left(T=T_f,\mu_0 H_f\right)-s\left(T=T_f,\mu_0 H=\mu_0 H_{ref}\right)=\int_{\mu_0 H_{ref}}^{\mu_0 H_f}\left(\frac{\partial v M_{an}}{\partial T}\right)_{\mu_0 H,T=T_f}d\mu_0 H \tag{2-25}$$

where $c_{\mu_0 H=\mu_0 H_{ref}}$ is the constant field specific heat at $\mu_o H_{ref}$. Substituting Eq. (2-13) into Eq. (2-25) provides:

$$s\left(T=T_f,\mu_0 H_f\right)-s\left(T=T_f,\mu_0 H=\mu_0 H_{ref}\right)=-\int_{\mu_0 H_{ref}}^{\mu_0 H_f}\frac{C}{\mu_0}\frac{v\,\mu_o H}{T_f^2}d\,\mu_0 H=\frac{C}{\mu_0}\frac{v}{2T_f^2}\left(\mu_o H_{ref}^2-\mu_o H_f^2\right) \quad (2\text{-}26)$$

Adding Eqs. (2-25) and (2-26) together and defining $s_{ref} = 0$ at $T_{ref} = 1$ K and $\mu_o H_{ref} = 0$ provides:

$$s\left(T,\mu_0 H\right)=c_{\mu_0 H=0}\ln\left(T\right)-\frac{C}{\mu_0}\frac{v\left(\mu_o H\right)^2}{2T^2} \quad (2\text{-}27)$$

From Eq. (2-27), the constant field derivative of entropy with respect to temperature is:

$$\left(\frac{\partial s}{\partial T}\right)_{\mu_0 H}=\frac{c_{\mu_0 H}}{T}=\frac{c_{\mu_0 H=0}}{T}+\frac{C}{\mu_0}\frac{v\left(\mu_o H\right)^2}{T^3} \quad (2\text{-}28)$$

which shows that the constant field specific heat must be a function of temperature in order to agree with the Curie law equation of state:

$$c_{\mu_0 H}=c_{\mu_0 H=0}+\frac{C}{\mu_0}\frac{v\left(\mu_o H\right)^2}{T^2} \quad (2\text{-}29)$$

As the plot in Figure 2-4 indicates, the specific entropy remains constant for the case where there is no hysteresis. In the case where hysteresis is modeled, the entropy increases gradually as more cycles are completed, due to the entropy generation related to the irreversible magnetization term. The discontinuous slope in the entropy for the model with hysteresis is a consequence of the absolute value of the $\frac{d\,\mu_0 H}{dt}$ term in Eq. (2-8).

The entropy generation rate is plotted as a function of time in Figure 2-5 according to the relation given in Eq. (2-8). It reaches a minimum where the field is at either the maximum or minimum value, and it reaches a maximum where the irreversible magnetization is maximum (halfway between the minimum and maximum fields). This behavior is consistent with the idea that entropy generation is

related to the area of the hysteresis curve; Figure 2-2 shows that the differential area of the hysteresis curve approaches zero at $\mu_o H_{min}$ and $\mu_o H_{max}$. Figure 2-6 shows the entropy generation rate as a function of time over a larger range of times and with a larger maximum irreversible magnetization of $v\Delta M = 0.5\ \frac{A-m^2}{kg}$. The plot demonstrates that the entropy generation rate decreases steadily over time as the temperature of the material increases, which is a consequence of the entropy generation rate being inversely proportional to the material temperature per Eq. (2-8). The larger value of the maximum irreversible magnetization was chosen so that the behavior of the entropy generation rate as a function of time is obvious.

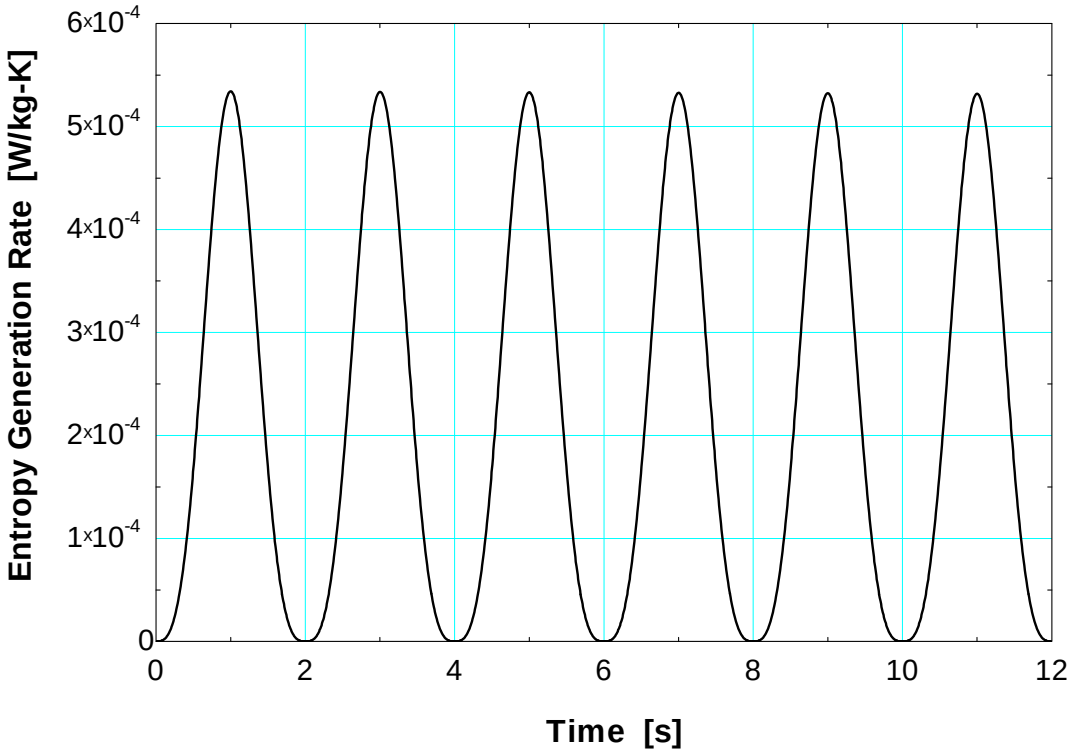

Figure 2-5. Entropy generation as a function of time as a result of hysteresis in the single-shot model. Note that the time scale is not large enough to show decrease in entropy generation rate with time.

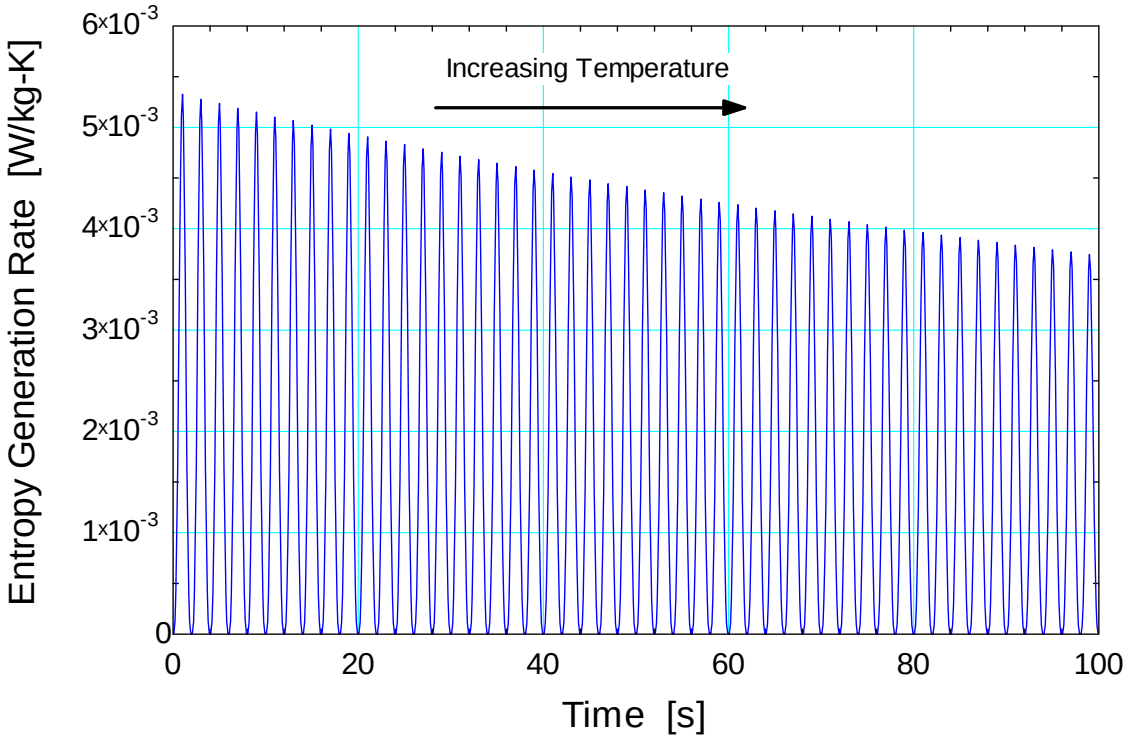

Figure 2-6. Entropy generation rate as a function of time with $v\Delta M$ = 0.5 [A-m^2/kg] to show steady decline in rate over time.

The total entropy generated should be equal to the difference in entropy between the initial and final states of the process since this is an adiabatic, closed process. In other words the area underneath the curve in Figure 2-5 should be equal to the difference between final entropy and initial entropy for the process with hysteresis shown in Figure 2-4. Mathematically, this can be stated in an integral:

$$s_f - s_i = \int_0^{t_f} \frac{\dot{S}_{gen}}{m} dt \tag{2-30}$$

where $t_f = 12$ sec in this case. By utilizing the trapezoidal method for integration, the integral in (2-30) yields a value of 0.0026 $^{J}/_{\text{kg-K}}$, which is exactly the same value of $s_f - s_i$. The MATLAB code used to generate these plots and data is included in Appendix A.

Also, the area of the hysteresis loop should be equivalent to the area swept by the irreversible magnetization function. Since the irreversible magnetization function is always positive and symmetrical, the total area swept by the irreversible magnetization function is equal to:

$$Area = T\frac{S_{gen}}{m} = \oint_{cycle} vM_{irr}\left|d\,\mu_0 H\right| = 2\int_0^{\mu_0 H_{\max}} vM_{irr}\,d\,\mu_0 H \tag{2-31}$$

This area is also equal to the area of the hysteresis loop for one complete cycle:

$$Area = T\frac{S_{gen}}{m} = \oint_{cycle} vM\,d\,\mu_0 H \tag{2-32}$$

By numerical integration of Eq. (2-31) using the trapezoidal rule function in MATLAB, the area is found to be $0.2546\ {}^{\mathrm{J}}\!/_{\mathrm{kg}}$ and by numerically integrating Eq. (2-32) in the same fashion, the area is found to be $0.2535\ {}^{\mathrm{J}}\!/_{\mathrm{kg}}$. This is a 0.43% difference, which is attributable to numerical estimation error. Figure 2-7 is a plot of the exergy loss per cycle as a function of the maximum irreversible magnetization constant ΔM. The solid line shows the energy loss calculated via Eq. (2-32) and the data points show the calculation via Eq. (2-31). There is very little difference in the values, and therefore the entropy generation is directly related to the area under the *M-H* curve for this model.

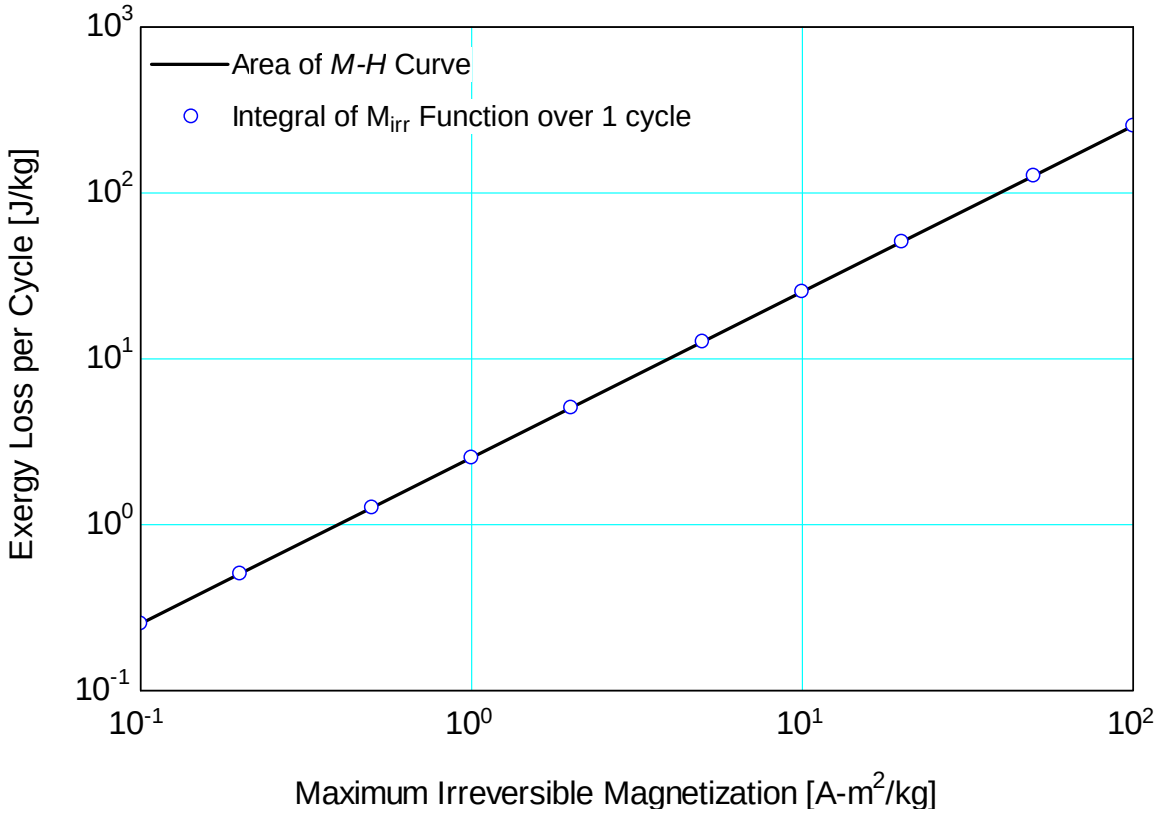

Figure 2-7. Comparison of calculation of exergy loss for various values of ΔM

2.3 Carnot Cycle Analysis

As an extension to the investigation of hysteretic effects on a single shot adiabatic magnetization/demagnetization model, a magnetic Carnot refrigeration cycle (or ADR cycle) is modeled to investigate the deterioration in its performance that occurs due to the entropy generation that arises from hysteresis. The magnetic Carnot cycle consists of four distinct processes listed as follows:

1. Adiabatic magnetization
2. Isothermal heat rejection
3. Adiabatic demagnetization
4. Isothermal heat addition

The same entropy generation term introduced in Eq. (2-8) is added to the entropy balance for the magnetization and demagnetization processes in order to simulate the irreversibility associated with magnetic hysteresis.

2.3.1 Governing Equations

Adiabatic magnetization and demagnetization

By performing an entropy balance on the magnetic material of interest, the following equation is obtained in the same manner as the single-shot model:

$$\frac{dS}{dt} = \dot{S}_{gen} \tag{2-33}$$

which can be rewritten on a mass specific basis in terms of the mass of the magnetic material *m*:

$$\frac{ds}{dt} = \frac{\dot{S}_{gen}}{m} \tag{2-34}$$

The derivative in Equation 34 can be expressed in terms of its magnetic and thermal contributions to entropy:

$$\frac{ds}{dt} = \frac{c_{\mu_0 H}}{T}\left(\frac{dT}{dt}\right) + \left(\frac{\partial v M_{an}}{\partial T}\right)_{\mu_0 H}\left(\frac{d\mu_0 H}{dt}\right) = \frac{\dot{S}_{gen}}{m} \tag{2-35}$$

which is identical to Eq. (2-11) in Section 2.1.2 . Similarly, the entropy generation can be expressed according to Eq. (2-8):

$$\frac{c_{\mu_0 H}}{T}\left(\frac{dT}{dt}\right) + \left(\frac{\partial v M_{an}}{\partial T}\right)_{\mu_0 H}\left(\frac{d\mu_0 H}{dt}\right) = \frac{v M_{irr}}{T}\left|\frac{d\mu_0 H}{dt}\right| \tag{2-36}$$

which is identical to Eq. (2-12). These equations are valid for both adiabatic magnetization and demagnetization because the processes are thermodynamically equivalent.

Isothermal heat rejection and addition

By performing an entropy balance on the magnetic material of interest:

$$\frac{dS}{dt} = \dot{S}_{gen} + \frac{\dot{Q}}{T} \tag{2-37}$$

and by dividing by the mass of the magnetic material *m*:

$$\frac{ds}{dt} = \frac{\dot{S}_{gen}}{m} + \frac{\dot{q}}{T} \tag{2-38}$$

where $\dot{q}$ is the rate of heat transfer per unit mass of magnetic material and *T* is the temperature of the material. Again by expanding the rate of change in entropy into its magnetic and thermal terms provides:

$$\frac{c_{\mu_0 H}}{T}\left(\frac{dT}{dt}\right) + \left(\frac{\partial v M_{an}}{\partial T}\right)_{\mu_0 H}\left(\frac{d\mu_0 H}{dt}\right) = \frac{\dot{S}_{gen}}{m} + \frac{\dot{q}}{T} \tag{2-39}$$

Since processes 2 and 4 are isothermal, the change in temperature with respect to time $\frac{dT}{dt}$ is equal to zero. Applying this relation and substituting the expression for the entropy generation from Eq. (2-8) leads to:

$$\left(\frac{\partial v M_{an}}{\partial T}\right)_{\mu_0 H}\left(\frac{d\mu_0 H}{dt}\right) = \frac{v M_{irr}}{T}\left|\frac{d\mu_0 H}{dt}\right| + \frac{\dot{q}}{T} \tag{2-40}$$

By rearranging this equation, the rate of heat transfer per unit mass of magnetic material can be recovered for both the heat rejection process ($\dot{q}_H$) and heat absorption process ($\dot{q}_C$). For the heat rejection to the hot thermal reservoir:

$$\dot{q}_H = T_H\left[\left(\frac{\partial v M_{an}}{\partial T}\right)_{\mu_0 H}\left(\frac{d\mu_0 H}{dt}\right) - \frac{v M_{irr}}{T_H}\left|\frac{d\mu_0 H}{dt}\right|\right] \tag{2-41}$$

and for the heat absorption from the cold thermal reservoir:

$$\dot{q}_C = T_C \left[\left(\frac{\partial v M_{an}}{\partial T} \right)_{\mu_0 H} \left(\frac{d\mu_0 H}{dt} \right) - \frac{v M_{irr}}{T_C} \left| \frac{d\mu_0 H}{dt} \right| \right] \tag{2-42}$$

It is important to note that the positive direction for heat flow is defined to be *into* the material, and thus $\dot{q}_H$ is a negative quantity and $\dot{q}_C$ is a positive quantity for this model.

2.3.2 Model Parameters

For this model, the equation of state relating the magnetization and applied magnetic field that is used is the Curie law (the same equation of state that was used previously in the single-shot model):

$$M_{an} = \frac{C}{\mu_0} \frac{\mu_0 H}{T} \tag{2-43}$$

The irreversible magnetization will again be applied to describe the effects of hysteresis on the magnetization of the material:

$$M = M_{an} - M_{irr} \operatorname{sign}\left(\frac{d\mu_0 H}{dt} \right) \tag{2-44}$$

For simplicity, M_{irr} can be described by a sinusoidal relationship described in Eq. (2-15) which is positive for all values of applied field except at the minimum and maximum applied fields, where it is equal to zero. In this simple model the minimum applied field will be equal to zero, $\mu_0 H_{\min} = 0$, which yields and equation for the magnetization *M* of the form:

$$M = \frac{C}{\mu_0} \frac{\mu_0 H}{T} - \Delta M \sin\left(\pi \frac{\mu_0 H}{\mu_0 H_{\max}} \right) \operatorname{sign}\left(\frac{d\mu_0 H}{dt} \right) \tag{2-45}$$

Substituting the equation of state in (2-43) into Eq. (2-36) and eliminating the time derivatives provides:

$$\frac{c_{\mu_0 H}}{T} dT - \frac{C}{\mu_0} \frac{v \mu_0 H}{T^2} d\mu_0 H = \frac{v M_{irr}}{T} \left| d\mu_0 H \right| \tag{2-46}$$

Doing the same for equations (2-41) and (2-42) respectively:

$$\delta q_H = T_H \left[\frac{C}{\mu_0} \frac{v \mu_0 H}{T_H^{\,2}} d\mu_0 H - \frac{v M_{irr}}{T_H} \left| d\mu_0 H \right| \right] \tag{2-47}$$

$$\delta q_C = T_C \left[\frac{C}{\mu_0} \frac{v \mu_0 H}{T_C^{\,2}} d\mu_0 H - \frac{v M_{irr}}{T_C} \left| d\mu_0 H \right| \right] \tag{2-48}$$

where δq_H and δq_C are the differential heat transfers per unit mass of magnetic material to the hot and cold reservoirs, respectively.

2.3.3 Model Results

Table 2-2 is a summary of the input parameters used in this model. These inputs are arbitrary and are chosen to be realistic; however, they are not specific to any magnetic refrigerant material.

Table 2-2. Properties specified for Carnot cycle model simulation

Variable	Value	Variable	Value
$\mu_0 H_{\max}$	2 *Tesla*	C	20 K
$\mu_0 H_{\min}$	0 *Tesla*	τ	4 s
$c_{\mu_0 H=0}$	0.5 $^{J}/_{kg-K}$	T_H	280 K
ρ	7900 $^{kg}/_{m^3}$	T_C	273 K

In this model, each of the equations were evaluated numerically using a second order Runge-Kutta method. This method solves for a point one step forward in magnetic field by using the slope of the function evaluated halfway between the current point and the point 1 step forward, multiplying that slope by the step size, and adding it to the value of the current point. Mathematically, this process appears as:

$$\left[f(\mu_0 H) \right]_{i+1} = \left[f(\mu_0 H) \right]_i + \Delta\mu_0 H \frac{df}{d\mu_0 H} \left(\mu_0 H_i + \tfrac{\Delta\mu_0 H}{2}, f_i + \tfrac{\Delta\mu_0 H}{2} \tfrac{df}{d\mu_0 H} (\mu_0 H_i, f_i) \right) \qquad i = 1..N \tag{2-49}$$

where $\Delta\mu_0 H$ is a finite step size for the magnetic field and *i* is the current step. The function $f(\mu_0 H)$ can be any function that has a known derivative with respect to magnetic field and a known initial condition. For this problem, *f* can be the temperature *T*, specific entropy *s*, or heat transfer q for the isothermal heat addition/rejection processes. The entropy is defined using the same method described in Eqs. (2-24)-(2-27), where a reference field is set at 0 Tesla and a reference temperature is 1 K.

By applying the equations for adiabatic magnetization or demagnetization outlined in Section 2.3.1 the state of the system can be described. Writing numerical estimates explicitly based on Eq. (2-49), the temperature during the adiabatic magnetization or demagnetization at any node step in magnetic field *i* can be expressed as:

$$T_{i+1} \cong T_i + \frac{v M_{irr,mid,i}}{\left(c_{\mu_0 H}\right)_{mid,i}} \left|\Delta\mu_0 H\right| + \frac{C}{\mu_0} \frac{v\left(\mu_0 H\right)_{mid,i}}{\left(c_{\mu_0 H}\right)_{mid,i} T_{mid,i}} \Delta\mu_0 H \quad i = 1..N \tag{2-50}$$

where $\left(\mu_0 H\right)_{mid}$ and T_{mid} are evaluated at the midpoint between the steps *i* and $i+1$. Note that the irreversible magnetization function is also evaluated at $\left(\mu_0 H\right)_{mid}$. The midpoint applied magnetic field is:

$$\left(\mu_0 H\right)_{mid,i} = \mu_0 H_i + \tfrac{\Delta\mu_0 H}{2} \tag{2-51}$$

and midpoint temperature:

$$T_{mid,i} \cong T_i + \frac{v M_{irr,i}}{\left(c_{\mu_0 H}\right)_i} \left|\tfrac{\Delta\mu_0 H}{2}\right| + \frac{C}{\mu_0} \frac{v\left(\mu_0 H\right)_i}{\left(c_{\mu_0 H}\right)_i T_i} \tfrac{\Delta\mu_0 H}{2} \tag{2-52}$$

The constant field specific heat is a function of the temperature and applied magnetic field as well:

$$\left(c_{\mu_0 H}\right)_{mid,i} = c_{\mu_0 H=0} + \frac{C}{\mu_0} \frac{v\left(\mu_o H\right)^2_{mid,i}}{T^2_{mid,i}} \tag{2-53}$$

The irreversible magnetization is described in terms of the applied magnetic field for this problem by:

$$M_{irr,i} = \Delta M \sin\left(\pi \frac{\mu_0 H_i}{\mu_0 H_{\max}}\right)$$
$$M_{irr,mid,i} = \Delta M \sin\left(\pi \frac{\mu_0 H_i + \frac{\Delta\mu_0 H}{2}}{\mu_0 H_{\max}}\right) \tag{2-54}$$

For the entropy calculation, the midpoint temperature is also used:

$$s_{i+1} = s_i + \frac{v M_{irr,mid,i}}{T_{mid,i}} \left|\Delta\mu_0 H\right| \quad i = 1..N \tag{2-55}$$

Note that in these equations, $\Delta\mu_0 H$ is positive for magnetization and negative for demagnetization.

The isothermal heat addition/rejection processes are treated with a different set of equations (described in Section 2.3.1) and therefore must be solved separately. Since the temperature at any time is known, it does not have to be determined numerically: it is T_H for the heat rejection process and T_C for the heat addition process. However, since the magnetic field is not constant during these processes, the entropy changes according to:

$$s_{i+1} = s_i - \frac{C}{\mu_0} \frac{v \mu_0 H_{mid,i}}{T_H{}^2} \Delta\mu_0 H \tag{2-56}$$

$$s_{i+1} = s_i - \frac{C}{\mu_0} \frac{v \mu_0 H_{mid,i}}{T_C{}^2} \Delta\mu_0 H \tag{2-57}$$

and the total amount of heat transferred up to node *i* is expressed as follows:

$$q_{i+1} = q_i - \frac{C}{\mu_0} \frac{v \mu_0 H_{mid,i}}{T_H} \Delta\mu_0 H - v M_{irr,mid,i} \left|\Delta\mu_0 H\right| \tag{2-58}$$

$$q_{i+1} = q_i - \frac{C}{\mu_0} \frac{v \mu_0 H_{mid,i}}{T_C} \Delta\mu_0 H - v M_{irr,mid,i} \left|\Delta\mu_0 H\right| \tag{2-59}$$

In the previous equations (2-56)-(2-59), the temperature is the temperature of the thermal sink (T_H for heat rejection and T_C for heat addition). Again it should be noted that the magnetic field step $\Delta\mu_0 H$ is positive for isothermal heat rejection and negative for heat addition..

These equations are evaluated numerically (using the MATLAB code included in Appendix A) and the resulting Carnot cycles are plotted on a *T*-*s* diagram. Figures 2-8, 2-9 and 2-10 show the cycle plotted on a *T*-*s* diagram for $v\Delta M$ = 0, 0.5, and 5 $\frac{A-m^2}{kg}$, respectively, with pertinent isofield entropy lines drawn. The hot and cold reservoirs are 280 K and 273 K respectively for each plot. These diagrams also show the numerical result for entropy as a function of temperature obtained from Eqs. (2-55) and (2-56) or (2-57) as compared to the analytical result obtained from evaluating Eq. (2-27). As these plots illustrate, there is nearly perfect agreement between the numerical results to the analytical results, which verifies the numerical calculations. Also, by examining the plots, it is evident that as the irreversible magnetization is increased, the adiabatic magnetization and demagnetization processes have a characteristic curvature (seen in Figure 2-10) in the direction of increasing entropy. This behavior is a direct result of entropy generation and has a significant effect on the performance of the refrigeration cycle.

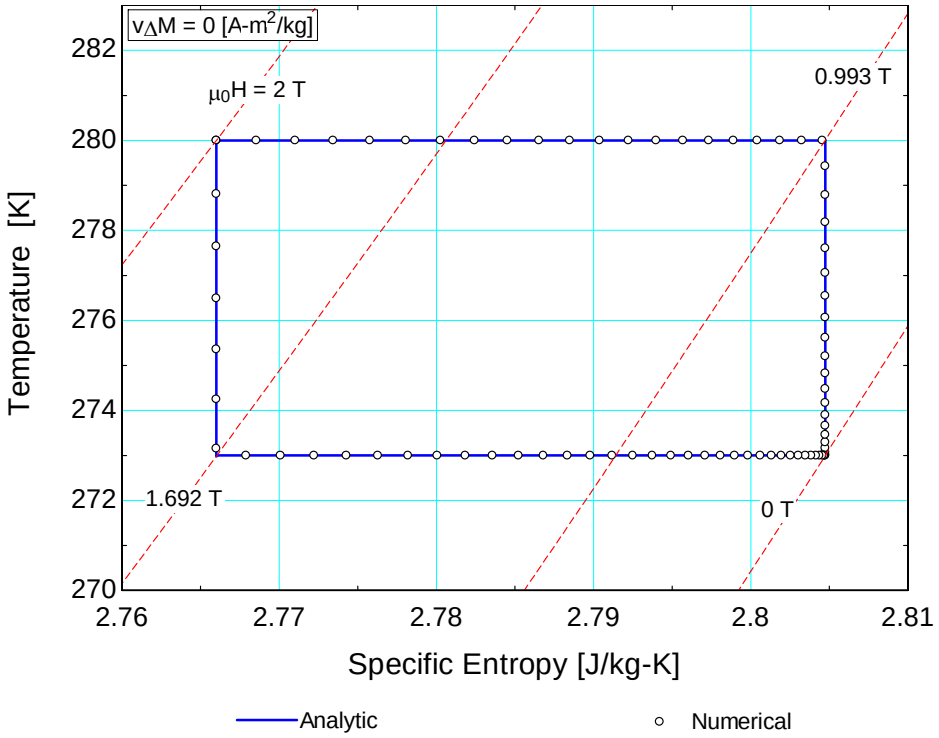

Figure 2-8. *T-s* diagram for Carnot cycle operating between T_H = 280 K and T_C = 273 K with ΔM = 0 A-m²/kg and isofield entropy lines shown

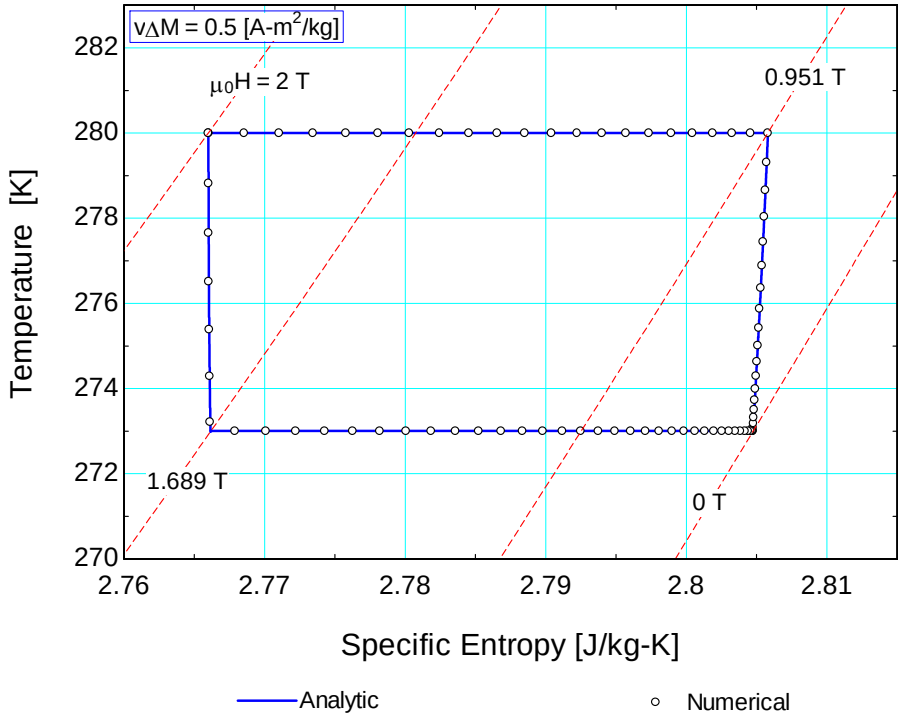

Figure 2-9. *T-s* diagram for Carnot cycle operating between T_H = 280 K and T_C = 273 K with ΔM = 0.5 A-m²/kg and isofield entropy lines shown

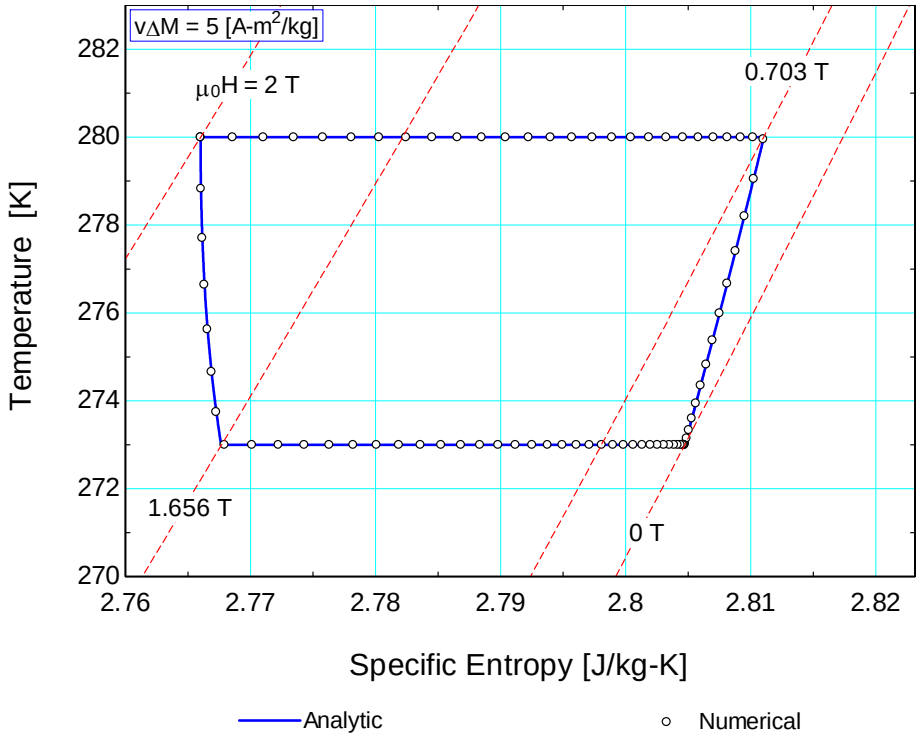

Figure 2-10. *T-s* diagram for Carnot cycle operating between T_H = 280 K and T_C = 273 K with vΔM = 5 A-m²/kg

Figure 2-11 shows the coefficient of performance as a function of the maximum irreversible magnetization $v\Delta M$ for the magnetic Carnot cycle presented in Figure 2-8, Figure 2-9, and Figure 2-10. The *COP* decreases sharply with increasing maximum irreversible magnetization, with the Carnot *COP* occurring where $v\Delta M = 0$. Such a sharp decline in *COP* relative to a small increase in $v\Delta M$ suggests that the performance of a magnetic refrigerator is adversely affected by even a small amount of hysteresis that occurs in the material. However, magnetic materials that exhibit hysteresis also exhibit larger adiabatic temperature changes of magnetization, which may offset the negative effect of hysteresis and the characteristics of an AMRR cycle may be substantially different than this Carnot cycle.

Figure 2-12 shows the coefficient of performance of a Carnot refrigerator with hysteresis as a function of the refrigeration temperature (T_C) for various values of $v\Delta M$ with the hot reservoir held fixed at $T_H = 293$ K. Like Figure 2-11, it shows that the *COP* decreases as $v\Delta M$ increases for all refrigeration temperatures. Also, it indicates that as the temperature difference between the hot and cold

thermal reservoirs increases, the relative impact of increasing $v\Delta M$ on the *COP* remains approximately the same. For example, the *COP* with $v\Delta M = 0.2\ \frac{A-m^2}{kg}$ is approximately $\frac{1}{3}$ the value of the *COP* with $v\Delta M = 0\ \frac{A-m^2}{kg}$ for all values of T_C.

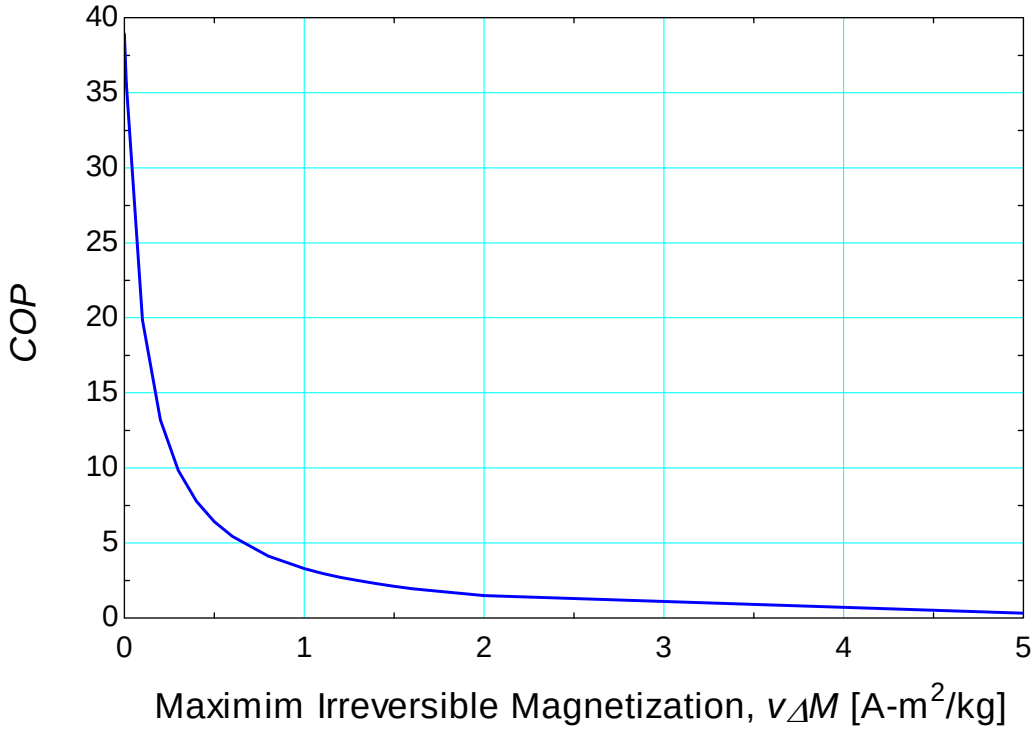

Figure 2-11. COP as a function of the maximum irreversible magnetization for magnetic Carnot cycle with T_H = 280 K and T_C = 273 K

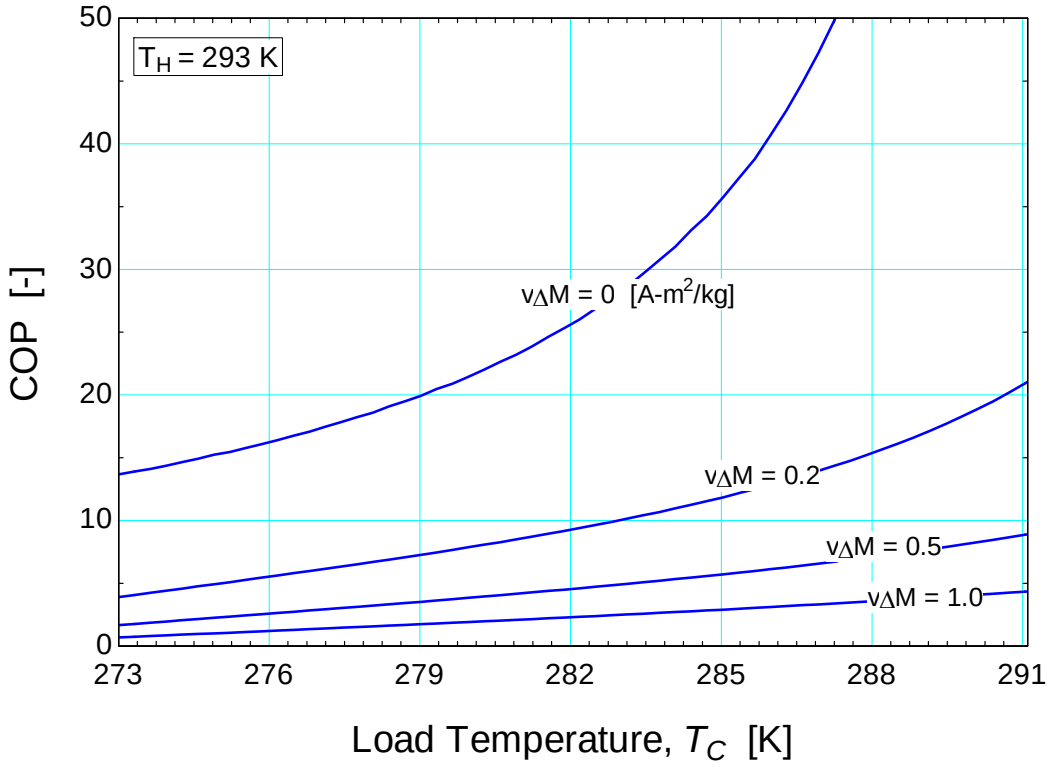

Figure 2-12. COP as a function of the load temperature (T_C) for various values of the maximum irreversible magnetization and T_H = 293 K

Figure 2-13 illustrates the refrigeration capacity per mass of a Carnot refrigerator with hysteresis as a function of the refrigerator temperature (T_C) for various values of ΔM with the hot reservoir held fixed at $T_H = 293$ K. Like the *COP*, the refrigeration capacity decreases with increasing ΔM for all T_C.

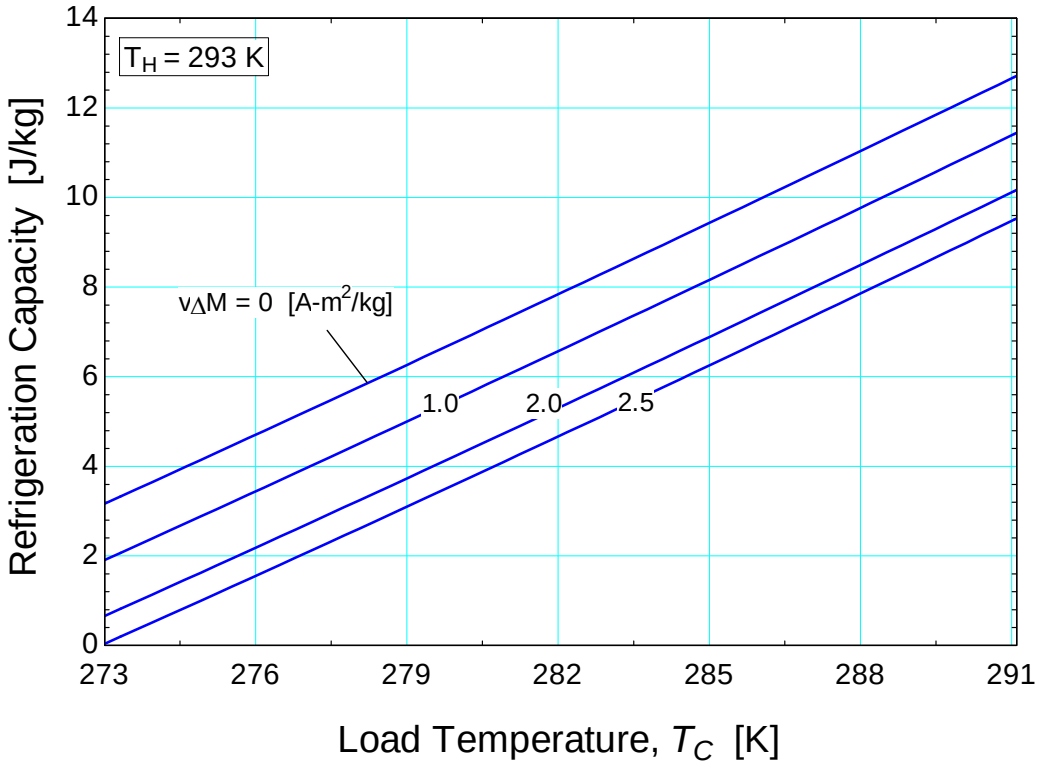

Figure 2-13. Refrigeration capacity per mass as a function of the load temperature (T_C) for various values of the maximum irreversible magnetization and T_H = 293 K

REFERENCES

1. Bertotti, G., *Hysteresis in magnetism : for physicists, materials scientists, and engineers*. 1998, San Diego, CA: Academic Press. 558.

2. Jiles, D.C. and D.L. Atherton, *Theory of ferromagnetic hysteresis.* Journal of Magnetism and Magnetic Materials, 1986. **61**(1-2): p. 48-60.

3. Nellis, G., *Stirling/Magnetic Cryocooler*, in *Department of Mechanical Engineering*. 1997, Massachusettes Institute of Technology: Cambridge, MA. p. 198.

Chapter 3 NUMERICAL MODEL DESCRIPTION

The numerical model used in this this thesis is described by Engelbrecht (2004, 2008) with modifications to account for magnetic hysteresis in the regenerator energy balance equations [1, 2]. The modified MATLAB code for the model is included in Appendix C. Engelbrecht (2008) provides a detailed description of the AMR model used in this thesis, and outlines the governing heat transfer fluid energy equations as well as Nusselt number, pressure drop, and heat transfer fluid property correlations used in the model. Corrections for internal temperature gradients that exist in a packed sphere regenerator are also discussed in depth. This chapter focuses on the modification of the regenerator magnetocaloric material governing energy equations presented by Engelbrecht (2008) to account for magnetic hysteresis.

3.1 Model Input Parameters

Figure 3-1 is a conceptual schematic of the one-dimensional AMRR regenerator bed model with important model input parameters shown. The model requires input parameters that define the heat transfer fluid, the magnetic regenerator material, the regenerator geometry, and the applied magnetic field.

The heat transfer fluid properties required by the model are the fluid specific heat capacity (c_f), density (ρ_f), thermal conductivity (k_f), and viscosity (μ_f). The temperatures of the fluid hot (T_H) and cold (T_C) reservoirs must also be specified, and are assumed to be constant. The time-dependent mass flow ($\dot{m}$) profile of the heat transfer fluid must also be defined, and should be based on the profile of the applied magnetic field ($\mu_o H$), which also must be specified in space (x) and time (t). A positive mass flow rate indicates flow from the hot to cold reservoir and a negative mass flow rate flows from the cold to hot reservoir. The heat transfer fluid is assumed to be incompressible and the flow is assumed to be perfectly distributed, meaning there is no spatial variation in the flow.

The magnetocaloric material properties required by the model are the regenerator material thermal conductivity (k_r), partial derivative of entropy with applied field at constant temperature $\left(\frac{\partial s_r}{\partial \mu_o H}\right)_T$, constant

field specific heat capacity ($c_{\mu_o H}$), and density (ρ_f). Also, if the bed is layered, the model requires a spatially-dependent Curie temperature (T_{Curie}) input. The regenerator geometry is specified by the cross-sectional area (A_c), bed length (L), volume specific particle surface area (a_s), particle hydraulic diameter (d_h), and bed porosity (ε). A Nusselt number dependent on the regenerator geometry, Reynolds number of the flow (Re_f), and Prandtl number of the fluid (Pr_f) is required. Likewise, a friction factor (f_f) that is dependent on the regenerator geometry and the Reynolds number of the fluid flow is required. Finally, an effective thermal conductivity of the regenerator matrix is specified (k_{eff}) that depends on the thermal conductivity of the fluid, the thermal conductivity of the magnetocaloric material, the regenerator geometry, the Reynolds number of the fluid flow, and the Prandtl number of the fluid.

The outputs of the model are the regenerator material (T_r) and heat transfer fluid (T_f) temperature distributions as a function of regenerator position (x) and cycle time (t). These temperature distributions are used along with the material property data to calculate performance parameters that characterize the system, such as refrigeration capacity ($\dot{Q}_{ref}$) and the system coefficient of performance (COP).

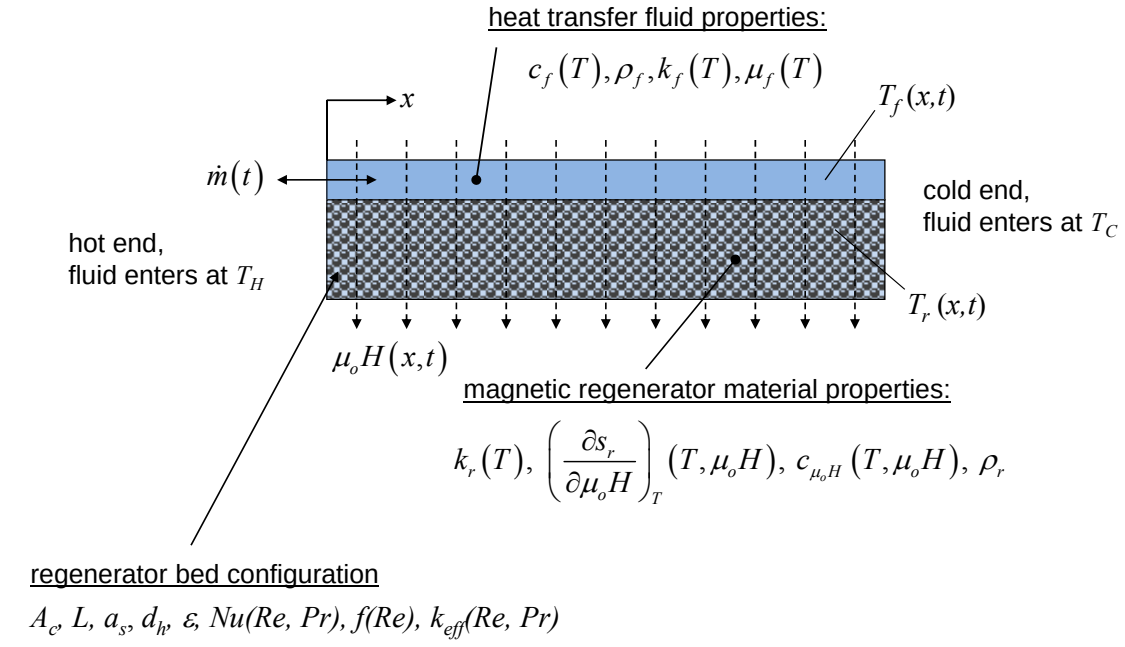

Figure 3-1. Conceptual schematic of the one-dimensional regenerator bed showing heat transfer fluid, magnetocaloric regenerator material, and bed geometry input parameters.

The coefficient of performance (*COP*) used in this thesis is defined as:

$$COP = \frac{\left|Q_{ref}\right|}{\left|W_{pump}\right| + \left|W_{motor}\right|} \tag{3-1}$$

where Q_{ref} is the refrigeration load, W_{pump} is the pump work, and W_{motor} is the motor work per cycle. The motor work per cycle is defined as:

$$W_{motor} = \frac{W_{mag}}{\eta_{motor}} \tag{3-2}$$

where W_{mag} is the magnetic work per cycle and η_{motor} is the motor efficiency. The pump work per cycle is defined in terms of the pressure gradient ($\frac{dP}{dx}$) across the regenerator bed:

$$W_{pump} = \frac{1}{\eta_{pump}} \int_0^L \int_0^\tau \left(\left| \frac{\dot{m}(t)}{\rho_f} \frac{dP}{dx} \right| \right) dt\, dx \tag{3-3}$$

where η_{pump} is the pump efficiency, L is the length of the regenerator bed, and τ is the cycle time.

Engelbrecht (2008) presents correlations for the pressure gradient in packed sphere and parallel plate regenerator geometries. A typographical error exists in this reference in the presentation of the Ergun (1952) equation to model the pressure drop in a packed sphere regenerator (Eqs. (2.57) and (2.58) in reference [2]). The Ergun equation for the pressure gradient in a packed sphere regenerator is [3]:

$$\frac{dP}{dx} = \left(\frac{A \alpha \mu_f}{d_p^2} \right) v + \left(\frac{B \beta \mu_f}{d_p} \right) v^2 \tag{3-4}$$

where the parameters *A* and *B* are based on the surface roughness of the particles and d_p is the particle diameter. Kaviany suggests values of $A = 180$ and $B = 1.8$ for smooth particles [4]. The particle diameter is expressed in terms of the hydraulic diameter (d_h) according to:

$$d_p = \frac{3}{2} \frac{1-\varepsilon}{\varepsilon} d_h \tag{3-5}$$

where ε is the porosity of the packed sphere bed. Eq. (3-4) can be rearranged and the spatial pressure gradient can be converted into a friction factor according to:

$$\frac{dP}{dx} = \frac{f_f \dot{m}^2}{2 \rho_f A_c^2 d_h} \tag{3-6}$$

Combining Eqs. (3-4) and (3-6) yields an equation for the friction factor based on the particle hydraulic diameter:

$$f_f = \frac{8}{9} \frac{A}{Re_f \varepsilon} + \frac{4}{3} \frac{B}{\varepsilon} \tag{3-7}$$

where Re_f is the Reynolds number of the fluid based on the hydraulic diameter of the packed particles.

The refrigeration load per cycle (Q_{ref}) is defined as:

$$Q_{ref} = \int_0^{\tau} \left[h_f\left(T_C\right) - h_f\left(T_{f,x=L}\right) \right] \dot{m}(t)\, dt \qquad \text{for } \dot{m}(t) > 0 \tag{3-8}$$

where $h_f\left(T_C\right)$ is the enthalpy of the fluid evaluated at the cold reservoir temperature and $h_f\left(T_{f,x=L}\right)$ is the enthalpy of the fluid evaluated at the temperature of the fluid at the cold end of the bed ($x = L$) at cycle time t. Note that a positive mass flow rate indicates a hot-to-cold blow providing refrigeration and the integral in Eq. (3-8) is only evaluated during cycle times where the mass flow rate is positive.

3.2 Regenerator Governing Equations

For the spatially one-dimensional active magnetic refrigerator model developed at the UW, the regenerator energy balance equation is modified to include an irreversible entropy generation source that can be used to represent the effect of hysteresis on the thermodynamic cycle. The model solves a pair of coupled partial differential equations in time and space for a cycle steady state condition. One equation describes the energy balance for the fluid flow through the matrix, and the other describes the energy

balance for magnetocaloric material and entrained fluid in the matrix. A schematic of the energy balance for a differential segment of the regenerator is shown in Figure 3-2:

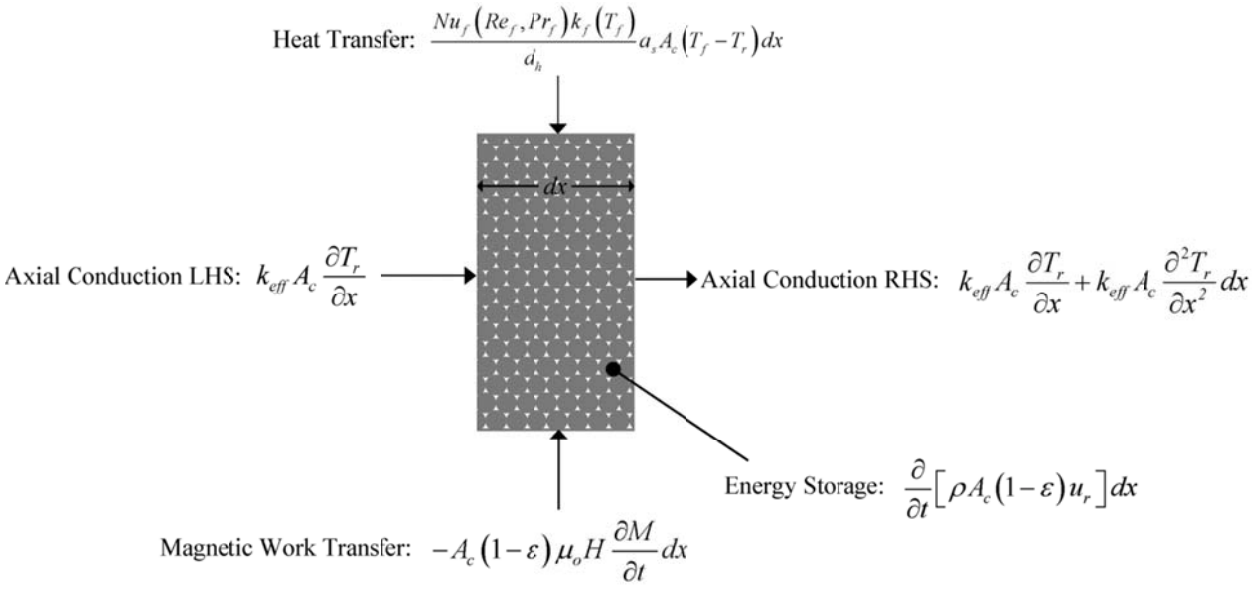

Figure 3-2. Differential segment of the regenerator with energy balance terms included

where the differential control volume has differential length *dx* and cross-sectional area A_c.

The energy balance in Figure 3-2 is written as:

$$\frac{Nu\cdot k_f}{d_h}a_sA_s\left(T_f-T_r\right)+A_c\left(1-\varepsilon\right)\mu_0 H\frac{\partial M}{\partial t}+k_{eff}A_c\frac{\partial^2 T_r}{\partial x^2}=\rho_r A_c(1-\varepsilon)\frac{\partial u_r}{\partial t} \tag{3-9}$$

An entropy balance on a differential piece of magnetocaloric material is given by:

$$dS=\frac{\delta Q}{T_r}+S_{gen} \tag{3-10}$$

where S_{gen} is the internal entropy generation related to hysteresis. By combining the energy balance for a magnetocaloric material represented by Eq. (1-4) and the entropy balance for the same magnetocaloric material represented by Eq. (3-10) we obtain:

$$dU=T_r\,dS-T_r\,S_{gen}+\mu_0 H\cdot d\left(V\cdot M\right) \tag{3-11}$$

Dividing through by the mass of the material leads to:

$$du = T_r\, ds - T_r\left(\frac{S_{gen}}{m}\right) + \mu_0 H \cdot d\left(v \cdot M\right) \tag{3-12}$$

where (S_{gen}/m) is the mass specific entropy generation. Equation (3-12) can be rearranged:

$$\frac{\partial u}{\partial t} - \frac{\mu_0 H}{\rho_r}\frac{\partial M}{\partial t} = T_r\frac{\partial s}{\partial t} - T_r\left(\frac{\dot{S}_{gen}}{m}\right) \tag{3-13}$$

Substituting Eq. (3-13) into Eq. (3-9) provides the overall energy balance equation for the regenerator:

$$\frac{Nu \cdot k_f}{d_h} a_s A_s \left(T_f - T_r\right) + k_{eff} A_c \frac{\partial^2 T_r}{\partial x^2} = \rho_r A_c (1-\varepsilon) \cdot T_r\left(\frac{\partial s_r}{\partial t} - \frac{\dot{S}_{gen}}{m}\right) \tag{3-14}$$

which can be further simplified by expressing the change in the regenerator specific entropy in terms of the its magnetic field and temperature driven components:

$$\frac{Nu \cdot k_f}{d_h} a_s A_s \left(T_f - T_r\right) + k_{eff} A_c \frac{\partial^2 T_r}{\partial x^2} = \rho_r A_c (1-\varepsilon) \cdot \left[c_{\mu_0 H} \frac{\partial T_r}{\partial t} + T_r\left(\left.\frac{\partial s_r}{\partial \mu_0 H}\right|_T \cdot \frac{\partial \mu_0 H}{\partial t} - \frac{\dot{S}_{gen}}{m}\right)\right] \tag{3-15}$$

The last term in Eq. (3-15) is related to internal entropy generation due to hysteresis. From Chapter 2, the specific entropy generation rate is resolved in terms of an irreversible magnetization according to Eq. (2-8). Substituting Eq. (2-8) into Eq. (3-15) yields:

$$\frac{Nu \cdot k_f}{d_h} a_s A_s \left(T_f - T_r\right) + k_{eff} A_c \frac{\partial^2 T_r}{\partial x^2} = \rho_r A_c (1-\varepsilon) \cdot \left[c_{\mu_0 H} \frac{\partial T_r}{\partial t} + T_r \left.\frac{\partial s_r}{\partial \mu_0 H}\right|_T \cdot \frac{\partial \mu_0 H}{\partial t} - v_r M_{irr} \left|\frac{\partial \mu_0 H}{\partial t}\right|\right] \tag{3-16}$$

as the final regenerator energy balance equation including hysteresis effects, which are expressed in terms of the irreversible mass specific magnetization (vM_{irr}).

3.3 Discretization of Governing Regenerator Equations

The regenerator is discretized into Nx spatial nodes where the axial location of each node is given by:

$$x_i = \left(i - \frac{1}{2} \right) \frac{L}{Nx} \quad i = 1..Nx \tag{3-17}$$

where i is the axial subscript and L is the length of the regenerator bed. The temporal grid is similarly separated into Nt nodes where the cycle time is given by:

$$t_j = j \frac{\tau}{Nt} \quad j = 0..Nt \tag{3-18}$$

where j is the temporal subscript.

Following Eq. (3-16), the regenerator energy balance equation for each control volume can be discretized as follows:

$$\begin{aligned} &\frac{Nu_{f\,i,j}\, k_{f\,i,j}}{d_h} a_s A_s \frac{L}{Nx} \left(T_{r\,i,j+1} - T_{f\,i,j+1} \right) + A_c \frac{L}{Nx} (1-\varepsilon) \rho_r c_{\mu_0 H\,i,j} \frac{\left(T_{r\,i,j+1} - T_{r\,i,j} \right) Nt}{\tau} \\ &+ \frac{Nx\, k_{eff\,i,j} A_c}{L} \left[T_{r\,i,j+1} - T_{r\,i\text{-}1,j+1} \right] + \frac{Nx\, k_{eff\,i,j} A_c}{L} \left[T_{r\,i,j+1} - T_{r\,i+1,j+1} \right] = \\ &- A_c (1-\varepsilon) \rho_r T_{r\,i,j} \left(\frac{\partial s_r}{\partial \mu_0 H} \right)_{i,j} \frac{\partial \mu_0 H}{\partial t} \left(x_i, \frac{t_{j+1} + t_j}{2} \right) + \\ &A_c (1-\varepsilon) \rho_r \left(v_r M_{irr} \right)_{i,j} \left| \frac{\partial \mu_0 H}{\partial t} \left(x_{Nx}, \frac{t_{j+1} + t_j}{2} \right) \right| \qquad i = 2..Nx-1 \end{aligned} \tag{3-19}$$

Since the ends of the bed are assumed to be insulated, the conduction terms vanish at the hot end ($i = 1$) and the cold end ($i = Nx$). The regenerator energy balance at the hot end is:

$$\frac{Nu_{f\ 1,j}\,k_{f\ 1,j}}{d_h}a_s A_s\frac{L}{Nx}\left(T_{r\ 1,j+1}-T_{f\ 1,j+1}\right)+A_c\frac{L}{Nx}\left(1-\varepsilon\right)\rho_r c_{\mu_0 H\ 1,j}\frac{\left(T_{r\ 1,j+1}-T_{r\ 1,j}\right)Nt}{\tau}$$
$$+\frac{Nx\,k_{eff\ 1,j}A_c}{L}\left[T_{r\ 1,j+1}-T_{r\ 2,j+1}\right]=-A_c\left(1-\varepsilon\right)\rho_r T_{r\ 1,j}\left(\frac{\partial s_r}{\partial\mu_0 H}\right)_{1,j}\frac{\partial\mu_0 H}{\partial t}\left(x_1,\frac{t_{j+1}+t_j}{2}\right) \qquad (3\text{-}20)$$
$$+A_c\left(1-\varepsilon\right)\rho_r\left(v_r M_{irr}\right)_{i,j}\left|\frac{\partial\mu_0 H}{\partial t}\left(x_{Nx},\frac{t_{j+1}+t_j}{2}\right)\right|$$

Similarly, by neglecting conduction at the cold end of the bed, the regenerator energy balance at the cold end is:

$$\frac{Nu_{f\ Nx,j}\,k_{f\ Nx,j}}{d_h}a_s A_s\frac{L}{Nx}\left(T_{r\ Nx,j+1}-T_{f\ Nx,j+1}\right)+A_c\frac{L}{Nx}\left(1-\varepsilon\right)\rho_r c_{\mu_0 H\ 1,j}\frac{\left(T_{r\ Nx,j+1}-T_{r\ Nx,j}\right)Nt}{\tau}$$
$$+\frac{Nx\,k_{eff\ Nx,j}A_c}{L}\left[T_{r\ Nx,j+1}-T_{r\ Nx\text{-}1,j+1}\right]=-A_c\left(1-\varepsilon\right)\rho_r T_{r\ Nx,j}\left(\frac{\partial s_r}{\partial\mu_0 H}\right)_{Nx,j}\frac{\partial\mu_0 H}{\partial t}\left(x_{Nx},\frac{t_{j+1}+t_j}{2}\right) \qquad (3\text{-}21)$$
$$+A_c\left(1-\varepsilon\right)\rho_r\left(v_r M_{irr}\right)_{i,j}\left|\frac{\partial\mu_0 H}{\partial t}\left(x_{Nx},\frac{t_{j+1}+t_j}{2}\right)\right|$$

where $\left(v_r M_{irr}\right)$ is the mass specific irreversible magnetization due to magnetic hysteresis. The final term in Eqs. (3-19) - (3-21) represents the energy lost due to the hysteresis entropy generation rate.

REFERENCES

1. Engelbrecht, K., *A Numerical Model of an Active Magnetic Regenerator Refrigeration System*, in *Mechanical Engineering*. 2004, The University of Wisconsin at Madison: Madison, WI. p. 157.

2. Engelbrecht, K., *A Numerical Model of an Active Magnetic Regenerator Refrigerator with Experimental Validation* in *Mechanical Engineering*. 2008, The University of Wisconsin at Madison: Madison, WI. p. 267.

3. Ergun, S., *Fluid flow through packed columns.* Chemical Engineering Progress, 1952. **48**(2): p. 89-94.

4. Kaviany, M., *Principles of Heat Transfer in Porous Media*. 1995, New York, NY: Springer.

Chapter 4 MAGNETIC EQUATIONS OF STATE

The thermodynamics of the magnetic phase change has become a growing field of interest since the discovery of the near room temperature giant magnetocaloric effect (GMCE) in $Gd_5(Si_xGe_{1-x})_4$ type compounds by Pecharsky and Gschneider in 1997 [1].

Despite the magnetocaloric effect being well-documented, it is difficult to model accurately for most materials since a general magnetic equation of state (akin to the Redlich-Kwong-Soave or Peng-Robinson equations of state for compressible substances) does not exist. The Brillouin function is widely used as the general equation of state for magnetic materials, and works well for second-order magnetic transition (SOMT) materials such as pure gadolinium [2, 3]. The second-order magnetic transition is a continuous phase transition, meaning that the partial derivative of the free energy with respect to any intensive state variable is continuous [4]. Jiles (1998) presents equations of state for paramagnetic and ferromagnetic materials based on the Brillouin function.

For first-order magnetic transition (FOMT) materials, where the magnetic phase change is discontinuous, the quantum Brillouin model presented by Jiles is not accurate. Von Ranke, Oliveira, and Gama (2004) propose a model for the first-order magnetic phase change through modifications to the Brillouin equation of state [5]. Their model is a two-parameter equation of state that also accounts for pressure effects.

4.1 Paramagnetic Equation of State

At temperatures above the Curie temperature (T_{Curie}), a ferromagnetic material becomes completely paramagnetic. A fundamental equation of state for paramagnetism allows the thermodynamic properties of a magnetic material to be evaluated above these temperatures. The quantum mean-field theory of paramagnetism states that the volumetric magnetization for a multi-electron magnetic material can be expressed as a function of applied field ($\mu_0 H$) and temperature (T) [3]:

$$M\left(\mu_0 H, T\right) = M_s\, B_J\left(z\right) = N\, g_L\, J\, \mu_B\, B_J\left(\frac{g_L J \mu_B \mu_o H}{k_B T}\right) \tag{4-1}$$

where M_s is the saturation magnetization, N is the number of atoms per unit volume, g_L is the material-dependent Lande factor, J is the total molecular angular momentum number, μ_B is the Bohr magneton, and k_B is the Boltzmann constant. The Brillouin function ($B_J\left(z\right)$) is defined as [3]:

$$B_J\left(z\right) = \left(\frac{2J+1}{2J}\right)\coth\left(\frac{2J+1}{2J}z\right) - \left(\frac{1}{2J}\right)\coth\left(\frac{z}{2J}\right) \tag{4-2}$$

where the argument $z = g_L J \mu_B \mu_o H / (k_B T)$ is the ratio of the energy due to the applied magnetic field to the thermal energy. In the limit of an ideal paramagnet (in small fields or high temperatures), the Brillouin function can be estimated by a first order series expansion:

$$N\, g_L\, J\, \mu_B B_J\left(z\right) \approx \frac{N\, g_L^2\, \mu_B^2\, J\,(J+1)\, \mu_o H}{3 k_B T} \tag{4-3}$$

Eq. (4-3) is simply the Curie law:

$$M = \frac{N\, g_L^2\, \mu_B^2\, J\,(J+1)\, \mu_o}{3 k_B}\frac{H}{T} = C\frac{H}{T} \tag{4-4}$$

which implies that:

$$C = \frac{N\, \mu_o g_L^2\, \mu_B^2\, J\,(J+1)}{3 k_B} \tag{4-5}$$

where C is the Curie constant.

Eq. (4-1) is effectively a two-parameter magnetic equation of state, where the Lande factor (g_L) and the total angular momentum (J) can be adjusted to fit the characteristics of a certain material.

4.2 Ferromagnetic Equation of State

For temperatures below the Curie temperature, a magnetic material exists in the ferromagnetic phase. The quantum mean-field equation of state for a ferromagnetic material is related to the quantum mean-field equation of state for a paramagnetic material, the difference is that ferromagnetic materials have magnetic domains that interact with one another. The interaction leads to an effective internal field (H_{eff}) that is dependent on both the applied field and magnetization. Thus the equation of state for a ferromagnetic material can be written as:

$$M\left(\mu_0 H, T\right) = N g_L J \mu_B B_J\left(\frac{g_L J \mu_B \mu_o \left(H + \alpha M\right)}{k_B T}\right) \tag{4-6}$$

where α is the domain coupling constant that is representative of the strength of interactions between neighboring domains. The magnetization of a ferromagnetic material is thus implicitly defined by itself. Eq. (4-6) has three free parameters: α , *J*, and g_L . In a high temperature limit, a ferromagnetic system becomes paramagnetic, and the Brillouin function can be estimated by a first order series expansion:

$$N g_L J \mu_B B_J\left(z\right) \approx \frac{N g_L^2 \mu_B^2 J(J+1) \mu_o \left(H + \alpha M\right)}{3 k_B T} \tag{4-7}$$

where the argument $z = g_L J \mu_B \mu_o \left(H + \alpha M\right) \big/ (k_B T)$. The volumetric magnetization is thus:

$$M = \frac{N g_L^2 \mu_B^2 J(J+1) \mu_o \left(H + \alpha M\right)}{3 k_B T} \tag{4-8}$$

which can be rearranged to solve explicitly for *M*:

$$M = \frac{N g_L^2 \mu_B^2 J(J+1) \mu_o H \big/ (3 k_B T)}{1 - \alpha N g_L^2 \mu_B^2 J(J+1) \mu_o H \big/ (3 k_B T)} = \frac{N g_L^2 \mu_B^2 J(J+1) \mu_o H \big/ (3 k_B)}{T - \alpha N g_L^2 \mu_B^2 J(J+1) \mu_o H \big/ (3 k_B)} \tag{4-9}$$

Under close inspection, Eq. (4-9) is the Curie-Weiss law:

$$M = \frac{C_W}{T - T_{Curie}} H \tag{4-10}$$

where the Curie-Weiss constant is $C_W = N\mu_o g_L^2 \mu_B^2 J(J+1)/(3k_B)$ and the Curie temperature is $T_{Curie} = \alpha N\mu_o g_L^2 \mu_B^2 J(J+1)/(3k_B)$. Since the Curie temperature is a measurable quantity, it is useful to express the domain coupling constant (α) as a function of T_{Curie}:

$$\alpha = \frac{3k_B T_{Curie}}{N\mu_o g_L^2 \mu_B^2 J(J+1)} \tag{4-11}$$

The expression for the domain coupling constant can be substituted into the argument of the Brillouin function in Eq. (4-6) to yield:

$$M(\mu_0 H, T) = N g_L J \mu_B B_J\left(\frac{g_L J \mu_B \mu_o H}{k_B T} + \frac{3T_{Curie} M}{N g_L \mu_B (J+1) T}\right) \tag{4-12}$$

which is dependent on the Curie temperature rather than the domain coupling constant.

Figure 4-1 shows the isothermal magnetic entropy change for pure gadolinium predicted by Eq. (4-12) compared to experimental data for an applied field change from 0 to 1.5 Tesla. For gadolinium, the Landé g-factor has a value of g_L = 2 and the total angular momentum has a value of J = 3.5; these values were used to generate the curve in Figure 4-1 [3]. The ferromagnetic equation of state generally over-predicts the magnitude of the magnetic entropy change for temperatures below the Curie temperature (293 K) and under-predicts it for temperatures above the Curie temperature.

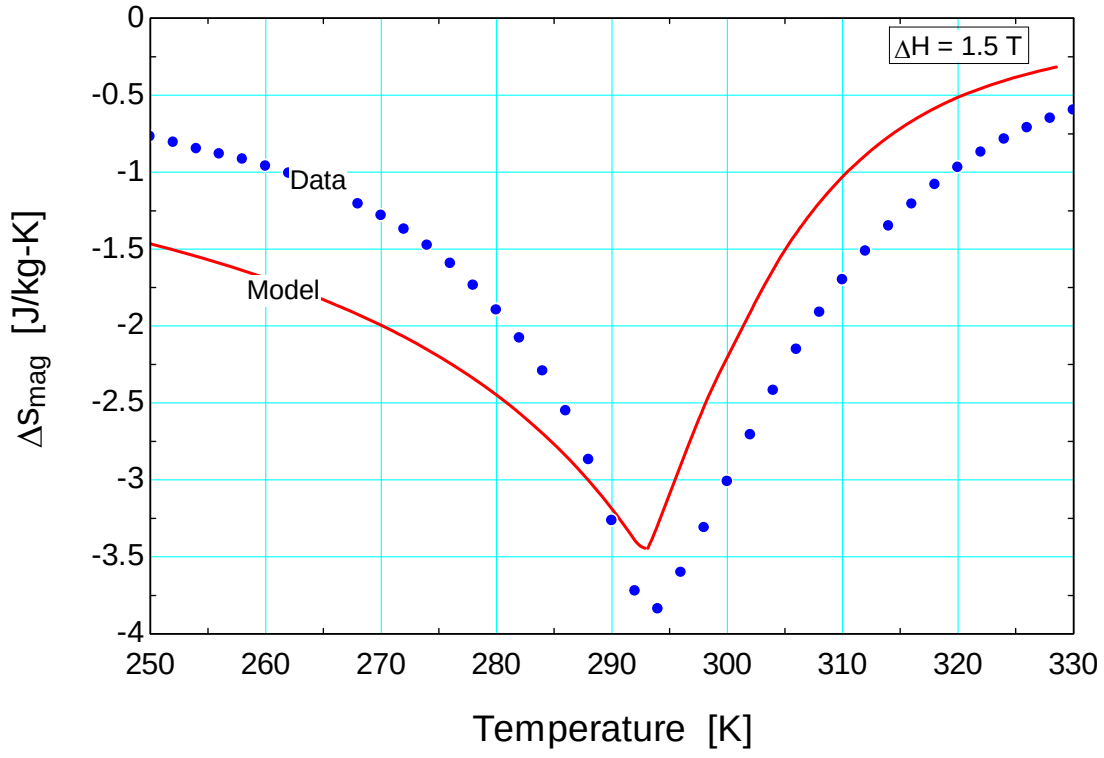

Figure 4-1. Isothermal magnetic entropy change for gadolinium for a magnetic field change of 0 to 1.5 Tesla computed using the mean field model and from experimental specific heat data. Data provided by Astronautics Corporation of America.

4.3 Metamagnetic Phase Transitions

4.3.1 Equation of State Model

Von Ranke et al. (2004) propose an equation of state model for the metamagnetic phase transition of first-order magnetic transition materials. The underlying assumption of the model is that the Curie temperature (T_{Curie}) is linearly dependent on the change in volume due to magnetostriction that occurs during the phase change:

$$T_{Curie} = T_0\left(1+\beta\omega\right) \tag{4-13}$$

where T_0 is the Curie temperature in the absence of an external magnetic field at atmospheric pressure, ω is the dimensionless change in volume, and β is a material-dependent, dimensionless parameter that

is proportional to the derivative of Curie temperature with respect to volume (dT_{Curie}/dV). The dimensionless change in volume ω is defined as:

$$\omega = \frac{V - V_0}{V_0} \tag{4-14}$$

where V_0 is the material volume in the absence of an external magnetic field at the reference pressure. In general, the Gibbs free energy for a magnetic, compressible material is defined as:

$$G \equiv U + PV - H M - T S \tag{4-15}$$

where U is the internal energy, P is pressure, V is volume, H is the external magnetic field, M is the total magnetic moment, T is the temperature, and S is the entropy. Using a molecular field approximation for a ferromagnetic lattice that includes exchange, Zeeman, distortion, and pressure effects, the Gibbs free energy is:

$$G = -\frac{3}{2}\left(\frac{J}{J+1}\right)\frac{N}{V_0}k_B T_C \sigma^2 - H g_L \mu_B J N \sigma + \frac{1}{2K}\omega^2 + P\omega - T S \tag{4-16}$$

where J is the total angular momentum, N is the number of magnetic spins, k_B is the Boltzmann constant, T_C is the Curie temperature, σ is the dimensionless magnetization, H is the external magnetic field, g_L is the Landé g-factor, K is the compressibility, P is the externally applied pressure, and S is the magnetic entropy. The dimensionless magnetization (σ) is defined as:

$$\sigma = \frac{M}{g_L \mu_B J N} \tag{4-17}$$

The minimum of the Gibbs free energy defined in Eq. (4-16) determines the equilibrium condition. To determine the equilibrium condition, the partial derivative of the Gibbs free energy with respect to the dimensionless change in volume at constant temperature, pressure, applied magnetic field, and number of magnetic spins is set to zero:

$$\left(\frac{\partial G}{\partial \omega}\right)_{T,P,H,N} = -\frac{3}{2}\left(\frac{J}{J+1}\right)\frac{N}{V_0}k_B T_0 \beta\sigma^2 + \frac{\omega}{K} + P = 0 \tag{4-18}$$

Rearranging Eq (4-18), the dimensionless volume change that minimizes the Gibbs free energy is:

$$\omega = \frac{3}{2}\frac{J^2}{J(J+1)}\frac{N}{V_0}k_B K T_0 \beta\sigma^2 - PK \tag{4-19}$$

By substituting Eq. (4-19) into Eq. (4-16) and taking the derivative of the Gibbs free energy with respect to the dimensionless magnetization (σ), the magnetic equation of state is obtained:

$$\sigma = B_J\left[3\frac{T_0}{T}\left(\frac{J}{J+1}\right)\sigma + \frac{g_L \mu_B J}{k_B T}H + \frac{9}{5}\left(\frac{(2J+1)^4 - 1}{[2(J+1)]^4}\right)\frac{T_0 \eta \sigma^3}{T} - 3\frac{J\beta PK}{(J+1)}\frac{T_0}{T}\sigma\right] \tag{4-20}$$

where B_J indicates the Brillouin function, which is defined as:

$$B_J(x) = \left(\frac{2J+1}{2J}\right)\coth\left(\frac{2J+1}{2J}x\right) - \left(\frac{1}{2J}\right)\coth\left(\frac{1}{2J}x\right) \tag{4-21}$$

The parameter η indicates the order of the magnetic phase transition and is directly related to the parameter β by:

$$\eta = \frac{5}{2}\frac{[4J(J+1)]^2}{[(2J+1)^4 - 1]}\frac{N}{V_0}k_B K T_0 \beta^2 \tag{4-22}$$

Thus, η is proportional to the square of the derivative of the Curie temperature with respect to volume. In other words, it is indicative of the magnitude of the magneto-structural volume change.

4.3.2 Application to $La(Fe_{1-x}Si_x)_{13}H_y$

A promising material for use in magnetic coolers is the $La(Fe_{1-x}Si_x)_{13}H_y$ family of compounds. These materials exhibit a large magnetocaloric effect resulting from a first order magnetic phase change. For compositions with $0.87 \leq x \leq 0.90$, the Curie temperature ranges from approximately 180 K to 330 K, depending on the concentration of hydrogen (y).

The only element to exhibit ferromagnetism in $La(Fe_{1-x}Si_x)_{13}H_y$ near its transition temperature is iron (Fe). Hence, the total angular momentum of isolated elemental iron is used to approximate that of $La(Fe_{1-x}Si_x)_{13}H_y$. The Landé g-factor for isolated iron is approximately equal to its value for gadolinium and is $g_L = 2$ and the total angular momentum has a value of $J = 1.5$ [3].

Entropy data for the specific composition of $La(Fe_{1-x}Si_x)_{13}H_y$ with $x \approx 0.115$ and $y \approx 1.21$ is available for comparison. For this specific composition, the number of magnetic spins per mole is $N = 11.5 N_A$, where the coefficient of N_A represents the number of iron atoms per mole. Figure 4-2 shows the isothermal entropy change predicted by the mean field model and experimental magnetization data for a applied magnetic field change from 0 to 1.5 Tesla for $La(Fe_{0.885}Si_{0.115})_{13}H_{1.21}$. The parameters chosen for the mean field model are η =1.39 and T_0 = 283.5 K. These parameters most closely match the data and were chosen based on trial-and-error. The model is fairly accurate in predicting the isothermal entropy change for this material, but tends to over-predict the effect below 290 K, and under-predict for temperatures above 290 K.

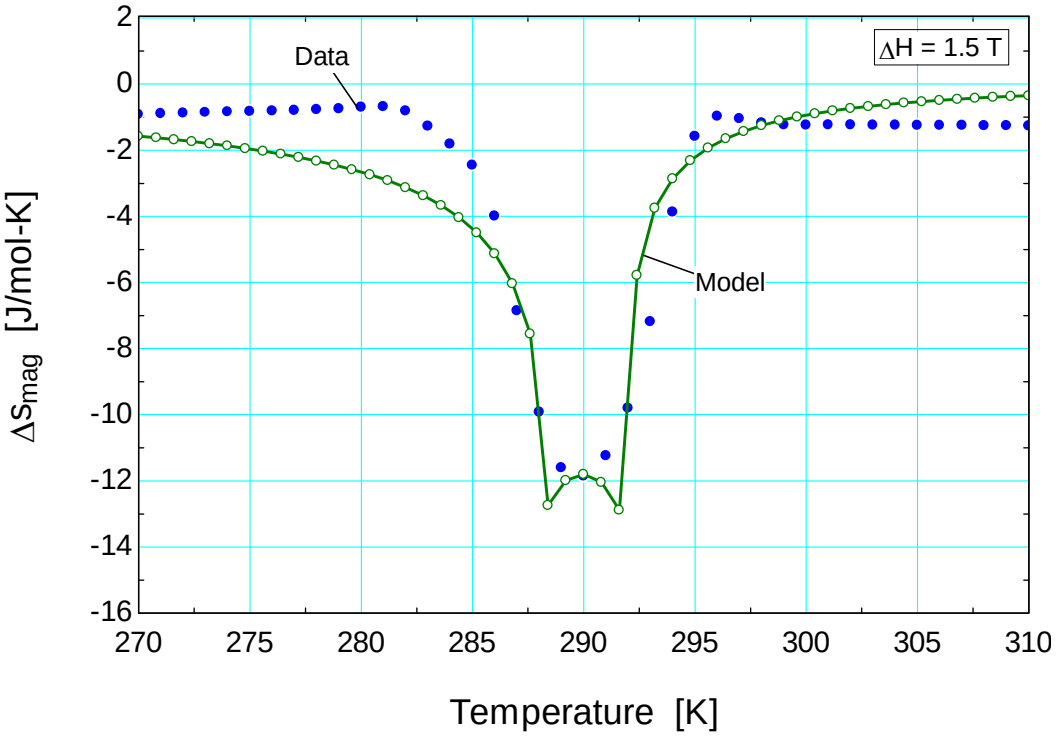

Figure 4-2. Isothermal entropy change for $La(Fe_{0.885}Si_{0.115})_{13}H_{1.21}$ predicted by mean field model and from experimental magnetization data. Data provided by Astronautics Corporation of America.

4.4 Raw Data

Another method for characterizing magnetic material properties is through interpolation of raw data for that material. The purpose of this section is to demonstrate how raw magnetization and specific heat data can be used in lieu of an equation of state.

The raw data used in this demonstration were provided from Astronautics Corporation of America and include four sets of magnetization measurements as a function of applied field taken along 12 isotherms for the FOMT material $La(Fe_{0.885}Si_{0.115})_{13}H_{1.21}$. A set of data was taken for increasing applied field and temperature, another for decreasing applied field and increasing temperature, a third for increasing applied field and decreasing temperature, and a final set for decreasing applied field and temperature. Table 4-1 lists the physical properties of the sample tested. Figure 4-3 is a photo of the mounting apparatus used for a magnetization sample.

Table 4-1. Test specimen details

Density	7170 $^{kg}/_{m^3}$
Sample Mass	0.0163 *g*
Geometry	Packed spheres w/~0.37 porosity inside cylindrical housing with 0.10 *in* diameter.
Applied Field Direction	Parallel to the axis of cylindrical sample holder.
Chemical Formula	$La(Fe_{1-x}Si_x)_{13}H_y$ where $x \approx 0.115$ and $y \approx 1.21$

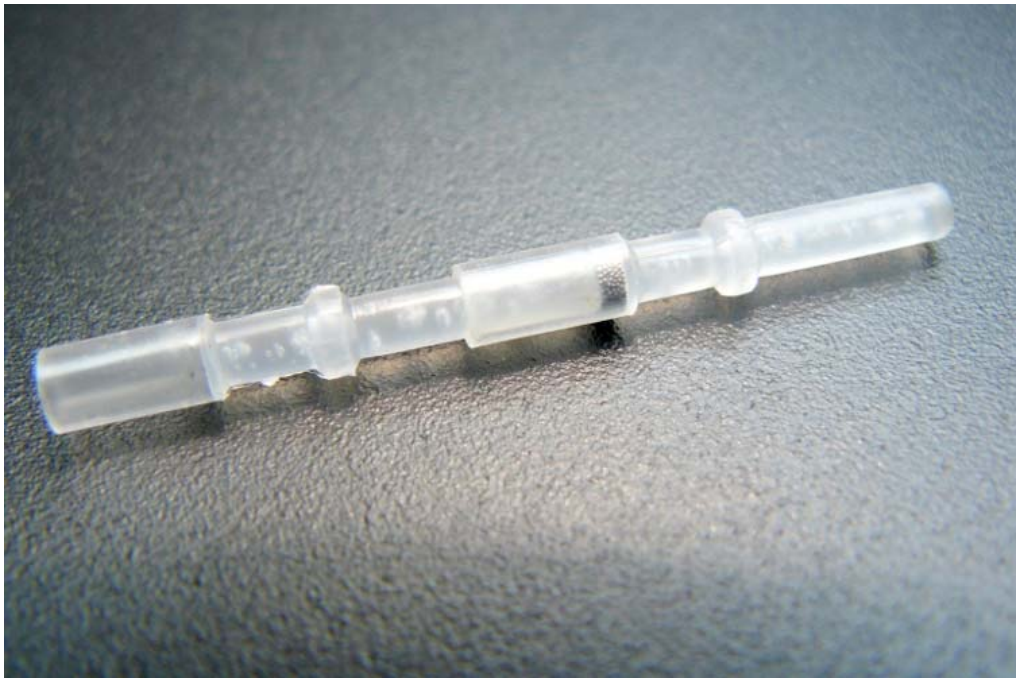

Figure 4-3. Typical mounting apparatus for a magnetization sample. Photo courtesy of Astronautics Corporation of America.

Figure 4-4 shows the mass-specific magnetization as a function of applied field for various temperatures when the temperature is increasing. The solid lines are representative of the magnetization while the field is increasing with time, and the dotted lines represent the magnetization in a decreasing field. Figure 4-5 is the mass-specific magnetization as a function of applied field for various temperatures when the temperature is decreasing. Comparison of these two plots indicate that $La(Fe_{0.885}Si_{0.115})_{13}H_{1.21}$ exhibits large magnetic hysteresis but little thermal hysteresis near the Curie temperature.

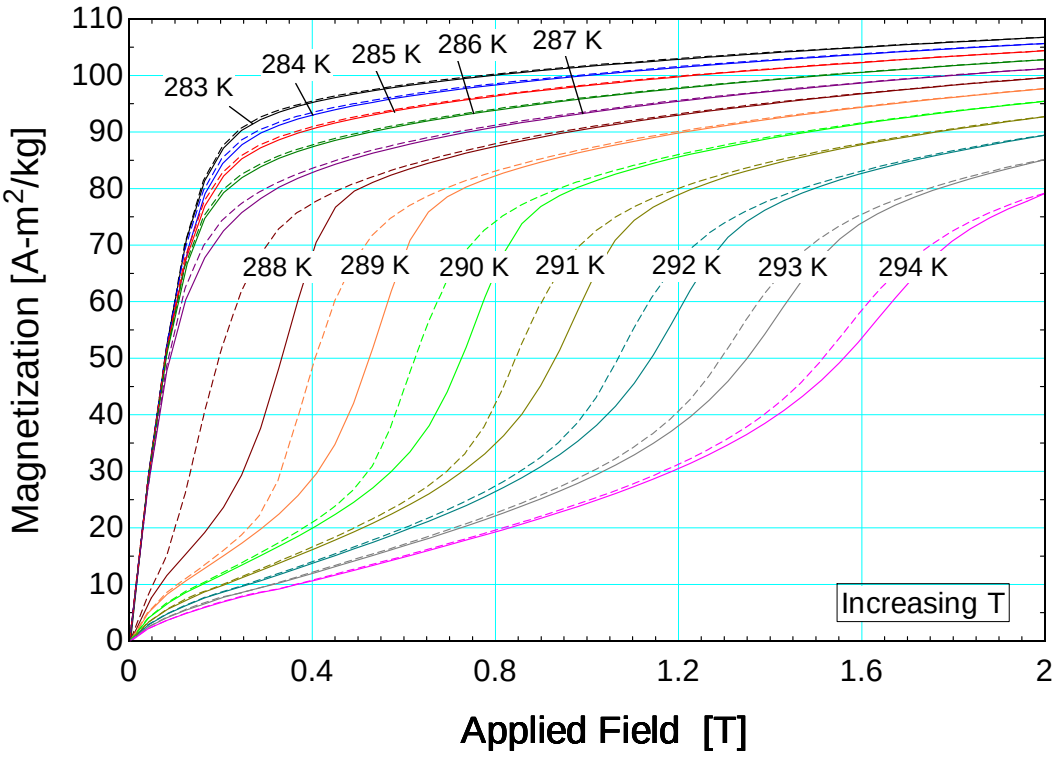

Figure 4-4. Magnetization as a function of applied field for increasing temperatures in JF1-142A. Solid lines indicate increasing field and dotted lines indicate decreasing field.

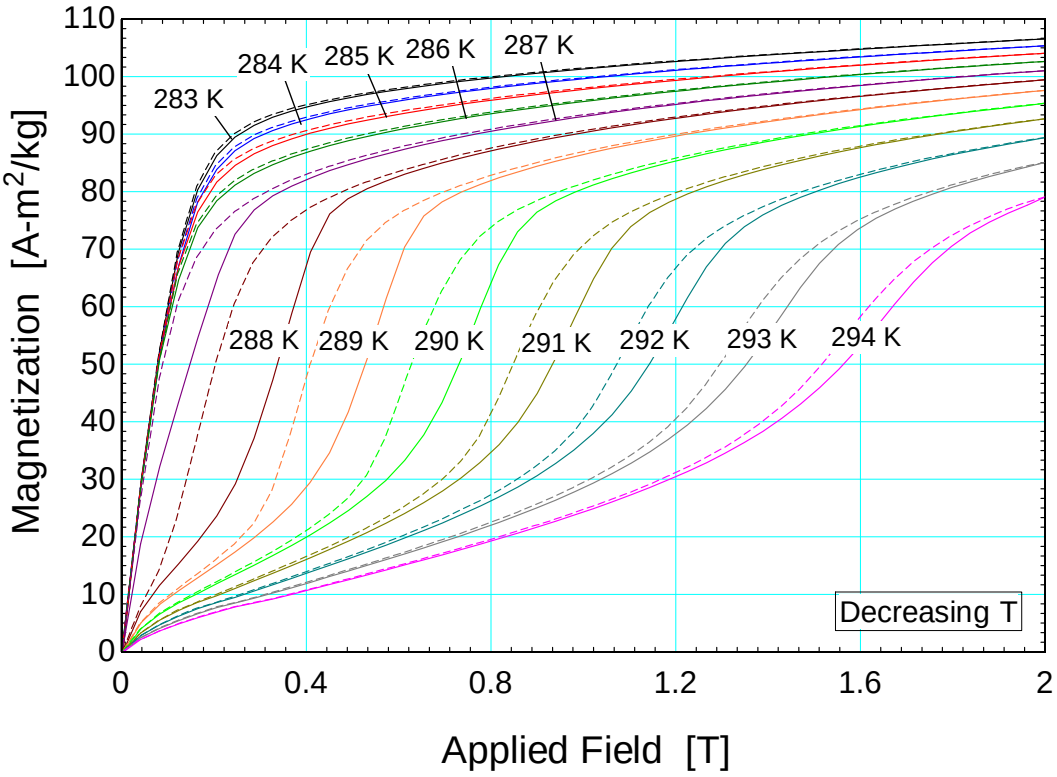

Figure 4-5. Magnetization as a function of applied field for decreasing temperatures in JF1-142A. Solid lines indicate increasing field and dotted lines indicate decreasing field.

4.4.1 Demagnetization Effects

A magnetization (*M*) is induced within the material when it is subjected to an applied magnetic field (H_a). Inside a material of finite geometry, these fields are oriented in opposite directions and result in an internal magnetic field (H_{int}) that is smaller in magnitude than the applied magnetic field [3]. To calculate the internal field, first the demagnetizing field (H_d) is defined as:

$$H_d = N_d M \tag{4-23}$$

where *M* is the volume magnetization of the material and N_d is the material demagnetization factor. The demagnetization factor is a function of material geometry, applied field, and temperature. The demagnetization factor must be determined experimentally for complex geometries, but it can be found analytically for simple geometries such as cylinders and spheres. Suggested values for the demagnetization factor for many simple geometries have been published in the literature [3, 6]. Since the

demagnetizing field vector is opposite the applied field vector, the magnitude of internal field vector is simply expressed as:

$$H_{\text{int}} = H_a - H_d = H_a - N_d M \tag{4-24}$$

Expressing the magnetization as a function of the calculated internal field and temperature yields the corrected magnetization function. Demagnetizing effects should be accounted for in an efficient AMRR design and can be detrimental to the performance for cycles using low applied field (< 2 Tesla) permanent magnets [7].

4.4.2 Anhysteretic and Irreversible Magnetization

The anhysteretic magnetization function (M_{an}) is the hypothetical magnetization curve of a material in the absence of magnetic hysteresis. The anhysteretic magnetization is calculated by taking the average of the positive (M_{pos}) and negative (M_{neg}) magnetization curves for a given applied field and temperature:

$$M_{an}\left(\mu_0 H, T\right) = \frac{M_{pos}\left(\mu_0 H, T\right) + M_{neg}\left(\mu_0 H, T\right)}{2} \tag{4-25}$$

where M_{pos} is the magnetization when the change in field with time is positive and M_{neg} is the magnetization when the change in field with time is negative. Bozorth (1951) states that the average of the positive (M_{pos}) and negative (M_{neg}) magnetization branches of the hysteresis curve at a given applied field is an accurate estimate of the anhysteretic magnetization [8]. Figure 4-6 is the anhysteretic magnetization taken from the decreasing temperature magnetization data depicted in Figure 4-5 (not corrected for demagnetization effects).

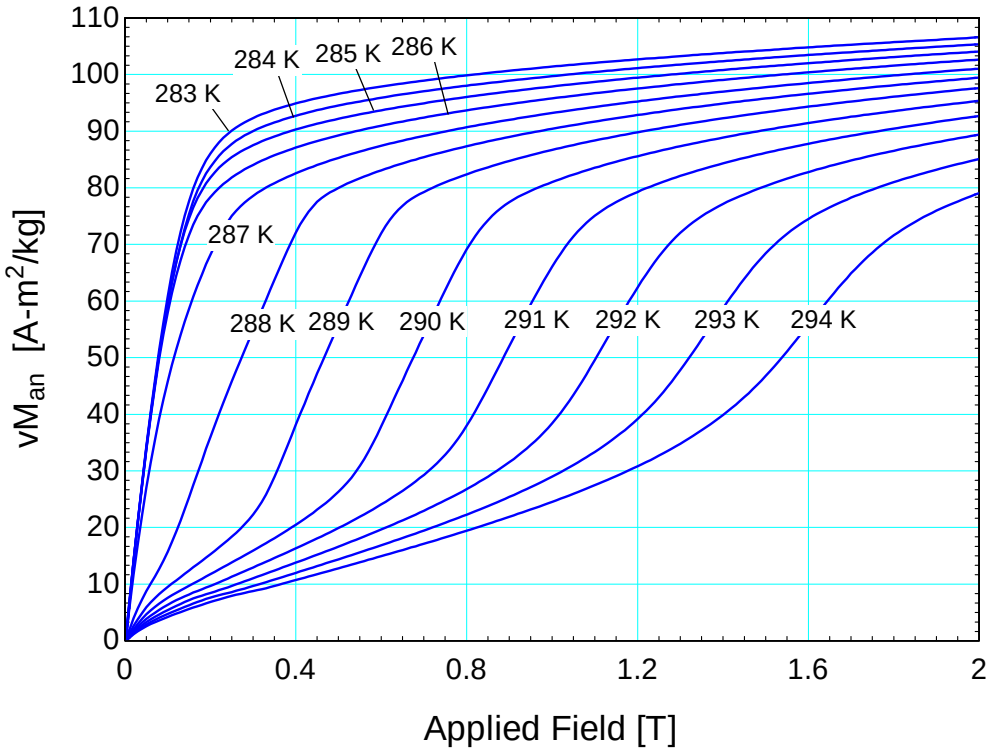

Figure 4-6. Anhysteretic magnetization for $La(Fe_{0.885}Si_{0.115})_{13}H_{1.21}$ for the decreasing temperature measurement. Not corrected for demagnetization.

Figure 4-7 shows the anhysteretic magnetization for $La(Fe_{0.885}Si_{0.115})_{13}H_{1.21}$ after correcting for demagnetization effects. The raw data were first corrected using Eq. (4-24), and the anhysteretic magnetization was subsequently calculated with Eq. (4-25). The magnetization curves below the Curie point (approximately 288 K for $La(Fe_{0.885}Si_{0.115})_{13}H_{1.21}$) should be tangent to the vertical axis at zero applied field. The demagnetization factor was therefore empirically determined in order to satisfy this requirement. The resulting demagnetization factor is approximately 0.15 for these data. For a perfect sphere, the demagnetization factor is 0.33 [3]. Since the total geometry consists of many closely packed spheres, the demagnetizing field will differ from that of a perfect sphere. There is no explicit recommendation in the literature for packed spheres, but air gaps in samples are known to reduce the effective demagnetizing field [9]. Thus, a value of 0.15 for the demagnetization factor is reasonable in this case. Note that the graphical effect of the demagnetization factor is counterclockwise rotation of each magnetization curve about the origin for the anhysteretic magnetization function.

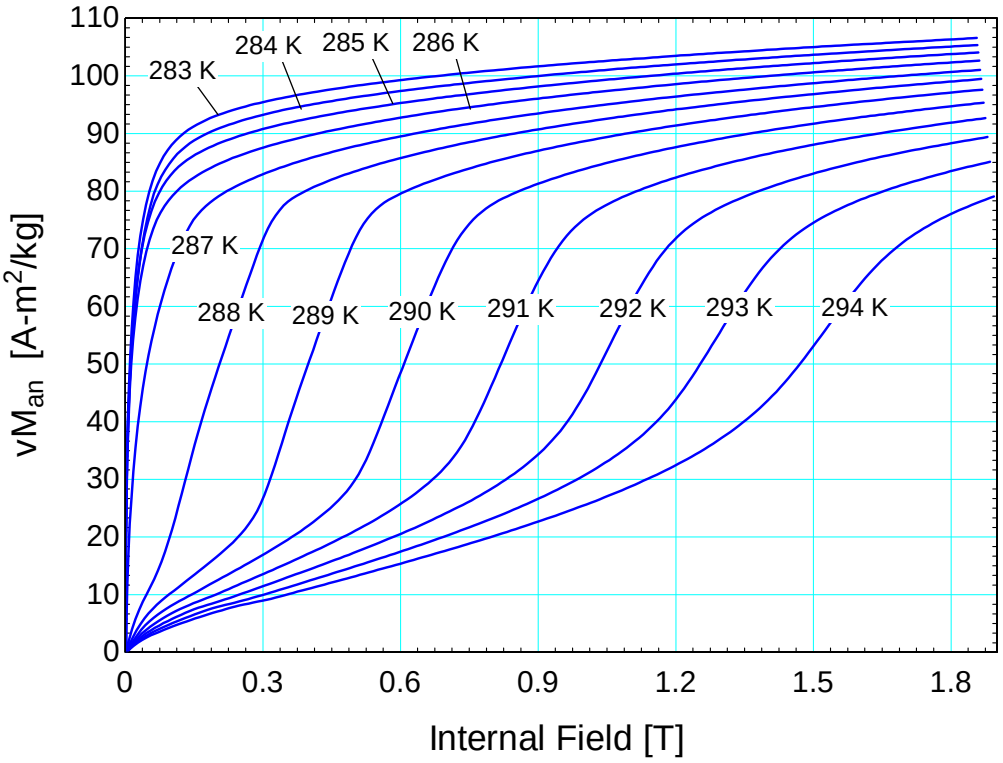

Figure 4-7. Anhysteretic magnetization for $La(Fe_{0.885}Si_{0.115})_{13}H_{1.21}$ for the decreasing temperature measurement. Corrected for demagnetization with $N_d = 0.15$.

The irreversible magnetization (M_{irr}) is defined in order to recover the area swept by a given hysteresis curve. The irreversible magnetization can be calculated according to:

$$M_{irr}\left(\mu_0 H,T\right)=\frac{\left|M_{neg}\left(\mu_0 H,T\right)-M_{pos}\left(\mu_0 H,T\right)\right|}{2} \tag{4-26}$$

The absolute value in Eq. (4-26) ensures a positive value for the irreversible magnetization which is necessary since it is directly related to the entropy generation. The positive and negative magnetization curves can be expressed in terms of the anhysteretic and irreversible magnetization:

$$M_{pos}\left(\mu_0 H,T\right)=M_{an}\left(\mu_0 H,T\right)-M_{irr}\left(\mu_0 H,T\right) \tag{4-27}$$

$$M_{neg}\left(\mu_0 H,T\right)=M_{an}\left(\mu_0 H,T\right)+M_{irr}\left(\mu_0 H,T\right) \tag{4-28}$$

Figure 4-8 shows the irreversible magnetization for $La(Fe_{0.885}Si_{0.115})_{13}H_{1.21}$ calculated using the data associated with temperatures between 287 and 294 K. At temperatures below the Curie point (~288 K), the irreversible magnetization becomes small. These data were extracted from the data shown in Figure 4-5 without the correction for demagnetization.

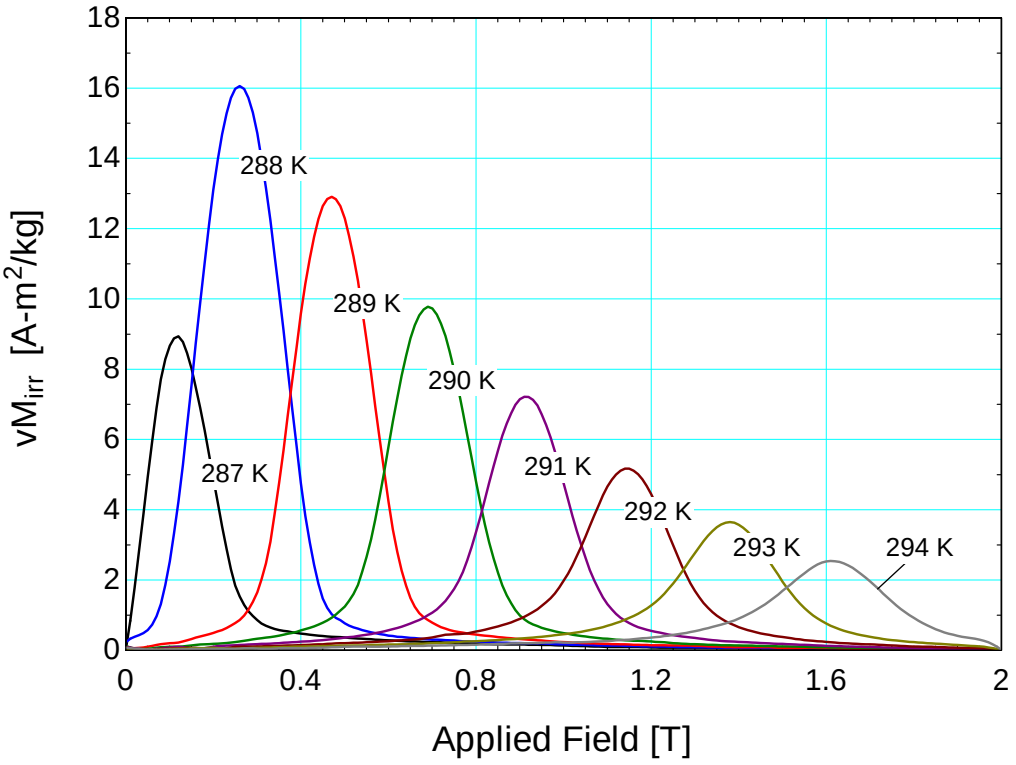

Figure 4-8. Irreversible magnetization for $La(Fe_{0.885}Si_{0.115})_{13}H_{1.21}$ for the decreasing temperature measurement. Not corrected for demagnetization effects.

Figure 4-9 is the irreversible magnetization for the decreasing temperature measurement after it has been corrected for demagnetization. Like the anhysteretic magnetization, the raw data were first corrected, and then the anhysteretic magnetization was derived from the corrected data. By comparing Figure 4-8 and Figure 4-9, the effect of applying the demagnetization factor becomes apparent. Graphically, it reduces the width of the peaks but also causes their peaks to become higher. Since the area underneath the curve is proportional the entropy generation and the entropy generation is constant

whether or not demagnetization effects occur, the area underneath each curve should remain constant before and after the application Eq. (4-24).

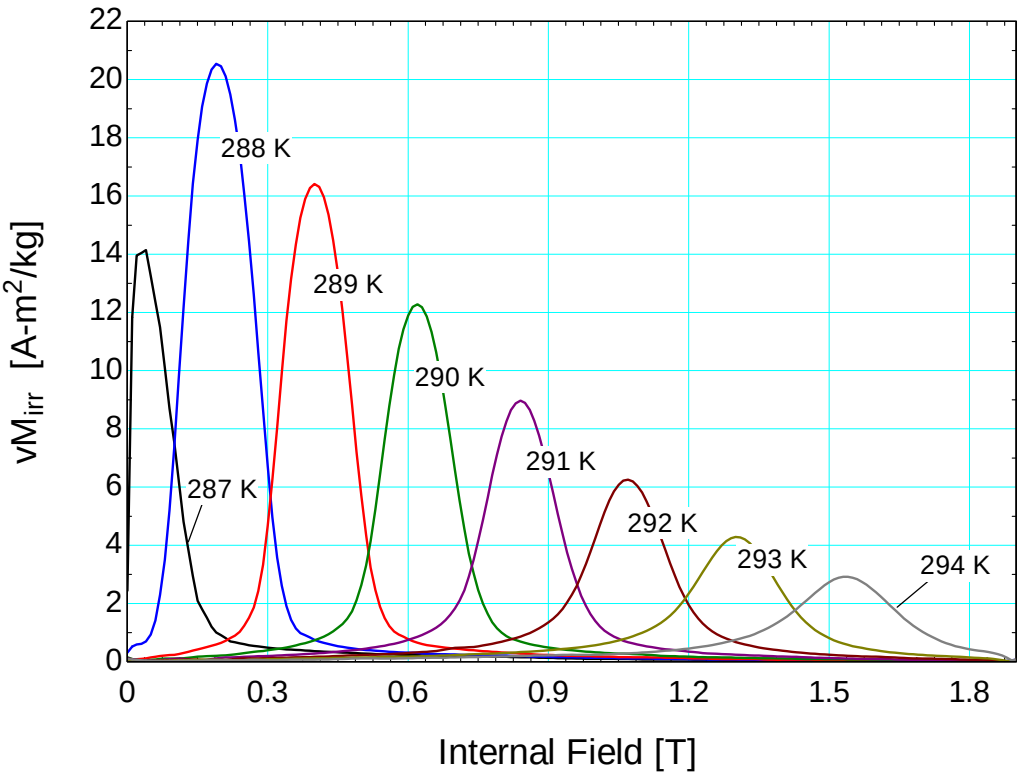

Figure 4-9. Irreversible magnetization for $La(Fe_{0.885}Si_{0.115})_{13}H_{1.21}$ for the decreasing temperature measurement. Corrected for demagnetization effects with $N_d = 0.15$.

4.4.3 Specific Entropy Calculation

With the anhysteretic and irreversible magnetization calculated, the specific entropy of $La(Fe_{0.885}Si_{0.115})_{13}H_{1.21}$ can be mapped as a function of both applied field and temperature. The total differential of the specific entropy (ds) of the material can be divided into its temperature-driven and applied magnetic field-driven components:

$$ds = \left(\frac{\partial s}{\partial T}\right)_{\mu_0 H} dT + \left(\frac{\partial s}{\partial \mu_0 H_{int}}\right)_T d\mu_0 H_{\text{int}} \tag{4-29}$$

where $\mu_0 H_{int}$ is the internal field. The Maxwell relation that relates the entropy to the anhysteretic magnetization can be utilized:

$$\left(\frac{\partial s}{\partial \mu_0 H}\right)_T = \left(\frac{\partial v M_{an}}{\partial T}\right)_{\mu_0 H} \tag{4-30}$$

as well as the definition of specific heat:

$$\left(\frac{\partial s}{\partial T}\right)_{\mu_0 H} = \frac{c_{\mu_0 H}}{T} \tag{4-31}$$

where $c_{\mu_0 H}$ is the constant field specific heat. Substituting Eqs. (4-30) and (4-31) into Eq. (4-29) yields:

$$ds = \frac{c_{\mu_0 H}}{T} dT + \left(\frac{\partial v M_{an}}{\partial T}\right)_{\mu_0 H} d\mu_0 H_{int} \tag{4-32}$$

Since only the zero-field specific heat is known for this material (this information was also obtained from Astronautics), Eq. (4-32) must be integrated first along a line of constant reference applied field ($\mu_0 H_{ref}$ = 0 Tesla) from a reference temperature (T_{ref}) to the temperature of interest (T) :

$$s\left(T = T, \mu_0 H = \mu_0 H_{ref}\right) - s\left(T = T_{ref}, \mu_0 H = \mu_0 H_{ref}\right) = \int_{T_{ref}}^{T} \frac{c_{\mu_0 H = \mu_0 H_{ref}}}{T} dT \tag{4-33}$$

where $c_{\mu_0 H = \mu_0 H_{ref}}$ is the constant field specific heat at the reference field. Note that the second term on the right hand side of Eq. (4-32) vanishes for this integration since the field is not changing ($d\mu_0 H = 0$). Equation (4-32) can subsequently be integrated from the reference field and the temperature of interest to the field of interest ($\mu_0 H$):

$$s\left(T = T, \mu_0 H = \mu_0 H\right) - s\left(T = T, \mu_0 H = \mu_0 H_{ref}\right) = \int_{\mu_0 H_{ref}}^{\mu_0 H} \left(\frac{\partial v M_{an}}{\partial T}\right)_{\mu_0 H, T} d\mu_0 H_{int} \tag{4-34}$$

Now note that, in this case, the first term on the right side of Eq. (4-32) vanishes since the temperature is not changing. Also, the derivative of the anhysteretic magnetization with respect to temperature at constant field must be evaluated at the temperature of interest (T). Adding Eqs. (4-33) and (4-34) allows for a full mapping of the entropy function:

$$s\left(T,\mu_0 H\right)-s\left(T=T_{ref},\mu_0 H=\mu_0 H_{ref}\right)=\int_{T_{ref}}^{T}\frac{c_{\mu_0 H=\mu_0 H_{ref}}}{T}dT+\int_{\mu_0 H_{ref}}^{\mu_0 H}\left(\frac{\partial v M_{an}}{\partial T}\right)_{\mu_0 H,T}d\mu_0 H_{int} \qquad (4\text{-}35)$$

For this data set, a reference entropy of 0 was set at a reference temperature of 283 K and a reference field of 0 Tesla:

$$s\left(T=283\text{ K},\mu_0 H=0\text{ T}\right)=0 \qquad (4\text{-}36)$$

Substituting these reference states into (4-35) provides:

$$s\left(T,\mu_0 H\right)=\int_{283\text{ K}}^{T}\frac{c_{\mu_0 H=0}}{T}dT+\int_{0}^{\mu_0 H}\left(\frac{\partial v M_{an}}{\partial T}\right)_{\mu_0 H,T}d\mu_0 H_{\text{int}} \qquad (4\text{-}37)$$

The zero field specific heat capacity ($c_{\mu_0 H=0}$) is known as a function of temperature for $La(Fe_{0.885}Si_{0.115})_{13}H_{1.21}$ and is presented in Figure 4-10 below. Note that the zero field specific heat becomes very large at the Curie temperature due to the ferromagnetic to paramagnetic phase transition.

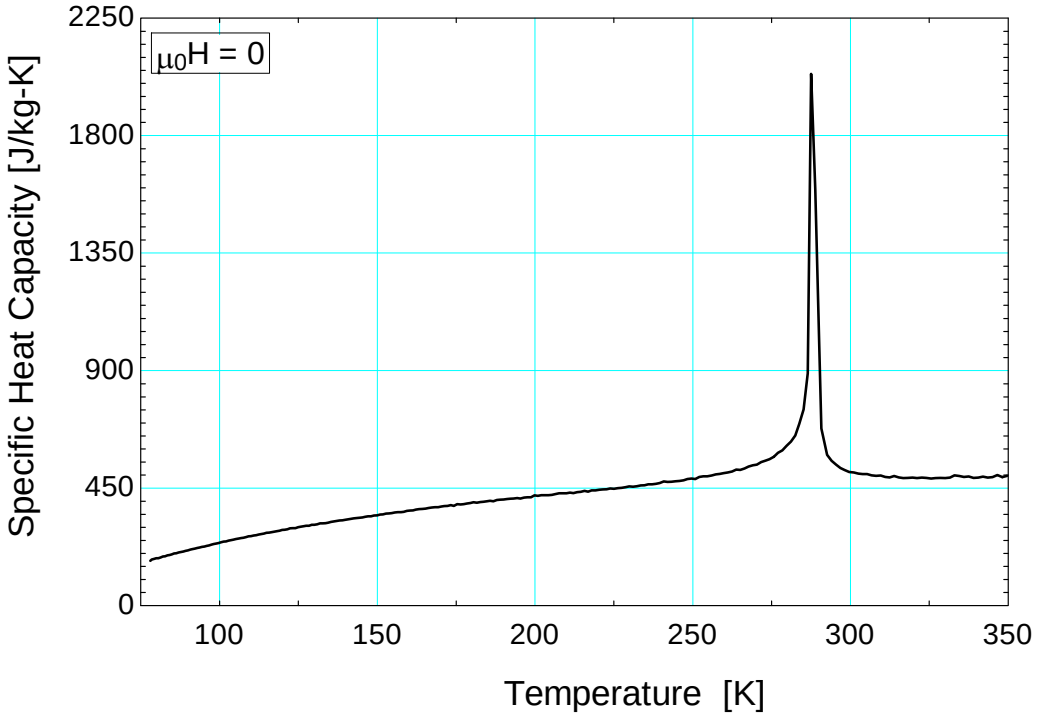

Figure 4-10. Zero field specific heat for $La(Fe_{0.885}Si_{0.115})_{13}H_{1.21}$ as a function of temperature.

Utilizing the specific heat capacity data presented in Figure 4-10 and the adjusted anhysteretic magnetization data provided in Figure 4-7, the specific entropy can be calculated with Eq. (4-37). The specific entropy as a function of temperature and applied field near the Curie temperature for $La(Fe_{0.885}Si_{0.115})_{13}H_{1.21}$ is shown in Figure 4-11. The large dip in the specific entropy surface along the Curie temperature isotherm illustrates the magnetocaloric effect. For this material, the maximum isothermal specific entropy decrease is approximately 15.7 $\frac{J}{kg\text{-}K}$ for a field change from 0 to 2 Tesla.

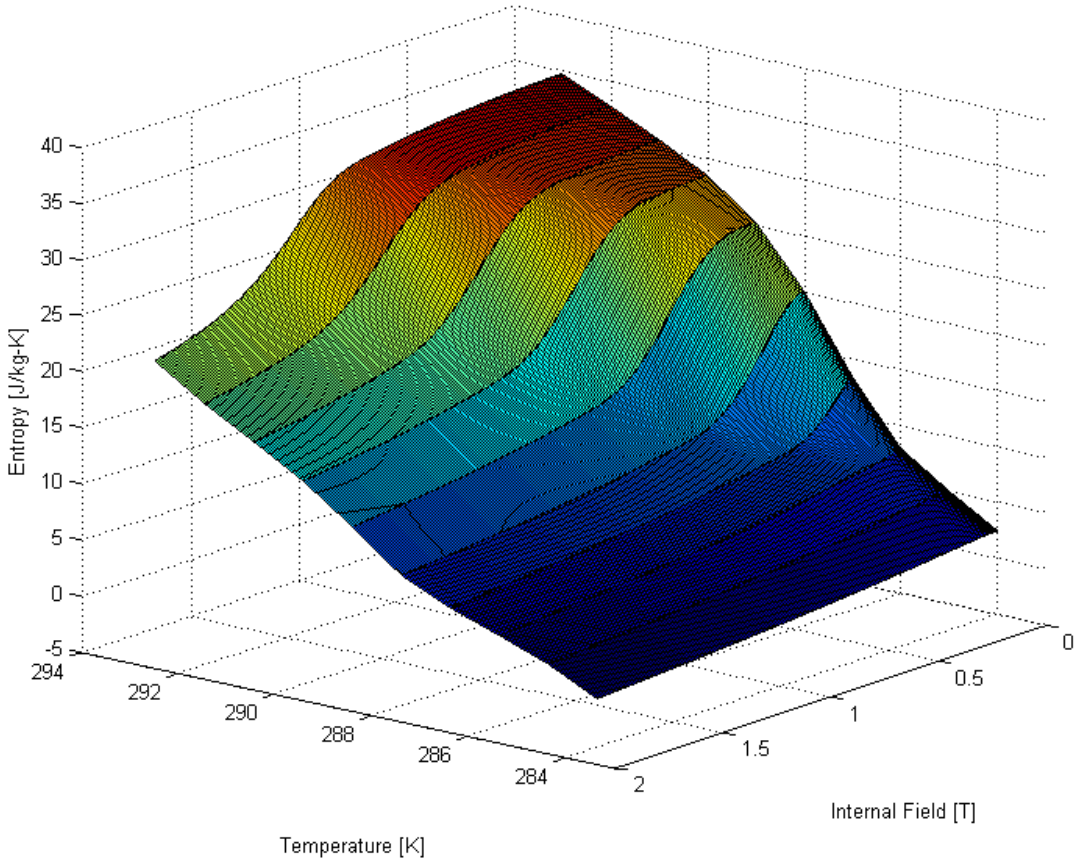

Figure 4-11. Specific entropy of $La(Fe_{0.885}Si_{0.115})_{13}H_{1.21}$ as a function of temperature and internal field with. Reference entropy of 0 is set at 283 K and 0 applied field.

REFERENCES

1. Pecharsky, V.K. and J.K.A. Gschneidner, *Giant Magnetocaloric Effect in $Gd_5(Si_2Ge_2)$.* Physical Review Letters, 1997. **78**(23): p. 4494.

2. Brillouin, L., *Les moments de rotation et le magnétisme dans la mécanique ondulatoire.* J. Phys. Radium, 1927. **8**(2): p. 74-84.

3. Jiles, D., *Introduction to Magnetism and Magnetic Materials*. 2nd Edition ed. 1998: CRC Press. 568.

4. Gschneidner, K.A., V.K. Pecharsky, and A.O. Tsokol, *Recent developments in magnetocaloric materials.* Reports on Progress in Physics, 2005. **68**(6): p. 1479.

5. Von Ranke, P.J., N.A. de Oliveira, and S. Gama, *Understanding the influence of the first-order magnetic phase transition on the magnetocaloric effect: application to Gd5(SixGe1-x)4.* Journal of Magnetism and Magnetic Materials, 2004. **277**(1-2): p. 78-83.

6. Goldfarb, R.B., *Demagnetization Factors*, in *Concise Encyclopedia of Magnetic & Superconducting Materials*, J. Evetts, Editor. 1992: Oxford.

7. Peksoy, O. and A. Rowe, *Demagnetizing effects in active magnetic regenerators.* Journal of Magnetism and Magnetic Materials, 2005. **288**: p. 424-432.

8. Bozorth, R.M., *Ferromagnetism*. Bell Telephone Laboratories series. 1951: Van Nostrand. xvii, 968 p.

9. Dai, W., et al., *Application of high-energy Nd-Fe-B magnets in the magnetic refrigeration.* Journal of Magnetism and Magnetic Materials, 2000. **218**(1): p. 25-30.

Chapter 5 PARAMETRIC STUDIES

5.1 Refrigeration Capacity Curves

Magnetic coolers, like vapor compression refrigeration systems, have characteristic refrigeration capacity curves that show the refrigeration capacity and coefficient of performance (*COP*) as a function of the heat transfer fluid mass flow rate. In the case of vapor compression systems, the working fluid is both the refrigerant and the heat transfer fluid. For an AMRR system, the thermodynamic working substance is the solid magnetocaloric material and the mass flow rate refers to the heat transfer fluid. Figure 5-1 shows the *COP* and refrigeration capacity ($\dot{Q}_{ref}$) as a function of the heat transfer fluid mass flow rate amplitude for a properly configured AMRR system with SOMT material Gd-Er as the magnetic refrigerant. Shown are curves depicting beds that are consist of a single material and infinitely layered. Table 5-1 presents the inputs to the AMRR model used to generate Figure 5-1 and Figure 5-2. The mass flow and magnetic field profiles used for this study are shown in Figure 5-3 and Figure 5-4, respectively.

Table 5-1. Inputs to AMRR model for refrigeration curves

Parameter	Value	Parameter	Value
cycle time	0.2 s	dwell ratio	1/2
max magnetic field	1.5 T	regenerator type	packed sphere
heat transfer fluid	water	particle diameter	0.0002 m
porosity	0.36	motor efficiency	0.9
heat rejection temperature	310 K	pump efficiency	0.7
load temperature	299 K	number of beds	6
aspect ratio	0.2	regenerator volume	6 L

In the case of an infinitely layered bed, the Curie temperature (T_{Curie}) is assumed to vary linearly between the hot and cold reservoirs according to:

$$T_{Curie}(x) = T_H - (T_H - T_C)\frac{x}{L} \tag{5-1}$$

where x/L is the dimensionless regenerator position, and T_H and T_C are the hot and cold reservoir temperatures, respectively. In the case of a bed composed of a single material (i.e., a single layer bed), the Curie temperature is assumed to be a constant and is evaluated as the arithmetic mean of the hot and cold reservoir temperatures:

$$T_{Curie} = \frac{(T_H + T_C)}{2} \tag{5-2}$$

Note the Curie temperature is not a function of regenerator position in this case.

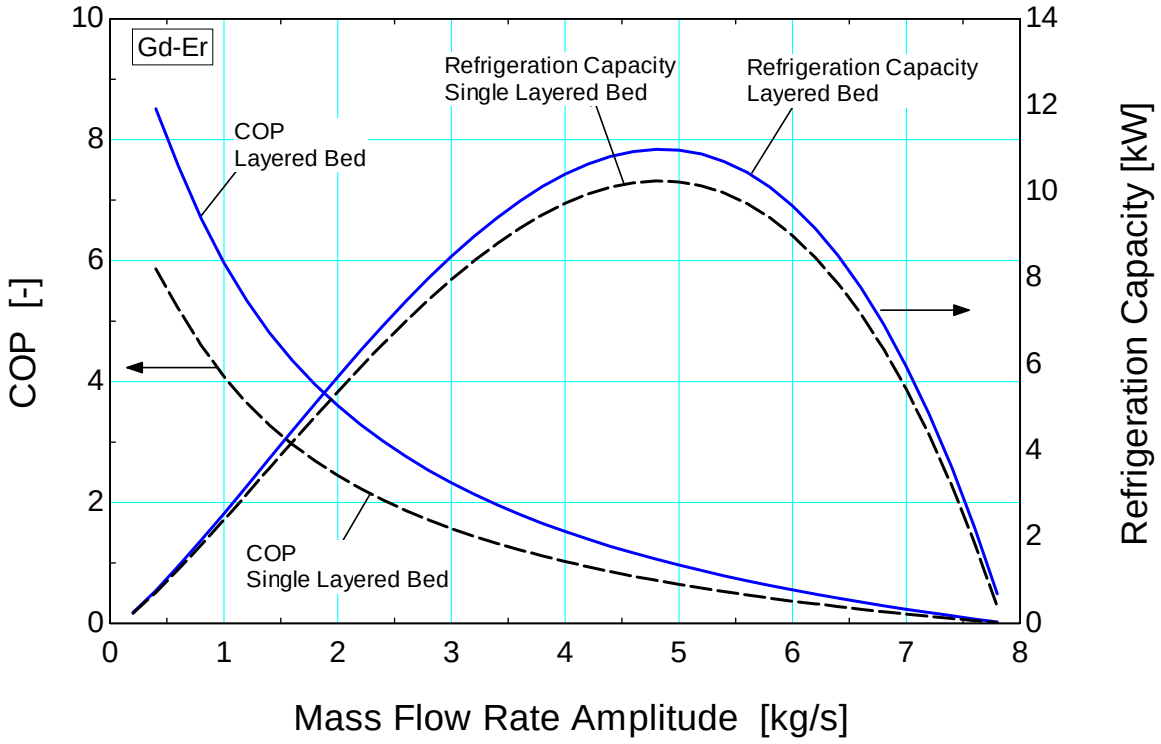

Figure 5-1. *COP* and refrigeration capacity as a function of heat transfer fluid mass flow rate amplitude for Gd-Er. Curves for single layered and infinitely layered beds are shown.

As Figure 5-1 illustrates, there exist two mass flow rate amplitudes that can achieve a given refrigeration capacity, up to some maximum possible refrigeration capacity for the bed. The larger mass flow rate amplitude value corresponds to a condition where the regenerator matrix is flooded with heat transfer fluid. This condition is undesirable since the value of the *COP* is reduced dramatically by an increased pump work requirement. For a given refrigeration capacity, the operating condition that

corresponds to the smaller value of mass flow rate should be chosen, since this condition yields a higher *COP*. Also, shown in Figure 5-1 is the effect of layering the regenerator bed. For a given refrigeration capacity, the *COP* at the optimal operating condition is increased by layering.

Figure 5-2 is the refrigeration capacity curve for the FOMT hysteretic material $La(Fe_{1-x}Si_x)_{13}H_y$ showing the curves for cases with and without magnetic hysteresis modeled. The bed is infinitely layered and operates under the condition listed in Table 5-1. The effect of hysteresis on cycle performance becomes less significant at large mass flow rate amplitudes, since hysteretic losses are becoming small relative to the pump work. Additionally, by comparison of Figure 5-2 and Figure 5-1, the potential advantage of FOMT materials over SOMT materials is an increased refrigeration capacity for a given operating condition. For example, the refrigeration capacity for a layered bed with hysteretic $La(Fe_{1-x}Si_x)_{13}H_y$ is approximately five greater than that of the same system operating with a layered bed of Gd-Er for an operating point where the *COP* = 4. Also, Figure 5-2 shows that FOMT type materials may be particularly advantageous for applications requiring large refrigeration capacities.

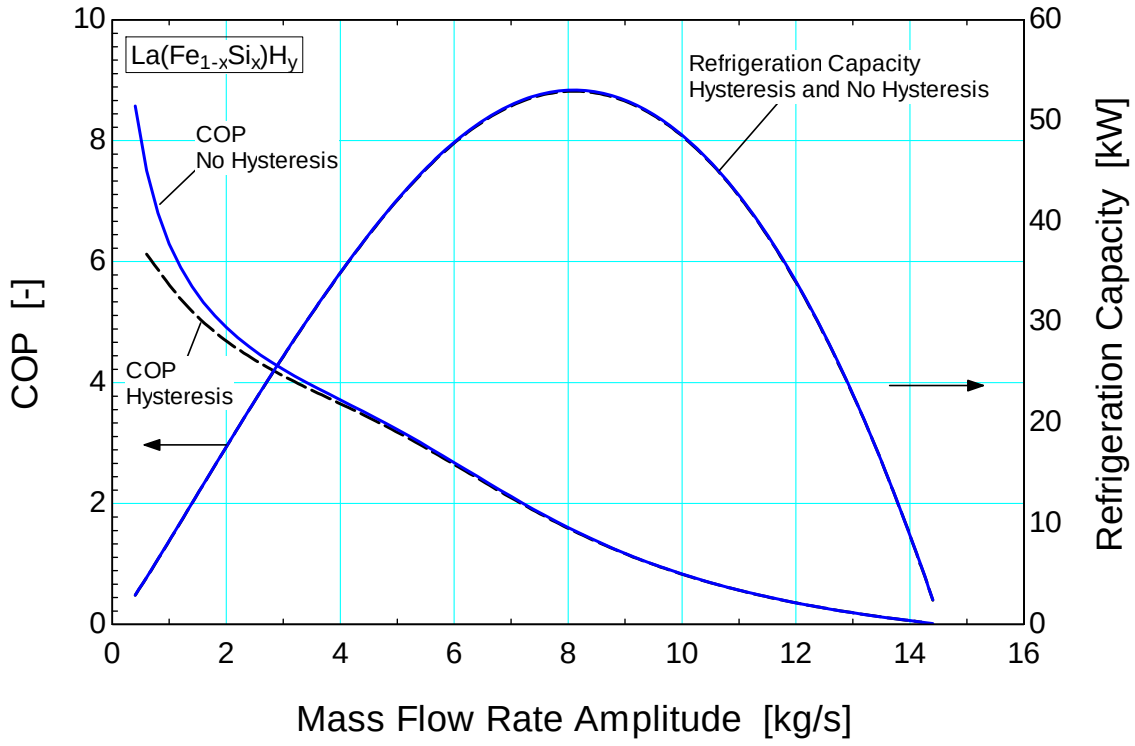

Figure 5-2. *COP* and refrigeration capacity as a function of heat transfer fluid mass flow rate amplitude for $La(Fe_{1-x}Si_x)_{13}H_y$. Curves for infinitely layered beds with and without hysteresis are shown.

5.2 Space Conditioning Study

One potential use for magnetic coolers is space conditioning. A refrigeration capacity of $\dot{Q}_{ref,d} = 5.00$ kW is chosen as a design criteria for a typical space cooling application in this study. A gadolinium-erbium compound ($Gd_{1-x}Er_x$) with a tunable Curie temperature is used to model a second-order magnetic transition (SOMT) material and a lanthanum-iron-silicon hydride compound ($La(Fe_{1-x}Si_x)_{13}H_y$) with a tunable Curie temperature is used to model a first-order magnetic transition (FOMT) material. The beds are layered such that the Curie temperature of each layer varies linearly between load and heat rejection temperatures. Heat exchangers are not explicitly modeled in this study.

5.2.1 Model Inputs

Table 5-2 lists the inputs for the AMRR model for the space conditioning parametric study. These parameters are held constant, while the total regenerator volume (V), aspect ratio (AR), mass flow rate

amplitude ($\dot{m}_{amp}$) are varied. The dwell ratio is defined as the ratio of the time in which the mass flow rate is zero to the total cycle time. The aspect ratio is defined as the length of a single regenerator bed to its diameter.

Table 5-2. Inputs to AMRR model for space conditioning study

Parameter	Value	Parameter	Value
cycle time	0.2 s	dwell ratio	1/2
max magnetic field	1.5 T	regenerator type	packed sphere
heat transfer fluid	water	particle diameter	0.0002 m
porosity	0.36	motor efficiency	0.9
heat rejection temperature	310 K	pump efficiency	0.7
load temperature	299 K	number of beds	6

Figure 5-3 illustrates the mass flow rate as a function of cycle time, where the peak and trough represent the positive and negative of the specified mass flow rate amplitude, respectively. Note that the mass flow rate is zero for half of the cycle time, as specified by the dwell ratio listed in Table 5-2.

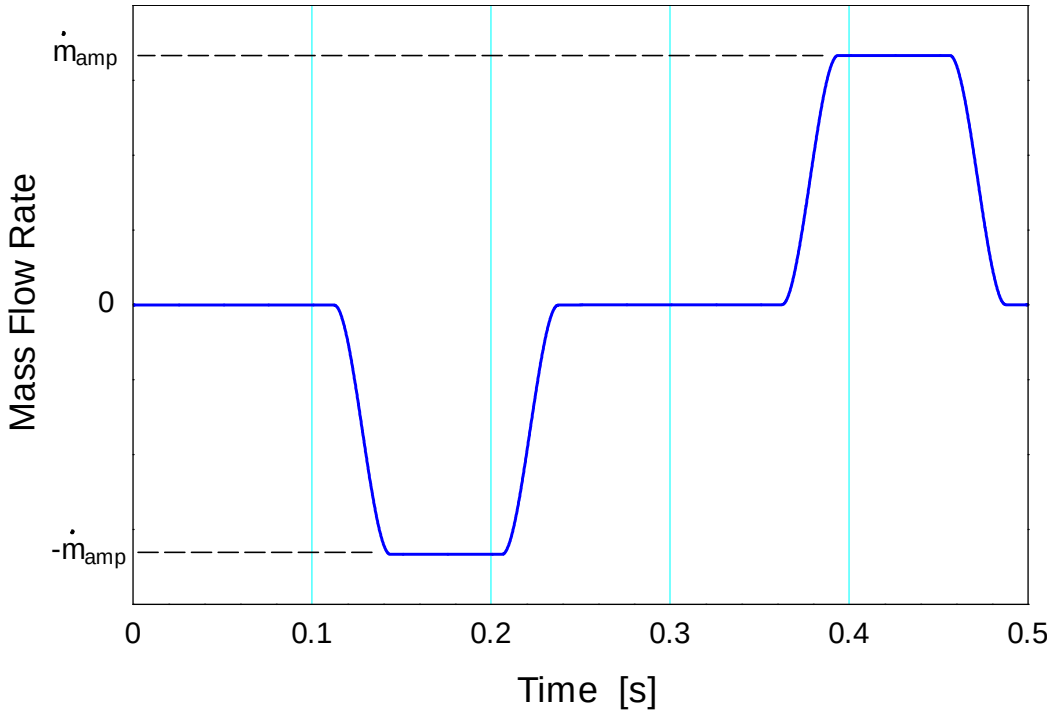

Figure 5-3. Mass flow rate as a function of cycle time.

Figure 5-4 shows the applied magnetic field as a function of time. During the first quarter of the cycle, the magnetic field is linearly ramped from zero to its maximum value; it then remains at its maximum value for the next quarter, decreases linearly from its maximum value to zero during the third quarter, and finally is zero for the final quarter of cycle time. The mass flow rate and magnetic field profiles are only functions of time, and do not vary spatially across the regenerator bed.

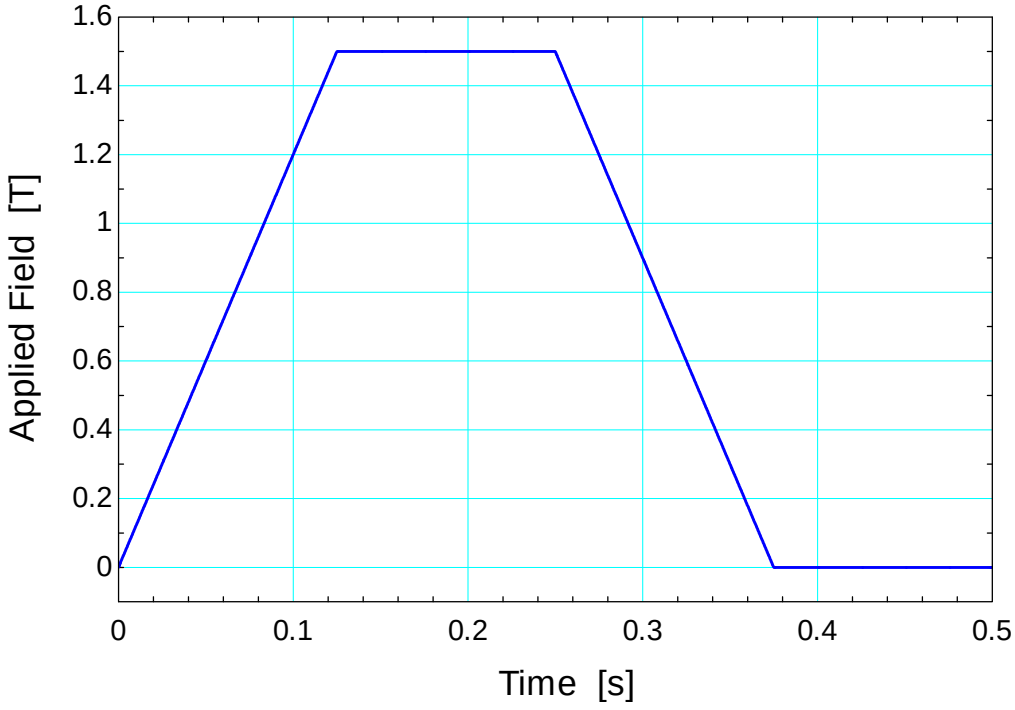

Figure 5-4. Applied magnetic field as a function of cycle time.

5.2.2 Design Strategy

The UW AMRR model requires inputs such as an initial temperature distribution, magnetocaloric refrigerant material, working fluid, regenerator geometry, magnetic field profile, and mass flow profile. The model begins with an initial temperature distribution and numerically iterates the partial differential equations forward through time until it reaches a temperature distribution that satisfies the convergence criteria for steady state regenerator operation. The main outputs of the model include the regenerator and fluid temperature distributions, from which important performance metrics such as the coefficient of

performance (*COP*) and refrigeration capacity ($\dot{Q}_{ref}$) can be calculated for a given magnetocaloric refrigerant. The list of required inputs is outlined in detail in Chapter 3.

In order to specify a refrigeration capacity for a given regenerator volume and aspect ratio and determine the corresponding mass flow rate amplitude, it is necessary to provide a guess value for the fluid flow rate amplitude and check the refrigeration capacity that is output against the desired capacity. It is best to provide a small mass flow rate as a guess value. A "small" mass flow rate in this sense is taken relative to the size of the regenerator and desired cooling capacity. A small mass flow rate initial guess ensures that the bed is not in the overloaded region of the refrigeration curve (as explained in Section 5.1), which ensures that the operating condition that is ultimately identified will correspond to the optimal *COP*. If the refrigeration capacity is above the design refrigeration capacity, then a smaller mass flow rate amplitude than the initial guess is required to achieve the desired cooling capacity at the optimal *COP*. If it is less than the design refrigeration capacity, then the mass flow rate amplitude must be incrementally increased until the design refrigeration capacity is reached. The iterative process is outlined in the flow diagram presented as Figure 5-5. This process is repeated for various combinations of volume and aspect ratio.

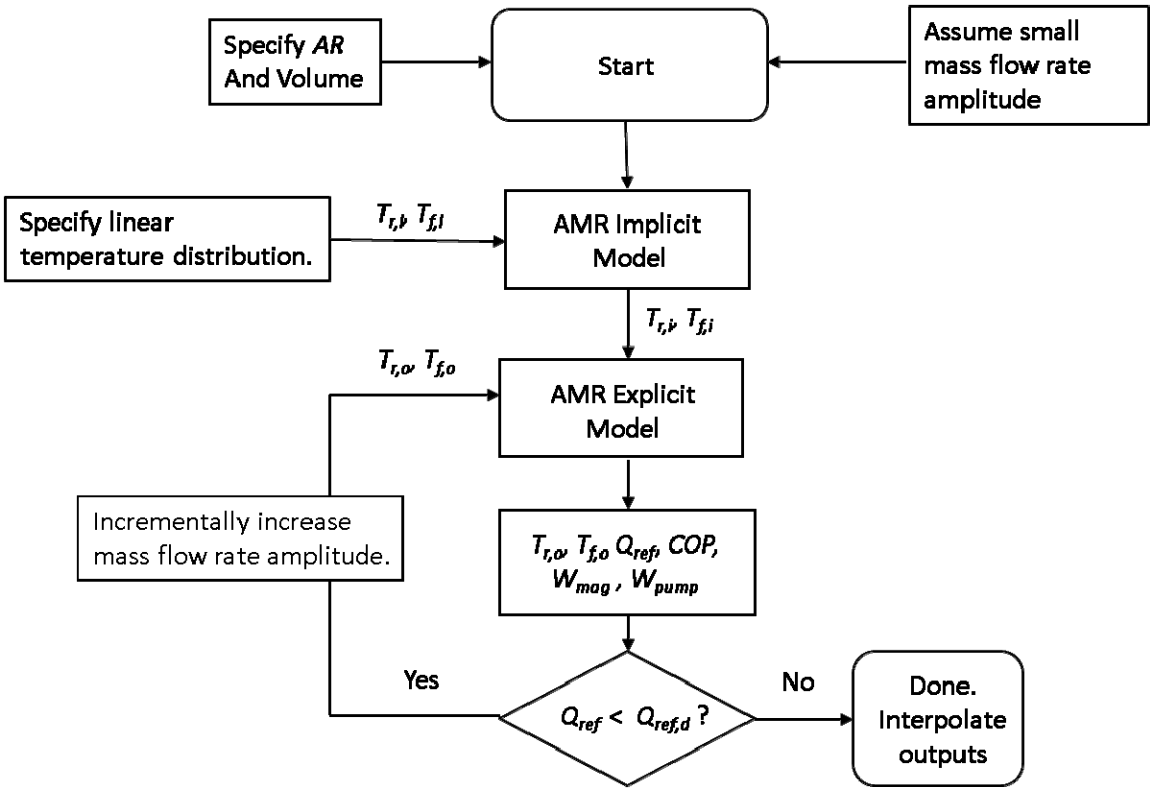

Figure 5-5. Model flow chart to find specified refrigeration capacity.

5.2.3 Modeling Results

For a given regenerator volume and refrigeration capacity, there exists an optimal aspect ratio that balances axial conduction and pressure drop losses and therefore yields a maximum coefficient of performance. Thus, for each volume, the aspect ratio is varied until an optimal value of the *COP* is found using the golden section search optimization technique.

Regenerator Volume

For a fixed load temperature of T_C = 299 K, the regenerator volume is varied to examine its effect on *COP* at the optimal aspect ratio for each volume. All other model parameters are held constant at the values listed in Table 5-2. Figure 5-6 shows the coefficient of performance (*COP*) as a function of regenerator volume; each point on the curve is associated with a unique, optimal aspect ratio and assumes

a layered bed with 60 layers for each material. Figure 5-7 shows the corresponding optimal aspect ratio as a function of volume for each material. The three materials simulated are the SOMT material $Gd_{1-x}Er_x$, and the FOMT material $La(Fe_{1-x}Si_x)_{13}H_y$; the FOMT material is modeled with and without hysteresis effects.

By inspection of Figure 5-6, it is clear that the hysteresis losses become greater with an increasing volume. Consequently, for a given refrigeration capacity and temperature span, there exists an optimal regenerator volume where the *COP* is maximized. For a 5 kW application with T_C = 299 K and T_H = 310 K, Figure 5-6 demonstrates that a magnetic cooler with layered $La(Fe_{1-x}Si_x)_{13}H_y$ as the active refrigerant performs better at this optimal volume (~ 4.3 L) than it would with layered $Gd_{1-x}Er_x$. At larger regenerator volumes, above approximately 7 liters, the layered gadolinium-erbium refrigerant outperforms the FOMT $La(Fe_{1-x}Si_x)_{13}H_y$ refrigerant.

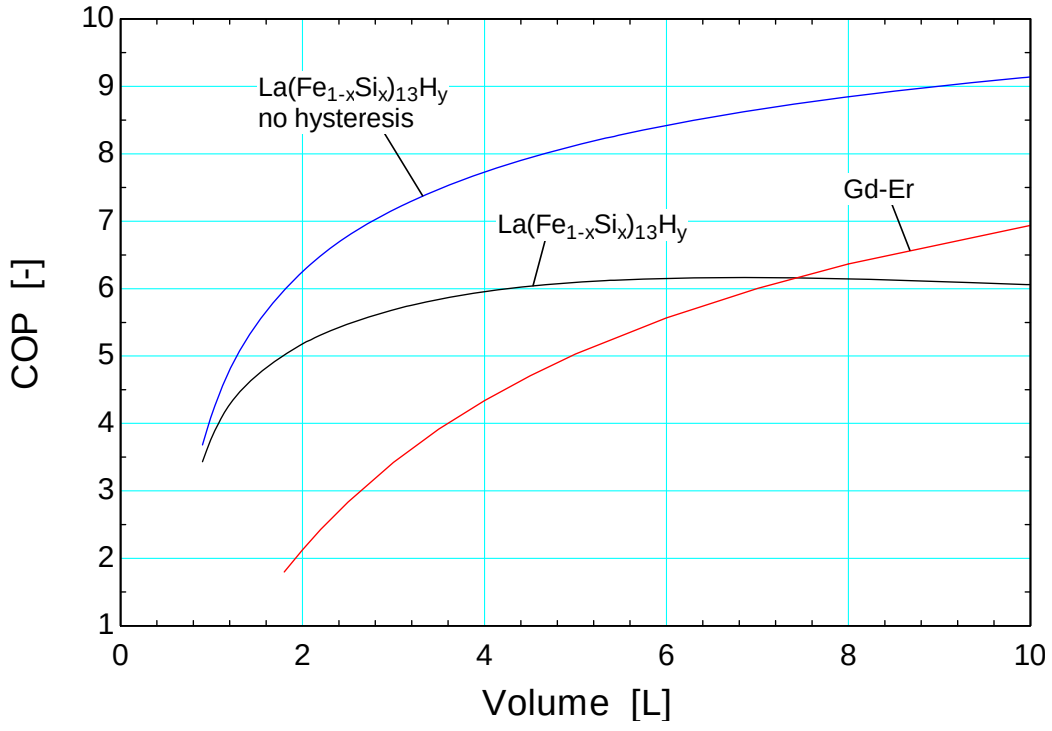

Figure 5-6. *COP* as a function of regenerator volume at its optimal aspect ratio and a load temperature of T_C = 299 K for a layered bed with each material indicated.

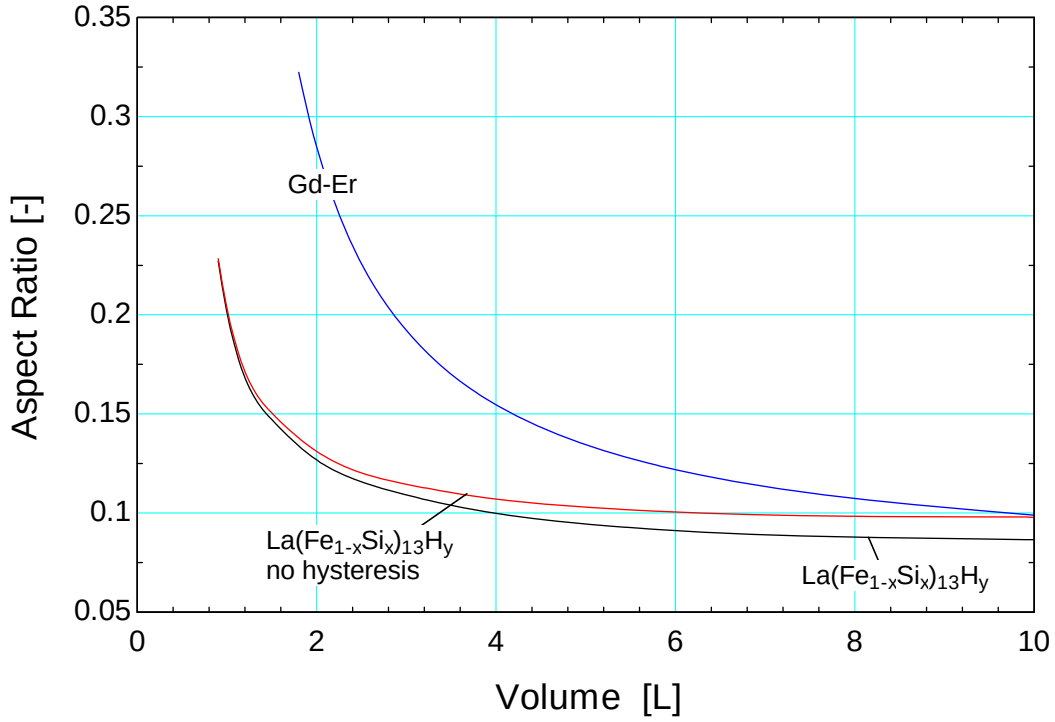

Figure 5-7. Optimal *AR* as a function of regenerator volume at a load temperature of T_C = 299 K for each material.

Load Temperature

In this study, the load temperature (T_C) is varied while the volume is held constant at 8 liters in order to examine the effect of load temperature on the cycle *COP*. The aspect ratio is optimized at each value of load temperature in order to yield the highest *COP*. The number of bed layers for each material is fixed at N_L = 60. Other pertinent model inputs are listed in Table 5-2. Figure 5-8 illustrates the *COP* as a function of the load temperature with the bed set to its optimal aspect ratio for each material. Figure 5-9 shows the aspect ratio that yields the optimal *COP* as a function of the load temperature.

If hysteresis is neglected for $La(Fe_{1-x}Si_x)_{13}H_y$ then it is more efficient than the gadolinium-erbium compound for all load temperatures. However, when hysteresis is accounted for, $La(Fe_{1-x}Si_x)_{13}H_y$ is only more efficient than $Gd_{1-x}Er_x$ at load temperatures that are below approximately 297.5 K, for this particular application and bed volume. For a load temperature of 294 K, the *COP* resulting from $La(Fe_{1-x}Si_x)_{13}H_y$ is approximately 25% greater than that of $Gd_{1-x}Er_x$.

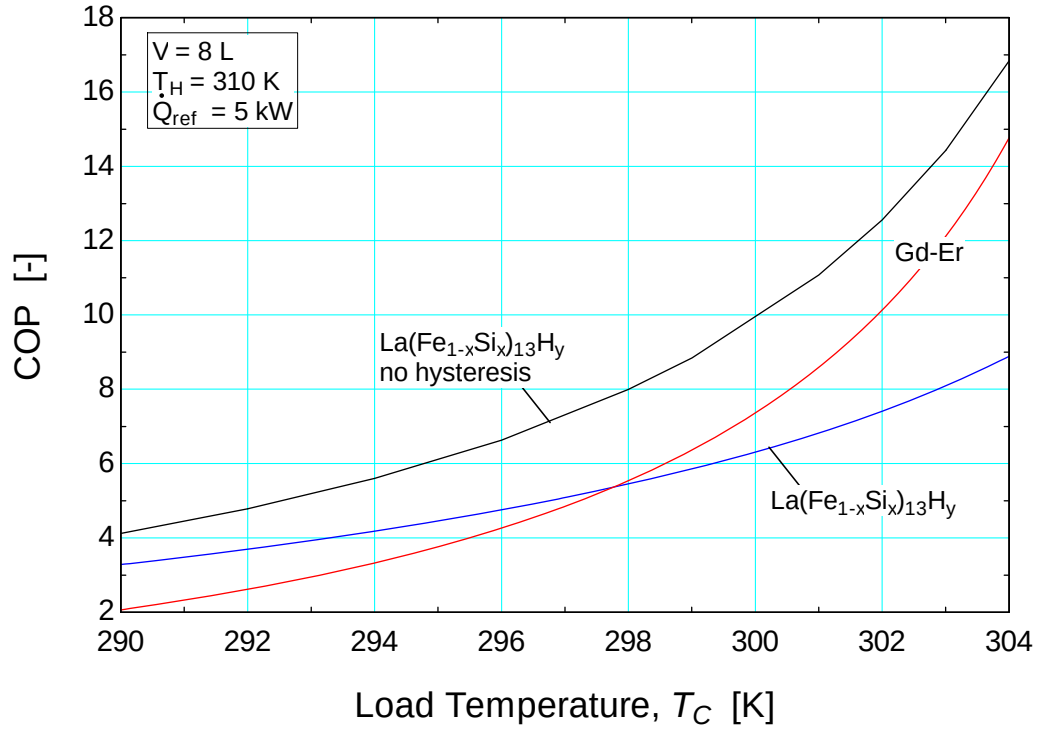

Figure 5-8. *COP* as a function of load temperature (T_C) at the optimal aspect ratio for an infinitely layered regenerator bed with volume of 8 liters.

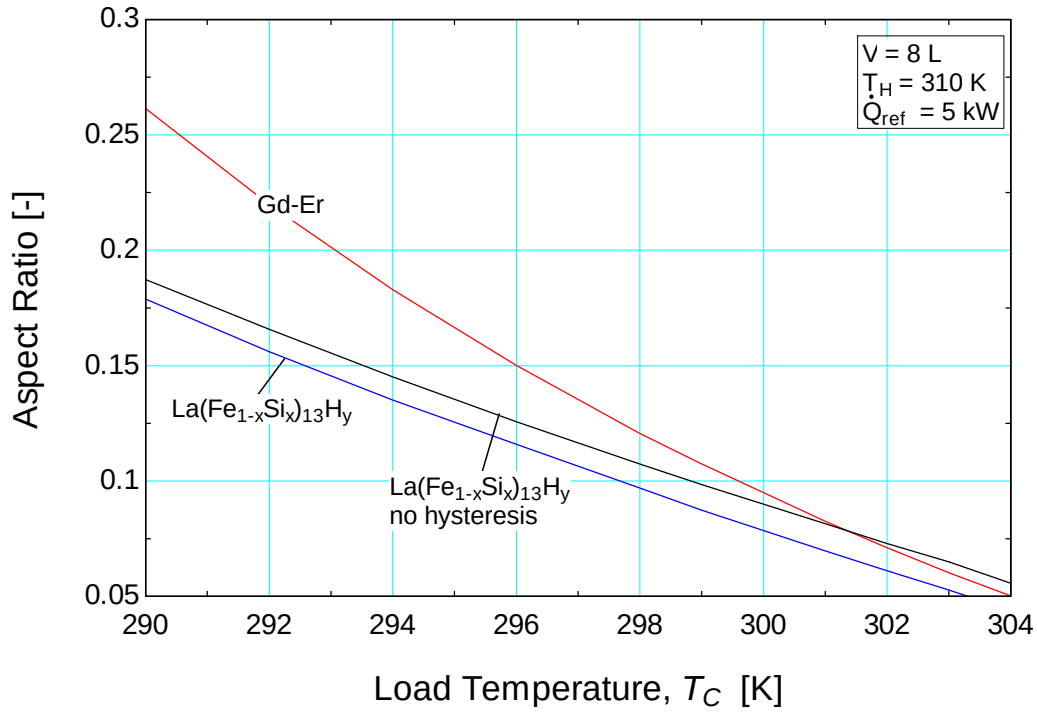

Figure 5-9. Optimal aspect ratio as a function of load temperature (T_C) for a, an infinitely layered regenerator with volume of 8 L.

Figure 5-10 shows the *COP* as a function of load temperature (T_C) at the optimal aspect ratio for a regenerator bed volume of 2 liters. Figure 5-11 and Figure 5-12 show the *COP* as a function of load temperature (T_C) at the optimal aspect ratio for a regenerator bed volume of 4 and 6 liters, respectively. Comparing the figures for regenerator volumes between 2 and 8 liters, the performance of a layered bed with lanthanum-iron-silicon hydride is less sensitive to changes in regenerator volumes than the performance of a bed layered with gadolinium-erbium. As the volume is increased, the load temperature at which the *COP* of an AMR cycle with layered $La(Fe_{1-x}Si_x)_{13}H_y$ and layered Gd-Er is identical decreases. Hence for smaller volumes (2 L), $La(Fe_{1-x}Si_x)_{13}H_y$ will outperform Gd-Er for load temperatures below at least 304 K with a heat rejection temperature (T_H) of 310 K for a 5 kW cooling application.

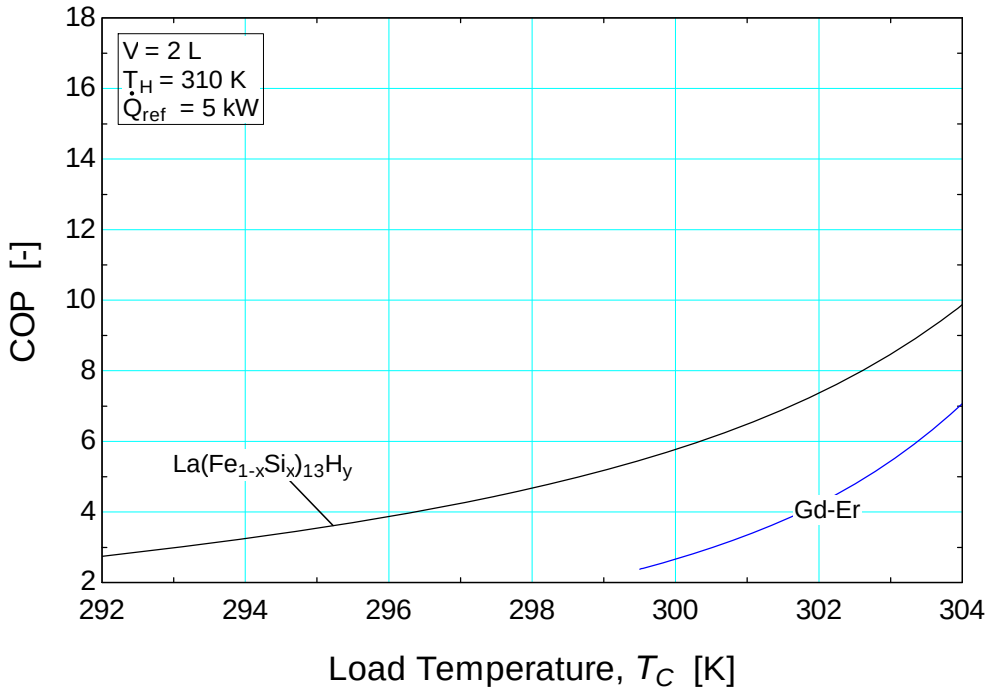

Figure 5-10. *COP* as a function of load temperature (T_C) at the optimal aspect ratio for an infinitely layered regenerator bed with a volume of 2 liters.

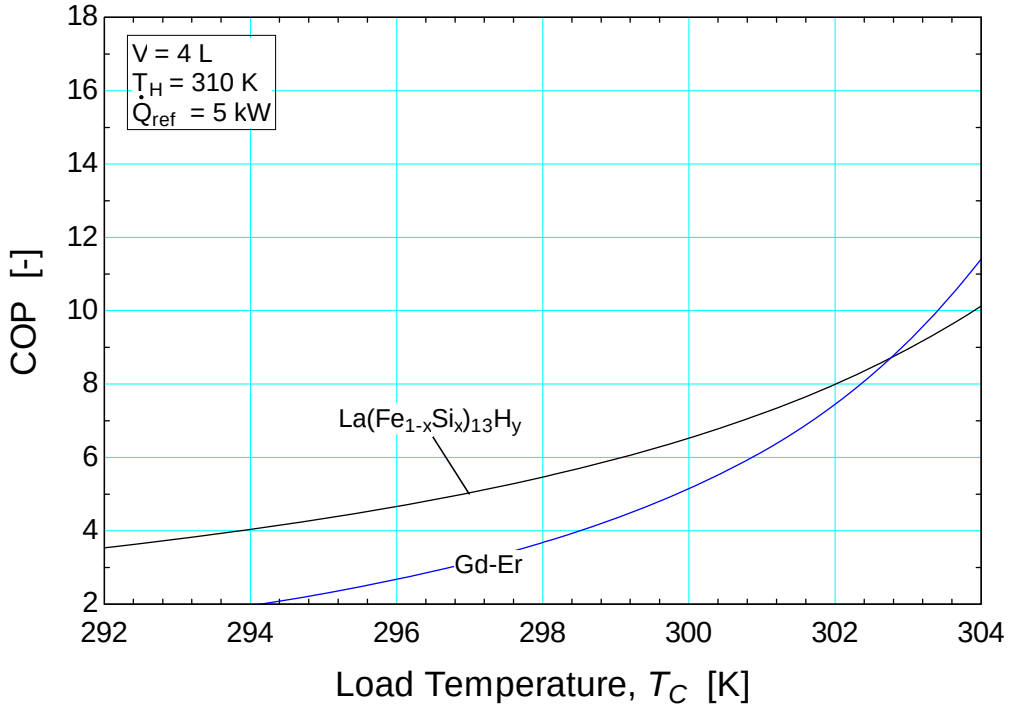

Figure 5-11. *COP* as a function of load temperature (T_C) at the optimal aspect ratio for an infinitely layered regenerator bed with a volume of 4 liters.

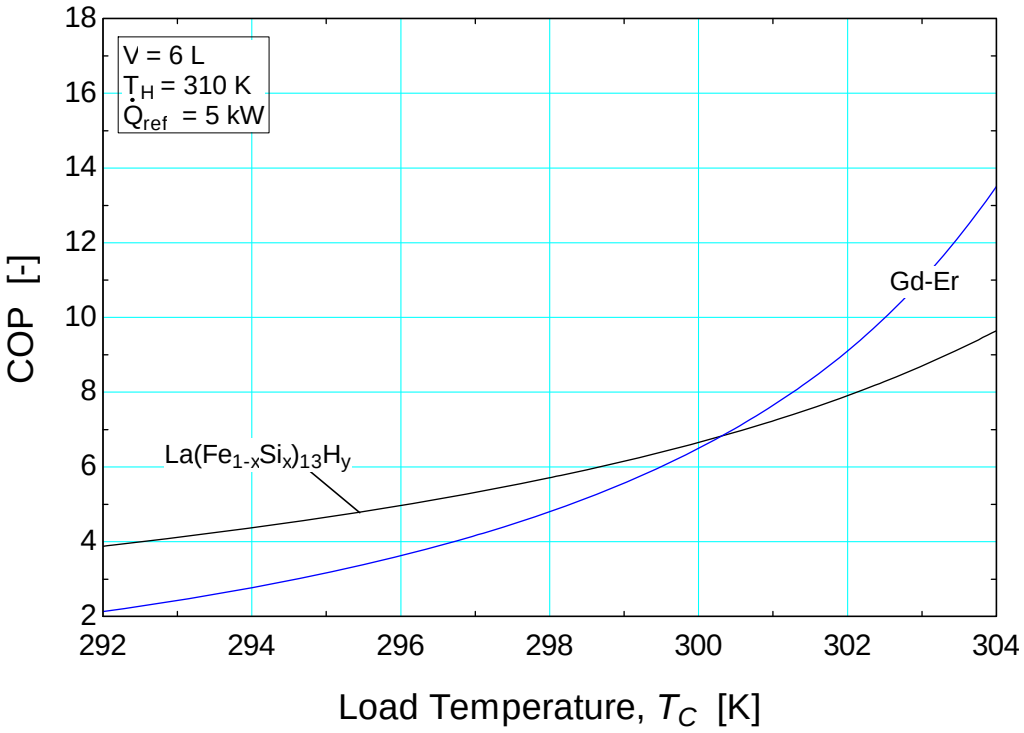

Figure 5-12. *COP* as a function of load temperature (T_C) at the optimal aspect ratio for an infinitely layered regenerator bed with a volume of 6 liters.

In order to compare the performance of the AMR cycle with each refrigerant, the *COP* of Gd-Er can be used as a baseline for comparison. The percent deviation (*%dev*) of the *COP* of $La(Fe_{1-x}Si_x)_{13}H_y$ from the *COP* of Gd-Er can be represented as:

$$\%dev = \frac{COP_{LaFeSiH} - COP_{GdEr}}{COP_{GdEr}} \cdot (100\%) \tag{5-3}$$

where $COP_{LaFeSiH}$ is the coefficient of performance of the AMR cycle with $La(Fe_{1-x}Si_x)_{13}H_y$ as the refrigerant and COP_{GdEr} is the coefficient of performance of the AMR cycle with Gd-Er as the refrigerant. In this study, the *COP* of each material will be evaluated at their respective optimal aspect ratios.

Figure 5-13 presents the *COP* percent deviation as a function of load temperature for various values of regenerator volume. Lines are only drawn for operation points (load temperatures and volumes) where both refrigerants are physically capable of producing 5 kW of refrigeration capacity. Positive percent deviation indicates a performance advantage for $La(Fe_{1-x}Si_x)_{13}H_y$ whereas a negative percent deviation indicates a performance advantage for Gd-Er. For regenerator volumes below 8 liters, the plot indicates that a cycle with $La(Fe_{1-x}Si_x)_{13}H_y$ runs more efficiently than one with Gd-Er for load temperatures below 297 K.

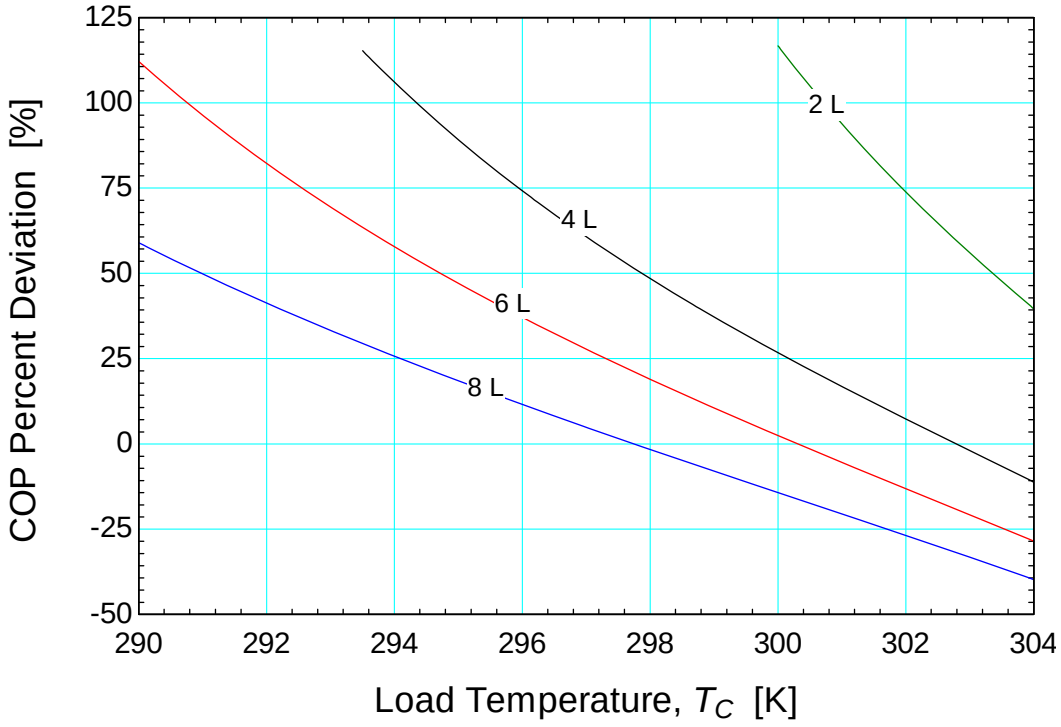

Figure 5-13. *COP* percent deviation as a function of load temperature for various values of regenerator volume for a 5 kW cooling application.

Bed Layering

In the studies presented in the previous sections, the number of layers across each bed was assumed constant at $N_L = 60$. In each regenerator bed, the Curie temperature of each layer varies linearly between the load and heat rejection temperatures. In this study, the effect of the number of layers on cycle performance is evaluated at a specified refrigeration capacity of 5 kW, a regenerator volume of 8 liters, and a heat rejection temperature of 310 K for various load temperatures. Other pertinent model inputs are listed in Table 5-2. The equation used to model the spatial distribution of the Curie temperature is:

$$T_{Curie,i} = T_H - (T_H - T_C)\frac{\left\lceil (i-0.5)\frac{N_L}{Nx} \right\rceil - 0.5}{N_L} \tag{5-4}$$

where i is the spatial node number, Nx is the number of spatial nodes, and N_L is the number of layers. The argument of the $\lceil\ \rceil$ operator indicates rounding up to the nearest integer.

Figure 5-14 shows the coefficient of performance as a function of the number of layers in each regenerator bed for various values of load temperature at their optimal aspect ratio with $Gd_{1-x}Er_x$ as the working refrigerant. For all load temperatures, the *COP* is negligibly affected by an increase in the number of layers above approximately 10 layers. Thus, for applications in this range of load temperatures, a bed with 10 layers is sufficient.

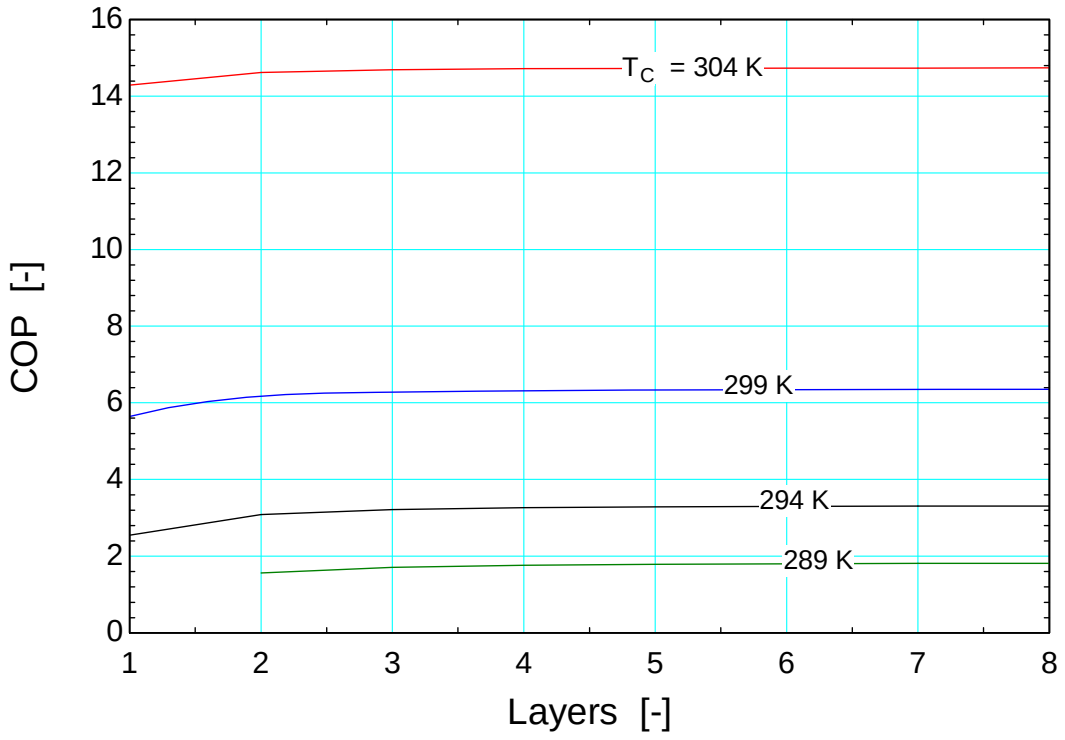

Figure 5-14. *COP* as a function of the number of layers in each regenerator bed for various load temperatures at their respective optimal aspect ratios with $Gd_{1-x}Er_x$ as the refrigerant.

Figure 5-15 shows the *COP* as a function of the number of layers in each regenerator bed for various load temperatures at their respective optimal aspect ratios with $La(Fe_{1-x}Si_x)_{13}H_y$ as the active refrigerant. For each temperature span, there exists a number of layers below which the cycle cannot produce the specified refrigeration capacity of 5 kW. As the temperature span increases, the minimum number of layers required to achieve the desired refrigeration capacity also increases; larger temperature spans require more layers to operate properly. Figure 5-16 shows the minimum number of layers required by an AMRR cycle running with regenerator beds layered with Gd-Er and $La(Fe_{1-x}Si_x)_{13}H_y$ to achieve a

refrigeration capacity of 5 kW at the optimal aspect ratio. The minimum number of layers for a load temperature of 294 K is N_L = 19, as illustrated by Figure 5-16. Thus, in general, a FOMT refrigerant requires more bed layers than a SOMT refrigerant to operate properly at the same refrigeration capacity.

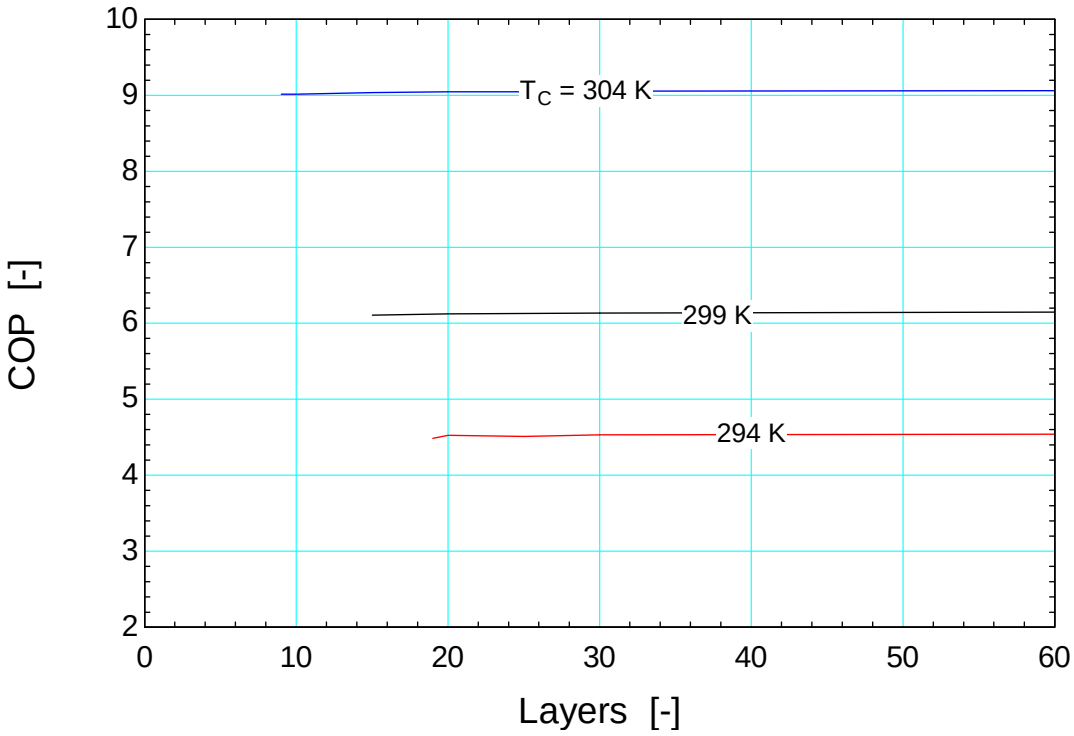

Figure 5-15. *COP* as a function of the number of layers in each regenerator bed for various load temperatures at their respective optimal aspect ratios with $La(Fe_{1-x}Si_x)_{13}H_y$ as the refrigerant.

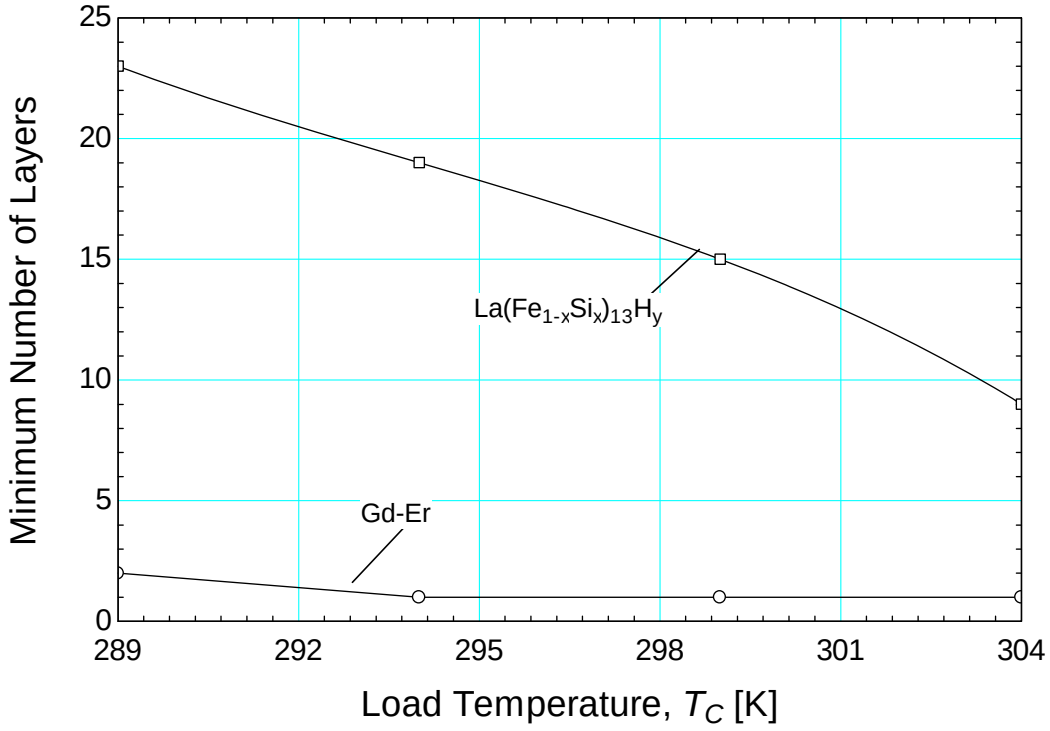

Figure 5-16. Minimum number of layers required each regenerator bed to achieve a refrigeration capacity of 5 kW for AMRR cycle running with Gd-Er and $La(Fe_{1-x}Si_x)_{13}H_y$.

Hysteresis Scaling

In this study, the load temperature, the heat rejection temperature, volume and other model inputs listed in Table 5-2 are held constant, while the hysteresis scaling factor (C_h) is varied from 0 to 6 (0 to 600%). $La(Fe_{1-x}Si_x)_{13}H_y$ is used as the refrigerant in this study and the number of layers is fixed at N_L = 60. A hysteresis scaling factor of 0 indicates no hysteresis in the model while a factor of 1 indicates the amount of hysteresis that $La(Fe_{1-x}Si_x)_{13}H_y$ would normally exhibit under these conditions. Figure 5-17 shows the *COP* at the optimal aspect ratio as a function of percent hysteresis for $La(Fe_{1-x}Si_x)_{13}H_y$ for various regenerator volumes. Percent hysteresis is defined as the hysteresis scaling factor multiplied by 100%.

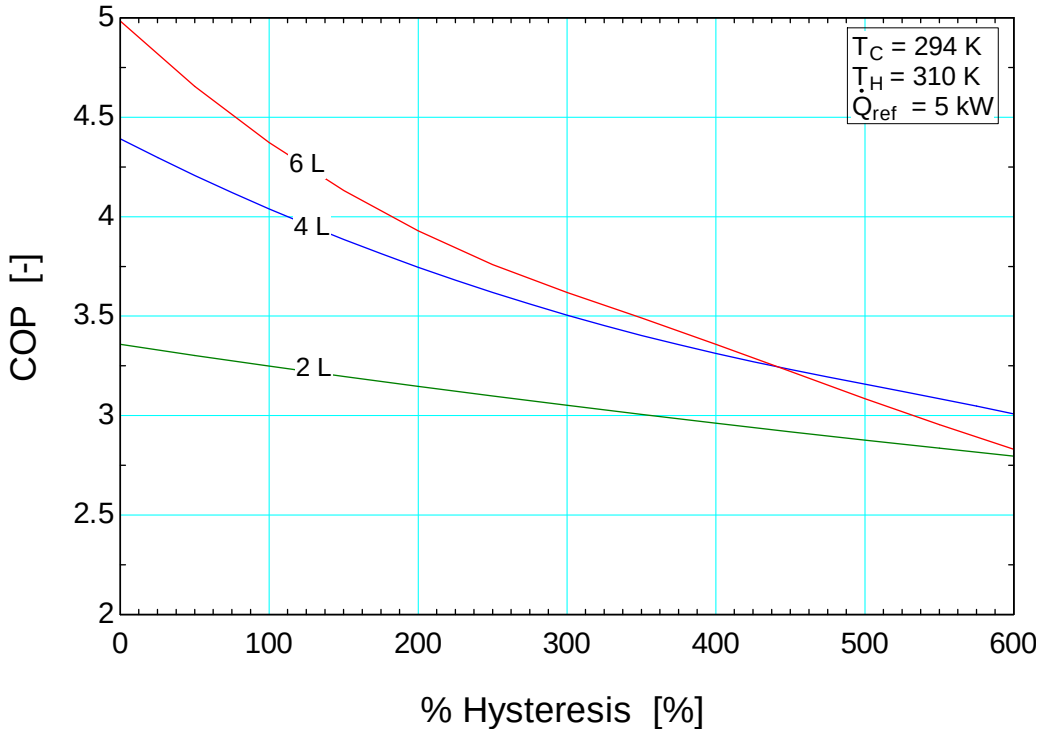

Figure 5-17. COP at the optimal aspect ratio as a function of percent hysteresis for $La(Fe_{1-x}Si_x)_{13}H_y$ for various regenerator volumes. 100% hysteresis indicates normal hysteresis losses for $La(Fe_{1-x}Si_x)_{13}H_y$ under specified conditions.

As shown by Figure 5-17, increasing the hysteresis is detrimental to the *COP* of the cycle for all regenerator volumes. However, for smaller volumes, increasing the percent hysteresis has less effect on cycle performance than it does for larger volumes. This behavior is due to hysteresis being a volumetric loss, which therefore becomes more substantial at larger regenerator volumes. Thus, a well-designed regenerator with a FOMT refrigerant should be small enough to negate hysteretic losses but large enough to provide the required cooling power at an acceptable *COP*.

5.3 Magnetocaloric Property Modulation

There are two parameters that are often used in the literature to characterize magnetocaloric materials: the adiabatic temperature change (ΔT_{ad}) and the isothermal entropy change (Δs_M). These values are expressed for a given change in magnetic field ($\Delta \mu_0 H$), generally from 0 Tesla to a specified value. The specific isothermal entropy change is determined from a material's partial derivative of entropy with respect to magnetic field at constant temperature according to:

$$\Delta s_M\left(T,\mu_0 H,\mu_0 H_1,\mu_0 H_2\right)=\int_{\mu_0 H_1}^{\mu_0 H_2}\left(\frac{\partial s_r}{\partial \mu_0 H}\right)_T d\mu_0 H \tag{5-5}$$

which, by use of the Maxwell relation shown as Eq. (2-4) can be rewritten as:

$$\Delta s_M\left(T,\mu_0 H,\mu_0 H_1,\mu_0 H_2\right)=\int_{\mu_0 H_1}^{\mu_0 H_2}\left(\frac{\partial v_r M_{an}}{\partial T}\right)_{\mu_0 H} d\mu_0 H \tag{5-6}$$

where $\left(\frac{\partial v_r M_{an}}{\partial T}\right)_{\mu_0 H}$ is the partial derivative of the mass specific anhysteretic magnetization with respect to temperature at constant applied field. The parameters $\mu_0 H_1$ and $\mu_0 H_2$ are the initial and final applied magnetic field of integration.

The adiabatic temperature change can be written as:

$$\Delta T_{ad}\left(T,\mu_0 H,\mu_0 H_1,\mu_0 H_2\right)=\int_{\mu_0 H_1}^{\mu_0 H_2}\frac{T}{c_{\mu_0 H}}\left(\frac{\partial v_r M_{an}}{\partial T}\right)_{\mu_0 H} d\mu_0 H \tag{5-7}$$

where $c_{\mu_0 H}$ is the magnetic material mass specific heat capacity at a constant magnetic field. By inspection of Eq. (5-6), the isothermal entropy change is proportional to the partial derivative of the mass specific anhysteretic magnetization with respect to temperature at constant applied field. From Eq. (5-7), the adiabatic temperature change is also proportional to the partial derivative of the mass specific anhysteretic magnetization with respect to temperature at constant applied field and is inversely proportional to the constant applied field specific heat capacity.

Using a set of property data or an equation of state, the adiabatic temperature and isothermal entropy changes can be computed. These values can then be artificially modulated using scaling factors. Changing these parameters with scaling factors allows parametric studies on the mutual effect of ΔT_{ad} and Δs_M on AMRR system performance. The scaling factor C_M is chosen to modify partial derivative of the mass specific anhysteretic magnetization with respect to temperature at constant applied field and the

scaling factor C_c is chosen to modify the mass specific heat at constant applied field. The entropy derivative is written as:

$$ds = C_M \frac{c_{\mu_0 H}}{C_c} dT + C_M \left(\frac{\partial v_r M_{an}}{\partial T} \right)_{\mu_0 H} d\mu_0 H \tag{5-8}$$

In a similar fashion, Eqs. (5-6) and (5-7) can be written to include the scaling factors:

$$\Delta s_M \left(T, \mu_0 H, \mu_0 H_1, \mu_0 H_2, C_M \right) = \int_{\mu_0 H_1}^{\mu_0 H_2} C_M \left(\frac{\partial v_r M_{an}}{\partial T} \right)_{\mu_0 H} d\mu_0 H \tag{5-9}$$

$$\Delta T_{ad} \left(T, \mu_0 H, \mu_0 H_1, \mu_0 H_2, C_c \right) = \int_{\mu_0 H_1}^{\mu_0 H_2} C_c \frac{T}{c_{\mu_0 H}} \left(\frac{\partial v_r M_{an}}{\partial T} \right)_{\mu_0 H} d\mu_0 H \tag{5-10}$$

Note that now the isothermal entropy change and adiabatic temperature change are functions of C_M and C_c, respectively.

Utilizing the scaling factors, a parametric study is conducted to examine the effect of the adiabatic temperature and isothermal entropy changes on AMRR cycle performance. The inputs for the UW AMRR model are listed in Table 5-3. The mass flow and magnetic field profiles are same as described in Section 5.2 .

Table 5-3. Inputs to AMRR model for magnetocaloric parameter study

Parameter	Value	Parameter	Value
cycle time	0.2 s	dwell ratio	1/2
max magnetic field	1.5 T	regenerator type	packed sphere
heat transfer fluid	water	particle diameter	0.0002 m
porosity	0.36	motor efficiency	0.9
heat rejection temperature	310 K	pump efficiency	0.7
load temperature	299 K	number of beds	6

Figure 5-18 shows the *COP* at the optimal aspect ratio of layered bed with a Gd-Er compound as a function of adiabatic temperature and (negative) isothermal entropy change. The field change is from 0 to

1.5 Tesla. The base properties of the SOMT Gd-Er compound were modified according to Eqs. (5-8), (5-9), and (5-10). The volume-specific refrigeration capacity ($\dot{Q}_{ref}/V$) is held constant at 1.25 kW/L. By examination of Figure 5-18, the *COP* of this system is not a strong function of adiabatic temperature change for values above $\Delta T_{ad} = 4$ K, below this value of ΔT_{ad} the *COP* begins to decrease rapidly.

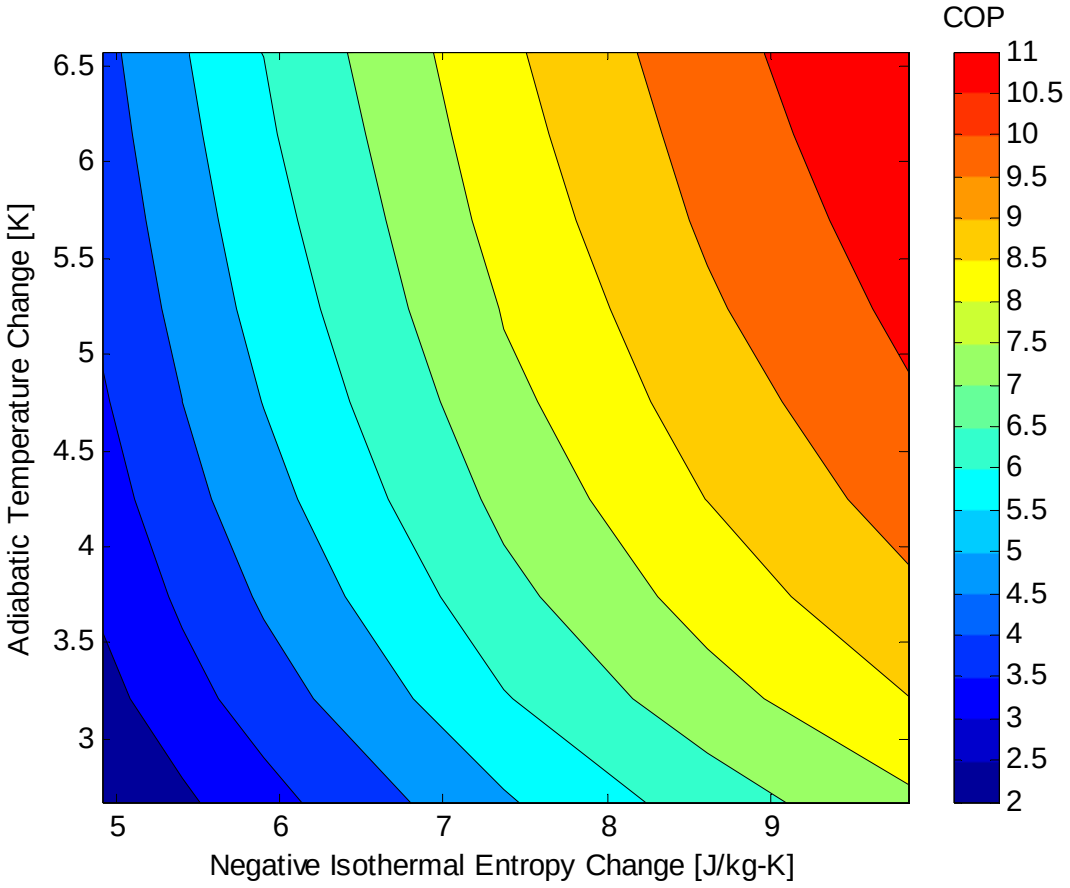

Figure 5-18. *COP* at the optimal aspect ratio as a function of negative isothermal entropy change and adiabatic entropy change for Gd-Er layered bed with a volume specific refrigeration capacity of 1.25 kW/L.

Figure 5-19 shows the regenerator volume specific refrigeration capacity as a function of adiabatic temperature change and isothermal entropy change for a infinitely layered regenerator bed of Gd-Er with a specified *COP* = 4. As the figure shows, the volume specific refrigeration capacity is not a strong

function of adiabatic temperature change above $\Delta T_{ad} = 4$ K for negative isothermal entropy changes below $\Delta s_M = 20 \frac{\text{J}}{\text{kg-K}}$.

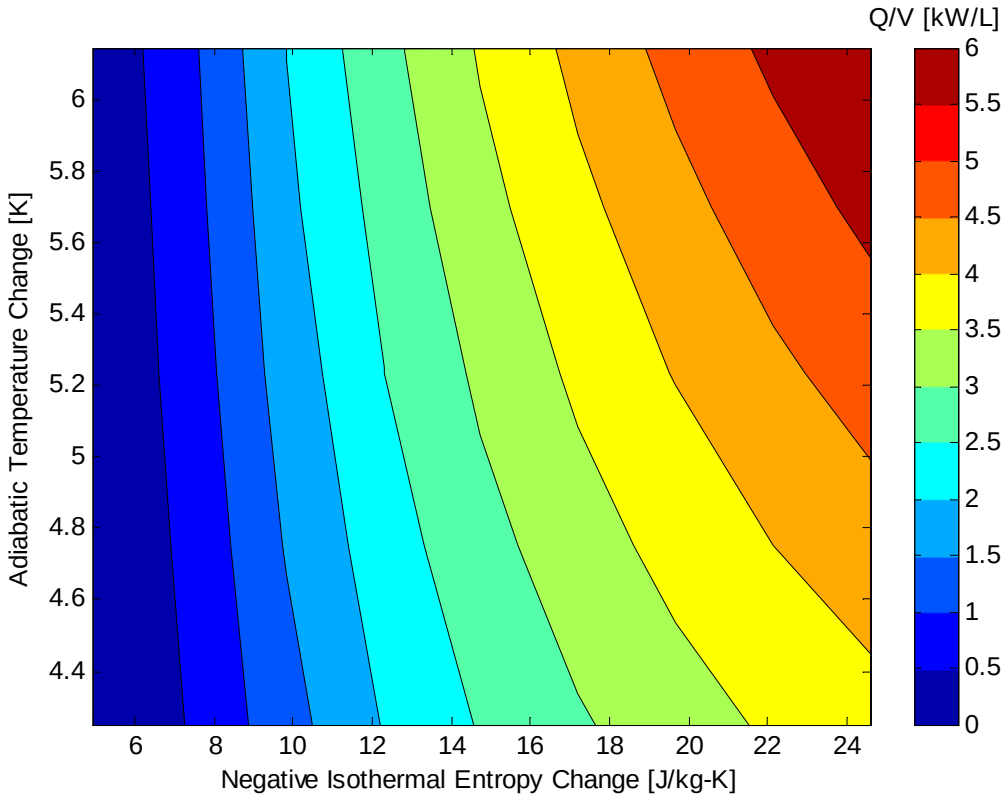

Figure 5-19. Volume Specific refrigeration capacity at the optimal aspect ratio as a function of negative isothermal entropy change and adiabatic entropy change for Gd-Er layered bed with a specified *COP* of 4.

Figure 5-20 is the *COP* at the optimal aspect ratio of a layered bed with modified $La(Fe_{1-x}Si_x)_{13}H_y$ as a function of adiabatic temperature and (negative) isothermal entropy change. The field change is from 0 to 1.5 Tesla and the hysteresis is set to zero. Adiabatic temperature changes below 4 K are shown. In this range, the *COP* becomes a strong function of ΔT_{ad} and only weakly depends on Δs_M.

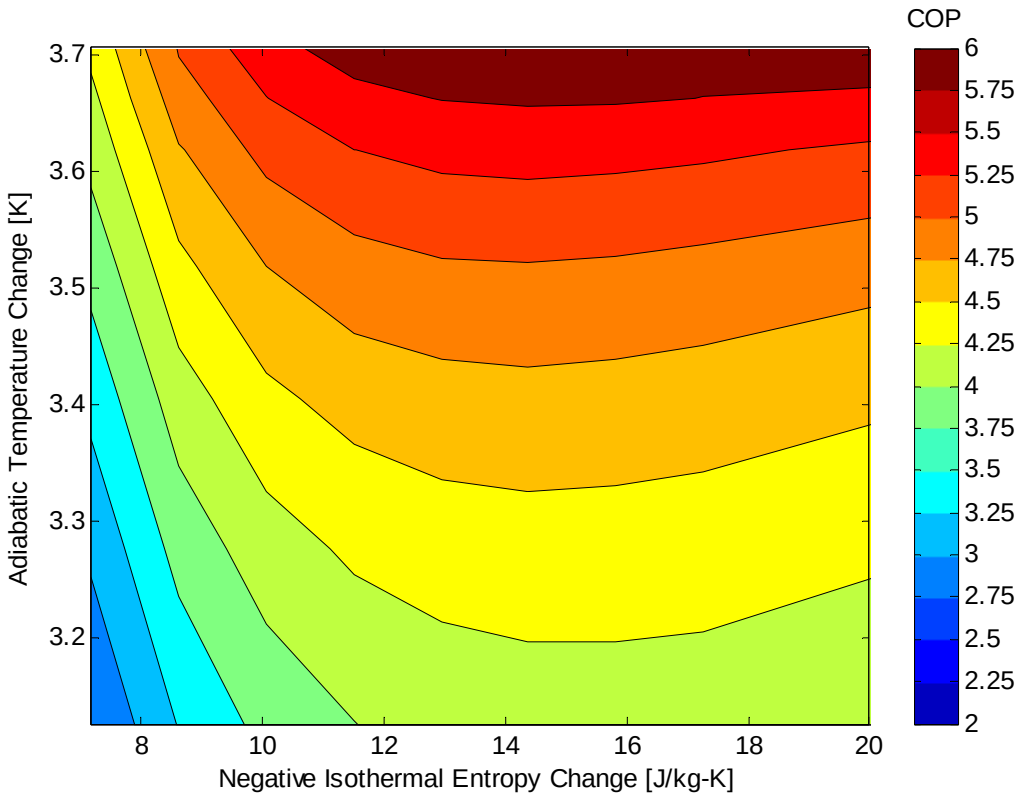

Figure 5-20. *COP* at the optimal aspect ratio as a function of negative isothermal entropy change and adiabatic entropy change for $La(Fe_{1-x}Si_x)_{13}H_y$ layered bed with a volume specific refrigeration capacity of 1.25 kW/L. Hysteresis is set to zero.

Figure 5-21 is the *COP* at the optimal aspect ratio of a layered bed with modified $La(Fe_{1-x}Si_x)_{13}H_y$ as a function of adiabatic temperature and (negative) isothermal entropy change with hysteresis set to unity for a volume of 4 liters. The field change is from 0 to 1.5. Adiabatic temperature changes below 4 K are shown. By comparison to Figure 5-20, the *COP* is slightly less for a hysteretic material. The detriment to hysteresis is relatively small since it was used for a relatively small bed of 4 liters. Again, because hysteresis is a volumetric loss, increasing the bed size increases the hysteretic losses.

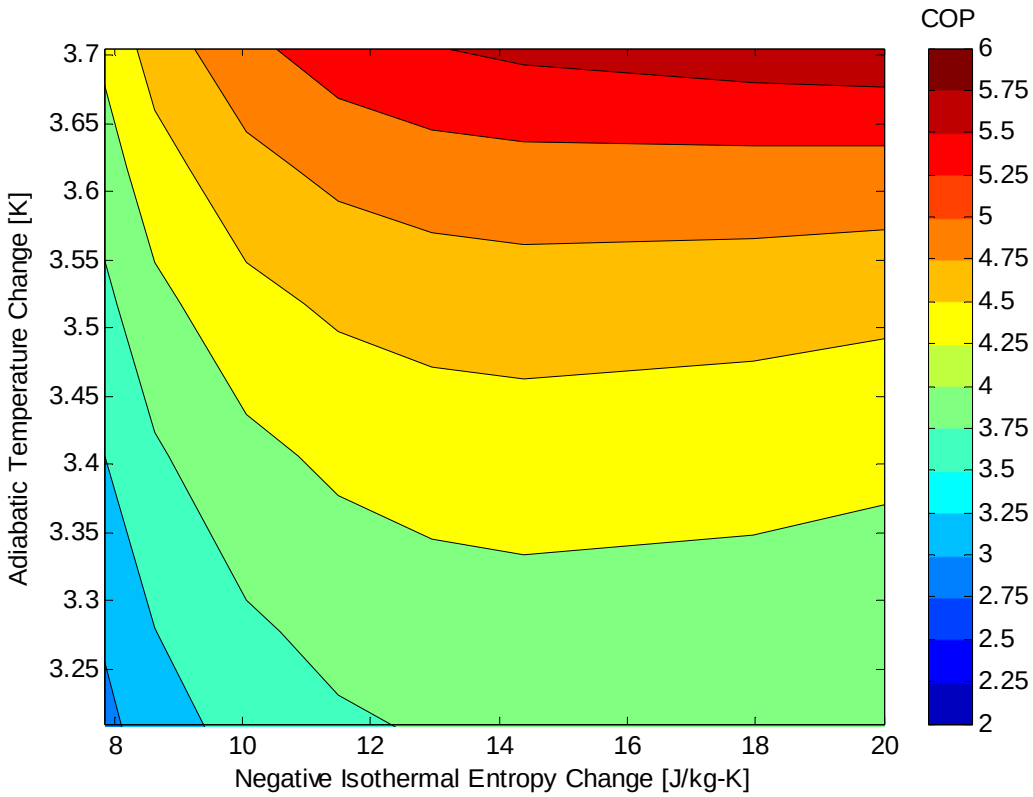

Figure 5-21. *COP* at the optimal aspect ratio as a function of negative isothermal entropy change and adiabatic entropy change for $La(Fe_{1-x}Si_x)_{13}H_y$ layered bed with a volume specific refrigeration capacity of 1.25 kW/L. Hysteresis is set to unity for a volume of 4 L.

For an infinitely layered regenerator bed in an AMRR cycle for a field change from 0 to 1.5 Tesla, an ideal material would have an adiabatic temperature change above 4 Kelvin and large isothermal entropy change near room temperature, with minimal hysteresis. However, hysteretic losses can be mitigated by designing for a minimal regenerator volume for a particular application.

Chapter 6 CONCLUSIONS

Room temperature magnetic refrigeration is a promising alternative to vapor compression refrigeration because it has a high theoretical efficiency, uses non-ozone depleting refrigerants, and exhibits relatively quiet operation. However, magnetic cooling system design presents numerous challenges that must be overcome before becoming a practical alternative to vapor compression systems. The most encouraging thermodynamic cycle for magnetic refrigeration is the active magnetic regenerative refrigeration (AMRR) cycle using a layered magnetocaloric refrigerant. By the nature of the solid state refrigerant, magnetic coolers require a separate heat transfer fluid to physically transport heat from one location to another, which requires complex pumping systems. These systems also require large magnets and high magnetic fields to operate properly. Additionally, there is currently difficulty understanding the thermodynamics of these systems since detailed magnetocaloric equations of state are not readily available for exotic refrigerants that exhibit the most promise for use in magnetic coolers.

Pure gadolinium is considered the baseline magnetic refrigerant for use in magnetic coolers because its magnetocaloric properties near room temperature have been measured and modeled most precisely. Gadolinium exhibits a modest magnetocaloric effect and has been successfully used in prototype magnetic coolers. In 1997, Pecharsky and Gschneidner announced the discovery of the giant magnetocaloric effect (GMCE) in $Gd_5(Si_{1-x}Ge_x)_4$ type compounds. Due to the nature of their phase transition near room temperature, these compounds exhibit a large magnetocaloric effect but also exhibit magnetic hysteresis. Since the discovery of the GMCE, several promising hysteretic compounds that exhibit a GMCE under magnetic field changes have been discovered, including $La(Fe_{1-x}Si_x)_{13}H_y$ compounds. These materials have a tunable Curie temperature, making them ideal for use in a layered regenerator bed. Extensive property data of these materials are not publically available, and the effects of magnetic hysteresis on AMRR performance are not well understood.

This thesis presents a thermodynamic model of magnetic hysteresis that treats the phenomenon as a form of internal entropy generation. This model of magnetic hysteresis is based on the Jiles-Atherton

model of magnetic hysteresis. The proposed model defines the magnetization induced in the material in terms of reversible, anhysteretic magnetization and irreversible, hysteretic magnetization components. For an incompressible substance, the anhysteretic magnetization (M_{an}) is a function of applied magnetic field and temperature only. However, for the same incompressible substance (assuming no thermal hysteresis), the irreversible magnetization (M_{irr}) is a complex function of instantaneous applied magnetic field ($\mu_0 H$), temperature (T), maximum applied magnetic field ($\mu_0 H_{max}$), minimum applied magnetic field ($\mu_0 H_{min}$), and the rate of change of applied magnetic field in time ($\frac{\partial \mu_o H}{\partial t}$). Since there are limited property data for hysteretic materials, the irreversible magnetization is treated as being independent of the rate of change of applied field in this thesis.

The proposed thermodynamic model of irreversible magnetization was tested for its effect on the performance of a magnetic Carnot cycle. The irreversible magnetization was defined as a sinusoidal function that is zero at the minimum and maximum applied magnetic fields. The area enclosed by the hysteretic *H-M* curve was shown to be equivalent to the integral of the irreversible magnetization function over 1 cycle, and is representative of the exergy destroyed per cycle due to hysteresis. At a given load and rejection temperature, as the irreversible magnetization function was increased in magnitude, the *COP* of the cycle was shown to decrease. This simple model verified the thermodynamic treatment of hysteresis as a source of internal entropy generation in the ideal limit of a Carnot cycle.

The model of entropy generation that was implemented in the Carnot cycle model was subsequently implemented into the governing regenerator equations used in the the one-dimensional University of Wisconsin numerical model developed by Engelbrecht (2005, 2008). By combining the first and second laws of thermodynamics, the internal energy of the regenerator material is resolved in terms of the temperature and magnetic field driven components, the latter of which includes the entropy generated due to hysteresis. The entropy generation rate can be further resolved in terms of the irreversible magnetization according to Eq. (2-8). The equations are subsequently discretized and can be solved for steady state operating conditions.

Chapter 4 discussed magnetic equations of state for ferromagnetic, paramagnetic, and metamagnetic phase transition materials. These equations of state are all based on the Brillouin function. For first order magnetic transition type materials, the magnetic equation of state model proposed by Von Ranke et al. (2004) may be appropriate. The anhysteretic magnetization as a function of applied field and temperature can be estimated from raw magnetization data. One method is to estimate it as the arithmetic mean of the induced magnetization while the applied field is increasing and magnetization wiled the field is for a given temperature and applied magnetic field. For a given temperature and applied field, the irreversible magnetization is thus the absolute value of the difference between the anhysteretic magnetization and actual magnetization (field increasing or decreasing). These data can, along with data for a constant field specific heat, be used to create a map of the magnetocaloric material entropy as a function of temperature and applied field to be used by the 1D UW model.

The effect of magnetic hysteresis of AMRR systems was quantified through parametric studies with the hysteresis-modified 1D UW model. For a specified refrigeration capacity and load temperature, a bed layered with $La(Fe_{1-x}Si_x)_{13}H_y$ showed a higher *COP* at relatively small volumes when compared to a bed layered with Gd-Er. Furthermore, for a specified refrigeration capacity and regenerator volume, a bed layered with $La(Fe_{1-x}Si_x)_{13}H_y$ was shown to outperform a bed layered with Gd-Er at large temperature spans. As regenerator volume increases, hysteretic losses outweigh the capacity gains associated with adding more refrigerant. Parametric studies also implied that the adiabatic temperature change may not have a significant effect on the performance of a layered bed for $\Delta T_{ad} > 4$ K.

6.1 Recommendations for Future Work

There are several areas for future work to improve upon the accuracy of the model:

- Implementation of an accurate equation of state for a hysteretic material, which includes the irreversible magnetization.
- Investigate the dependence of irreversible magnetization for a given material on the minimum and maximum applied magnetic fields and the rate at which the applied field is ramped.
- Experimental validation of the magnetic hysteresis model.
- Investigate the effect of hysteresis on an AMRR heat pump cycle.
- Model the thermal interaction between the regenerator bed and the regenerator housing.

Appendix A SINGLE SHOT MATLAB MODEL

```
clear;
muH_max=2;          %maximum applied magnetic field in Tesla
vdM_max=0.1;        %mass specific irreversible magnetization in A-m^2/kg
cmu0H=0.5;          %specific heat in J/kg-k
rho=1;              %density of fictional material in kg/m^3
tau=4;              %period of magnetic field oscillation in s
c=273;              %Curie constant in K-A/T-m
h=0.008;            %time step in s
t=0:h:12;
n=length(t)-1;
T(1)=293;           %initial temperature in K
vM(1)=0;
muH=muH_max*(1-cos(2*pi*t/tau))/2;  %sinusoidal function for magnetic field

for i=1:n
    dmuHdt=muH_max*pi*sin(2*pi*t(i)/tau)/tau; %derivative of magnetic field
w.r.t. time
    dsdT=cmu0H/T(i);    %partial derivative of entropy w.r.t. temperature
    dvMandT=-c*muH(i)/(rho*(T(i)^2));   %partial derivative of entropy w.r.t.
magnetic field
    vM_irr(i)=vdM_max*sin(muH(i)*pi/muH_max);   %irreversible magnetization

    dTdt=((vM_irr(i)/T(i))*abs(dmuHdt)-dvMandT*dmuHdt)/dsdT;
    T(i+1)=T(i)+h*dTdt;
    vM(i)=c*muH(i)/T(i)-vM_irr(i)*sign(dmuHdt); %magnetization
    muHi(i)=muH(i);
    S_gen_dot(i)=vM_irr(i)*abs(dmuHdt)/T(i);    %entropy generation rate
    ti(i)=t(i);         %new time vector for plotting
end
Tiso=(290:15/(n):305)';

for i=1:n+1       %entropy calculation - analytical
    s(i)=cmu0H*log(T(i))-c*((muH(i)/T(i))^2)/(2*rho);
    s_min(i)=cmu0H*log(Tiso(i));
    s_max(i)=cmu0H*log(Tiso(i))-c*((muH_max/Tiso(i))^2)/(2*rho);
end

for i=1:n-1
    dmuHdt=muH_max*pi*sin(2*pi*t(i)/tau)/tau;
    dS_gen(i)=((vM_irr(i+1)+vM_irr(i))/(T(i+1)+T(i)))*abs(dmuHdt)*(t(i+1)-
t(i));    %integrate S_gen function numerically; trapezoidal rule
end

%compare area of curve to area of irreversible curve
A_mag=trapz(vM,muHi)                %evaluate @ t=tau
A_magirr=2*trapz(vM_irr,muHi)       %evaluate @ t=tau/2

%calculate total entropy generated
S_gen=sum(dS_gen)   %result of integrating S_gen_dot function
S_gen2=max(s)-min(s)    %result of subtracting the final entropy from the
initial entropy, should be equal.
```

Appendix B CARNOT CYCLE MATLAB MODEL

```
clear all;
muH_max=2;              %maximum applied magnetic field in Tesla
rho=7900;               %Desnity in kg/m^3
cmu0H0=0.5;             %constant field specific heat in J/kg-K
C=20;                   %Curie constant in K
mu0=4*pi*10^-7;         %Permeability of free space in T-m/A
c=C/mu0;                %adjusted curie constant A-K/T-m
tau=4;                  %cycle duration in seconds
dM_max=5*rho;           %maximum irreversible magnetization in A/m
T_H=280.00;             %hot reservoir temperature in K
h=0.001;                %applied magnetic field step size in Tesla
muH=0:h:muH_max;        %ramp up magnetic field
n=length(muH)-1;        %number of iterations
m=1;

%preallocate space for matricies
T=zeros(n,m);
s_pos=zeros(n,m);
T1=zeros(n,m);
s_neg=zeros(n,m);

for k=1:m
    T_C=273;            %cold reservoir temperature in K
    T(1,k)=T_C(k);      %Initial condition for magnetizatiom
    T1(n+1,k)=T_H;      %initial condition for demagnetization
    s_pos(1,k)=cmu0H0*log(T_C(k)); %Initial entropy w/ref @ 0 applied field
and T=1 K
    %dM_max=linspace(0,rho*5,m)';  %various maximum irreversible
magnetization constants in A/m
    k
for i=1:n   %increment magnetic field from minimum to maximum
     if (T(i,k)<T_H)  %adiabatic magnetization
            Mirr=dM_max*sin(pi*muH(i)/muH_max); %irreversible magnetization
function
            dvMdT=-(c*muH(i))/(rho*(T(i,k))^2);   %maxwell relation for
dsdmuH
            cmu0H=cmu0H0+c*muH(i)^2/(rho*T(i,k)^2); %function for constant
field specific heat
            dsdT=cmu0H/T(i,k); %partial derivative of entropy wrt temperature
            dTdmuH=((Mirr/(rho*T(i,k)))-dvMdT)/dsdT;  %eliminate time
derivatives and rearrange entropy balance

            %calculate midpoint values
            T_mid=T(i,k)+h*dTdmuH/2;
            dvMdT_mid=-(c*(muH(i)+h/2))/(rho*(T_mid)^2);
            cmu0Hmid=cmu0H0+c*(muH(i)+h/2)^2/(rho*T_mid^2);
            dsdT_mid=cmu0Hmid/T_mid;
            Mirr_mid=dM_max*sin(pi*(muH(i)+h/2)/muH_max);
            dTdmuH_mid=((Mirr_mid/(rho*T_mid))-dvMdT_mid)/dsdT_mid;

            %calculate properties
            s_pos(i+1,k)=s_pos(i,k)+h*(Mirr_mid/(rho*T_mid)); %entropy vector
            T(i+1,k)=T(i,k)+h*dTdmuH_mid;   %temperature
```

```
     else   %isothermal heat rejection
            Mirr=dM_max*sin(pi*(muH(i)+h/2)/muH_max);
            dvMdT=-(c*muH(i))/(rho*(T_H)^2);    %only derivative for dsdmuH
exists since T=constant
            dvMdT_mid=-(c*(muH(i)+h/2))/(rho*(T_H)^2);
            s_pos(i+1,k)=s_pos(i,k)+h*dvMdT_mid;

            %calculate entriopy and heat rejection
            dq_o(i+1,k)=h*T_H*(dvMdT_mid-(Mirr/(rho*T_H)));
            T(i+1)=T_H; %temperature is constant
     end
end
q_out=sum(dq_o)';    %total amount of heat rejection
s_min=cmu0H0*log(T_H)-c*((muH_max/T_H)^2)/(2*rho); %initial condition for
demag @ T=T_H & muH=muH_max
s_max=cmu0H0*log(T_C(k));
s_neg(n+1,k)=s_min; %IC
for i=n+1:(-1):2    %decrement magnetic field from maximum to minimum
    if (T1(i)>T_C) %adiabatic demagnetization
            Mirr=dM_max*sin(pi*muH(i)/muH_max);  %irreversible magnetization
function
            dvMdT=-(c*muH(i))/(2*rho*(T1(i,k))^2);
            cmu0H=cmu0H0+c*muH(i)^2/(rho*T1(i,k)^2);
            dsdT=cmu0H/T1(i,k);
            dTdmuH=((-Mirr/(rho*T1(i,k)))-dvMdT)/dsdT;

            %calculate midpoint values
            T1_mid=T1(i,k)+h*dTdmuH/2;
            dvMdT_mid=-(c*(muH(i)-h/2))/(rho*(T1_mid)^2);
            cmu0Hmid=cmu0H0+c*(muH(i)+h/2)^2/(rho*T1_mid^2);
            dsdT_mid=cmu0Hmid/T1_mid;
            Mirr_mid=dM_max*sin(pi*(muH(i)-h/2)/muH_max);
            dTdmuH_mid=((-Mirr_mid/(rho*T1_mid))-dvMdT_mid)/dsdT_mid;

            %calculate temperature and entropy
            T1(i-1,k)=T1(i,k)-h*dTdmuH_mid; %temperature; steps are negative
since field is decreasing
            s_neg(i-1,k)=s_neg(i,k)-h*dvMdT_mid-h*dTdmuH_mid*dsdT_mid;

    else    %isothermal heat addition from cold reservoir
            Mirr=dM_max*sin(pi*(muH(i)-h/2)/muH_max);
            dvMdT=-(c*muH(i))/(rho*(T_C(k))^2);
            dvMdT_mid=-(c*(muH(i)-h/2))/(rho*(T_C(k))^2);

            %calculate entropy and heat absorption
            s_neg(i-1,k)=s_neg(i,k)-h*dvMdT_mid;
            dq_i(i-1,k)=-h*T_C(k)*(dvMdT_mid+(Mirr/(rho*T_C(k))));
            T1(i-1,k)=T_C(k);
    end
end
q_in=sum(dq_i)'; %total amount of heat absorption

for i=1:n+1
```

```
     s_pos_ana(i,k)=cmu0H0*log(T(i,k))-c*((muH(i)/T(i,k))^2)/(2*rho);
%analytical calculation of entropy for magnetization
end
for i=1:n+1
    s_neg_ana(i)=cmu0H0*log(T1(i,k))-c*((muH(i)^2)/T1(i,k)^2)/(2*rho);
%analytical calculation of entropy for demagnetization
end

COP(1,k)=q_in(k)/abs(q_in(k)+q_out(k))  %coefficient of performance for cycle
COP_carnot=T_C(k)/(T_H-T_C(k))    %COP for an ideal carnot cycle
end
```

Appendix C MATLAB AMRR REGENERATOR BED MODEL CODE

```
%% This is the main regenerator model developed at UW.  This function takes
%% inputs that define the system and forcing functions, such as mass flow
%% profile, and calculates the regenerator performance.  This model does
%% not account for heat exchangers.  The main outputs of the model are the
%% cyclical steady state temperatures of the fluid and solid over an entire
%% cycle and the heat rejection, cooling power, and pumping power of the
%% system.

%% This model has been modified to include the effects of hysteresis

function[mdot,muoH,heat_rej,ref_load,ref_cap,COP,COP_h,Wmag,Wpump,mdot_amp,Ql
oss,Qent,Qentt,DS_iso,DT_ad]=AMR_pl_imp(TC,TH,TCurie,mdot_amp,Vol,AR,n,Ch,Cx,
Cy,tau)
%%Bed paramters
fluid='eg50';
n_beds=6;
bed_vol=Vol/n_beds;
D=(4*bed_vol/(AR*pi))^(1/3);
L=AR*D;
muoH_max=1.5; %Tesla
dwell=1/2;
delay=(1-dwell)*.45*tau;
unbal=0.0;
flow_ramp=0.25;
dh=0.0002; %m
Ac=pi*D^2/4; %m^2
eps=0.36;
as=6*(1-eps)/dh; %m^2/m^3
L_flow=1*L; %ratio of bed length to bed length in which there is flow
n_motor=.9; %electric motor efficiency
n_pump=.7; %pump efficiency

massflowinputs=[dwell,delay,flow_ramp,unbal];

m=120;
% n=60;
reltol=0.0002;
wt=1;
N=2*m*n+m+n;
A=spalloc(N,N,4*N);
B=spalloc(N,1,N);
%modelcheck=0; %1=show T-s and enthalpy flux graphs 0=don't show them

i=0:n;
xf=L*i'/n;
j=1:m;
tf=(j'-0.5)*tau/m;
i=1:n;
xr=(i'-0.5)*L/n';
j=0:m;
tr=j'*tau/m;
```

```
mdot=mdotsmoothunbal_delay(tf,tau,mdot_amp,massflowinputs);
muoH=muoH_ramp(xr,tr,tau,muoH_max);

for j=0:m
    Trg(:,j+1)=TH-xr*(TH-TC)/L;
end
for j=1:m
    Tfg(:,j)=TH-xf*(TH-TC)/L;
end

%Calculate lumped cap correction factor
if(strcmp(fluid,'water'))
    [muf,kf,cf,rhof,hf,sf]=props_water(Tfg);
elseif(strcmp(fluid,'air'))
    [muf,kf,cf,rhof,hf,sf]=props_air(Tfg);
elseif(strcmp(fluid,'water_const'))
    [muf,kf,cf,rhof,cfunc,T_ref]=fluidprops(Tfg);
elseif(strcmp(fluid,'eg50'))
    [muf,kf,cf,rhof,hf,sf]=props_ethgly50_3(Tfg);
end

[cmuoH,dsdmuoH,rhor,kr,sr,hr,vM_irr,DS_iso,DT_ad]=JF1142A(Trg,TCurie,muoH,Cx,
Cy);
cf_av=mean(mean(cf));
cmuoH_av=mean(mean(cmuoH));

done=0;
while(done==0)
   if(strcmp(fluid,'water'))
       [muf,kf,cf,rhof,hf,sf]=props_water(Tfg);
   elseif(strcmp(fluid,'air'))
       [muf,kf,cf,rhof,hf,sf]=props_air(Tfg);
   elseif(strcmp(fluid,'water_const'))
       [muf,kf,cf,rhof,cfunc,T_ref]=fluidprops(Tfg);
   elseif(strcmp(fluid,'eg50'))
       [muf,kf,cf,rhof,hf,sf]=props_ethgly50_3(Tfg);
   end
   for i=1:n
      mufn(i,:)=(muf(i,:)+muf(i+1,:))/2;
      cfn(i,:)=(cf(i,:)+cf(i+1,:))/2;
      kfn(i,:)=(kf(i,:)+kf(i+1,:))/2;
   end
   Prf=cfn.*mufn./(kfn);
   Ref=ones(n,1)*abs(mdot')*dh./(Ac*mufn);

[cmuoH,dsdmuoH,rhor,kr,sr,hr,vM_irr,DS_iso,DT_ad]=JF1142A(Trg,TCurie,muoH,Cx,
Cy); %JF1142A_nh Gd94Er6
   cf_av=mean(mean(cf));
   cmuoH_av=mean(mean(cmuoH));
   R=(rhof*eps*cf_av)/(rhor*(1-eps)*cmuoH_av);
   AF=1+1.764*R+1.0064*R^2; %correction factor
   v=mdot/(Ac*rhof);
   [Nuf,dP,keff]=sph_part_1(Ref,Prf,eps, kfn, kr,v,dh,mufn,rhof,1,1,1);
%cNu,cff,cnk
   for j=1:m
       ff(:,j)=dP(:,j)*2*dh./(rhof*v(j)^2);
```

```
   end
   Bi=(Nuf.*kfn)/(2*kr);
   Fo=kfn*tau./(rhof*cfn*(dh/2)^2);
   Fo_av=mean(mean(Fo));
   Bi_av=mean(mean(Bi));
   chi=Fo_av*exp(0.246196-0.84878*log(Fo_av)-0.05639*(log(Fo_av))^2);
   DFFc=1/(1+Bi_av*chi/5);
   eta_c=1/(1+(2*pi/(3*Bi_av*Fo_av)*(1/DFFc))^2)^(1/2);
   rhor=eta_c*rhor;

   for j=1:m
    cmuoH(:,j)=(cmuoH(:,j)+cmuoH(:,j+1))/2;
    dsdmuoH(:,j)=(dsdmuoH(:,j)+dsdmuoH(:,j+1))/2;
    vM_irr(:,j)=(vM_irr(:,j)+vM_irr(:,j+1))/2;
   end
%Fill matrices used to solved temperature profile
   for j=1:m
      if(mdot(j)>=0)
         %hot-to-cold flow
         i=1:n;
         A(((n+1)*(j-1)+i+1-1)*N+(n+1)*(j-
1)+i+1)=Nuf(:,j).*kfn(:,j)*as*Ac./((1+chi(:,j).*Bi(:,j)/5)*(2*dh))+n*mdot(j)*
cfn(:,j)/L;
         A(((n+1)*(j-1)+i-1+1-1)*N+(n+1)*(j-
1)+i+1)=Nuf(:,j).*kfn(:,j)*as*Ac./((1+chi(:,j).*Bi(:,j)/5)*(2*dh))-
n*mdot(j)*cfn(:,j)/L;
         A(((n+1)*m+n*j+i-1)*N+(n+1)*(j-1)+i+1)=-
Nuf(:,j).*kfn(:,j)*as*Ac./((1+chi(:,j).*Bi(:,j)/5)*(2*dh));
         A(((n+1)*m+n*(j-1)+i-1)*N+(n+1)*(j-1)+i+1)=-
Nuf(:,j).*kfn(:,j)*as*Ac./((1+chi(:,j).*Bi(:,j)/5)*(2*dh));
        B((n+1)*(j-1)+i+1,1)=abs(ff(:,j).*mdot(j)^3/(2*rhof^2*Ac^2*dh));
%Viscous dissipation
         i=0;
         A((n+1)*(j-1)+i+1,(n+1)*(j-1)+i+1)=1;
         B((n+1)*(j-1)+i+1,1)=TH;

      else
         if(mdot(j)<0)
            %cold-to-hot flow
             i=0:(n-1);
             A(((n+1)*(j-1)+i+1-1)*N+(n+1)*(j-
1)+i+1)=Nuf(:,j).*kfn(:,j)*as*Ac./((1+chi(:,j).*Bi(:,j)/5)*(2*dh))-
mdot(j)*cfn(:,j)*n/L;
             A(((n+1)*(j-1)+i+1+1-1)*N+(n+1)*(j-
1)+i+1)=Nuf(:,j).*kfn(:,j)*as*Ac./((1+chi(:,j).*Bi(:,j)/5)*(2*dh))+mdot(j)*cf
n(:,j)*n/L;
             A(((n+1)*m+n*j+i+1-1)*N+(n+1)*(j-1)+i+1)=-
Nuf(:,j).*kfn(:,j)*as*Ac./((1+chi(:,j).*Bi(:,j)/5)*(2*dh));
             A(((n+1)*m+n*(j-1)+i+1-1)*N+(n+1)*(j-1)+i+1)=-
Nuf(:,j).*kfn(:,j)*as*Ac./((1+chi(:,j).*Bi(:,j)/5)*(2*dh));
                B((n+1)*(j-
1)+i+1,1)=abs(ff(:,j).*mdot(j)^3/(2*rhof^2*Ac^2*dh)); %viscous dissipation
             i=n;
             A((n+1)*(j-1)+i+1,(n+1)*(j-1)+i+1)=1;
             B((n+1)*(j-1)+i+1,1)=TC;
         else
```

```
            %no flow

         end
      end
   end
   for j=1:m
      i=1:n;
      A(((n+1)*(j-1)+i+1-1)*N+(n+1)*m+n*j+i)=-
Nuf(:,j).*kfn(:,j)*as*Ac./((1+chi(:,j).*Bi(:,j)/5)*(2*dh));
      A(((n+1)*(j-1)+i-1+1-1)*N+(n+1)*m+n*j+i)=-
Nuf(:,j).*kfn(:,j)*as*Ac./((1+chi(:,j).*Bi(:,j)/5)*(2*dh));
      B((n+1)*m+n*j+i,1)=-Ac*(1-
eps)*rhor*((Trg(:,j+1)+Trg(:,j))/2).*dsdmuoH(:,j).*(muoH(:,j+1)-
muoH(:,j))*m/tau...
        +Ch*Ac*(1-eps)*rhor.*vM_irr(:,j).*abs(muoH(:,j+1)-muoH(:,j))*m/tau;
      i=2:(n-1);
      A(((n+1)*m+n*j+i-
1)*N+(n+1)*m+n*j+i)=Nuf(i',j).*kfn(i',j)*as*Ac./((1+chi(i',j).*Bi(i',j)/5)*(2
*dh))+Ac*(rhof*eps*cfn(i',j)+(1-
eps)*rhor*cmuoH(i',j))*m/tau+n^2*keff(i',j)*Ac/L^2;
      A(((n+1)*m+n*(j-1)+i-
1)*N+(n+1)*m+n*j+i)=Nuf(i',j).*kfn(i',j)*as*Ac./((1+chi(i',j).*Bi(i',j)/5)*(2
*dh))-Ac*(rhof*eps*cfn(i',j)+(1-
eps)*rhor*cmuoH(i',j))*m/tau+n^2*keff(i',j)*Ac/L^2;
      A(((n+1)*m+n*(j-1)+(i-1)-1)*N+(n+1)*m+n*j+i)=-
n^2*keff(i',j)*Ac/(2*L^2);
      A(((n+1)*m+n*(j)+(i-1)-1)*N+(n+1)*m+n*j+i)=-n^2*keff(i',j)*Ac/(2*L^2);
      A(((n+1)*m+n*(j-1)+(i+1)-1)*N+(n+1)*m+n*j+i)=-
n^2*keff(i',j)*Ac/(2*L^2);
      A(((n+1)*m+n*(j)+(i+1)-1)*N+(n+1)*m+n*j+i)=-n^2*keff(i',j)*Ac/(2*L^2);
      i=1;
      A(((n+1)*m+n*j+i-
1)*N+(n+1)*m+n*j+i)=Nuf(i',j).*kfn(i',j)*as*Ac./((1+chi(i',j).*Bi(i',j)/5)*(2
*dh))+Ac*(rhof*eps*cfn(i',j)+(1-
eps)*rhor*cmuoH(i',j))*m/tau+n^2*keff(i',j)*Ac/(2*L^2);;
      A(((n+1)*m+n*(j-1)+i-
1)*N+(n+1)*m+n*j+i)=Nuf(i',j).*kfn(i',j)*as*Ac./((1+chi(i',j).*Bi(i',j)/5)*(2
*dh))-Ac*(rhof*eps*cfn(i',j)+(1-
eps)*rhor*cmuoH(i',j))*m/tau+n^2*keff(i',j)*Ac/(2*L^2);
      A(((n+1)*m+n*(j-1)+(i+1)-1)*N+(n+1)*m+n*j+i)=-
n^2*keff(i',j)*Ac./(2*L^2);
      A(((n+1)*m+n*(j)+(i+1)-1)*N+(n+1)*m+n*j+i)=-n^2*keff(i',j)*Ac./(2*L^2);
      i=n;
      A(((n+1)*m+n*j+i-
1)*N+(n+1)*m+n*j+i)=Nuf(i',j).*kfn(i',j)*as*Ac./((1+chi(i',j).*Bi(i',j)/5)*(2
*dh))+Ac*(rhof*eps*cfn(i',j)+(1-
eps)*rhor*cmuoH(i',j))*m/tau+n^2*keff(i',j)*Ac/(2*L^2);;
      A(((n+1)*m+n*(j-1)+i-
1)*N+(n+1)*m+n*j+i)=Nuf(i',j).*kfn(i',j)*as*Ac./((1+chi(i',j).*Bi(i',j)/5)*(2
*dh))-Ac*(rhof*eps*cfn(i',j)+(1-
eps)*rhor*cmuoH(i',j))*m/tau+n^2*keff(i',j)*Ac/(2*L^2);
      A(((n+1)*m+n*(j-1)+(i-1)-1)*N+(n+1)*m+n*j+i)=-
n^2*keff(i',j)*Ac./(2*L^2);
      A(((n+1)*m+n*(j)+(i-1)-1)*N+(n+1)*m+n*j+i)=-n^2*keff(i',j)*Ac./(2*L^2);
   end
   j=0;
   i=1:n;
```

```
   A(((n+1)*m+n*j+i-1)*N+(n+1)*m+n*j+i)=1;
   A(((n+1)*m+n*m+i-1)*N+(n+1)*m+n*j+i)=-1;
   X=A\B;
   for j=1:m
      i=0:n;
      Tf(:,j)=full(X((n+1)*(j-1)+i+1));
   end
   for j=0:m
      i=1:n;
        Tr(:,j+1)=full(X((n+1)*m+n*j+i));
   end
   err=max(max(max(abs(Tf-Tfg))),max(max(abs(Tr-Trg))))
   if(err<reltol)
       if(strcmp(fluid,'water'))
           [muf,kf,cf,rhof,hf,sf]=props_water(Tf);
       elseif(strcmp(fluid,'air'))
           [muf,kf,cf,rhof,hf,sf]=props_air(Tf);
       elseif(strcmp(fluid,'water_const'))
           [muf,kf,cf,rhof,hf,sf]=fluidprops(Tf);
       elseif(strcmp(fluid,'eg50'))
           [muf,kf,cf,rhof,hf,sf]=props_ethgly50_3(Tf);
       end

[cmuoH,dsdmuoH,rhor,kr,sr,hr,vM_irr,DS_iso,DT_ad]=JF1142A(Trg,TCurie,muoH,Cx,
Cy); %JF1142A_nh Gd94Er6
      done=1;%Relaxation process complete
   else
      Tfg=Tf*wt+Tfg*(1-wt);
      Trg=Tr*wt+Trg*(1-wt);
   end %Update guess temp values
end
for i=1:n
   for j=1:m
      Tfn(i,j)=(Tf(i,j)+Tf(i+1,j))/2;
      Trn(i,j)=(Tf(i,j)+Tr(i,j+1))/2;
   end
end
for i=1:m
    if abs(mdot(i))<mdot_amp
        Tfa(:,i)=Tfn(:,i);
    else
        Tfa(:,i)=Tfn(:,i);
    end
end

Tout_avg=trapz(tf(1:m/2),Tf(n+1,1:m/2)')/(tf(m/2,1)-tf(1,1));
eff=(TH-Tout_avg)/(TH-TC);
U=mdot_amp*cf(1,1)*tau/(2*Ac*L*(1-eps)*rhor*cmuoH(1,1));
Crat=Ac*L*(1-eps)*rhor*cmuoH(1,1)/(mdot_amp*cf(1,1)*tau/2);

%Calculate regenerator bed capacity
for i=1:n
    dcapr(i)=trapz(tr,cmuoH(i,:))/tau;
end
capr=sum(dcapr)*rhor*Ac*L/n;
```

```
%Calculate parameters for lumped heat capacitance corrections
V=Ac*L;
crtot=mean(mean(cmuoH));
cftot=mean(mean(cf));
Cr=rhor*V*(1-eps)*crtot;
Cf=rhof*V*(eps)*cftot;
R=Cf/Cr;
lambda=tau*L_flow/(L*n_beds);
U=mdot_amp*cftot*lambda/(Cr+Cf);
NTU=Nuf(1,19)*kf(1,19)*Ac*L*as/(dh*mdot_amp*cf(1,19));

for i=1:(n+1)
   hflux(i,1)=sum(mdot.*hf(i,:)')*tau/m;
   sflux(i,1)=sum(mdot.*sf(i,:)')*tau/m;
end
%Calculate energy loss due to pressure drop across the bed and pumping
%power
v=mdot/(Ac*rhof);
alpha=(1-eps)^2/eps^3;
beta=(1-eps)/eps^3;
A=180; %for Ergun model from Fand et al
B=1.8; %for Ergun model from Fand et al
for j=1:m
    dP(:,j)=abs(ff(:,j).*mdot(j)^2/(2*rhof*Ac^2)*L/(n*dh)); %delta P in Pa
    dWpump(:,j)=abs(mdot(j)/rhof*dP(:,j)); %W

dP_ergun(:,j)=(A*alpha*muf(:,j)/dh^2*abs(v(j))+B*beta*rhof/dh*v(j)^2)*L/n;
%Pa
end
deltaP=sum(dP,1);
deltaP_ergun=sum(dP_ergun,1);
Wpump=sum(sum(dWpump,1),2)*tau/m; %J
%Calculate Energy Change due to Thermal Entropy Change per cycle
for j=1:m
    dQentt(:,j)=(Tr(:,j+1)-Tr(:,j)).*L/n*Ac*(1-eps)*rhor.*cmuoH(:,j);
end
Qentt=sum(sum(dQentt,1),2);

%Calculate Energy Change due to Magnetic Entropy Change per cycle
for j=1:m
    dQent(:,j)=Ac*(1-
eps)*rhor*((Tr(:,j+1)+Tr(:,j))/2).*dsdmuoH(:,j).*(muoH(:,j+1)-muoH(:,j))*L/n;
end
Qent=sum(sum(dQent,1),2);

%Calculate Heat Loss Per Cycle Due to Hysteresis
for j=1:m
    dQloss(:,j)=-Ch*Ac*(1-eps)*rhor.*vM_irr(:,j).*abs(muoH(:,j+1)-
muoH(:,j))*L/n;
end
Qloss=sum(sum(dQloss,1),2);

%calculate total cooling in the cycle (J) and cooling rate (W)
ref_load=-hflux(n+1); %J
ref_cap=ref_load/tau/1000*n_beds %kW
```

```
%calculate heat rejection in the cycle (J) and heat rejection rate (W)
heat_load=-hflux(1); %J
heat_rej=heat_load*n_beds/tau/1000 %kW
Wmag=heat_load-ref_load-Wpump;%hflux(n+1)-hflux(1);
Wmotor=(Wmag)/n_motor;

%Calculate COP from cooling power, magnetic work and pump work
COP=ref_load/(Wmotor+Wpump/n_pump)
COP_h=heat_load/(Wmotor+Wpump/n_pump)
COP_Carnot=(TC)/(TH-TC);
```

Part 2

A 2-D NUMERICAL MODEL TO DETERMINE THE IMPACT OF REGENERATOR HOUSING HEAT CAPACITY ON ACTIVE MAGNETIC REGENERATIVE REFRIGERATORS

Abstract

Magnetic refrigeration is based on the magnetocaloric effect, which couples the entropy in a magnetic material to a change in magnetic field. Consequently, a magnetocaloric material may be used as the thermodynamic working fluid in a cycle that produces refrigeration. The magnetocaloric effect is highest around the Curie temperature and may produce a maximum adiabatic temperature change of about 2K/Tesla. Because this temperature change is too small for any practical refrigeration application, the concept of an Active Magnetic Regenerative Refrigeration (AMRR) system was introduced as a means of producing a larger temperature lift. Pecharsky et al. [1] provide a thorough background of the magnetocaloric effect, magnetic refrigeration, and the AMRR cycle.

The performance of the AMRR cycle is highly dependent on the heat transfer coefficient between the heat transfer fluid and the magnetic material, which is typically represented in terms of a Nusselt number. When operating at room temperature, these systems generally require high Prandtl number fluids and operate at low Reynolds numbers ($Re <$ 100). Since the heat transfer coefficient is a function of Reynolds number and Prandtl number, correlations are used to determine the Nusselt number. However, Nusselt number correlations for flow through a packed bed are typically determined using a gaseous test fluid with a moderate Prandtl number and high Reynolds number. Few correlations exist for high Prandtl, low Reynolds number flows and therefore these moderate Prandtl number correlations are often used in AMRR models to determine the heat transfer coefficient. Frishmann et al [2] discuss the difficulty in determining the Nusselt correlations for high Prandtl number fluids when the Reynolds number becomes relatively low ($Re < 10$) and suggest that at such low Reynolds numbers, the heat capacity of the regenerator housing can have a large impact on the behavior of the regenerator. Nielsen et al. developed a 2-D transient model of a passive magnetic regenerative regenerator system in order to examine the impact of the regenerator housing on the behavior of the device and therefore on the measurement of the Nusselt number using single-blow type testing [3]. It was concluded that at low Reynolds numbers, the regenerator wall housing reduced the regenerator's effectiveness by as much as 18%.

A 2-D, transient numerical model of an active magnetic regenerative refrigeration system has been developed based on the 2-D passive model developed by Nielsen. The model couples the working heat transfer fluid with the regenerator housing heat capacity. The key modification presented in this project is the addition of the magnetocaloric effect to the regenerator solid. The numerical model is then used to quantify the cycle performance of the AMRR with respect to the housing heat capacity.

Nomenclature

ΔP	Pressure drop [Pa]	nr	Number of radial nodes
ΔT_{ad}	Adiabatic temperature change [K]	nt	Number of timesteps
Δr_j	Spacing between radial nodes [m]	nx	Number of axial nodes
ΔS_M	Magnetic entropy change [J/kg-K]	ρ	Density [kg/m^3]
Δt	Time change between nodes [s]	Pr	Prandtl number
Δx	Spacing between axial nodes [m]	$\dot{q}$	Heat transfer rate[W]
$\Delta V_{i,j}$	Volume of grid cell at location i, j [m^3]	Q_{ref}	Refrigeration load [J]
α	Thermal Diffusivity [m^2/s]	Q_{rej}	Heat rejection [J]
A_C	Cross-sectional area [m^2]	r	Radial direction
c	Specific heat [J/kg-K]	$R_{f,s}$	Radius of fluid-solid domain [m]
CFL	Courant-Friedrichs-Lewy Number	R_w	Radius of wall domain [m]
COP	Coefficient of Performance [-]	r_j	Radial location at j [m]
d_h	Hydraulic diameter [m]	Re	Reynolds number
d_p	Diameter of bed sphere [m]	s	Entropy [J/kg-K]
δ	Thermal wave propagation fraction [-]	T	Temperature [K]
ε	Porosity [-]	t_{sim}	Simulation time [s]
h	Convective heat transfer coefficient [W/(m-K)]	u	Velocity [m/s]
k	Thermal conductivity [W/(m-K)]	μ	Dynamic viscosity [Pa-s]
k_{disp}	Thermal dispersion [W/(w-K)]	$\mu_0 H$	Magnetic field strength [Tesla]
k_{stat}	Static thermal conductivity of bed [W/(w-K)]	x	Axial direction
L	Length of regenerator [m]	W_{mag}	Magnetic Work [J]
$\dot{m}$	Mass flow rate [kg/s]	φ	Thermal Utilization [-]
Nu	Nusselt number	ψ	Thermal mass ratio [-]

1 Introduction

Warburg discovered the magnetocaloric effect (MCE) in 1881 after noticing that there was a resulting temperature change in iron when an external magnetic field was applied [4]. However, it wasn't until 1926 and 1927 when Debye [5] and Giauque [6] independently explained the MCE in detail and proposed the first practical use of this effect. The process, known as adiabatic demagnetization, was suggested to reach ultra-low temperatures (below 1K). In 1933 Giauque and MacDougall [7] experimentally proved that ultra-low temperatures were attainable with the MCE by cooling $Gd_2(SO_4)_3 \cdot 8H_2O$ to 0.25K. In recent years, there has been a great deal of interest in using the MCE not only cryogenic refrigeration but also room temperature refrigeration.

1.1 The Magnetocaloric Effect

The First Law of Thermodynamics for a closed system gives the following differential energy balance:

$$\delta Q_{in} = \delta W_{out} + dU \tag{1.1}$$

where δQ_{in} is the differential amount of heat transferred into the system, δW_{out} is the differential amount of work done by the system, and dU is the differential change in internal energy of the system. There are many different types of work that can be done on a system: mechanical, electrical, magnetic, chemical, etc. By substituting in the

definition of mechanical work and the Second Law of Thermodynamics, Equation 1.1 can be rewritten in terms of the well known Fundamental Property Relation:

$$dU = TdS - PdV \tag{1.2}$$

It can be seen that the variables used to appropriately substitute for heat and work in Equation 1.2 are the product of an extensive property and an intensive property of the system. The heat transfer is defined as the product of the intensive property, temperature, and the extensive property, entropy. Similarly, mechanical work is defined by the product of the intensive property, pressure, and the extensive property, volume. These pairs of variables are defined as the canonically conjugate thermodynamic variables [8] and can be used to define other energy transfers such as magnetic work. Guggenheim defined magnetic work as the product of applied magnetic field ($\mu_0 H$) and magnetic moment (VM) [9]. Rewriting Equation 1.2 in terms of the magnetic work gives:

$$dU = TdS + \mu_0 Hd(VM) \tag{1.3}$$

A comparison can be made between terms in Equations 1.2 and 1.3 such that applied magnetic field is analogous to pressure of a mechanical system and magnetic moment is analogous to the inverse of volume. Note the difference in signs in Equations 1.2 and 1.3 is due to the fact that mechanical work is required to decrease the volume of a compressible substance however magnetic work is required to increase the magnetic moment of a paramagnetic material.

This analogy between mechanical work and magnetic work can be extended further. In the isothermal compression and expansion of a gas, the entropy will increase as the gas is being compressed and will decrease as the gas is being expanded. Similarly, as a paramagnetic material is being isothermally magnetized, the magnetic moments become aligned and the entropy will decrease. When the material is isothermally demagnetized, the entropy will increase back to its zero field entropy state. The parallelism between mechanical work and magnetic work make it possible to use certain thermodynamic results usually constrained to pure compressible substances such as Maxwell's relations. Therefore, temperature-entropy plots of magnetic materials will have the same qualitative profile as pure compressible substance. For a magnetocaloric material such as pure Gadolinium, a temperature-entropy plot will display lines of constant applied magnetic field as seen in Figure 1.

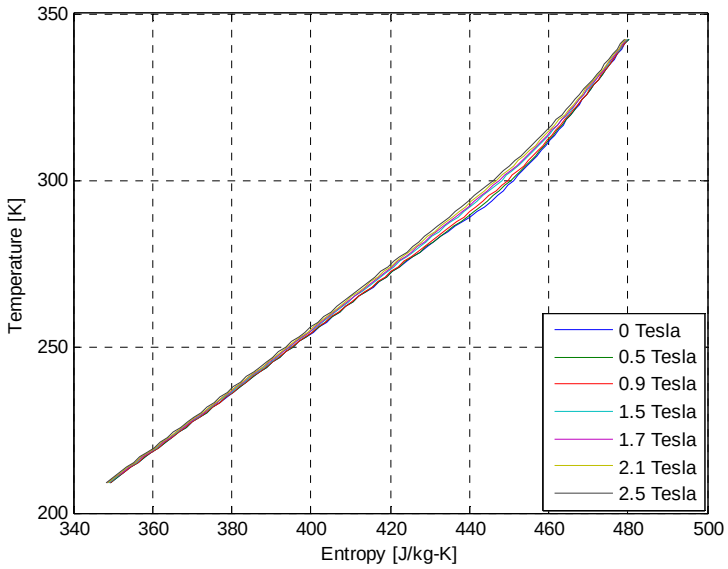

Figure 1: T-s diagram for Gadolinium

It can be seen from Figure 1 that adiabatic magnetization leads to a temperature increase in the Gadolinium. However, it is clear that the magnetization effects in pure Gadolinium do not produce very large temperature changes and therefore magnetocaloric material such as $Gd_{94}Er_6$ seen in Figure 2, are used.

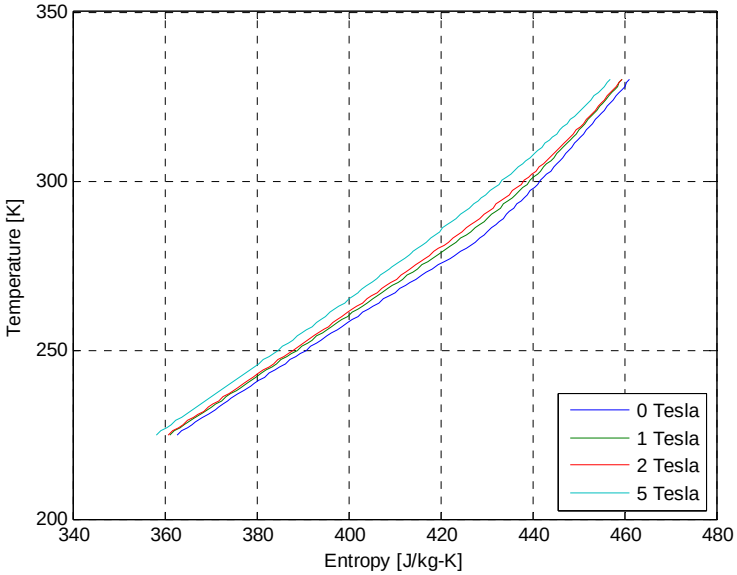

Figure 2: T-s diagram for $Gd_{94}Er_6$

The corresponding adiabatic magnetization of $Gd_{94}Er_6$ for varying magnetic field changes can be seen in Figure 3. There are a few interesting consequences of the magnetocaloric effect. First, as the change in magnetic field strength increases, the adiabatic temperature change also increases. In addition, the magnitude of the adiabatic temperature change depends on the initial temperature of the material. The temperature where the adiabatic temperature change is at a maximum is known as the Curie temperature.

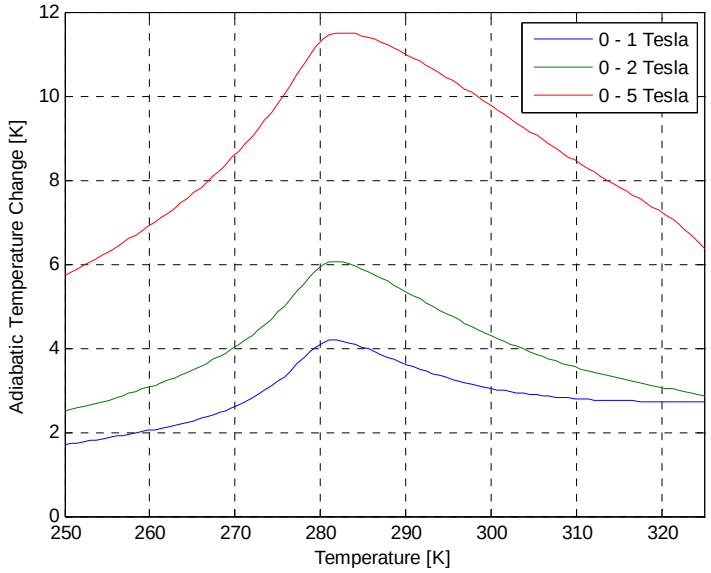

Figure 3: Adiabatic temperature lift in $Gd_{94}Er_6$

1.2 Magnetic Refrigeration

Adiabatic Demagnetization Refrigeration Cycle (ADR)

When Giauque and MacDougall experimentally proved that ultra-low temperatures were attainable with the MCE they did so by using the adiabatic demagnetization refrigeration (ADR) cycle. As previously mentioned, the magnetic work term is synonymous with mechanical work and therefore it is appropriate to assume a parallelism between the ADR cycle and the vapor compression refrigeration cycle. For the ADR cycle there are four main processes that occur and are illustrated in Figure 4 and summarized below:

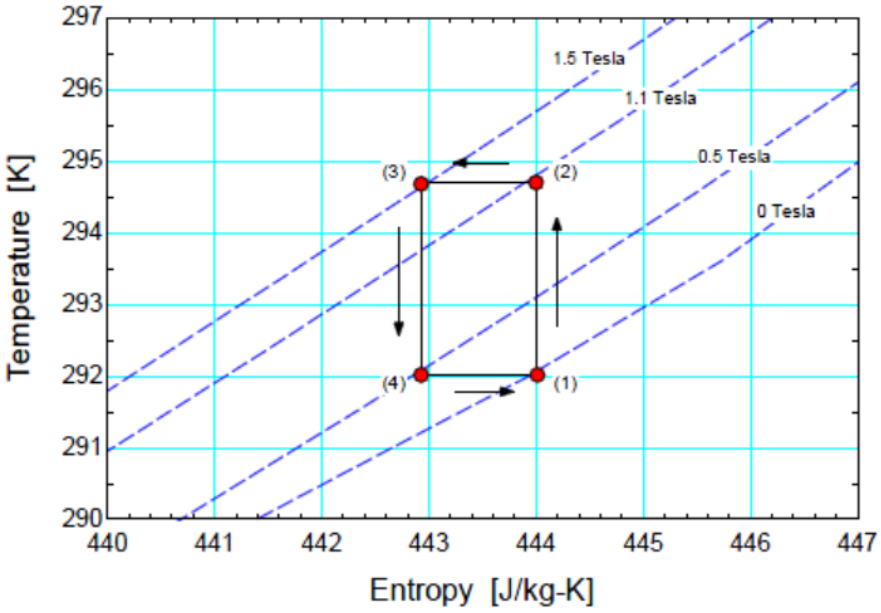

Figure 4: ADR cycle [10]

i. Adiabatic magnetization (Process 1 → 2): When the magnetocaloric material is magnetized the magnetic dipoles in material to align and consequently leads to a decrease in the entropy. However since the magnetization process is adiabatic, the temperature of the magnetocaloric material increases.

ii. Isothermal heat rejection (Process 2 → 3): Heat is removed isothermally and rejected to the hot reservoir which causes the entropy of the MCM to decrease.

iii. Adiabatic demagnetization (Process 3 → 4): The material is partially demagnetized adiabatically until it reaches the temperature of the cold reservoir.

iv. Isothermal heat addition (Process 4 → 1): Heat is added isothermally to the MCM from the cold reservoir.

The ADR cycle is considered a one-shot refrigeration cycle and has several drawbacks. During the isothermal heat rejection/addition processes, the magnetic field must be modified in order to properly achieve the constant temperature. This is a major drawback to the ADR cycle mainly due to the level of complexity required to adjust the magnetic field while maintaining isothermal conditions. In addition, the temperature change in the cycle is limited to the adiabatic temperature difference of the magnetocaloric material.

Active Magnetic Regenerative Refrigeration (AMRR) Cycle

The active magnetic refrigeration (AMR) cycle is a modified version of the ADR cycle. In the AMR cycle, process 2 → 3 is no longer an isothermal heat rejection process. Instead, heat rejection occurs at a constant magnetic field instead of at a constant temperature. In addition, process 4 → 1 occurs at a constant magnetic field instead of a constant temperature. The AMR cycle is seen in Figure 5 and summarized below.

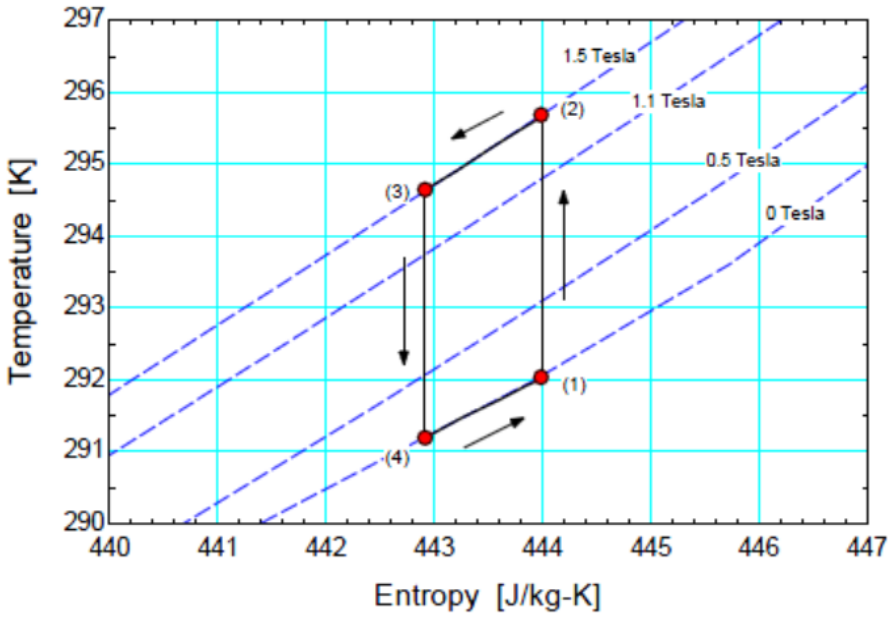

Figure 5: AMR cycle [10]

i. Adiabatic magnetization (Process 1 → 2): When the magnetocaloric material is magnetized the magnetic dipoles in material to align and consequently leads to a decrease in the entropy. However since the magnetization process is adiabatic, the temperature of the magnetocaloric material increases.

ii. Isofield heat rejection (Process 2 → 3): Heat is removed at a constant magnetic field and rejected to the hot reservoir which causes the entropy and temperature of the MCM to decrease.

iii. Adiabatic demagnetization (Process 3 → 4): The material is partially demagnetized adiabatically until it reaches the temperature of the cold reservoir.

iv. Isofield heat addition (Process 4 → 1): Heat is accepted from the cold temperature at a constant magnetic field which causes the entropy and temperature of the MCM to increase.

For an AMR cycle at room temperature, the maximum possible temperature lift is limited to the adiabatic temperature change of the magnetocaloric material. For a material such as pure Gadolinium, the adiabatic temperature change at the Curie temperature is approximately 3.5 K. For a single cycle, this temperature lift is not useful for room temperature refrigeration applications. In order to overcome this limitation, the MCM was incorporated into a regenerative heat exchanger. The magnetocaloric material is arranged into a porous matrix and packed into a casing. The casing is exposed to a magnetic field and a heat transfer fluid is passed over the MCM to accomplish the cycle mentioned above. By cascading the fluid over the matrix of magnetocaloric materials, a larger temperature lift can be established. This cycle is known as the active magnetic regenerative refrigeration cycle (AMRR).

1.3 Research Objectives

The primary goal of this project is to determine a way of quantifying the effects of the housing heat capacity on the performance of an AMRR system. Currently, there is no numerical model that couples the wall of the active magnetic regenerator to the heat transfer fluid and/or regenerator solid. There are 1-D numerical models of AMRR systems such as the one presented by Engelbrecht [11] but these does not include the regenerator housing and assume adiabatic boundary conditions. There is a 2-D numerical model of passive regenerators such as the one presented by Nielsen [3] that includes the housing effects but does not incorporate the magnetocaloric effect. In order to accomplish the main objectives of this project, the passive numerical model developed by Nielsen will be augmented to include the magnetocaloric effect. In doing so, this 2-D passive model will become a 2-D active model which allows for the study of the walls effect on the regenerator performance. Once the numerical model is validated, the overall effect of the housing on the regenerator needs to be quantified. A non-dimensional approach is used as a means of generalizing the effects by relating the wall properties to the regenerator properties.

2 Numerical Model

2.1 Geometry

The regenerator geometry for this numerical model is cylindrical with an axis of symmetry about the centerline corresponding to a radial location $r = 0$. A 2-D grid, shown in Figure 6 (not to scale), is used to represent a cut plane in the cylinder where the bottom boundary represents the axis of the cylinder, the left boundary and right boundaries are the cold and hot sides of the regenerator respectively, and the top boundary designates the outer edge of the housing wall.

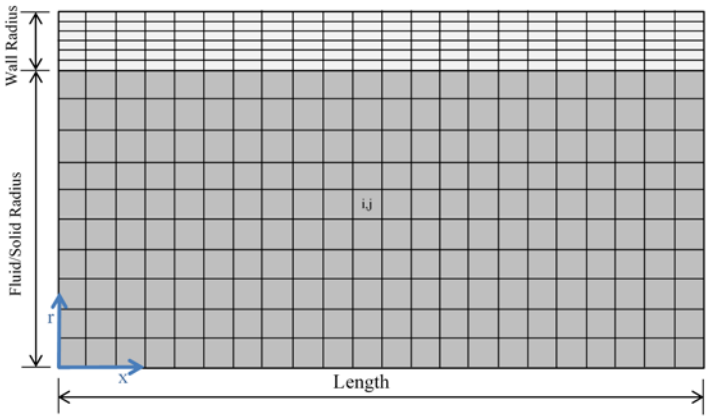

Figure 6: Grid

The grid is subdivided into three major domains: the housing wall domain, the regenerator solid domain, and the fluid domain. The housing wall domain lies within the radial coordinates, $R_{f,s} \leq r \leq (R_{f,s} + R_w)$, while the fluid and regenerator solid domains lie within the radial coordinates, $0 \leq r \leq R_{f,s}$, for all axial locations. Since the geometry is inherently cylindrical, each cell has a volume defined as:

$$\Delta V_{i,j} = 2\pi r_j \Delta r_j \Delta x \tag{2.1}$$

The *i* index corresponds to the nodal location in the axial direction and the *j* index corresponds to the nodal location in the radial direction. Note that the nodal locations (*i, j*) are cell-centered.

2.2 Governing Equations

The foundation of this numerical model is based on a 2-D transient passive regenerator model developed by Nielsen. The passive model has been modified by integrating the magnetic work term presented by Engelbretcht [11] into the governing equations. Since there are three domains present in this model, a coupled set of partial differential equations is needed to define the temperature distribution in the fluid, regenerator and regenerator housing. Energy balances around the fluid nodes, regenerator solid nodes, and wall nodes are performed. Figure 7 illustrates a differential control volume about a fluid node at location *(i,j)*.

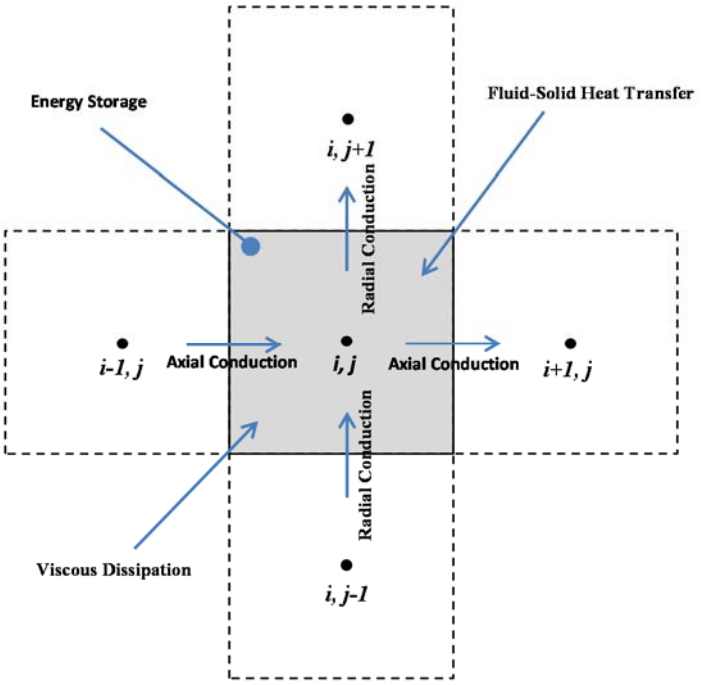

Figure 7: Control volume energy balance on fluid node

After simplification, the energy balance for the fluid node suggested by Figure 7 is:

$$\varepsilon\rho_{f_{i,j}}c_{f_{i,j}}\Delta V_{i,j}\left(\underbrace{\frac{T_{f_{i,j}}^{n+1}-T_{f_{i,j}}^{n}}{\Delta t}}_{energy\ storage}+\underbrace{u_{i,j}\frac{T_{f_{i+1,j}}^{n+1}-T_{f_{i-1,j}}^{n+1}}{2\Delta x}}_{convection}\right)$$
$$=\underbrace{D_{f_{i,j+1}}\left(T_{f_{i,j+1}}^{n+1}-T_{f_{i,j}}^{n+1}\right)}_{radial\ conduction\ i,j\rightarrow i,j+1}-\underbrace{D_{f_{i,j-1}}\left(T_{f_{i,j}}^{n+1}-T_{f_{i,j-1}}^{n+1}\right)}_{radial\ conduction\ i,j\rightarrow i,j-1}+\underbrace{D_{f_{i+1,j}}\left(T_{f_{i+1,j}}^{n+1}-T_{f_{i,j}}^{n+1}\right)}_{axial\ conduction\ i,j\rightarrow i+1,j}$$
$$-\underbrace{D_{f_{i-1,j}}\left(T_{f_{i,j}}^{n+1}-T_{f_{i-1,j}}^{n+1}\right)}_{axial\ conduction\ i,j\rightarrow i-1,j}+\underbrace{hA_{s_{i,j}}\left(T_{f_{i,j}}^{n+1}-T_{s_{i,j}}^{n+1}\right)}_{Convection\ between\ fluid\ and\ solid}+\underbrace{\left|\dot{g}_{v}'''\Delta V_{i,j}\right|}_{Viscous\ dissipation} \tag{2.2}$$

The terms $D_{f_{i,j+1}}, D_{f_{i,j-1}}, D_{f_{i+1,j}}$, and $D_{f_{i-1,j}}$ represent the thermal conductance's of the corresponding nodal locations and $\dot{g}_{v}'''$ represents the volumetric generation due to viscous dissipation. Definitions for these terms can be found in Appendix A. In the limit where the spatial domain becomes continuous (i.e. Δx → 0 and Δr → 0) and the timestep approaches zero, the following governing PDE emerges for the fluid domain:

$$\rho_f c_f \varepsilon\left(\frac{\partial T_f}{\partial t}+u\frac{\partial T_f}{\partial x}\right)=\frac{1}{r}\frac{\partial}{\partial r}\left(k_{disp,r}r\frac{\partial T_f}{\partial r}\right)+\frac{\partial}{\partial x}\left(k_{disp,x}\frac{\partial T_f}{\partial x}\right)-hA_s\left(T_f-T_s\right)+\left|\frac{\Delta P\dot{m}}{\rho_f L A_c}\right| \tag{2.3}$$

The terms from the left to the right represent: energy storage, convection, radial conduction, axial conduction, convection between the fluid and the solid and viscous dissipation.

Figure 8 illustrates a differential control volume about a regenerator solid node at location (i, j).

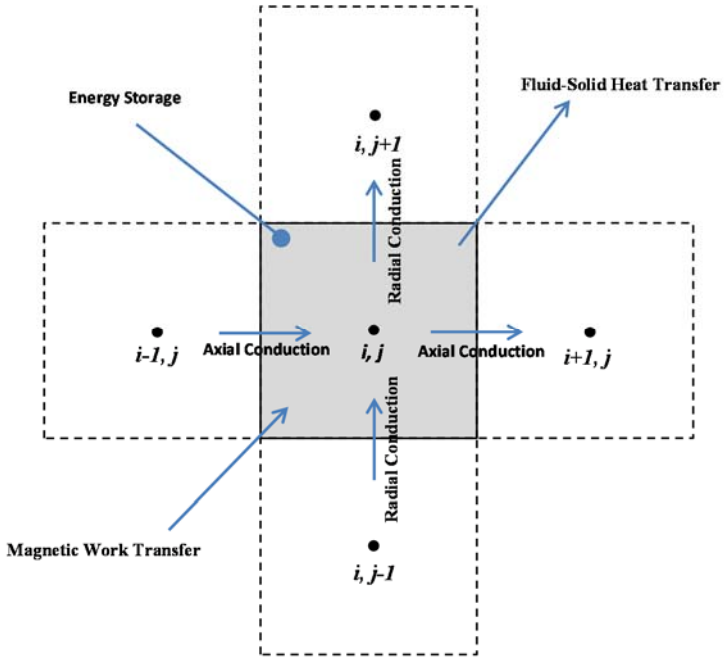

Figure 8: Control volume energy balance on solid node

The energy balance for the solid node suggested by Figure 8 reduces to:

$$(1-\varepsilon)\rho_{s_{i,j}} c_{s,\mu_o H_{i,j}} \Delta V_{i,j} \left(\underbrace{\frac{T_{s_{i,j}}^{n+1} - T_{s_{i,j}}^{n}}{\Delta t}}_{energy\ storage} \right) =$$

$$\underbrace{D_{s_{i,j+1}} \left(T_{s_{i,j+1}}^{n+1} - T_{s_{i,j}}^{n+1} \right)}_{radial\ conduction\ i,j \rightarrow i,j+1} - \underbrace{D_{s_{i,j-1}} \left(T_{s_{i,j}}^{n+1} - T_{s_{i,j-1}}^{n+1} \right)}_{radial\ conduction\ i,j \rightarrow i,j-1} + \underbrace{D_{s_{i+1,j}} \left(T_{s_{i+1,j}}^{n+1} - T_{s_{i,j}}^{n+1} \right)}_{axial\ conduction\ i,j \rightarrow i+1,j}$$

$$- \underbrace{D_{s_{i-1,j}} \left(T_{s_{i,j}}^{n+1} - T_{s_{i-1,j}}^{n+1} \right)}_{axial\ conduction\ i,j \rightarrow i-1,j} - \underbrace{D_{s_{i-1,j}} \left(T_{s_{i,j}}^{n+1} - T_{s_{i-1,j}}^{n+1} \right)}_{axial\ conduction\ i,j \rightarrow i-1,j} \tag{2.4}$$

$$+ \underbrace{hA_{s_{i,j}} \left(T_{f_{i,j}}^{n+1} - T_{s_{i,j}}^{n+1} \right)}_{Convection\ between\ fluid\ and\ solid} + \underbrace{(1-\varepsilon)\rho_{s_{i,j}} \Delta V_{i,j} \left[\frac{c_{s,\mu_o H_{i,j}}}{\Delta t} - \left(\frac{\partial s}{\partial \mu_o H} \right)_{T_{s_{i,j}}^{n}} \left(\frac{\partial \mu_o H}{\partial t} \right) \right]}_{Magnetic\ Work}$$

The $\left(\frac{\partial s}{\partial \mu_o H}\right)_{T_{s_{i,j}}^{n}}$ term is determined by interpolating experimental data for the specific magnetocaloric material that is being simulated. In addition, the $\left(\frac{\partial \mu_o H}{\partial t}\right)$ term is set in the operating conditions of the simulation, representing the applied magnetic field as a function of time. Definitions for $D_{s_{i,j+1}}$, $D_{s_{i,j-1}}$, $D_{s_{i+1,j}}$, and $D_{s_{i-1,j}}$ can be found in Appendix A. In the limit where the spatial domain becomes continuous (i.e. $\Delta x \rightarrow 0$ and $\Delta r \rightarrow 0$) and the timestep approaches zero, the following governing PDE emerges for the solid domain:

$$\rho_s c_{\mu_0 H}(1-\varepsilon)\left(\frac{\partial T_s}{\partial t} + \frac{T_s}{c_{\mu_0 H}} \frac{\partial s_r}{\partial \mu_0 H} \frac{\partial \mu_0 H}{\partial t}\right) = \frac{1}{r}\frac{\partial}{\partial r}\left(k_{stat} r \frac{\partial T_s}{\partial r}\right) + \frac{\partial}{\partial x}\left(k_{stat} \frac{\partial T_s}{\partial x}\right) + hA_s(T_f - T_s) \tag{2.5}$$

The terms from the left to the right represent: energy storage, magnetic work transfer, radial conduction, axial conduction, and convection between the fluid and the solid.

Figure 9 illustrates the differential control volume about a wall node at location (i, j).

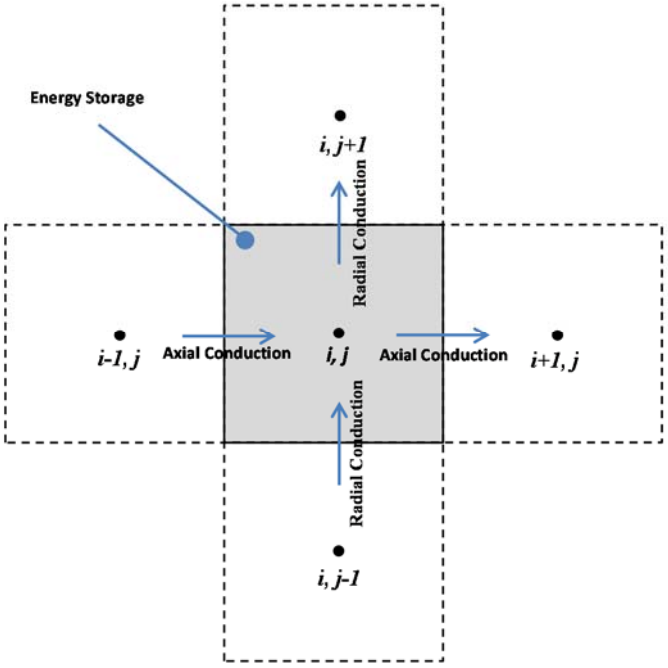

Figure 9: Control volume energy balance for wall node

The energy balance for the wall node suggested by Figure 9 is:

$$\rho_{w_{i,j}} c_{w_{i,j}} \Delta V_{i,j} \left(\frac{T_{w_{i,j}}^{n+1} - T_{w_{i,j}}^{n}}{\Delta t} \right) = \underbrace{D_{w_{i,j+1}} \left(T_{w_{i,j+1}}^{n+1} - T_{w_{i,j}}^{n+1} \right)}_{radial\ conduction\ \ i,j \rightarrow i,j+1} - \underbrace{D_{w_{i,j-1}} \left(T_{w_{i,j}}^{n+1} - T_{w_{i,j-1}}^{n+1} \right)}_{radial\ conduction\ \ i,j \rightarrow i,j-1} + \underbrace{D_{w_{i+1,j}} \left(T_{w_{i+1,j}}^{n+1} - T_{w_{i,j}}^{n+1} \right)}_{axial\ conduction\ i,j \rightarrow i+1,j} - \underbrace{D_{w_{i-1,j}} \left(T_{w_{i,j}}^{n+1} - T_{w_{i-1,j}}^{n+1} \right)}_{axial\ conduction\ i,j \rightarrow i-1,j} \tag{2.6}$$

Definitions for $D_{w_{i,j+1}}$, $D_{w_{i,j-1}}$, $D_{w_{i+1,j}}$, and $D_{w_{i-1,j}}$ can be found in Appendix A. In the limit where the spatial domain becomes continuous (i.e. $\Delta x \rightarrow 0$ and $\Delta r \rightarrow 0$) and the timestep approaches zero, the following governing PDE emerges for the wall domain:

$$\rho_w c_w \frac{\partial T_w}{\partial t} = \frac{1}{r} \frac{\partial}{\partial r} \left(k_w r \frac{\partial T_w}{\partial r} \right) + \frac{\partial}{\partial x} \left(k_w \frac{\partial T_w}{\partial x} \right) \tag{2.7}$$

The terms from the left to the right represent: energy storage, radial conduction, and axial conduction.

2.3 Boundary Conditions

As presented by Nielsen, the fluid equation is coupled to the wall equation by recognizing that the fluid is in contact with the wall at the radial location $r = R_{f,s}$ for all axial nodes. This condition can be described by the resistance network in Figure 10.

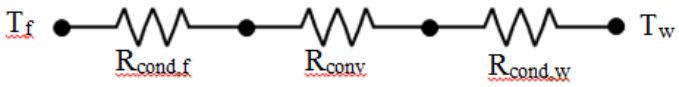

Figure 10: Resistance network at fluid-wall boundary

This resistance network acts in the radial direction and couples the wall nodes at the fluid/wall boundary to the corresponding fluid nodes. The equation for the net heat flux corresponding to this resistance network is given by:

$$\dot{q}_{fw,i} = \frac{T_{w_{i,1+nr,sf}}^{n+1} - T_{f_{i,nr,sf}}^{n+1}}{\frac{1}{2\pi(r_{nr,sf} + \Delta r_{nr,sf})\Delta x}\left(\frac{\Delta r_{1+nr,sf}/2}{k_{w_{i,1+nr,sf}}} + \frac{\Delta r_{nr,sf}/2}{k_{f_{i,nr,sf}}} + \frac{1}{h_w}\right)} \tag{2.8}$$

Here Δr is the distance between the fluid node and the wall node. In the limit where the heat transfer coefficient gets very large (i.e. $h_w \to \infty$) the resistance to convection goes to zero. This causes the thermal resistance between the fluid and the wall to be only a function of the conductivities of the materials. To incorporate this boundary condition into the numerical mode, Equation 2.8 is added to the right hand side of the governing fluid Equation 2.2 and subtracted from the right hand side of the wall Equation 2.6 at the appropriate radial locations. The remaining boundary conditions are summarized in **Table 1**, 2, and 3 where each table indicates the fluid, solid, and wall domain respectively. It should be noted that the boundary conditions for the fluid at the left and right boundaries depend on the sign of the mass flow rate. If the mass flow rate is positive, the fluid flows from the cold end to the hot end. Conversely, if the mass flow rate is negative, the fluid flows from the hot end to the cold end. The temperature T_C corresponds to the temperature at the cold side of the regenerator whereas T_H corresponds to the temperature at the hot side.

Table 1: Boundary conditions for fluid domain

	Radial Location	Axial Location	Boundary Condition
Bottom Boundary	$r = 0$	$0 < x < L$	*Adiabatic/Symmetry*
Top Boundary	$r = R_{f,s}$	$0 < x < L$	*See equation 2.8*
Left Boundary	$0 < r < R_{f,s}$	$x = 0$	$T_f = T_C$ *if* $\dot{m} > 0$ *Adiabatic if* $\dot{m} < 0$
Right Boundary	$0 < r < R_{f,s}$	$x = L$	*Adiabatic if* $\dot{m} > 0$ $T_f = T_H$ *if* $\dot{m} < 0$

Table 2: Boundary Conditions for solid domain

	Radial Location	Axial Location	Boundary Condition
Bottom Boundary	$r = 0$	$0 < x < L$	*Adiabatic/Symmetry*
Left Boundary	$0 < r < R_{f,s}$	$x = 0$	*Adiabatic*
Right Boundary	$0 < r < R_{f,s}$	$x = L$	*Adiabatic*

Table 3: Boundary conditions for wall domain

	Radial Location	Axial Location	Boundary Condition
Top Boundary	$r = R_{f,s}+R_w$	$0 < x < L$	*Adiabatic*
Left Boundary	$R_{f,s} < r < R_{f,s}+R_w$	$x = 0$	*Adiabatic*
Right Boundary	$R_{f,s} < r < R_{f,s}+R_w$	$x = L$	*Adiabatic*

2.4 Numerical Solution

Solution Algorithm

The temporal derivative is approximated using Euler's implicit method as seen in Equation 2.9. This results in a system of linear equations that can be written in matrix form as:

$$Ax = B \tag{2.9}$$

where A is a square coefficient matrix, x is a solution vector of all temperatures in the domains, and B is a vector containing the right hand side or known quantities. The coefficient matrix is a sparse matrix. The x vector contains all of the temperatures values at the next timestep and is set up as follows:

$$x = \begin{pmatrix} \begin{pmatrix} T_{1,1} \\ \vdots \\ T_{i,j} \\ \vdots \\ T_{nx,nr_{s,f}} \end{pmatrix}_f \\ \vdots \\ \begin{pmatrix} T_{1,1} \\ \vdots \\ T_{i,j} \\ \vdots \\ T_{nx,nr_{s,f}} \end{pmatrix}_s \\ \vdots \\ \begin{pmatrix} T_{1,1} \\ \vdots \\ T_{i,j} \\ \vdots \\ T_{nx,nr_w} \end{pmatrix}_w \end{pmatrix}^{n+1}$$

The coefficient matrix and the right hand side vectors are hardcoded and Equation 2.9 is solved directly using the Intel Math Kernel Library (MKL) which is capable of efficiently solving a non-symmetric, sparse system directly. The flowchart algorithm for the entire numerical model is seen in Figure 11. When the program is executed, an

input file with all the appropriate operation conditions is read and the code will execute commands according to those input parameters. Based on the input parameters, the model will simulate either the single blow mode or periodic steady state mode. When the model is set to perform a single blow operation, there is no iterative process. When the model is set to perform a periodic steady state operation, the code will iterate until its specified convergence criteria is met. This occurs when the heat flux at the cold and hot ends are equal at the initial and final time steps. Within the iteration loop is a time loop which captures the transient temperature variation over a specified simulation time. At the beginning of each time step, the model will calculate the temperature and magnetic field dependent properties based on the nodal temperature values from the previous time step. When all of the appropriate properties are determined, the code begins to assemble the coefficient matrix and right hand side vectors mentioned in Equation 2.9. The MKL direct sparse solver (DSS) requires the coefficient matrix be broken down into three separate 1-D arrays. Each array contains a different value that corresponds with the magnitude and location of each non zero element. The first 1-D has a size that corresponds to the total number of non-zero elements in the coefficient matrix. This array stores every non zero value in every row. The next 1-D array has the same size as the first array and includes the column number associated with each value that is stored in the first array. The final 1-D array includes the indexing for the first non-zero element in each row. The size of this array corresponds to the number of rows in the coefficient matrix and the value will match with the index of the first array that indicates the number is in the next row. When the entire program is compiled with the Intel Fortran Compiler, the entire code is vectorized which in combination with the MKL DSS, allows for this model to run quickly and efficiently.

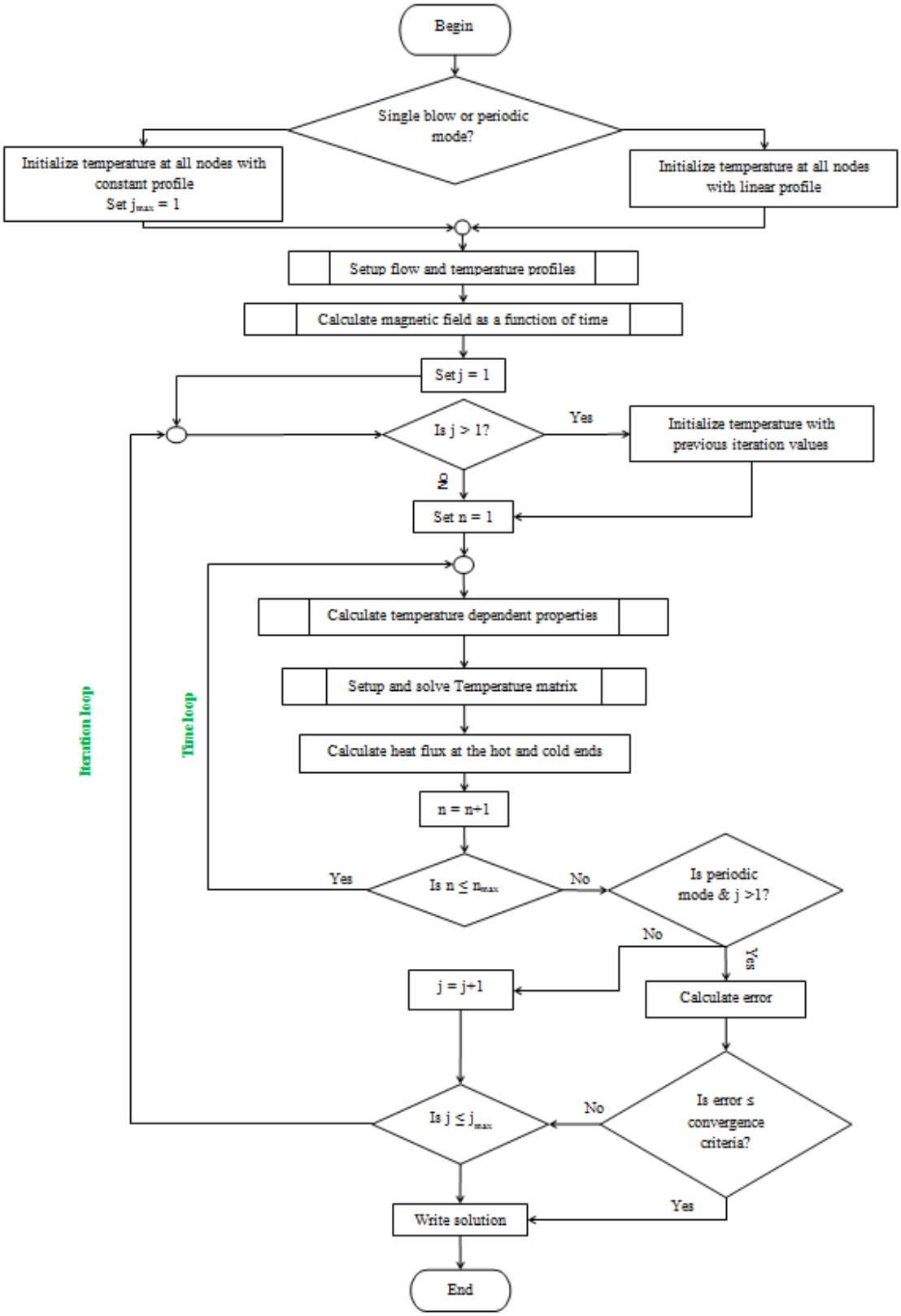

Figure 11: Flowchart of numerical model

Model Assumptions

There were several assumptions made when developing this numerical model. Below is a list of all the assumptions made:

i. The heat transfer fluid is incompressible (i.e. the density of the fluid remains constant and consequently the mass flow rate does not vary spatially within the regenerator)
ii. The regenerator bed has a uniform geometry (i.e. the porosity does not vary spatially)
iii. The magnetization and demagnetization process are assumed to be reversible (i.e. there is no hysteresis nor temperature gradients)
iv. Thermal properties variation per time step is negligible (i.e. temperature dependent properties are determined explicitly at the beginning on each time step based on the solution from the previous time step)
v. The wall interacts only with the heat transfer fluid (i.e. The regenerator and wall are coupled only through the fluid nodes and wall nodes)

2.5 Material Properties

Fluid Properties

The default heat transfer fluid used in this model is water assuming the fluid to be incompressible. For the simulations performed in the report, the thermophysical properties of water (c_f, ρ_f, k_f, and μ_f) are assumed to be constant. However, the numerical model has two options for dealing with property data. The first option is to assume the data is constant and the second option is to numerically interpolate the data to utilize temperature variant properties. The latter is useful since the numerical model calculates the temperature dependent properties at each time step. For water, the thermophysical properties that range around room temperature are nearly constant and therefore it is appropriate to assume so in the simulations. However, other heat transfer fluids that are being considered in AMRR applications do not have the same consistency as water and therefore it is necessary to include the interpolation.

Wall Properties

There are three wall material options that are built into the numerical model: plastic nylon, stainless steel, and aluminum. For the simulations presented in this report, the wall material chosen is nylon. Like the fluid properties mentioned above, the model defaults to assuming the wall properties are constant however there is the option to incorporate temperature varying property data for interpolation.

2.6 Magnetocaloric Material Properties

The magnetocaloric material (MCM) initially being studied in this model is commercial grade gadolinium. While pure gadolinium does not have a very strong magnetocaloric effect, it is the simplest MCM to incorporate into the numerical model. The property data of gadolinium, i.e. the temperature and entropy variation with respect to magnetic field strength was obtained from Engelbrecht and can be seen in Figure 12. Since the magnetocaloric

properties of the regenerator solid ($c_{\mu_0 H}$ and $\partial s/\partial \mu_0 H$) are functions of temperature and applied magnetic field, interpolation is required to ensure smooth property values.

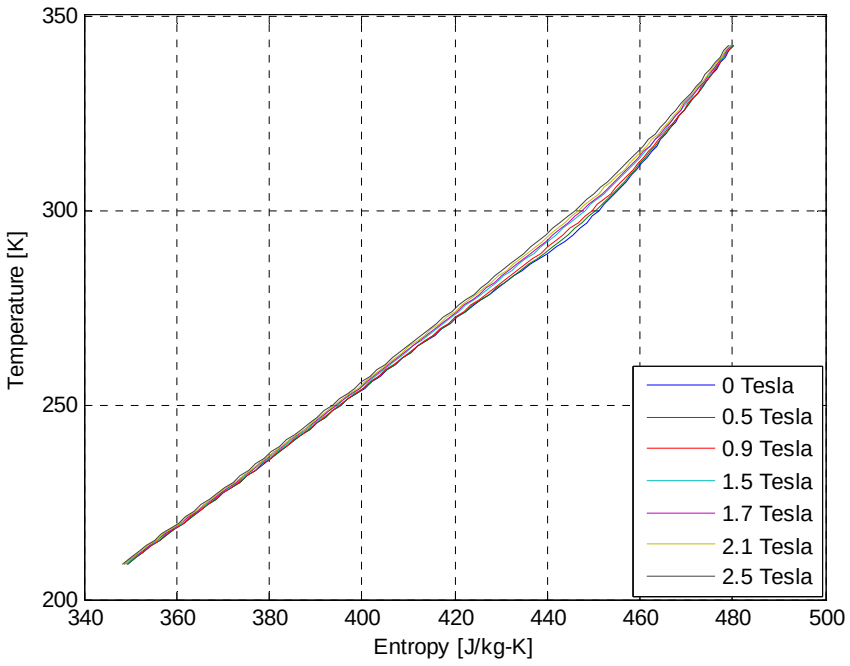

Figure 12: T-s diagram of Gadolinium

Interpolation of Property Data

Upon examination of Equation 2.5 we see that there are two important terms that quantify the magnetocaloric effect: the specific heat capacity at a constant magnetic field, $c_{\mu_0 H}$, and the partial derivative of entropy with respect to the magnetic field, $\left(\partial s/\partial \mu_0 H\right)_T$. In order to properly evaluate these terms at each nodal location for every time step, it is important to numerically differentiate entropy data for the specific material. The property data that are used in this model was obtained from Engelbrecht and provides the entropy of the material for a range of magnetic fields and temperatures.

Equation 2.10 is used to determine the specific heat capacity of the magnetocaloric material.

$$c_{\mu_0 H} = T\left(\frac{\partial s}{\partial T}\right)_{\mu_0 H} \tag{2.10}$$

The partial derivative of entropy with respect to temperature can be numerically differentiated using a second order central differencing:

$$\left(\frac{\partial s}{\partial T}\right)_{\mu_0 H} \cong \left(\frac{s_{\mu_0 H, T+\Delta T} - s_{\mu_0 H, T-\Delta T}}{2\Delta T}\right) \tag{2.11}$$

Here ΔT is a small but finite change in temperature that is a quantity smaller than the difference between two ascending temperatures present in the property data table. Similarly, the partial derivative of entropy with respect to magnetic field can be numerically differentiated using a first order differencing:

$$\left(\frac{\partial s}{\partial \mu_0 H}\right)_T \cong \left(\frac{s_{T,\mu_0 H+\Delta\mu_0 H} - s_{T,\mu_0 H}}{\Delta\mu_0 H}\right) \tag{2.12}$$

Again $\Delta\mu_0 H$ is a small but finite change in magnetic field strength that is a quantity smaller than the difference between two ascending magnetic field strengths present in the property data.

Since the values of ΔT and $\Delta\mu_0 H$ are chosen to be so small, the calculations of $s_{\mu_0 H,T+\Delta T}$, $s_{\mu_0 H,T-\Delta T}$, and $s_{T,\mu_0 H+\Delta\mu_0 H}$ require interpolation of the magnetocaloric property data to ensure smooth and accurate results. Two interpolation methods were investigated to determine which approach would provide the smoothest results: linear interpolation and bilinear interpolation.

The simplest way to compare the interpolation methods are to calculate the adiabatic temperature change of the magnetocaloric material when a magnetic field is applied. The numerical model calculates the adiabatic temperature change in the limit where there is no fluid flow, porosity, housing wall effects, nor conduction. Figure 13 displays the adiabatic temperature difference for varying temperatures when the magnetic field is changed from 0 to 1 Tesla.

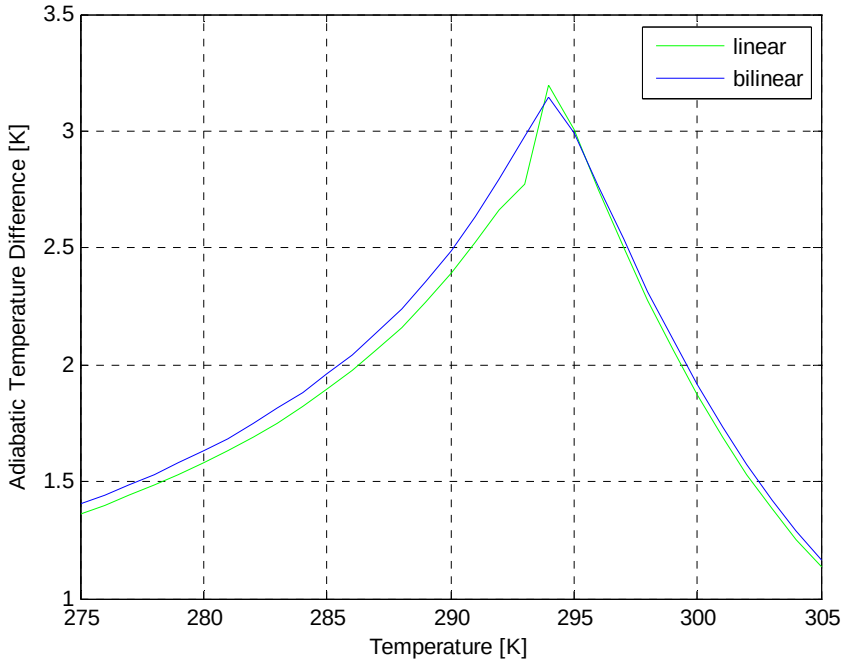

Figure 13: Comparison between linear and bilinear interpolation

It can be seen that near the Curie temperature, the linear interpolation is unable to smoothly resolve the peak in the temperature difference. Also, it seems that the linear interpolation method under predicts the temperature change before and after the Curie temperature. Based on the comparison, using a bilinear interpolation property data is a better option to ensure accuracy of the magnetocaloric effect.

2.7 Regenerator Correlations

The Nusselt number correlation established by Wakao and Kaguei [12] in Equation 2.13 is used in this numerical model.

$$Nu = 2 + 1.1Re_p^{0.6}Pr^{1/3} \tag{2.13}$$

Here the Reynolds number is a function of the particle sphere size, d_p, and is defined as follows:

$$Re_p = \frac{\rho_f u d_p \varepsilon}{\mu_f} \tag{2.14}$$

The heat transfer coefficient, h, is calculated using the Nusselt number.

$$h = \frac{k_f Nu}{d_h} \tag{2.15}$$

where, d_h symbolizes the hydraulic diameter which is a function of the regenerator sphere diameter and the porosity.

$$d_h = \frac{2}{3}\frac{\varepsilon}{1-\varepsilon}d_p \tag{2.16}$$

The Reynolds number of the fluid is a function of the hydraulic diameter and is computed as follows:

$$Re_f = \frac{\rho_f u d_h \varepsilon}{\mu_f} \tag{2.17}$$

The pressure drop across the regenerator bed was calculated using the Ergun equation [13] and is shown below:

$$\frac{dp}{dx} = A\frac{(1-\varepsilon)^2}{\varepsilon^2}\frac{\mu_f v}{d_p^2} + B\frac{(1-\varepsilon)}{\varepsilon^3}\frac{\rho_f v^2}{d_p} \tag{2.18}$$

Kaviany [14] suggests that A = 180 and B = 1.8 for smooth particles.

Effective Conductivity of the Regenerator

The fluid that moves through a porous medium is a complex, 3-D flow which makes it very difficult to calculate the velocity and temperature fields. To deal with this added complexity, a macroscopic or continuum approach via volume averaging is performed on the governing equations. During this averaging process, an additional term known as thermal dispersion appears in the equation. The thermal dispersion term can be written in the form of diffusion transport which depends on the thermal dispersion conductivity of the medium. When the governing equations are simplified, the thermal diffusion conductivity is lumped with the thermal conductivity of the porous continuum domain to give the effective thermal conductivity [15].

$$k_{eff} = k_{stat} + k_f D^d \tag{2.19}$$

Here, k_{stat} is the static effective thermal conductivity when there is no fluid motion and $k_f D^d$ is the thermal dispersion conductivity where D^d is a dispersion coefficient that is a function of the Peclet number. To calculate the static effective thermal conductivity, Hadley [16] suggested the following correlation for $\varepsilon < 0.58$:

$$k_{stat} = k_f \left[(1-\alpha_0) \frac{\varepsilon f_0 + \frac{k_s}{k_f(1-\varepsilon f_0)}}{1-\varepsilon(1-f_0)+\frac{k_s}{k_f \varepsilon(1-f_0)}} + \alpha_0 \frac{2\left(\frac{k_s}{k_f}\right)^2 (1-\varepsilon) + (1+2\varepsilon)\frac{k_s}{k_f}}{\frac{(2+\varepsilon)k_s}{k_f} + 1 - \varepsilon} \right] \tag{2.20}$$

Here, f_0 and α_0 are defined as follows:

$$f_0 = 0.8 + 0.1\varepsilon \tag{2.21}$$

$$\log \alpha_0 = -4.898\varepsilon \qquad for \qquad 0 \leq \varepsilon \leq 0.0827 \tag{2.22a}$$

$$\log \alpha_0 = -0.405 - 3.154(\varepsilon - 0.0827) \qquad for \qquad 0.0827 \leq \varepsilon \leq 0.298 \tag{2.22b}$$

$$\log \alpha_0 = -1.084 - 6.778(\varepsilon - 0.298) \qquad for \qquad 0.298 \leq \varepsilon \leq 0.580 \tag{2.22c}$$

Kaviany [14] suggested the calculation of the thermal dispersion conductivity in the axial direction of a uniformly packed bed of spheres as:

$$k_{disp,x} = k_f D^d = k_f \frac{3}{4} \varepsilon Re_f Pr \tag{2.23}$$

This equation is only valid for the Reynolds number range of $1 < Re_f < 10$. If the Reynolds number of the fluid is less than 1, then the dispersion assumption becomes negligible and the intrinsic fluid conductivity is used. Delgado [17] suggested that the dispersion in the radial direction is a function of the dispersion in the axial direction and is calculated as:

$$k_{disp,r} = \frac{1}{5} k_f \tag{2.24}$$

Like the equation for axial dispersion, Equation 2.24 is valid only within the range of $1 < Re_f < 10$. If the Reynolds number of the fluid is less than 1, then the radial dispersion value is the same as the axial dispersion value.

2.8 Model Validation

Passive Mode Verification

Several steps were taken in order to validate the numerical model. As previously mentioned, the AMRR model presented in this paper is an extension of the passive regenerator model developed by Nielsen. As such, several of the initial validation steps were performed by Nielsen and will be mentioned for completeness. The first step was to verify that the passive regenerator model accurately predicts the temperature distribution during a single blow operation. Nielsen shows that in the limit where there is no magnetocaloric effect, axial conduction, viscous dissipation, nor internal temperature gradients in the solid, the numerical model agrees with the Schumann solution [18] to within 0.3% accuracy when using 150 axial nodes and a CFL number of 0.1. The CFL number is defined in the model as:

$$CFL = \frac{\dot{m}\Delta t}{\rho_f \pi R^2 \varepsilon \Delta x} \tag{2.25}$$

Nielsen also compares the passive model to the regenerator effectiveness solution provided by Dragutinov and Baclic [19]. In this case, the numerical model assumes periodic boundary conditions, no entrained fluid heat capacity, no axial conduction, no dispersion, no viscous dissipation, and all thermal properties are constant. Using the same axial nodes and CFL number previously mentioned, it was shown that the model agrees with the analytical solution to within 0.3% accuracy.

Consistency of Numerical Model

Once the magnetic work term was incorporated into the model, it was important to verify that the passive mode (i.e. the original code) remained unchanged. One way to do this was to reproduce the effectiveness results of the 2-D passive regenerator with wall effects that were presented by Nielsen. If the mass flow rate and specific heat capacity of the fluid is constant, then the effectiveness of a passive regenerator is defined as follows:

$$effectivenss = \frac{\int_0^{t_{sim}/2}(T_H - T_{C,out})dt}{(T_H - T_C)\,t_{sim}/2} \tag{2.26}$$

In his paper, Nielsen uses several non-dimensional numbers to represent variation in specific operating conditions. The first non-dimensional number used is the thermal utilization:

$$\varphi = \frac{\dot{m}c_f}{2fm_sc_s} \tag{2.27}$$

where f is the operating frequency of the regenerator and is defined as $f = 1/t_{sim}$. The thermal utilization describes the ratio of the thermal mass of the fluid that is moved through the regenerator to the total thermal mass of the regenerator solid. The next non-dimensional number used is the ratio between the thermal mass of the wall to the thermal mass of the regenerator solid:

$$\psi = \frac{m_wc_w}{m_sc_s} \tag{2.28}$$

In addition to Equations 2.27 and 2.28, the Reynolds number seen in Equation 2.17 is used. Lastly, the dimensional number known as thermal diffusivity is used:

$$\alpha = \frac{k_w}{\rho_wc_w} \tag{2.29}$$

The following four operating conditions are varied and quantified by the aforementioned non-dimensional and dimensional quantities: mass flow rate ($\dot{m}$), wall thickness (W_{th}), simulation time (t_{sim}), and wall conductivity (k_w). Figure 14 displays a comparison between the original results from Nielsen's model and the results from the new model. This figure shows the effectiveness of the regenerator when running in passive, cyclic steady-state mode at varying Reynolds numbers for a range of wall to solid thermal mass ratios. It can be seen that by modifying the code to add the magnetocaloric material has not changed the results for passive regenerators.

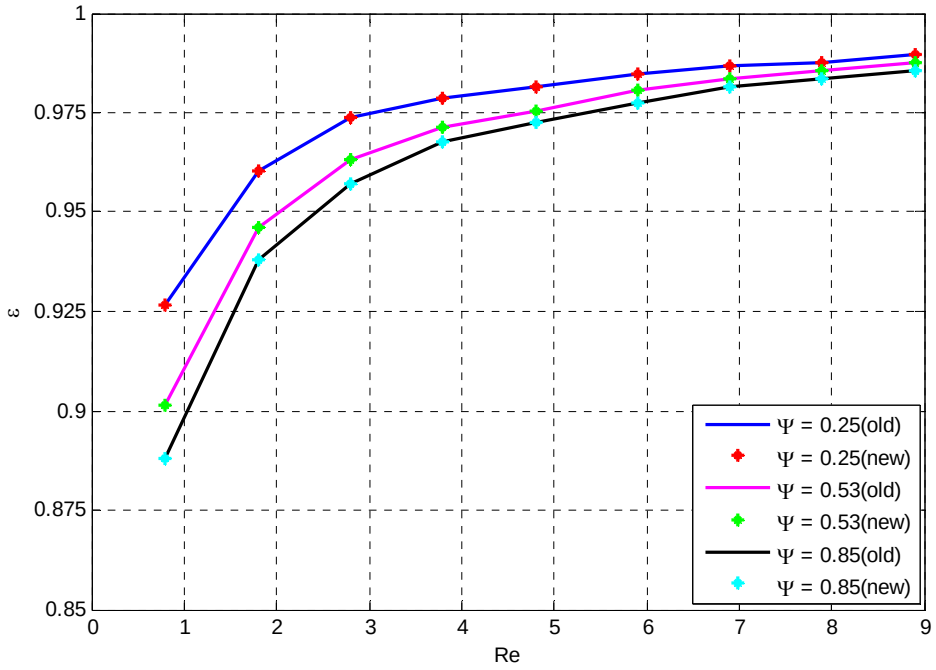

Figure 14: Check for comparison between old code and node code

Validation of Magnetic Work Interaction

The next step was to verify that the magnetic work term and the magnetocaloric property data were implemented correctly into the model. In general, magnetocaloric materials are characterized by the adiabatic temperature change produced when a magnetic field is applied. The adiabatic temperature change can be calculated with Equation 2.30:

$$\Delta T_{ad} = -\left(\frac{T}{c_{\mu_0 H}}\right)\Delta S_M \tag{2.30}$$

Here ΔS_M represents the magnetic entropy change:

$$\Delta S_M = \mu_0 \int_0^{H_{max}} \left(\frac{\partial s}{\partial H}\right)_T dH \tag{2.31}$$

The adiabatic temperature difference can be calculated independent of the numerical model and compared to the model results in the limit where there is no fluid flow, porosity, housing wall effects, nor conduction. When all of these limits are enforced in the numerical model, Equations 2.3 and 2.7 are effectively zero and therefore not solved in the numerical model. In addition, the right hand side of Equation 2.5 goes to zero, leaving only the energy storage and magnetic work transfer terms. Figure 15 displays the adiabatic temperature difference for varying temperatures when the magnetic field is changed from 0 to 1 Tesla. It can be seen that the numerical model computes the same results that the theoretical calculations predict. This shows that the magnetic work transfer term was properly incorporated into the numerical model and that the numerical interpolation of the magnetocaloric property data was handled correctly.

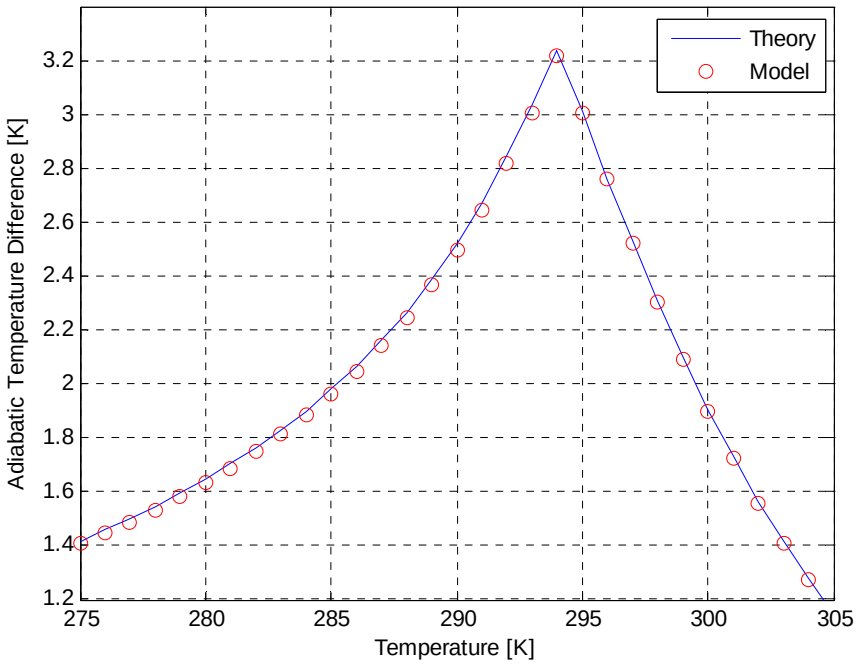

Figure 15: Comparison of adiabatic temperature difference between theory and model

Validation of Model

The final and most important step of the validation process was to compare the results of this numerical model to another well-established model. As previously mentioned, a 1-D AMRR model was developed by Engelbrecht. This model did not account for wall effects and was designed for a rotary AMRR system. In order to perform a comparison, the two numerical models were set to operate in similar conditions and the COP and Q_{ref} outputs were compared. Taking an energy balance on the cold end of the regenerator, the refrigeration load is defined as:

$$Q_{ref} = \sum_{n=1}^{nt} \dot{m}^n c_f^n \bar{T}_{f,i=1}^n \Delta t \tag{2.32}$$

where $\bar{T}_{f,i=1}^n$ is the area-weighted average of the fluid temperature at the cold end of the regenerator at time *n*. It should be noted that the superscript *n* always denotes the value at a specific time level. Similarly, the heat rejection can be calculated as follows:

$$Q_{rej} = \sum_{n=1}^{nt} \dot{m}^n c_f^n \bar{T}_{f,i=nx}^n \Delta t \tag{2.33}$$

where $\bar{T}_{f,i=nx}^n$ is the area-weighted average of the fluid temperature at the hot end of the regenerator at time *n*. To determine the COP, the magnetic work must be calculated by taking an energy balance on the entire regenerator which will provide Equation 2.34:

$$W_{mag} = Q_{rej} - Q_{ref} \tag{2.34}$$

From this, the COP can be calculated as:

$$COP = \frac{Q_{ref}}{W_{mag}} \tag{2.35}$$

The operating conditions used in both models are presented in **Table 4**. However, since the 1-D model was developed specifically for a rotary AMRR system, there are certain parameters that are not present in the model described in this report and can be seen in Table 5. For further understanding of the parameters listed in Table 5, please refer to reference [11].

Table 4: Operating conditions that are the same in both models

Operating Conditions	Value	Operating Conditions	Value
R [m]	0.0083	ρ_f [kg/m^3]	1000
L [m]	0.1	c_f[J/kg-K]	4200
$\mu_0 H$ [Tesla]	1.5	k_f[W/m-K]	0.6
ε [-]	0.36	T_C [K]	290
d_p[m]	0.005	T_H[K]	295
magnetocaloric material	Gd	t_{sim} [s]	0.5
ρ_s [kg/m^3]	7900	$\dot{m}$ [kg/s]	0.03
c_s [J/kg-K]	Based on prop. data	nx [-]	150
k_s [W/m-K]	10.5	nt [-]	578
fluid material	Water		

Table 5: Operating conditions that vary between both models

Operating Conditions	Engelbrecht's Model	Le Moine's Model
number of beds [-]	1	*N/A*
flow ramp period for fluid flow[s]	0.1	*N/A*
arc of magnet[°]	120	*N/A*
arc of ramp[°]	15	*N/A*
arc of each bed[°]	360	*N/A*
delay time[s]	15/360*t_{sim}	*N/A*
dwell ratio[-]	1/2	*N/A*

For this comparison the COP, refrigeration load, and heat rejections of both models were compared. The percent difference between the COP calculations is approximately 19.9% whereas the refrigeration load varied by only 0.9% and the heat rejection by 1.5%. Due to the fact that there are some inherent differences between the two models as seen in Table 5, the refrigeration load and heat rejection values are slightly different. While the differences are small, they ultimately lead to a large variance in the COP. This is due to the fact that the COP is a smaller number than the refrigeration power or heat rejection and therefore minor variations will lead to large percent differences. Thus, if we attribute the differences in refrigeration load and heat rejection to the intrinsic differences between the two models, we can conclude that if the two models were operating at exactly the same conditions, they would produce near similar results and the COP percent difference would be very small.

2.9 Grid Study

Before running case studies with the validated numerical model, it is important to determine the appropriate grid size and time step for the simulations. These parameters must be chosen to balance the total computational time required per simulation and the numerical accuracy of the results. If the number of spatial nodes in the computational domain is decreased, the computational time for each simulation will also decrease. However, as the number of spatial nodes becomes lower, the numerical accuracy of the solution begins to decline. It is therefore important ensure that the grid spacing is coarse enough to reduce the overall computational time for each simulation but also fine enough to ensure numerical accuracy. Similarly, the number of time steps for each simulation needs to be studied to make sure that the periodic steady state solution is accurate. The grid study was subdivided into three parts: determining the number of axial nodes, determining the number of radial nodes, and determining the CFL number (i.e. time stepping).

Number of Axial Nodes

Several cases were run at various values of axial nodes under the same operating conditions in order to determine the appropriate number of axial nodes. Table 6 provides a list of the operating conditions used for these cases:

Table 6: Operating conditions

Operating Conditions	Value	Operating Conditions	Value
R [m]	0.0083	ρ_f [kg/m^3]	1000
L [m]	0.1	c_f[J/kg-K]	4200
$\mu_0 H$ [Tesla]	1.5	k_f[W/m-K]	0.6
ε [-]	0.36	ρ_w [kg/m^3]	1000
d_p[m]	0.005	c_w[J/kg-K]	1500
magnetocaloric material	Gd	k_w[W/m-K]	0.25
ρ_s [kg/m^3]	7900	T_C [K]	290
c_s [J/kg-K]	Based on prop. data	T_H[K]	295
k_s [W/m-K]	10.5	t_{sim} [s]	0.5
fluid material	Water	$\dot{m}$ [kg/s]	0.03

For the passive regenerator model, Nielsen suggested that the radial nodes in both the fluid/solid and wall domains should be set to 10 and the CFL number to 0.5; therefore, these values are assumed for this grid study and verified later. Since the main value of interest for the regenerator is the efficiency, the COP will be used as the metric for the convergence study. The error in the COP is computed as the percent error between the COP predicted by the simulation relative to the COP predicted by the converged solution. The converged solution is obtained by modelling the same operating conditions with a very fine mesh that is much larger than the grids selected for the study. In this case, the converged solution was determined by setting the number of axial nodes to 500. Figure 16 shows the percent error in COP for various values of axial nodes. If the maximum allowable percent error for the COP is assumed to be 10 percent, then the smallest possible number of axial nodes is equal to 100.

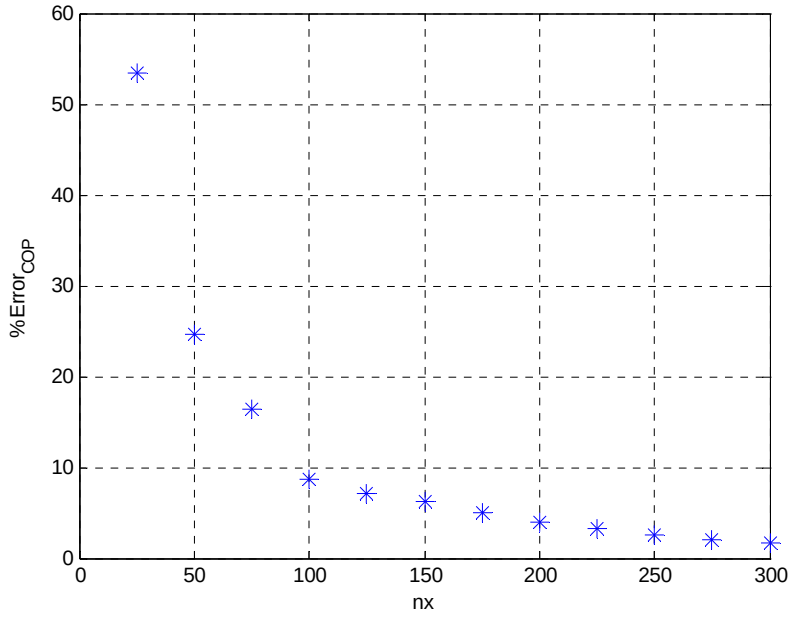

Figure 16: Axial node grid convergence

Number of Radial Nodes

The second grid sensitivity study examined the number of radial nodes in both the wall and fluid/solid domain. From this point forward the fluid/solid domain will be referred to as domain A and the wall domain will be referred to as domain B. Prior to this study, the nodes in domains A and B were both set to 10. As such the total number of equations solved in the numerical model becomes 3000 and is represented by the following equation:

$$N_{eq} = \left(2 * nx * nr_{s,f}\right) + \left(nx * nr_{w}\right) \tag{2.36}$$

Solving more equations (i.e. a finer grid) requires more computational time and therefore it was necessary to determine the minimum allowable number of radial nodes in both domains. Additionally, the radial nodes in domains A and B do not need to be the same and since the main focus of this project is to determine the impact of the wall on the regenerator performance, it would be beneficial to have more nodes in domain B than in A. This is important because the more nodes that there are in the wall domain, the more accurate the temperature distribution becomes. A grid study was performed that varied the number of nodes in domains A and B independently from each other. These numbers are varied from 3 to 10 and compared the percent error of COP values as well as the total CPU time. Figure 18 shows the percent error of the COP with respect to varying radial nodes in domains A and B. Here it can be seen that for all cases, the percent error of the COP is well below 10% with the maximum percent error being around 1.1%. From these results, it is clear that the number of radial nodes can be reduced in both domains. Before choosing the radial nodes for domains A and B, the computational time required for the different node options needs to be examined. Figure 18 shows the computational time required for each case corresponding to Figure 17. If the desired CPU time is under a minute, the corresponding values of nr_{sf} and nr_{w} that produce the greatest numerical accuracy are 4 and 5 respectively.

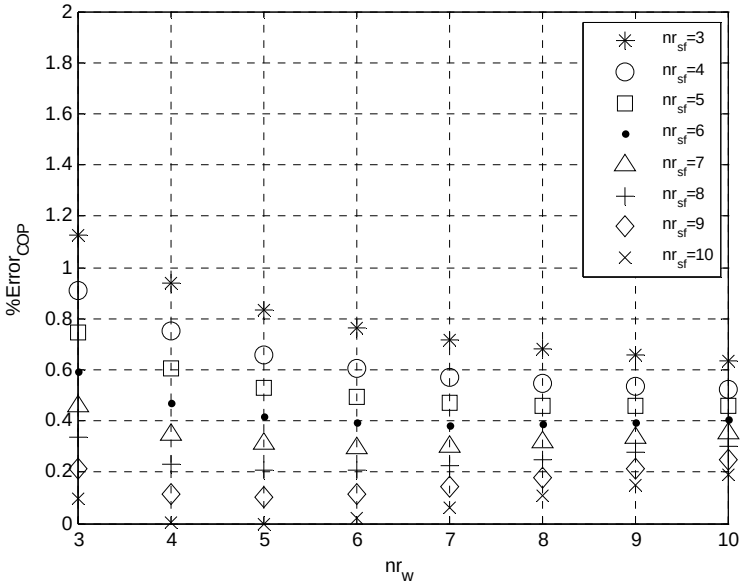

Figure 17: Radial node grid convergence

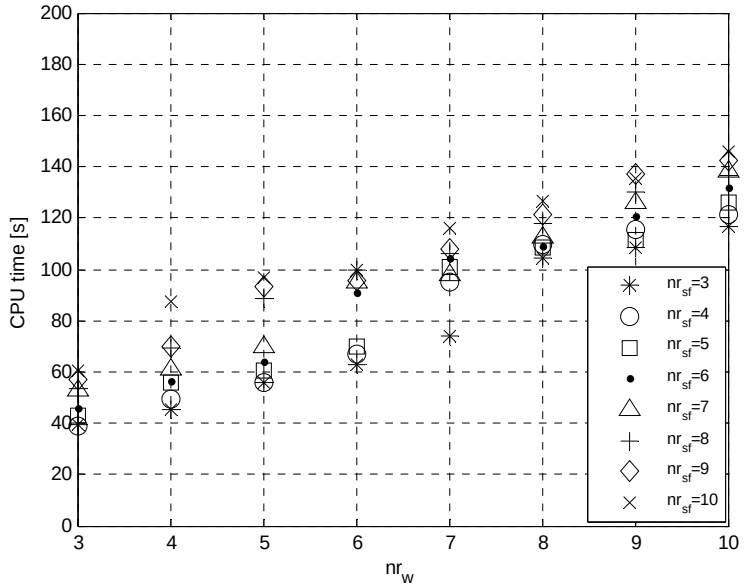

Figure 18: CPU time for corresponding radial node convergence study

CFL Number

Equation 2.37 defines the CFL condition, which is a way to relate the grid size to the number of timesteps:

$$CFL = \frac{u\Delta t}{\Delta x} \tag{2.37}$$

In Equation 2.37 u is the bulk fluid velocity, Δx is the spacing between axial nodes, and Δt is the time increment. For explicit solvers, the CFL condition is used to determine the largest allowable Δt that the solver needs to maintain numerical stability. The implicit solver used in this numerical model is unconditionally stable (i.e. there is no actual CFL criterion). Although the solver has no CFL criterion for stability, the value of CFL still affects the numerical

accuracy of the solution. The percent error of the COP was calculated for CFL numbers varying from 0.1 to 5. Figure 19 shows that at lower CFL numbers, the numerical accuracy of the solution increases. Assuming the allowable percent error to be 10%, the corresponding CFL number is equal to 0.35.

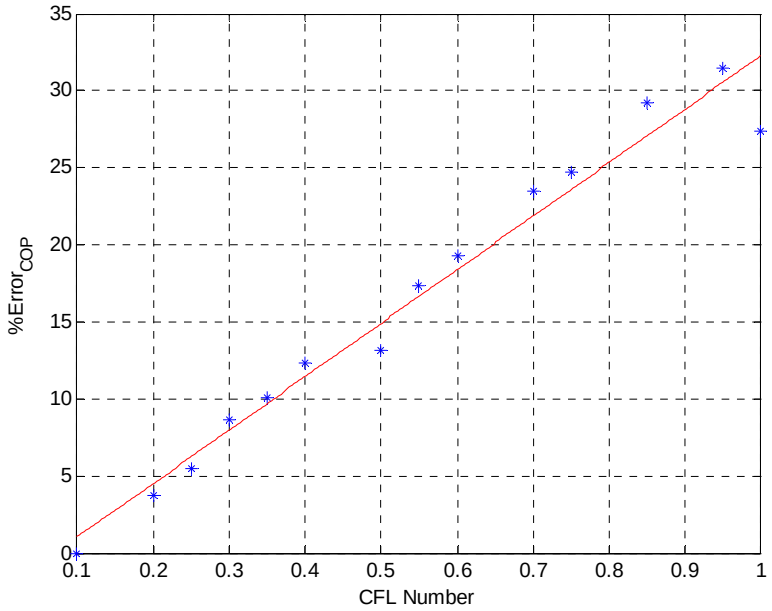

Figure 19: CFL number accuracy study

3 Parametric Study

3.1 Determination of Mass Flow Rate

As the mass flow rate applied to a magnetic refrigeration system of a specific size increases, the COP will tend to decrease because most losses will scale with mass flow rate. Conversely, the refrigeration capacity will first tend to increase with mass flow rate and then decrease once the bed performance becomes overwhelmed by the increasing losses. The refrigeration capacity will peak at a specific mass flow rate and as such there will be two mass flow rates which produce the same refrigeration capacity however the lower mass flow rate will correspond to a higher COP. It is interesting to understand how the housing would influence the COP and Q_{ref} curves. Figure 20 illustrates the refrigeration capacity and COP for the AMRR system represented by the operating conditions listed in Table 6 for the cases where thermal coupling with the wall was turned off and on. When the wall coupling is turned off, the wall equations are not solved and there is no coupling between the fluid domain and the wall domain. It can be seen that this particular system operates over the range of mass flow rates from 0.03 to 0.1 kg/s. When the wall coupling is turned on, both the COP and refrigeration capacity curves decrease in magnitude. The maximum decrease in the COP with respect to the no wall case is 7.5% and this at a small mass flow rate. As the mass flow rate increases, the percent decrease in the COP reaches a minimum value of 1.2% at around 0.08 kg/s. The maximum percent decrease in the refrigeration capacity is 2.9% at a mass flow rate of about 0.1 kg/s. As the mass flow rate decreases, the percent decrease ranges between 0.8% and 2.0%.

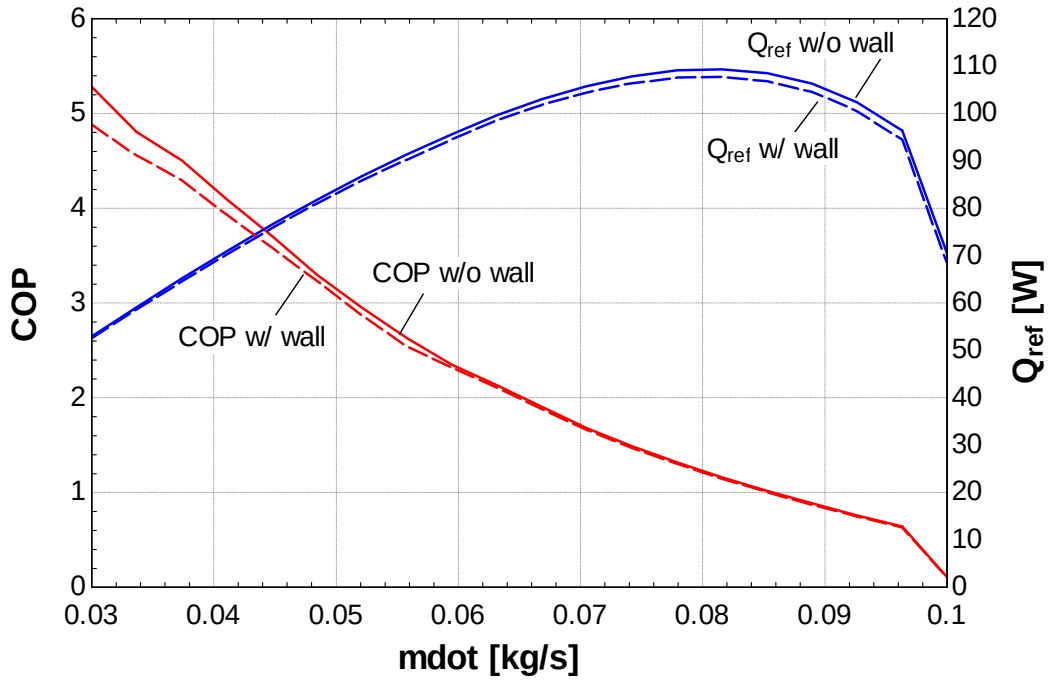

Figure 20: COP and refrigeration curve for k_w = 0.25 W/m-K

A second case was performed with the same operating conditions listed in Table 6. The only difference was that the thermal conductivity of the wall was increased to be 250 W/m-K. As in the previous figure, Figure 21 shows the refrigeration capacity and COP for various values of mass flow rate. Similar to the previous case, both the COP and refrigeration capacity curves decrease in magnitude when the wall coupling is turned on. The maximum decrease in the COP with respect to the no wall case is 13.3% and this at the lowerst mass flow rate of 0.3 kg/s. As the mass flow rate increases, the percent decrease in the COP reaches a minimum value of 2.6% at around 0.08 kg/s. The maximum percent decrease in the refrigeration capacity is 4.8% at a mass flow rate of about 0.1 kg/s. As the mass flow rate decreases, the percent decrease ranges between 2.5% and 3.6%. It is clear when comparing Figure 20 and Figure 21 that an increase in the thermal conductivity of the wall will lead to a larger decrease in the regenerator performance.

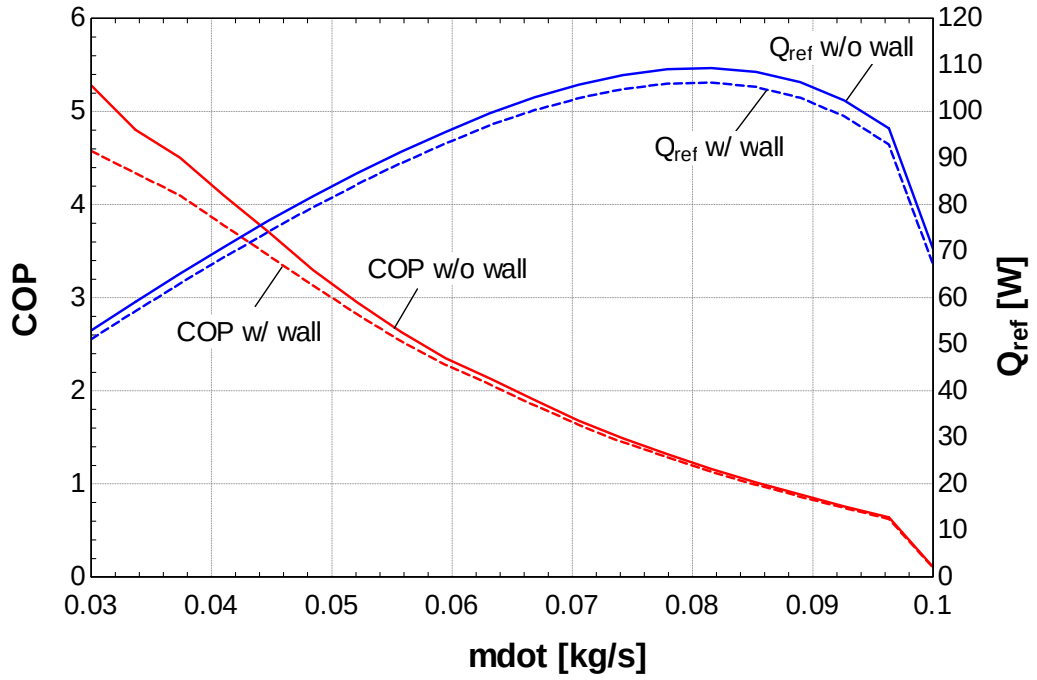

Figure 21: COP and refrigeration curve for k_w = 250 W/m-K

3.2 Dimensionless numbers

Determination of Dimensionless Numbers

From the mass flow rate study above, it is apparent that the housing can lead to a decrease in the regenerator performance. It is therefore important to establish design criteria for the housing that will minimize the adverse effects on the regenerator performance. To accomplish this, it is necessary to express relationships between the properties of the wall to other properties in the regenerator. By defining meaningful dimensionless numbers that relate the wall properties to either the fluid or regenerator solid properties, general design considerations can be established.

There are two main methods for determining the dimensionless numbers that govern a problem. The first is to non-dimensionalize the governing partial differential equations and see which non-dimensional numbers arise while the other method is to use Buckingham Pi theory to determine all possible dimensionless numbers. While option one is favorable to options two, non-dimensionalizing the governing PDE's for this model is difficult mainly due to the entropy change with respect to the magnetic field that appears in the magnetocaloric material equations. Therefore, Buckingham Pi analysis can be used to determine some of the possible dimensionless numbers. However, the Buckingham Pi method is tedious and does not always provide physically meaningful dimensionless quantities. So some intuition can be used to define potentially meaningful numbers. One of the first non-dimensional numbers that should be considered is the well-known Reynolds number based on the hydraulic diameter:

$$Re_f = \frac{\varepsilon \rho_f u d_h}{\mu_f} \tag{2.17}$$

The Reynolds number is useful for internal flow problems because it quantifies the flow regime based on the ratio between the inertial forces and the viscous forces. The Reynolds number for this analysis will be chosen based on the mass flow rates from section 3.1. The next non-dimensional number that is considered is the ratio between the total thermal mass of the wall to the total thermal mass of the regenerator solid.

$$\psi = \frac{m_w c_w}{m_s c_s} \tag{2.38}$$

The thermal mass ratio is interesting to examine because it dictates which material (the wall or the magnetocaloric material) is likely to absorb and retain thermal energy. Referring back to the boundary condition that couples the fluid to the wall, it can be seen that for this model the wall does not directly contact the magnetocaloric material. Therefore, as the fluid passes through the regenerator there will be a tendency for thermal energy to transfer to or from the wall and the regenerator solid. If the thermal mass of the wall is high enough, thermal energy will tend to transfer to the wall instead of the solid therefore causing a larger impact on the regenerator performance. In the limit where the thermal mass of the wall goes to zero, the wall does not participate and will not impact the regenerator performance. The last non-dimensional number of interest relates to the thermal diffusivity of the wall and is defined as follows:

$$\delta = \frac{\sqrt{\alpha_w t_{sim}}}{W} \tag{2.39}$$

In the limit where the axial conduction in the wall goes to zero, the numerator becomes the depth at which a thermal wave is able to propagate radially through the wall for a given simulation time. Normalizing this value by the wall thickness quantifies the fraction of the wall penetrated by the thermal wave.

3.3 Results

Equations 2.17, 2.38, and 2.39 provide three distinct dimensionless quantities that directly relate to the walls influence on the regenerator. In order to vary these numbers for the parametric study, a base geometry needs to be simulated. The geometry used in section 3.1 (based on Table 6) is used and the dimensionless numbers are varied by changing physical properties of the wall. For instance, Equation 2.38 depends on the mass and specific heat capacity of the wall as well as the mass and specific heat capacity of the solid. Since the magnetocaloric effect leads to a change in the value of the MCM specific heat capacity, the value of the specific heat capacity is set to the value that occurs at the Curie temperature with no magnetic field applied. In addition, the porosity of the regenerator is assumed to be constant and therefore the mass of the magnetocaloric material cannot change. This leaves two values that can be changed in Equation 2.38: the specific heat capacity of the wall or wall thickness. Since the product of the mass and specific heat capacity appear in Equation 2.7, it does not matter which value is augmented to obtain a specific value of ψ. Similarly Equation 2.39 depends on the wall thickness and thermal diffusivity. Equation 2.29 shows that the thermal diffusivity depends on the specific heat capacity, density, and conductivity of the wall. Since the specific heat capacity and density are required for defining ψ, the only values that will be varied for δ is the

thermal conductivity. From section 3.1, it is clear that for this particular geometry there are four cases of mass flow rates that provide the highest COP and refrigeration power: 0.3-0.6 kg/s. These mass flow rates correspond to the following Reynolds numbers: 25, 34, 43, and 52. For each Reynolds number, the thermal mass ratio, ψ, and the thermal wave propagation fraction, δ, will be independently varied from small to large numbers (relative to 1) as follows:

$$0.01 \leq \psi \leq 10 \tag{2.40}$$

$$0.01 \leq \delta \leq 10 \tag{2.41}$$

Looking at these ranges of ψ and δ will allow for a better understanding of what is happening when the dimensionless numbers are much less than 1 and much greater than 1.

Figure 22 shows surface plots of the COP for the corresponding ψ and δ values for the range of Reynolds numbers mentioned above. The COP values are normalized to the case when there is no wall effect (i.e. the wall equation is decoupled from the fluid equation).

Effect of Reynolds Number

Figure 22 shows that as the Reynolds number increases the wall tends to have less of an impact on the regenerator performance. Since the flow is laminar, the transport of energy is mainly due to molecular diffusion. As the Reynolds number increases, the fluid molecules have less time to interact with the wall and consequently transfer less energy than in the case where the Reynolds number is lower. It is clear from Figure 22 that the resulting regenerator performance depends largely on the combination of the thermal mass ratio and the thermal wave propagation fraction. It is therefore necessary to include all three considerations when designing the regenerators housing.

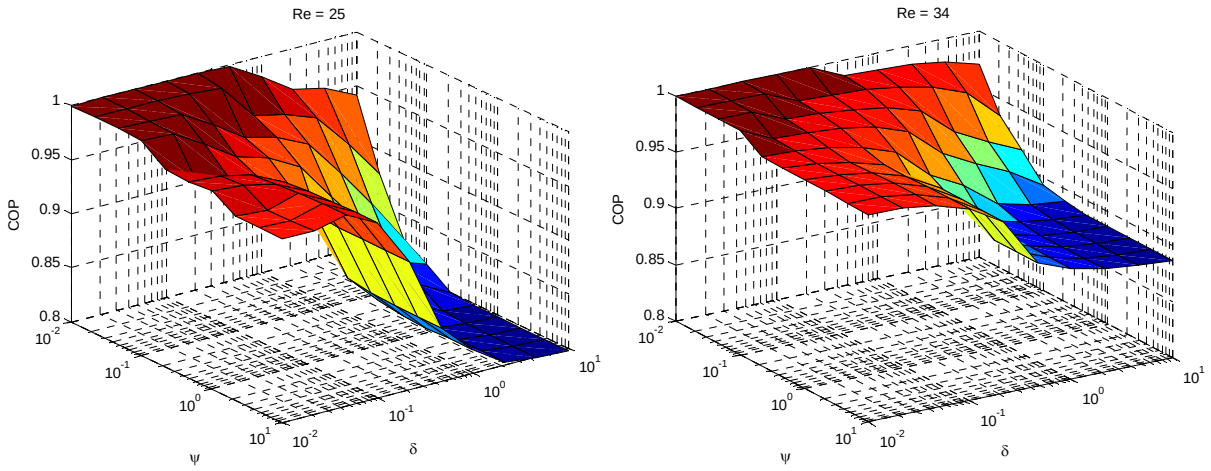

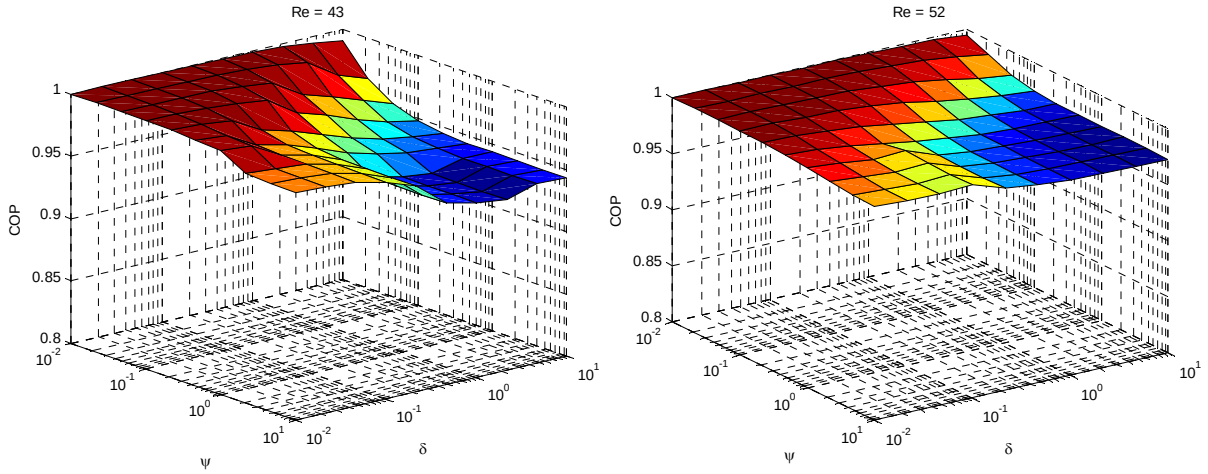

Figure 22: Surface plots of parametric study for various Reynold numbers

Effect of thermal mass ratio

Looking at the case where Reynolds number is the lowest, the effect of the thermal mass ratio is clearly observed. When following lines of constant δ, the COP decreases as the thermal mass ratio increases. This concept is perhaps the easiest to understand. For $\psi < 1$, the thermal mass of the wall is small relative to the thermal mass of the regenerator solid material and as such there is a higher tendency for thermal energy to pass from the fluid to the regenerator solid. Conversely, when $\psi > 1$, the thermal mass of the wall is large relative to the thermal mass of the solid and thermal energy tends to pass from the fluid to the wall. From this, it can be concluded that when designing the housing for a regenerator, the housing material and size must be chosen such that its thermal mass is much less than that of the regenerator solid. In addition to the thermal mass ratio, the regenerator performance also depends on the housing materials ability to conduct thermal energy.

Effect of thermal wave propagation fraction

From Figure 22, it is concluded that even at low thermal mass ratios, the thermal wave propagation fraction can still greatly affect the regenerator performance. As previously mentioned in Section 3.2, the dimensionless number δ is defined as the distance a thermal wave can propagate radially in the wall normalized to the wall thickness. This means that for $\delta = 1$, a thermal wave will propagate through the entire thickness of the wall. For a Reynolds number of 25, it can be seen that for moderately large thermal mass ratios the COP will drastically decrease for small increases in δ. To understand why this is happening, it is interesting to look at a few select cases to see how energy is transferring through the wall material. Figure 23, 24, and 25 show the transient temperature distribution through the wall for cases when $\psi = 10$ and $\delta = 0.01$, $\delta = 1$, and $\delta = 10$ respectively. For the first case when δ = 0.01, a thermal wave can only penetrate a small portion of the wall resulting in the majority of the wall remaining at a constant temperature. In addition, the temperature change of the wall is relatively small over time. In the second case when δ = 1, the thermal wave penetrates the entire thickness of the wall, resulting in a temperature change throughout the entire length. Throughout the simulation, the temperature profile throughout the wall changes with the largest change occurring at the region closest to the fluid. In the third case when δ = 10, the thermal wave

penetrates the entire thickness of the wall almost instantaneously resulting in large temperature changes throughout the entire wall. It is interesting to see that since the conduction occurs so quickly, the entire wall at any instant of time is near constant. Comparing Figure 23, 24, and 25 with Figure 22 , it is clear that large values of δ result in a decrease in COP mainly due to the amount of thermal energy that transfers throughout the entire wall length and it is therefore very important to consider the conduction of thermal energy through the wall.

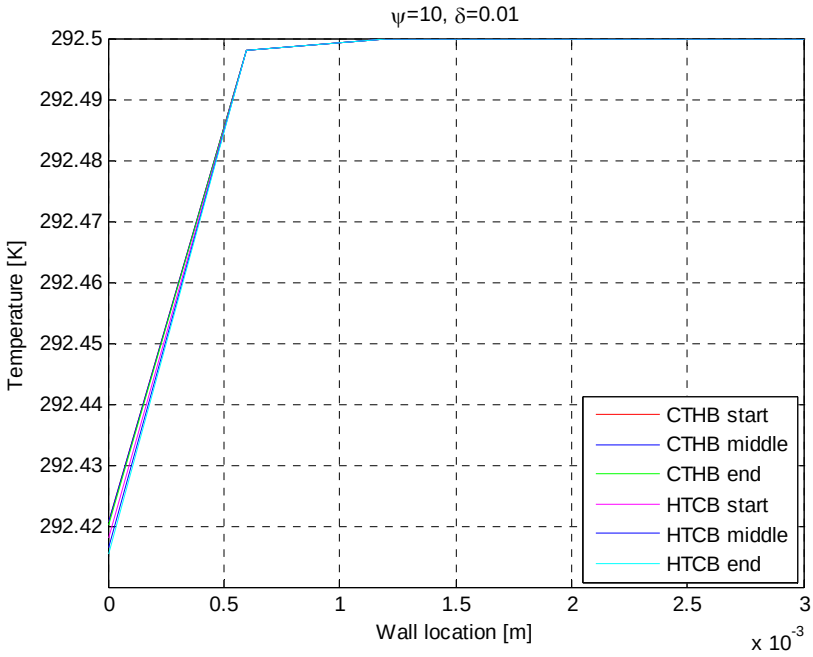

Figure 23: Transient temperature profile for case when ψ=10 and δ=0.01

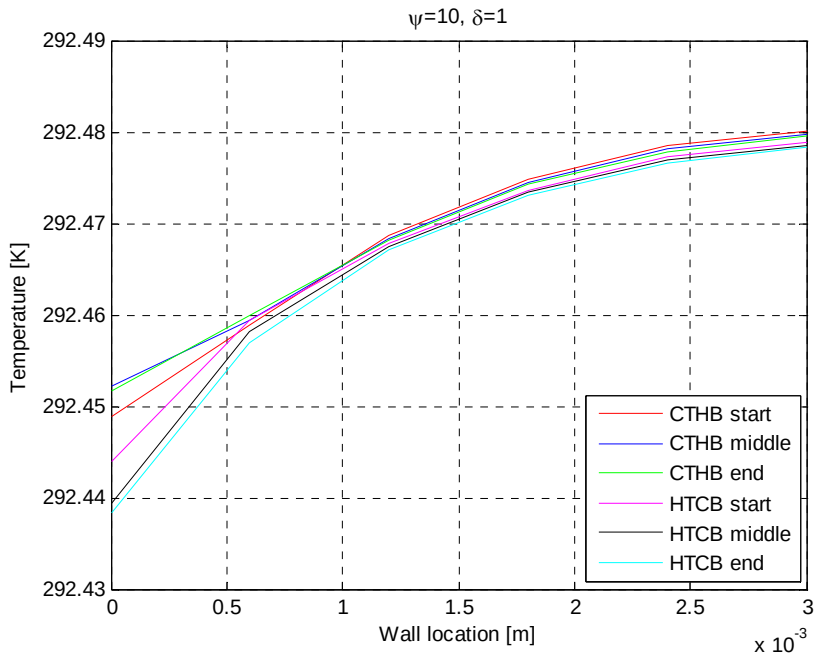

Figure 24: Transient temperature profile for case when ψ=10 and δ=1

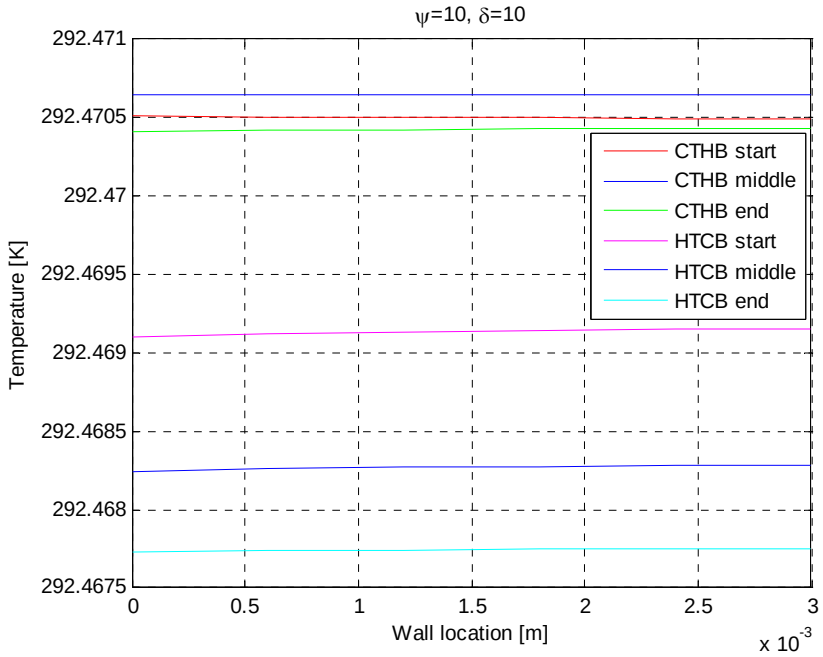

Figure 25: Transient temperature profile for case when ψ=10 and δ=10

Discussion and Conclusion

A 2-D numerical model that simulates the transient thermal process of an Active Magnetic Regenerative Refrigeration system was developed. This 2-D model utilizes a radial geometry and couples the housing to the heat transfer fluid and the regenerator solid. From this, the effect of the housing heat capacity on the regenerator

performance was able to be determined and quantified. Meaningful dimensionless numbers were established to analyze the impact of the housing. Through the study, it was concluded that great care must go into designing the housing for any AMRR system. There are three major considerations that need to be considered concurrently: the Reynolds number of the fluid, the thermal mass ratio of the wall to the solid, and the thermal conduction length through the wall with respect to its thickness. Generally speaking, at low Reynolds numbers, the wall should have a small thermal mass ratio in addition to a small thermal wave conduction length. As the Reynolds number increases, the effects of the wall begin to reduce drastically. The results from this study are very informative and interesting however there are simplifications to the model that could be addressed in future studies.

The model currently assumes the magnetocaloric effect to be reversible and it is suggested that the model be augmented to include the effects of hysteresis. In addition, it is suggested that additional magnetocaloric material properties be added to the model. The magnetocaloric effect of pure Gadolinium is very weak with respect to layered materials that are currently of interest in AMRR systems. It would be interesting to see how the wall impacts the performance when there is a larger temperature gradient in the regenerator.

4 References

[1] V. Pecharsky, K. Gschneidner, "Magnetocaloric effect and magnetic refrigerations,"*Journal of Magnetism and Magnetic Materials*, vol. 200: pp. 44-56, 1999

[2] M. Frischmann, S. Jacobs, G. Nellis, and S. Klein, "Measuring nusselt number using a single-blow regenerator facility," *Third International Conference on Magnetic Refrigeration at Room*, pages 443-448. International Insitute of Refrigeration, 2009

[3] K. Nielsen, G. Nellis, and S. Klein, "Numerical modeling of the impact of regenerator housing on the determination of Nusselt numbers," *International Journal of Heat and Mass Transfer*, pp. 552-560, 2013

[4] E. Warburg. "Magnetische Untersuchungen. I. Uber einige Wirkungen der Coercitivkraft." *Ann Phys* 1881;13:141-164

[5] P. Debye. "Einige Bemerkungen zur Magnetisierung bei tiefer temperature." *Ann Phys* 1926;81:1154-1160.

[6] W.F. Giauque. "A thermodynamic treatment of certain magnetic effects. A proposed method of producing temperatures considerably below 1° absolute." *J Amer Chem Soc* 1927;49:1864-1870

[7] W.F. Giauque, I.D.P. MacDougall. "Attainment of Temperatures Below 1° absolute by demagnetization of $Gd_2(SO_4)_3 \cdot 8H_2O$." *Phys. Rev.* 1933;43:768.

[8] J. Dunning-Davies. "Concise Thermodynamics: Principles and Applications in Physical Science and Engineering," Cambridge 2007:47

[9] Guggenheim E.A. "Thermodynamics, an Advanced Treatment for Chemists and Physicists," North Holland, Amsterdam, 1967.

[10] W. Brey, "A Thermodynamic Model of Magnetic Hysteresis in Active Magnetic Regenerative Refrigeration (AMRR) Cycles." M.S. Thesis, University of Wisconsin-Madison, 2012

[11] K. Engelbrecht, "A numerical model of an active magnetic regenerator refrigerator with experimental validation," Ph.D. Thesis, University of Wisconsin-Madison. 2008

[12] N. Wakao and S. Kaguei, *Heat and Mass Transfer in Packed Beds*. Gordon and Breach Science Publishers, New York, NY. Chapter 8, 1982.

[13] S. Ergun, "Fluid Flow through Packed Column," *Chemical Engineering Progress*, 48(2):125-127.

[14] M. Kaviany, *Principles of Heat Transfer in Porous Media*. Springer, New York, NY. Pp 33,46-47,130,228-229.

[15] T. Özgümüş. "Thermal Dispersion in Porous Media – A Review on Approaches in Experimental Studies." *6th International Advanced Technologies Symposium*. 266-271, 2011.

[16] G.R. Hadley, "Thermal Conductivity of Packed Metal Powders," *Internation Journal of Heat and Mass Transfer,* 78:23:3675,2001

[17] J.M.P.Q. Delgado. "A critical review of dispersion in packed beds." *Heat and Mass Transfer*, 29:909-920,1986.

[18] T. Schumann. "Heat Transfer: A liquid flowing through a porous prism," *Journal of The Franklin Institute*, 208(3): 405-416, 1929.

[19] G. Dragutinov and B. Baclic, *Operation of Counterflow Regenerators*, vol. 4 of *International Series on Developments in Heat Transfer*. Computational Mechanics Publications, 1998.

Appendix A – Definition of Terms

The thermal conductance terms that appear in Equations 2.2, 2.4, and 2.6 are presented. The thermal conductance terms for fluid Equations 2.2 are defined as follows:

$$D_{f_{i,j+1}} = \frac{1}{\frac{1}{2\pi\left(r_j + \Delta r_j/2\right)\Delta x}\left(\frac{\Delta r_{j+1}/2}{k_{disp,r_{i,j+1}}} + \frac{\Delta r_j/2}{k_{disp,r_{i,j}}}\right)} \tag{A.1}$$

$$D_{f_{i,j-1}} = \frac{1}{\frac{1}{2\pi\left(r_j - \Delta r_j/2\right)\Delta x}\left(\frac{\Delta r_j/2}{k_{disp,r_{i,j}}} + \frac{\Delta r_{j-1}/2}{k_{disp,r_{i,j-1}}}\right)} \tag{A.2}$$

$$D_{f_{i+1,j}} = \frac{1}{\frac{\Delta x/2}{2\pi r_j \Delta r_j}\left(\frac{1}{k_{disp,x_{i+1,j}}} + \frac{1}{k_{disp,x_{i,j}}}\right)} \tag{A.3}$$

$$D_{f_{i-1,j}} = \frac{1}{\frac{\Delta x/2}{2\pi r_j \Delta r_j}\left(\frac{1}{k_{disp,x_{i,j}}} + \frac{1}{k_{disp,x_{i-1,j}}}\right)} \tag{A.4}$$

The viscous dissipation generation term is defined as:

$$\dot{g}_v''' = \frac{\Delta P \dot{m}}{\rho_f L A_c} \tag{A.5}$$

The thermal conductance terms for solid Equation 2.4 are defined as:

$$D_{s_{i,j+1}} = \frac{1}{\frac{1}{2\pi(r_j + \Delta r_j/2)\Delta x}\left(\frac{\Delta r_{j+1}/2}{k_{stat_{i,j+1}}} + \frac{\Delta r_j/2}{k_{stat_{i,j}}}\right)} \tag{A.6}$$

$$D_{s_{i,j-1}} = \frac{1}{\frac{1}{2\pi(r_j - \Delta r_j/2)\Delta x}\left(\frac{\Delta r_j/2}{k_{stat_{i,j}}} + \frac{\Delta r_{j-1}/2}{k_{stat_{i,j-1}}}\right)} \tag{A.7}$$

$$D_{s_{i+1,j}} = \frac{1}{\frac{\Delta x/2}{2\pi r_j \Delta r_j}\left(\frac{1}{k_{stat_{i+1,j}}} + \frac{1}{k_{stat_{i,j}}}\right)} \tag{A.8}$$

$$D_{s_{i-1,j}} = \frac{1}{\frac{\Delta x/2}{2\pi r_j \Delta r_j}\left(\frac{1}{k_{stat_{i,j}}} + \frac{1}{k_{stat_{i-1,j}}}\right)} \tag{A.9}$$

The thermal conduction terms for wall Equation 2.6 are defined as:

$$D_{w_{i,j+1}} = \frac{1}{\frac{1}{2\pi(r_j + \Delta r_j/2)\Delta x}\left(\frac{\Delta r_{j+1}/2}{k_{w_{i,j+1}}} + \frac{\Delta r_j/2}{k_{w_{i,j}}}\right)} \tag{A.10}$$

$$D_{w_{i,j-1}} = \frac{1}{\frac{1}{2\pi(r_j - \Delta r_j/2)\Delta x}\left(\frac{\Delta r_j/2}{k_{w_{i,j}}} + \frac{\Delta r_{j-1}/2}{k_{w_{i,j-1}}}\right)} \tag{A.11}$$

$$D_{w_{i+1,j}} = \frac{1}{\frac{\Delta x/2}{2\pi r_j \Delta r_j}\left(\frac{1}{k_{w_{i+1,j}}} + \frac{1}{k_{w_{i,j}}}\right)} \tag{A.12}$$

$$D_{w_{i-1,j}} = \frac{1}{\frac{\Delta x/2}{2\pi r_j \Delta r_j}\left(\frac{1}{k_{w_{i,j}}} + \frac{1}{k_{w_{i-1,j}}}\right)} \tag{A.13}$$